Department of Physics and Astronomy
University of Heidelberg

Master Thesis in Physics
submitted by

Tim Zimmermann

born in Nürtingen (Germany)

2020

An Investigation of the Lower Dimensional Dynamics of Fuzzy Dark Matter

This Master Thesis has been carried out by Tim Zimmermann at the
Institute for Theoretical Physics
under the supervision of
Prof. Dr. Luca Amendola
and
Prof. Dr. Sandro Wimberger.

Abstract

Due to the lack of experimental evidence for weakly interacting particles (WIMPs) and the unsatisfying numerical predictions of the established cold dark matter (CDM) paradigm on galactic scales, alternative dark matter models remain an intriguing and active field of research.

A model of recent interest in cosmology is Fuzzy Dark Matter (FDM) which assumes the nonbaryonic matter component of the universe to consist of scalar bosons with mass $m \sim 10^{-22}$ eV. FDM possesses a rich phenomenology in $(3+1)$ dimensions recovering predictions of CDM on large scales while suppressing structure growth below the de-Broglie wavelength which, due to the miniscule boson mass, attains values of galactic size.

As full fledged $(3+1)$-dimensional, cosmological simulations, especially for FDM, are extremely time consuming this thesis investigates to what extend phenomena in three spatial dimensions can be observed with only one geometric degree of freedom. To this end, a first principle derivation of the governing equation of FDM, i.e. $(3+1)$-Schrödinger-Poisson (SP) is presented and dimensionally reduced to two distinct $(1+1)$-FDM representations, namely (i) the standard $(1+1)$-SP equation and (ii) the novel periodic, line adiabatic model (PLAM). After investigating the nature of FDM in linear theory, we present a comprehensive, unified and thoroughly tested numerical method capable of integrating both reduction models into the nonlinear regime. By analyzing an ensemble of high-resolution, cosmological simulation runs, we find standard $(1+1)$-SP to only partially recover the sought after asymptotic dynamics of $(3+1)$-FDM — a result which holds true even under simplified initial conditions or expansion free scenarios. PLAM, on the other hand, shows the most prominent feature of full fledged FDM — a solitonic, dynamical attractor — for both expanding and static background cosmologies. We argue the discrepancy between the models lies in the different nonlocality of the underlying nonlinear interaction and substantiate this with numerical and analytical arguments. Moreover, our results indicate that independent of the reduction model used, the long term dynamics is best understood as a consequence of thermodynamics aiming to maximize the system's entropy.

Zusammenfassung

Alternative Dark Matter Modelle stellen aufgrund fehlender experimenteller Evidenz für die Existenz von WIMPs sowie unzureichender numerischer Vorhersagen des etablierten Modells kalter, dunkler Materie (CDM) ein attraktives und aktives Forschungsgebiet dar.

Insbesondere Fuzzy Dark Matter (FDM) gilt als vielversprechende Dark Matter Theorie, in der nicht-baryonische Materie als skalare Bosonen mit Masse $m \sim 10^{-22}$ eV modelliert wird. Zu den wichtigsten Charakteristika FDMs zählen die Übereinstimmung mit dem CDM Paradigma auf großen Längenskalen sowie die Unterdrückung nicht-linearer Materiestrukturen unterhalb der bosonischen de-Broglie Wellenlänge, die aufgrund der winzigen Teilchenmasse kosmisch relevante Größe annimmt.

Da großskalige, hochauflösende (FDM) Simulationen dunkler Materie in $(3+1)$-Dimensionen extrem zeitaufwendig sind, stellt sich die Frage ob und wie charakteristische Eigenschaften FDMs auch in lediglich einer Raumdimension realisiert werden können. Untersuchung dieses Aspektes ist Gegenstand dieser Arbeit. Ausgangspunkt hierfür bildet die Herleitung der FDM Evolutionsgleichung, die $(3+1)$-Schrödinger-Poisson (SP) Gleichung, sowie eine detaillierte Dimensionsreduktion resultierend in (i) der Standard $(1+1)$-SP Gleichung und (ii) des periodisierten "line adiabatic models"(PLAM). Wir kontrastieren das Verhalten von FDM und CDM in linearer Ordnung und präsentieren des Weiteren eine einheitliche, ausführlich getestete, numerische Methode, mit derer beide niederdimensionale FDM Repräsentationen bis ins nichtlineare Regime integriert werden können. Die ausührliche Analyse eines Ensembles hochauflösender, kosmologischer Simulationen zeigt das Versagen $(1+1)$-SPs wesentliche Eigenschaften der $(3+1)$-FDM Phänomenologie in einer Dimension abzubilden — auch nicht unter vereinfachten Anfangsbedigungen oder expansionsfreien Szenarien. PLAM, anderseits, realisiert mit der Existenz eines solitonischen, dynamischen Attraktors die wohl wichtigste Eigenschaft FDMs, sowohl für statische wie auch expandierende Hintergrundkosmolgien. Auf Basis analytisch-numerischer Argumente interpretieren wir dieses Verhalten als Konsequenz der verschiedenen Nicht-Lokalitäteten in der Wechselwirkung beider Modelle. Unabhängig vom Reduktionsmodell indizieren die präsentierten Resultate die Anwendbarkeit thermodynamischer Prinzipien für die Beschreibung der asymptotischen Systemzustandes, insbesondere die Gültigkeit des Maximum Entropie Prinzips.

Contents

Chapter 1

Motivation

While ordinary, baryonic matter contributes only $\sim 5\%$ to the total energy budget of the observable universe, origin and physical nature of the remaining $\sim 95\%$ are still an open question. In fact, gaining a fundamental understanding of the "dark sector", which consists of dark matter ($\sim 25\%$) and dark energy ($\sim 70\%$), is arguably the largest challenge in modern cosmology.

Until such a fundamental understanding becomes available a parametrized theory — the standard model of cosmology — takes its place. In it, dark energy is interpreted as constant vacuum energy density set by the cosmological constant Λ. Dark matter, on the other hand, is modeled as massive, exclusively gravitationally interacting particles with vanishing thermal velocity. It is the latter property that qualifies dark matter to be cold (CDM) and gives the standard model its name — ΛCDM.

While the established ΛCDM paradigm, [64], is a long standing, well understood theory, it was only the advent of high resolution, large scale cosmological simulations [73] that allowed detailed predictions of structure growth in the deeply nonlinear evolution regime. Comparison with observation data proofed ΛCDM to be a superb description for the *large scale* structure of the universe and promoted the theory to a corner stone of modern cosmology.

Although successful on large scales, there are still significant discrepancies between the observed small scale structure and numerical predictions. These problems are commonly referred to as the "small scale crisis" of CDM, see [17] for a review.

For instance, according to simulations dark matter halos, i.e. gravitationally collapsed and dynamically relaxed dark matter clumps, are expected to have a rich substructure containing thousands of sub-halos many of which should be hosts to observable satellite galaxies. On the other hand, we only know about ~ 50 satellites of the Milky way. This overabundance of small scale structure under ΛCDM is coined the "missing satellite problem".

Also puzzling is the fact that dark matter halos of satellite galaxies which we *can* observe would not even be the largest sub-halos one has to expect from a Milky way-sized host galaxy — at least according the CDM simulations. Naturally, one must ask what happened to even more massive sub-halos, which would have been "too big to fail" their existence due to processes like baryonic feedback.

At last, we mention the quite universal shape of CDM halos well approximated by the famous NFW profiles, [61]. At small radii these predict $\rho(r) \propto r^{-1}$. However, such a steep, cuspy core is not suggested by dark matter dominated, dwarf spherical galaxies (dSphs). Instead, dSphs favor a flat, cored halo center and thus give rise to the "cusp-core problem".

There are multiple approaches in solving these dilemmas, all of which aim at smoothing out structure growth at galactic or sub-galactic scales and can be generally understood as extensions, modifications or replacements of CDM.

We already mentioned the incorporation of baryonic physics as a viable extension of cold dark matter dynamics. Here cataclysmic events auch as supernovae provide a baryonic feedback mechanism for dark matter potentially destroying small, gravitationally bound structures or influencing the internal structure of larger halos.

A common modification of CDM is to relax the assumption of it being perfectly cold, i.e. vanishing thermal velocity. Warming the nonbaryonic matter to $\sim 10\mathrm{m\,s}^{-1}$ implements a thermally driven dispersion effect, therefore smoothing out structure growth on small scales. This is warm dark matter (WDM).

More radically, one can also discard CDM all together and replace it with an alternative dark matter model that (i) recovers CDM at super-galactic scales and (ii) behaves different than CDM on sub-galactic distances. Note this approach is not at odds with the current understanding of dark matter. In fact, it's fundamental character is still an open question and CDM is therefore also just a phenomenological theory.

A particularly interesting alternative dark matter model is *Fuzzy Dark Matter*, [41], or FDM in short. FDM assumes dark matter to be a bosonic scalar field of ultralight particles with mass $m \approx 10^{-22}$ eV and in the nonrelativistic limit governed by the $(3+1)$ Schrödinger-Poisson (SP) equation. It is this miniscule mass which magnifies the de-Broglie wavelength to $\lambda_{\mathrm{dB}} \sim 1$kpc. We therefore expect quantum effects to act on galactic scales, in particular a spatial smoothing due to the uncertainty principle. On the other hand, casting the governing equations into hydrodynamic form reveals the scalar field to be well described by a comoving Euler-Poisson equation, at least on scales on which gradients of the matter density are small, i.e. at large wavelengths. Consequently, one expects FDM to behave as a classical cosmic fluid on super-galactic distances therefore recovering CDM predictions.

Although the following discussion will accept the scalar field approach as is, we quote ultralight axions as possible FDM particle candidate — pseudo Nambu-Goldstone bosons that arise from a spontaneous breaking of an approximate shift symmetry [4, 42].

One of the most prominent properties of FDM is the existence of stable density configurations, known as *solitons*. Already early on in the development of the model it was found that these special states act as dynamical attractor in the evolution of the scalar field, [37], and provide a natural realization of a flat halo core, free of any cusps. Moreover, high resolution $(3+1)$-dimensional simulations of cosmological initial conditions, [67], found solitons to not just constitute the core of each relaxed FDM structure but also being surrounded by a power-law like matter halo decaying as $\rho \propto r^{-3}$ — exactly as NFW profiles predict.

While possible on supercomputing clusters, numerical studies of (3+1) dimensional FDM remain extremely demanding. This is an inherent problem of the Eulerian point of view suggested by Schrödinger's equation and the vastly different spatial scales which need to be resolved. These range from $\sim 10\,\mathrm{Mpc}$ domains down to small scale structure of only $\sim 100\,\mathrm{pc}$. By contrast, N-Body problems, i.e. the canonical approach in simulating CDM, are inherently Lagrangian and the "spatial grid" does consequently not have any resolution limits. Sophisticated numerical methods, [67], are required to make the integration of $(3+1)$-SP a tractable problem for even mid-sized boxes. Naturally, one can ask if lower dimensional representations, being certainly cheaper to work with compared to $(3+1)$-SP, are useful to learn something about the behavior of full fledged $(3+1)$-FDM: How does power evolve on small and large scales as a function of redshift? Can we recover the large scale CDM evolution? Does nonlinear mode coupling occur? What is the physical character of the relaxation process? What its associated time scale? How does space-time expansion impact the relaxation process? Can we realize a lower dimensional analogue of the solitonic core? This thesis attempts to answer all these questions and is structured as follows:

Chapter 2 derives $(3+1)$-SP from first principles, section 2.1 - 2.2, and discusses a variety of different physical interpretations for it, section 2.2.1. A careful dimension reduction of the three-dimensional problem in section 2.3 leads up to two distinct one dimensional representations of FDM: (i) the naive $(1+1)$-SP equation and (ii) the novel line adiabatic model (PLAM) which is arguably closer to the original long range interaction of $(3+1)$-SP while not imposing any symmetry assumptions on the original scalar field. Crucial differences between both reduction models, especially in terms of their long range interactions and admitted symmetries, section 2.4, are discussed.

Chapter 3 introduces key statistical observables such as the matter power spectrum or correlation function, section 3.1, and investigates discrepancies in their evolution under FDM and CDM in linear theory, section 3.2. Moreover, construction of one-dimensional cosmological initial conditions for FDM will be discussed in section 3.3.

Before embarking on an in-depth analysis of the nonlinear $(1+1)$-SP evolution under cosmological conditions in chapter 5, we present a comprehensive, easy to implement and thoroughly tested numerical method for integrating both $(1+1)$-SP and PLAM in chapter 4. This entails an overview of existing techniques for integrating FDM, section 4.1, as well as an exposition of the spatial discretization and details of the time propagation under expanding space-time conditions, see sections 4.2 - 4.3. Properties of the devised scheme, especially concerning convergence and stability, are summarized in section 4.4.

Following the evolution of the matter power spectrum in section 5.2 shows clear imprints of the galactic-scale uncertainty principle. By investigating an ensemble of cosmological random fields in section 5.2.1, we are able to give a quantitative estimate on which spatial scales one should expect to see modifications of the nonlinear power spectrum. Systematic effects inherent to FDM and their impact on the large scale evolution and mode coupling are analyzed in section 5.2.2-5.2.3. Section 5.3 focuses on the failure of $(1+1)$-SP in reaching the asymptotic soliton configuration known from $(3+1)$-SP.

Chapter 6 analyses and explains dynamical discrepancies between both reduction models, especially with respect to the attained asymptotic state and underlying relaxation mechanism. More precisely, we discuss virialization and thermalization as possible processes driving the system towards equilibrium in section 6.1. Section 6.2 is devoted to the preparation and the distinctive properties of the FDM soliton in one spatial dimension. The static space-time considerations of section 6.3 reveal PLAM to follow "soliton turbulence" dynamics ultimately attaining the sought after single-soliton state known from $(3+1)$-SP. On the other hand, $(1+1)$-SP obeys "incoherent soliton dynamics" producing halo profiles consistent with lower dimensional models of CDM. However, it still fails to realize a solitonic density core. Inspired by results from nonlinear optics and the properties deduced in section 2.3 and 6.2, section 6.3.3 argues $(1+1)$-SP is incapable to form solitons, irrespective of the physical parameters used. The dynamic space-time considerations of section 6.4 substantiate this result.

We conclude and extend this thesis in chapter 7. To keep the discussion compact longer mathematical asides and supplementary material are deferred to Appendix A-C.

Chapter 2

Fuzzy Dark Matter from First Principles

Purpose of this chapter is to give a reasonably self-contained derivation of the governing dynamical equations of *Fuzzy Dark Matter* (FDM) in $d = 1, 2, 3$ spatial dimensions starting from first principles. In [85, 86] we only gave an a posteriori justification off the correctness of the $(3 + 1)$-dynamical equations by the correspondence with Vlasov's equation in the semi-classical limit $\hbar \to 0$, see [76]. Informations about the dimension reduction were completely omitted. The results of this chapter, in particular the one-dimensional models of FDM will form the basis of our numerical investigations in chapter 4 - 6

More rigorously, Schrödinger-Poisson (SP), i.e. the evolution equation of FDM, emerges as the non-relativistic limit of the Klein-Gordon-Einstein equation (KGE) for which the space-time geometry is set by a perturbed Friedmann-Lemaître-Robertson-Walker (FLRW) metric in Newtonian gauge.

After deriving the $(3 + 1)$-SP equation from first principles and discussing it's interpretation, we contrast two different approaches how the three dimensional problem can be reduced to lower dimensions. The result will be the (i) the $(d+1)$-SP equation and (ii) the periodic, line adiabatic model valid for $d = 1$ spatial degree of freedom. Crucial differences of both reduction procedures and their resulting dynamical models will be emphasized.

A unified description for both models is the nonlinear Schrödinger equation (NLSE) with a convolution-type, non-local interaction potential and it is only the convolution kernel which changes as one replaces $(1 + 1)$-SP with PLAM. The NLSE is therefore main subject in our closing discussion on conserved quantities and symmetries of the $(1 + 1)$-dimensional dynamics. It also builds the foundation for the numerical considerations in chapter 4.

The discussion follows closely the arguments given in [75] for the derivation of the $(3+1)$-SP equations and adopts the approach given in [9] for reducing the number of spatial dimensions. Along the way, we also hint at how relativistic corrections could be realized in future works. The latter is motivated by the results presented in [48, 33].

2.1 General Relativistic Considerations

Our starting point must be GR. We are somewhat brief in this section because the formalism is well established by any textbook on GR, e.g. [79], and calculation tend to be lengthy with limited physical insight.

2.1.1 Derivation of the Klein-Gordon-Einstein Equation

The dynamics of the space-time geometry as well as of all matter contained in it can be found by varying the action, [11]:

$$\mathcal{S} = \int \mathrm{d}^4 x \sqrt{-g} \left(\mathcal{R} - 2\Lambda + \frac{16\pi G}{c^4} \mathcal{L}_{\mathrm{matter}} \right) . \tag{2.1}$$

Here g denotes the determinant of the metric $g_{\mu\nu}$ for which we adopt the "mostly plus" sign convention $(- + + +)$. $\mathcal{R}$ and Λ are the Ricci scalar and the cosmological constant respectively, G is Newton's gravitational constant. Let dark matter now be modeled by means of a massive, complex scalar $\varphi(x^\mu)$ minimally coupled to the space-time geometry:

$$\mathcal{L}_{\mathrm{matter}} = \mathcal{L}_\varphi = -\frac{1}{2} \partial_\mu \varphi^* \partial^\mu \varphi - V(|\varphi|^2) , \tag{2.2}$$

with potential:

$$V(|\varphi|^2) = \frac{m^2 c^2}{2\hbar^2} |\varphi|^2 . \tag{2.3}$$

Here m is the dark matter particle mass. Note that (i) partial derivatives are sufficient in this context because φ is a scalar and (ii) we deliberately keep factors of c in our derivation as we later on perform an expansion in powers of $1/c$ to arrive at the non-relativistic limit of the theory.

Setting the variation of (2.1), δS, with respect to φ to zero is equivalent to solving the Euler-Lagrange equation,

$$\nabla_\mu \left(\frac{\partial \mathcal{L}}{\partial \left(\partial_\mu \varphi^* \right)} \right) - \frac{\partial \mathcal{L}}{\partial \varphi^*} = 0 , \tag{2.4}$$

which is readily done:

$$\Box \varphi \equiv \nabla_\mu (\partial^\mu \varphi) = \frac{m^2 c^2}{\hbar^2} \varphi . \tag{2.5}$$

This is *Klein-Gordon's equation.* In order to make further progress we need to express the covariant derivative on the left hand side more explicitely. This is most easily done by realizing that the covariant divergence of the vector $\partial^\mu \varphi$ can be written as:

$$\nabla_\mu \left(\partial^\mu \varphi \right) = \frac{1}{\sqrt{-g}} \partial_\mu \left(\sqrt{-g} g^{\mu\nu} \partial_\nu \right) . \tag{2.6}$$

If we consider a *zero curvature* FLRW universe, perturbed by a weak scalar field Φ then the space-time element reads:

$$\mathrm{d}s^2 = -\left(1 + \frac{2\Phi}{c^2} \right) c^2 \mathrm{d}t^2 + a(t)^2 \left(1 - \frac{2\Phi}{c^2} \right) \delta_{ij} \mathrm{d}x^i \mathrm{d}x^j . \tag{2.7}$$

Here weak is meant in the sense that $\Phi/c^2 \ll 1$, thus in the following, we will exclude terms up to $\mathcal{O}\left[\left(\frac{\Phi}{c^2}\right)^2\right]$. As always, x is understood as a comoving coordinate and $a(t)$ is the dimensionless scale factor found by solving Einsteins (or equivalently Friedmann's equation) for the unperturbed, $\Phi = 0$, problem. t denotes *cosmic time*.

To compute (2.6) both the inverse metric $g^{\mu\nu}$ and the metric determinant up the first order in Φ/c^2 are required. It is easily verified that:

$$g^{\mu\nu} = \begin{pmatrix} -\left(1-\frac{2\Phi}{c^2}\right) & 0 & 0 & 0 \\ 0 & \frac{1}{a^2}\left(1+\frac{2\Phi}{c^2}\right) & 0 & 0 \\ 0 & 0 & \frac{1}{a^2}\left(1+\frac{2\Phi}{c^2}\right) & 0 \\ 0 & 0 & 0 & \frac{1}{a^2}\left(1+\frac{2\Phi}{c^2}\right) \end{pmatrix} \tag{2.8}$$

satisfies $g_{\mu\sigma}g^{\sigma\nu} = \delta^\nu_\mu + \mathcal{O}\left[\left(\frac{\Phi}{c^2}\right)^2\right]$ and

$$g = -a^6\left(1 - 4\frac{\Phi}{c^2}\right) + \mathcal{O}\left[\left(\frac{\Phi}{c^2}\right)^2\right] . \tag{2.9}$$

Substituting (2.8) and (2.9) into (2.6) and dropping all terms quadratic in Φ yields after some algebra the Klein-Gordon equation incorporating our choice of the metric (2.7),

$$\frac{1}{c^2}\partial_t^2\varphi - \frac{1}{a^2}\left(1+4\frac{\Phi}{c^2}\right)\triangle\varphi + \frac{3H}{c^2}\partial_t\varphi - \frac{4}{c^4}\partial_t\Phi\partial_t\varphi + \left(1+2\frac{\Phi}{c^2}\right)\frac{m^2c^2}{\hbar^2}\varphi = 0 \ , \tag{2.10}$$

where we defined the Hubble parameter $H = \dot{a}/a$.

To close the system we need an equation for the scalar perturbation Φ which is found by considering *Einstein's field equation*:

$$R_{\mu\nu} - \frac{1}{2}\mathcal{R}g_{\mu\nu} + \Lambda g_{\mu\nu} = \frac{8\pi G}{c^4}T_{\mu\nu} \ . \tag{2.11}$$

with $R_{\mu\nu}$ as Ricci tensor. Eq. (2.11) is obtained by varying (2.1) with respect to the metric in the process of which we define the Einstein-Hilbert energy momentum tensor $T_{\mu\nu}$ as:

$$T_{\mu\nu} = -2\frac{\partial\mathcal{L}}{\partial g^{\mu\nu}} + \mathcal{L}g_{\mu\nu} \ . \tag{2.12}$$

Using the Lagrangian (2.2) and $\frac{\partial g^{\alpha\beta}}{\partial g^{\mu\nu}} = \frac{1}{2}\left(\delta^\alpha_\mu\delta^\beta_\nu + \delta^\beta_\mu\delta^\alpha_\nu\right)$, one arrives at the well known energy momentum tensor of a complex scalar field:

$$T_{\mu\nu} = \frac{1}{2}\left(\partial_\mu\varphi^*\partial_\nu\varphi + \partial_\mu\varphi^*\partial_\nu\varphi\right) - g_{\mu\nu}\left(\frac{1}{2}g^{\alpha\beta}\partial_\alpha\varphi^*\partial_\beta\varphi + \frac{m^2c^2}{2\hbar^2}|\varphi|^2\right) \ . \tag{2.13}$$

For later use we also compute the energy density ϵ of the field given by:

$$\epsilon = -T^0_0 = \frac{1}{2c^2}\left(1-2\frac{\Phi}{c^2}\right)|\partial_t\varphi|^2 + \frac{1}{2a^2}\left(1+2\frac{\Phi}{c^2}\right)|\nabla\varphi|^2 + V(|\varphi|^2) \tag{2.14}$$

as well as its pressure P:

$$\begin{aligned} T = T^\mu_\mu = -\epsilon + 3P \Rightarrow P &\overset{(2.14)}{=} \frac{1}{3}T^i_i \\ &= \frac{1}{2c^2}\left(1-2\frac{\Phi}{c^2}\right)|\partial_t\varphi|^2 + \frac{1}{6a^2}\left(1+2\frac{\Phi}{c^2}\right)|\nabla\varphi|^2 - V(|\varphi|^2) \ . \end{aligned} \tag{2.15}$$

Back to eq. (2.11) and our objective of deriving an equation for Φ. Consider the mixed tt-component of eq. (2.11):

$$R^0_0 - \frac{1}{2}\mathcal{R} + \Lambda = -\frac{8\pi G}{c^4}\epsilon \ . \tag{2.16}$$

The Ricci tensor, $R_{\mu\nu}$, and its trace, the Ricci scalar $\mathcal{R}$ are determined via:

$$R_{\mu\nu} = 2\left(\Gamma^\rho_{\mu[\nu,\rho]} + \Gamma^\rho_{\lambda[\rho}\Gamma^\lambda_{\nu]\mu}\right) \ , \qquad \mathcal{R} = g^{\mu\nu}R_{\nu\mu} \ , \tag{2.17}$$

with $\Gamma^\rho_{\mu\nu}$ as Chistoffel symbols and $[\dots]$ denoting index anti-symmetrization. Computing these objects is best done via a symbolic math program such as `Mathematica`. Up to first order in Φ/c^2 eq. (2.16) yields:

$$\begin{aligned}\triangle\Phi &= 4\pi G a^2\left[\frac{\epsilon}{c^2} - \frac{3H^2}{8\pi G} + \frac{3H}{4\pi G c^2}\left(\partial_t\Phi + H\Phi\right) + \frac{c^2}{8\pi G}\Lambda\right] \\ &= 4\pi G a^2\left[\frac{1}{2c^4}\left(1 - 2\frac{\Phi}{c^2}\right)|\partial_t\varphi|^2 + \frac{1}{2c^2a^2}\left(1 + 2\frac{\Phi}{c^2}\right)|\nabla\varphi|^2 + \frac{1}{c^2}V(|\varphi|^2)\right. \\ &\qquad\left. - \frac{3H^2}{8\pi G} + \frac{3H}{4\pi G c^2}\left(\partial_t\Phi + H\Phi\right) + \frac{c^2}{8\pi G}\Lambda\right] \ .\end{aligned} \tag{2.18}$$

Eq. (2.10) together with (2.18) constitute the weak field *Klein-Gordon-Einstein equations* (KGE).

2.1.2 Recovering the Homogeneous Universe

Although the previous section aimed at deriving the dynamics of a complex, inhomogeneous scalar field in a perturbed FLRW space-time, the formalism obviously contains the unperturbed problem. In fact, we can use the results derived up till now to determine the expansion rate of the background space-time $H(t)$ simply by reinterpreting the meaning of the energy density ϵ.

To see this, set $\varphi(x^\mu) = \varphi(t)$ and $\Phi(x^\mu) = 0$ in accordance with the assumption of an unperturbed, isotropic and homogeneous universe. Due to homogeneity, all off-diagonal components produced by the first term in eq. (2.13) vanish and $T_{\mu\nu}$ becomes the rest frame energy-momentum tensor of a perfect fluid:

$$T^\mu_\nu = \mathrm{Diag}(-\epsilon(t), P(t), P(t), P(t)) \ . \tag{2.19}$$

The standard ΛCDM background cosmology follows by forgetting about the fact that ϵ actually belongs to a scalar field and is given by eq. (2.14) but instead treat it as the energy density composed of a relativistic and non-relativistic perfect fluid component:

$$\epsilon(t) \equiv \epsilon_\gamma(t) + \epsilon_m(t) \ . \tag{2.20}$$

With these definitions in place, eq. (2.18) becomes:

$$H^2 = \left(\frac{\dot{a}}{a}\right)^2 = \frac{8\pi G}{3c^2}\left(\epsilon + \frac{c^4\Lambda}{8\pi G}\right) \quad \Rightarrow \quad E(a)^2 \equiv \left(\frac{H}{H_0}\right)^2 = \frac{1}{\epsilon_\mathrm{c}}\left(\epsilon_\gamma(t) + \epsilon_m(t) + \epsilon_\Lambda\right) \tag{2.21}$$

where we defined:

$$\epsilon_c(t) = \rho_c(t)c^2 = \frac{3H^2(t)c^2}{8\pi G}, \qquad \epsilon_c = \epsilon(t_0) \tag{2.22}$$

as (present day) critical energy density. $\epsilon_\Lambda = \rho_\Lambda c^2 = \frac{c^4\Lambda}{8\pi G}$ denotes the constant vacuum energy density. To keep the notation compact we distinguish present day densities from time dependent densities by an explicit time argument for the latter. Eq. (2.21) is simply the zero-curvature *Friedmann equation*.

Furthermore, if we consider the $\mu = 0$ component of the local energy-momentum conservation,

$$\nabla_\nu T^{0\nu} = 0, \tag{2.23}$$

the well known continuity equation follows:

$$\frac{\mathrm{d}\epsilon}{\mathrm{d}t} + 3H(\epsilon + P) = 0\ . \tag{2.24}$$

Let us summarize a couple of well known results and definitions associated with the Friedmann equation [23], which we will use later on.

Firstly, using the general equation of state $p = w\epsilon$ for non-relativistic matter, $w = 0$, and radiation, $w = \frac{1}{3}$, in eq. (2.24) shows:

$$\epsilon_m \propto a^{-3}, \qquad \epsilon_\gamma \propto a^{-4}\ . \tag{2.25}$$

Given that structure formation sets in deeply in the matter dominated era, we will neglect all radiation contributions and set $\epsilon(t) \equiv \rho_m(t)c^2$.

Next, define density parameters by $\Omega_i(t) \equiv \frac{\epsilon_i(t)}{\epsilon_c(t)}$ for $i \in \{m, \Lambda\}$ as well as their present day values by $\Omega_i \equiv \Omega_i(t_0)$. Eq. (2.21) then takes the form:

$$E(a)^2 = \Omega_m a^{-3} + \Omega_\Lambda\ . \tag{2.26}$$

Recall that with the choice of the metric in eq. (2.7) we restricted ourselves to *flat* FLRW models. Thus, with the definitions made above, one can easily check that for flat models:

$$1 = \Omega_m(t) + \Omega_\Lambda(t) \tag{2.27}$$

holds true for all values of cosmic time t. Let's rephrase this conclusion: The total, *homogeneous* rest mass density of the universe is critical:

$$\rho_c(t) = \rho_m(t) + \rho_\Lambda\ . \tag{2.28}$$

2.2 The Non-Relativistic Limit of KGE — (3+1)-SP

Following [81, 75] we now take

$$\begin{aligned} \varphi(x,t) &= A\exp\left(\frac{imc^2}{\hbar}t\right)\psi(x,t) \\ &= \frac{\hbar}{m}\exp\left(\frac{imc^2}{\hbar}t\right)\psi(x,t) \end{aligned} \tag{2.29}$$

as ansatz in order to arrive at the non-relativistic limit of our theory. This is justified by the solutions of the Klein-Gordon equation for a vanishing potential $\varphi \propto \exp\left(iE/\hbar t\right)$ with $E^2 = \left(mc^2\right)^2 + (pc)^2$. The rest mass energy has been factored out as it should dominate the total energy in the limit $c \to \infty$.

Alternatively, one could consider eq. (2.29) as a WKB-like expansion known from semiclassics, [48]. In this context, however, the expansion is not carried out in powers of $\hbar$ but in $1/c$ and takes the form:

$$\varphi(x,t) \propto \exp\left(\frac{it}{\hbar}\left(c^2 S_0(x,t) + c^0 S_1(x,t)\dots\right)\right) . \tag{2.30}$$

Plugging eq. (2.30) into eq. (2.10) and demanding that all orders in c vanish independently yields equations for the complex coefficients S_n. Ansatz (2.29) then corresponds to a truncation after two terms in the power series and the non-relativistic scalar $\psi = \exp\left(\frac{it}{\hbar}S_1(x,t)\right)$. In principle we could use this procedure to compute relativistic correction terms for the non-relativistic Schrödinger-Poisson equation. However, we will not pursue this idea further at this point but refer to [48, 33].

To fix the prefactor A proceed as outlined in [75] and plug eq. (2.29) into eq. (2.14):

$$\begin{aligned}\epsilon = V(A^2|\psi|^2) + \frac{A^2c^2m^2}{2\hbar^2}\left(1-\frac{2\Phi}{c^2}\right)|\psi|^2 + \frac{A^2}{2a^2}\left(1+\frac{2\Phi}{c^2}\right)|\nabla\psi|^2 \\ + \frac{A^2}{2c^2}\left(1-\frac{2\Phi}{c^2}\right)|\partial_t\psi|^2 - \frac{A^2m}{\hbar}\left(1-\frac{2\Phi}{c^2}\right)\mathrm{Im}\left[\psi^*\partial_t\psi\right] .\end{aligned} \tag{2.31}$$

As $c \to \infty$ we obtain the asymptotic relation:

$$\epsilon \sim \frac{A^2m^2}{\hbar^2}|\psi|^2c^2 , \tag{2.32}$$

where one half of the right hand side comes from the quadratic term of the potential in (2.3). Demanding $\epsilon \sim \rho_m c^2 = |\psi|^2c^2$ as $c \to \infty$, one justified the second equality in eq. (2.29). In the process we defined the proper *dark matter* density to be:

$$\rho_m(x,t) \equiv |\psi(x,t)|^2 . \tag{2.33}$$

Note that we treat all matter, including baryons, as dark matter, i.e. everything that interacts gravitationally is subsumed by the dynamics of $\psi(x,t)$ and all baryonic physics is neglected.

At last, insert ansatz (2.29) into Klein-Gordon's equation (2.10) as well as the tt-component of Einstein's field equation (2.18). After some algebra, this yields:

$$\begin{aligned}i\hbar\partial_t\psi + \frac{3}{2}i\hbar H\psi - \frac{\hbar^2}{2mc^2}\left(\partial_t^2\psi + 3H\partial_t\psi + \frac{4}{c^2}\partial_t\Phi\partial_t\psi\right) \\ = \left[-\frac{\hbar^2}{2ma^2}\left(1+\frac{4\Phi}{c^2}\right)\triangle + m\Phi + \frac{2i\hbar}{c^2}\partial_t\Phi\right]\psi ,\end{aligned} \tag{2.34}$$

$$\begin{aligned}\frac{1}{4\pi G}\left[\frac{1}{a^2}\triangle\Phi-\frac{3H}{c^2}\Big(\partial_t\Phi+H\Phi\Big)\right]=&\left(1-\frac{\Phi}{c^2}\right)|\psi|^2+\frac{c^2}{8\pi G}\Lambda-\frac{3H^2}{8\pi G}\\&+\frac{\hbar^2}{2m^2c^2}\left[\frac{1}{c^2}\left(1-2\frac{\Phi}{c^2}\right)|\partial_t\psi|^2+\frac{1}{a^2}\left(1+2\frac{\Phi}{c^2}\right)|\nabla\psi|^2\right.\\&\left.-\frac{2m}{\hbar}\left(1-2\frac{\Phi}{c^2}\right)\mathrm{Im}\left[\psi^*\partial_t\psi\right]\right]\ .\end{aligned}\tag{2.35}$$

Taking $c\to\infty$ one finds the *Schrödinger-Poisson equations*,

$$i\hbar\partial_t\psi+\frac{3}{2}i\hbar H\psi=\left[-\frac{\hbar^2}{2ma^2}\triangle+m\Phi\right]\psi\ ,\tag{2.36}$$

$$\begin{aligned}\triangle\Phi&=4\pi Ga^2\left(|\psi|^2+\frac{c^2}{8\pi G}\Lambda-\frac{3H^2}{8\pi G}\right)\\&=4\pi Ga^2\left(|\psi|^2+\rho_\Lambda-\rho_c(t)\right)\\&\overset{(2.28)}{=}4\pi Ga^2\left(|\psi|^2-\overline{\rho_m}(t)\right)\ .\end{aligned}\tag{2.37}$$

We never assumed that our scalar field is a perturbation. Therefore, $\rho_m(x,t)$ as defined in eq. (2.33) is the dark matter density that includes *both* the homogeneous dynamics,

$$\rho_m(t)=\overline{\rho}_m(t)\equiv\frac{1}{|\Omega|}\int_\Omega\mathrm{d}^3x|\psi(x,t)|^2,\tag{2.38}$$

as well as the perturbative deviations from it. The integration domain Ω will be defined shorty. Equation (2.37) shows that only the density perturbations source the peculiar, gravitational potential Φ.

The imaginary, dissipative term on the left hand side of eq. (2.36) is due to the Hubble flow. It simply states the fact that the matter density is still measured in a *proper* volume $|\psi|^2=\rho\propto a^{-3}$. Thus, in order to restore hermiticity of the Hamiltonian, we substitute $\psi\to a^{-3/2}\psi$ and arrive at:

$$\begin{aligned}i\hbar\partial_t\psi&=\left[-\frac{\hbar^2}{2ma^2}\triangle+m\Phi\right]\psi\\\triangle\Phi&=\frac{4\pi G}{a}\left(|\psi|^2-\rho_m\right)\end{aligned}\qquad\boldsymbol{x}\in\Omega\ .\tag{2.39}$$

By this substitution, $|\psi|^2$ now measures the matter density measured in a *comoving* volume.

So far the problem (2.39) is not completely specified as both wave function and potential lack suitable boundary conditions. The natural choice is to impose *periodic boundary conditions* on both fields. To this end, let us define a 3-dimensional cube $\Omega=\Omega_1\times\Omega_2\times\Omega_3\subset\mathbb{R}^3$ with $\Omega_i=[0,L_i]\subset\mathbb{R}$ as one dimensional intervals. We then demand a matching m^{th}-derivative with $m=0,1$ for the potential *and* the wave function across the domain boundaries:

$$\begin{aligned}\partial^m_{x_1}\Phi\left(0,x_2,x_3\right)&=\partial^m_{x_1}\Phi\left(L_1,x_2,x_3\right),\quad\partial^m_{x_1}\psi\left(0,x_2,x_3\right)=\partial^m_{x_1}\psi\left(L_1,x_2,x_3\right)\\\partial^m_{x_2}\Phi\left(x_1,0,x_3\right)&=\partial^m_{x_2}\Phi\left(x_1,L_2,x_3\right),\quad\partial^m_{x_2}\psi\left(x_1,0,x_3\right)=\partial^m_{x_2}\psi\left(x_1,L_2,x_3\right)\\\partial^m_{x_3}\Phi\left(x_1,x_2,0\right)&=\partial^m_{x_3}\Phi\left(x_1,x_2,L_3\right),\quad\partial^m_{x_3}\psi\left(x_1,x_2,0\right)=\partial^m_{x_3}\psi\left(x_1,x_2,L_3\right)\end{aligned}\tag{2.40}$$

2.2.1 Overview of Competing Interpretations

Before proceeding further, it is instructive to shed some physical light onto the character of the non-relativistic scalar ψ. In fact, although eq. (2.39) has the mathematical structure of Schrödinger's equation, there is a priori *nothing* quantum mechanical about the result — neither did we specify a Hilbert space for ψ nor did the derivation depart from a many-body Hamiltonian. Moreover, apart from the requirement for $\hbar$ to have dimensions of an action there was no point in the steps leading up eq. (2.39) that demanded a particular value for it. Hence, the least arcane way to interpret eq. (2.39) is in a literal sense, i.e. as the Euler-Lagrange equation of a classical field theory which happens to coincide with Schrödinger's equation. From this perspective, FDM should better be called *scalar field dark matter*. The field theoretic point of view will serve us well in section 2.4 when we identify symmetries and conserved quantities of FDM.

That said, there is significant value in finding (formal) correspondences between $(3+1)$-SP and other, potentially non-cosmological, theories as it enlarges the number of available tools with which FDM can be analyzed.

For instance, if we accept eq. (2.39) as an abstract evolutionary problem and forget momentarily about its interpretation as alternative dark matter model, we can associate the dynamics of ψ with a smoothed version of the *Vlasov-Poisson equation* (VP) or *collisonless Boltzmann equation* — the phase space description of CDM, [76]. More precisely, if $f_V(\boldsymbol{x}, \boldsymbol{p})$ denotes the solution to VP and $f_W(\boldsymbol{x}, \boldsymbol{p})$ the phase space distribution constructed from ψ via:

$$f_W(\boldsymbol{x}, \boldsymbol{p}) = \int \mathrm{d}^3x' \psi\left(\boldsymbol{x} - \frac{\boldsymbol{x}'}{2}\right) \psi^*\left(\boldsymbol{x} + \frac{\boldsymbol{x}'}{2}\right) e^{\frac{i}{\hbar}\boldsymbol{p}\cdot\boldsymbol{x}'} \,, \tag{2.41}$$

then the evolution of the *smoothed* distributions,

$$\bar{f}_{V/W}(\boldsymbol{x}, \boldsymbol{p}) = \int \mathrm{d}^3x' \int \mathrm{d}^3p' \frac{1}{(2\pi\sigma_x\sigma_p)^3} \exp\left(-\frac{(\boldsymbol{x}-\boldsymbol{x}')^2}{2\sigma_x^2} - \frac{(\boldsymbol{p}-\boldsymbol{p}')^2}{2\sigma_p^2}\right) f_{V/W}(\boldsymbol{x}', \boldsymbol{p}') \,, \tag{2.42}$$

obeys, [76]:

$$\partial_t(\bar{f}_W - \bar{f}_V) = \frac{\hbar^2}{24} \partial_{x_i}\partial_{x_j}\nabla_x \bar{V} \partial_{p_i}\partial_{p_j}\nabla_p \bar{f}_W + \mathcal{O}(\hbar^4, \hbar^2\sigma_x^2) \,. \tag{2.43}$$

We emphasize $\hbar$ is *not* Planck's constant but acts as an independent model parameter that sets the maximum resolution in phase space.

In that sense, eq. (2.39) can be understood as an alternative sampling of the CDM distribution compared to the N-body approach: Instead of following the evolution of N test particles sampling f_V, we coarse grain the phase space distribution directly and use ψ as a dynamical proxy for its evolution. This approach will be referred to as *Schrödinger's method* and will give us access to (i) classical CDM results such as asymptotic density profiles, cf. section 6.3.1, and (ii) a starting point for a thermodynamic analysis of FDM by means of an entropy functional based on eq. (2.42), see section 6.1.2.

Chapter 1 already alluded to the usefulness of the macroscopic de-Broglie wavelength of FDM, yet the foregoing discussion seems to abandon the quantum nature of ψ entirely. We now reestablish the quantum mechanical view point of FDM by arguing that eq. (2.39) is not just the governing equation of an abstract complex field but can in fact be identified with the evolution equation of a self-gravitating Bose-Einstein condensate with negligible local self-interaction. In other words: In addition to the simplistic field theoretic interpretation and Schrödinger's method there is a third interpretation for FDM, i.e. dark matter is a cosmic Bose-Einstein condensate (BEC) and ψ the condensate *wave function*.

Let us substantiate this claim. Significant condensation into the lowest energy state can only be achieved if the critical temperature of the boson gas T_c surpasses the cosmic background temperature T, here identified with the temperature of the cosmic microwave background (CMB). Practically, T_c is defined via the number density of *excited states*, n_b, at maximal chemical potential μ and in the thermodynamic limit, i.e. $N \to \infty$, $L^3 \to \infty$ while $N/L^3 < \infty$:

$$n_b = \frac{1}{L^3} \sum_{\boldsymbol{k}} \langle n_{\boldsymbol{k}}(\beta_c, \mu = mc^2) \rangle \to \frac{1}{2\pi^2} \int_0^\infty \mathrm{d}k\, k^2 \frac{1}{e^{\beta_c(\hbar k c - mc^2)} - 1} , \tag{2.44}$$

with $\langle n_{\boldsymbol{k}}(\beta, \mu) \rangle$ as mean occupation per state set by the Boson-Einstein statistic:

$$\langle n_{\boldsymbol{k}}(\beta, \mu) \rangle = \frac{1}{e^{\beta(E(\boldsymbol{k}) - \mu)} - 1} , \quad \mu < E(0) . \tag{2.45}$$

Moreover, assume:

$$E(\boldsymbol{k}) = \begin{cases} mc^2 & k = 0 \\ \hbar |\boldsymbol{k}| c & k > 0 \end{cases} , \tag{2.46}$$

so that only excited states are relativistic — a consequence of the tiny boson mass.

Unfortunately, this approach is to simplistic since $k_B T \gg mc^2$ implying thermal boson-antiboson pair production is significant. Thus, one cannot invoke the textbook result for T_c which would follow from direct inversion of eq. (2.44). The authors of [39] derive for the situation including pair production:

$$k_B T_c = \sqrt{\frac{3c\hbar^3 \left(n_b - n_{\bar{b}}\right)}{m}} . \tag{2.47}$$

To make further progress, follow [82] and set $n_b - n_{\bar{b}} \propto \frac{m}{T} n_b$. This may be justified by noting in chemical equilibrium $\mu_{\bar{b}} = -|\mu_b| \equiv -|\mu|$. Therefore, a single chemical potential determines the joint Bose-Einstein distribution:

$$\begin{aligned} n_b - n_{\bar{b}} &= \frac{1}{L^3} \sum_{\boldsymbol{k}} \langle n_{\boldsymbol{k}}(\beta, \mu) \rangle - \langle \bar{n}_{\boldsymbol{k}}(\beta, \mu) \rangle \\ &\to \frac{\sinh \beta\mu}{2\pi^2} \int_0^\infty \mathrm{d}k\, k^2 \frac{1}{\cosh \beta\hbar k c - \cosh \beta\mu} \end{aligned} \qquad \text{and} \quad |\mu| \leq mc^2 \tag{2.48}$$

to ensure $\langle n_{\boldsymbol{k}} \rangle$ and $\langle \bar{n}_{\boldsymbol{k}} \rangle$ are positive for all $\boldsymbol{k}$. Hence, an arbitrary not, necessarily extremal, chemical potential still satisfies $\beta|\mu| \ll 1$ under pair production. It is then straight forward to solve eq. (2.44) and eq. (2.48) to find:

$$n_b - n_{\bar{b}} = \frac{\pi^2}{3\zeta(3)} \frac{\mu}{k_B T} n_b \approx \frac{\pi^2}{3\zeta(3)} \frac{mc^2}{k_B T} n_b , \tag{2.49}$$

and consequently:

$$kT_c = \sqrt{\frac{\hbar^3 c^3 \pi^2 n_b}{\zeta(3) kT}} \propto a^{-1} \; . \tag{2.50}$$

A couple of remarks are in order. Firstly, $\hbar$ is now of course Planck's constant. Secondly, as $T_c \propto a^{-1}$, just like the CMB temperature scales as $T \propto a^{-1}$, it is enough to check whether the condensation condition is satisfied at $z = 0$. If so, FDM should be in the BEC phase for all of cosmic time. We find:

$$k_B T_c = \frac{6.3\,\mathrm{MeV}}{a} \left(\frac{m}{10^{-22}\,\mathrm{eV}}\right)^{-\frac{1}{2}} \left(\frac{T}{2.7\,\mathrm{K}}\right)^{-\frac{1}{2}} \left(\frac{\Omega_b}{3 \cdot 10^{-3}}\right)^{\frac{1}{2}} \left(\frac{H_0}{68\,\frac{\mathrm{km}}{\mathrm{s\,Mpc}}}\right) \; , \tag{2.51}$$

and denote with Ω_b the fraction of *excited* dark matter bosons, e.g. $\Omega_b = 0.01\,\Omega_m = 3 \cdot 10^{-3}$. Since present CMB photons have $kT \approx 2 \cdot 10^{-4}$ eV, we conclude FDM is fully condensed.

In that light, it is natural to ask what the evolution equation of the macroscopic BEC wave function is. A rigorous derivation could depart from a second quantized many-body Hamiltonian which is subsequently reduced to an effective Hamiltonian for the order parameter, i.e. the condensate wave function ψ. For the sake of brevity we omit the calculation at this point but mention it is conceptionally close to the procedure for a standard, locally interacting BEC, see [52]. The result is again eq. (2.39). From this point of view FDM should best be called *Bose-Einstein dark matter*, e.g. [60].

Having a quantum mechanical framework at hand is invaluable and will serve us in many ways, for instance in section 4.3 when we formulate the time integration for FDM as approximation to time evolution operator or in section 6.1.1 when we employ the quantum virial theorem to analyse the long term FDM dynamics.

2.2.2 SP as Nonlinear Schrödinger Equation

To keep the notation compact, but also in preparation for numerical considerations, it is advisable to recast eq. (2.39) into a dimensionless form. We follow the convention employed in [67, 85, 86] and define:

$$\boldsymbol{x}' \equiv \left(\frac{m}{\hbar}\right)^{\frac{1}{2}} \left[\frac{3}{2} H_0^2 \Omega_m\right]^{\frac{1}{4}} \boldsymbol{x} \; , \tag{2.52}$$

$$\mathrm{d}t' \equiv \frac{1}{a^2} \left[\frac{3}{2} H_0^2 \Omega_m\right]^{\frac{1}{2}} \mathrm{d}t \; . \tag{2.53}$$

Moreover, if we set:

$$\psi'(\boldsymbol{x}', t') \equiv \frac{\psi(\boldsymbol{x}', t')}{\sqrt{\rho_m}} \; , \tag{2.54}$$

$$V(\boldsymbol{x}', t') \equiv a \frac{m}{\hbar} \left[\frac{3}{2} H_0^2 \Omega_m\right]^{-\frac{1}{2}} \Phi \; , \tag{2.55}$$

then eq. (2.39) can be brought into a convenient *dimensionless* form. By dropping primes one arrive at:

$$i\partial_t\psi = \left[-\frac{1}{2}\triangle + a(t)V\right]\psi \tag{2.56}$$

$$\triangle V = |\psi|^2 - 1\ . \tag{2.57}$$

In this representation the role of the scale factor $a(t)$ becomes apparent: It acts as a time-dependent coupling strength for the nonlinear term in eq. (2.56) and increases its dominance as time progresses since $a(t)$ is monotonically increasing with t.

Moreover, realize the crucial role of the adimensional domain size L' in the chosen convention (2.52): It is influenced by *both* the boson mass m and the physical box size:

$$L' = \left(\frac{m}{\hbar}\right)^{\frac{1}{2}}\left[\frac{3}{2}H_0^2\Omega_m\right]^{\frac{1}{4}} L\ . \tag{2.58}$$

In practice this implies once the cosmology is fixed through Ω_m and H_0 then by solving eq. (2.56) for a particular value of dimensionless L', one obtains the solution for all physical scenarios for which $\sqrt{m}L = \text{const.}$. For the convenience of the reader Figure 2.1 illustrates the domain-mass relation (2.58) for typical boson masses of the order $m \sim 10^{-22}$ eV.

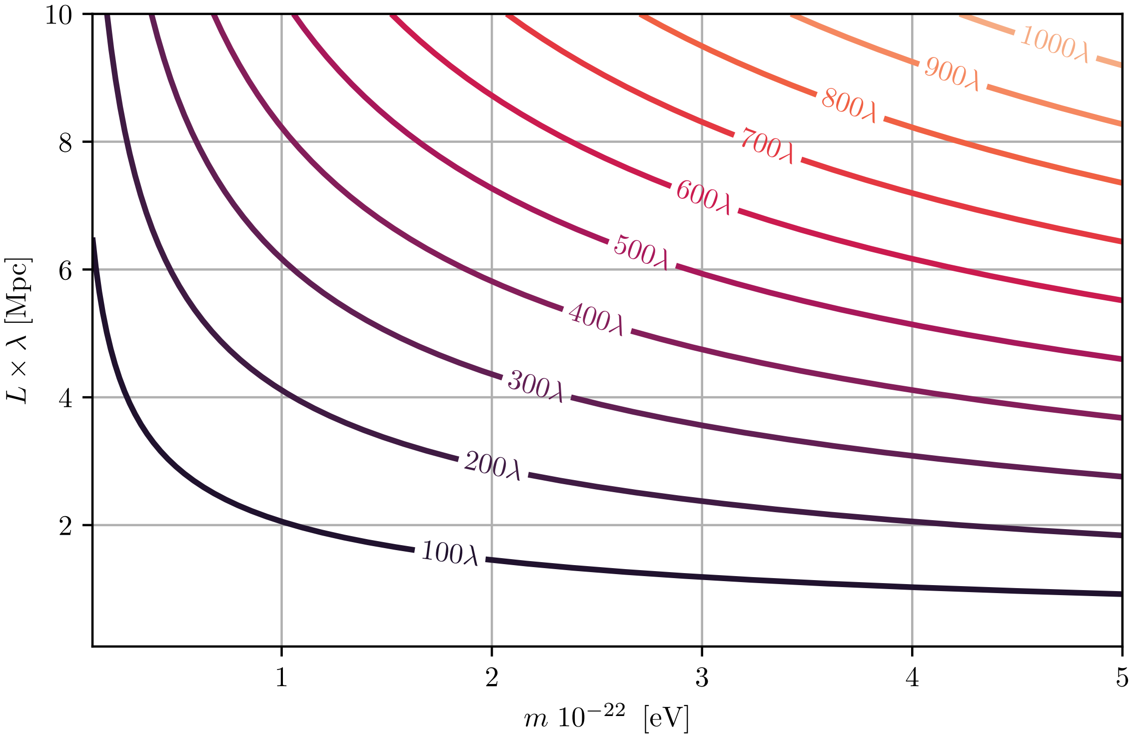

Figure 2.1: Domain-mass relation for $\Omega_m = 0.3$ and $H_0 = 68\frac{\text{km}}{\text{s}\cdot\text{Mpc}}$ in the range of typical boson masses m. The level lines depict the associated adimensional box size L'. Once equation eq. (2.56) is integrated for one particular value of L', one solved the dimensionfull problem (2.39) for all scenarios lying on the L'-level line. λ denotes a dimensionless parameter which can be used to adapt the domain size to the physical scenario in mind.

To make further progress in characterizing the interactions we recall Poisson's equation is equivalent to a convolution of it's source term with Green's function $G_{\triangle_3}(\boldsymbol{x}, \boldsymbol{x}')$ of the 3-dimensional Laplace operator. Physically speaking $G_{\triangle_3}(\boldsymbol{x}, \boldsymbol{x}')$ is then to be interpreted as a nonlocal interaction kernel the scalar field is subject to.

Realize that $G_{\triangle_3}(\boldsymbol{x}, \boldsymbol{x}')$ is *not* the well known $1/r$-potential:

$$G_{\triangle_3}(\boldsymbol{x}, \boldsymbol{x}') \neq G^{\text{free}}_{\triangle_3}(\boldsymbol{x}, \boldsymbol{x}') = -\frac{1}{4\pi|\boldsymbol{x} - \boldsymbol{x}'|} \,, \tag{2.59}$$

which only holds when *free space* or *asymptotic* boundary conditions are imposed. In $d = 3$ spatial dimensions this amounts to setting, [47]:

$$\lim_{|\boldsymbol{x}|\to\infty} |\boldsymbol{x}| V(\boldsymbol{x}) = -\frac{1}{4\pi} \,. \tag{2.60}$$

As discussed in section 2.2, eq. (2.57) is considered on a periodic domain. Consequently, we seek for a Green's function that satisfies the boundary conditions set in eq. (2.40) and eq. (2.59) certainly does not. Clearly, a sensible periodic Green's function is expected to approach eq. (2.59) as $|\Omega| \to \infty$.

The construction of the periodic interaction kernel $G^{\pi}_{\triangle}(\boldsymbol{x}, \boldsymbol{x}')$ in its canonical form is straight forward. We utilize this simple task to establish further conventions. Any Ω-periodic function, such as the potential, can be expanded in a Fourier series:

$$V(\boldsymbol{x}) = \frac{1}{L_1 L_2 L_3} \sum_{\boldsymbol{n}_3} V_{\boldsymbol{n}_3} e^{i\boldsymbol{k}_3\cdot\boldsymbol{x}} \qquad \text{with} \qquad V_{\boldsymbol{n}_3} = \int_\Omega \mathrm{d}^3x' V(\boldsymbol{x}') e^{-i\boldsymbol{k}_3\cdot\boldsymbol{x}'} \,, \tag{2.61}$$

where $\boldsymbol{n}_3 \in \mathbb{Z}^3$, $\boldsymbol{k}_3 \in \mathbb{R}^3$ and $(k_3)_i = \frac{2\pi}{L_i}(\boldsymbol{n}_3)_i$. Inserting eq. (2.61) as well as the series of $|\psi|^2 - 1$ into eq. (2.57) yields the expansion coefficients $V_{\boldsymbol{n}_3}$:

$$V_{\boldsymbol{n}_3} = \begin{cases} 0 & \|\boldsymbol{n}_3\| = 0 \\ -\frac{1}{\boldsymbol{k}_3^2} & \|\boldsymbol{n}_3\| > 0 \end{cases} \,. \tag{2.62}$$

It is important to realize that for $\|\boldsymbol{n}_3\| = 0$ the factor $-\boldsymbol{k}^{-2}$ diverges. This singularity is only circumvented by the fact that the density contrast, $|\psi|^2 - 1$, and not just the matter density, $|\psi|^2$, sources V. The former has a vanishing $\|\boldsymbol{n}_3\| = 0$ (DC)-mode and hence makes eq. (2.57) under periodic conditions well-defined.

To arrive at the periodic Green's function substitute eq. (2.62) into eq. (2.61) and reinsert the Fourier coefficient integral for $|\psi|^2$ to arrive at an expression in real-space:

$$V(\boldsymbol{x}) = \int_\Omega \mathrm{d}^3x' G^{\pi}_{\triangle_3}(\boldsymbol{x}, \boldsymbol{x}') |\psi(\boldsymbol{x}')|^2 \quad \text{with} \tag{2.63}$$

$$G^{\pi}_{\triangle_3}(\boldsymbol{x}, \boldsymbol{x}') = \frac{1}{L_1 L_2 L_3} \sum_{\|\boldsymbol{n}_3\|>0} \frac{-1}{\boldsymbol{k}_3^2} e^{i\boldsymbol{k}_3\cdot(\boldsymbol{x}-\boldsymbol{x}')} \,. \tag{2.64}$$

It should be noted the convolution integral in eq. (2.63) only convolves $|\psi|^2$ and not the density contrast, being the true source of the potential. This seeming inconsistency is remedied by the fact that we exclude the DC-mode in the periodic

Green's function. Recall that the DC-mode of $|\psi|^2$ is the sole difference between the density contrast and the matter density.

Eq. (2.64) is not particularly insightful to understand the behavior of the interaction. We will encounter more refined representations of eq. (2.64) in section 2.3 which also yield more physical insight. At this stage it suffices to see that eq. (2.63) is a convolution integral, making the nonlocality of the gravitational interaction manifest: The potential at a point $\mathcal{P}$ is the result of all matter inside the range of the interaction kernel and not just the density contrast at $\mathcal{P}$.

We can now rewrite eq. (2.56) and (2.57) into a single, *nonlinear Schrödinger equation* (NLSE):

$$i\partial_t\psi = \left[-\frac{1}{2}\triangle + a(t)\left(G^{\pi}_{\triangle_3} * |\psi|^2\right)\right]\psi \quad \boldsymbol{x} \in \Omega\,. \tag{2.65}$$

2.3 Dimension Reduction

So far, we succeeded in deriving the comoving $(3+1)$-SP in its standard, coupled partial differential equation (PDE) and NLSE representation. To reduce the computational complexity of the problem even further it seems reasonable to consider a lower dimensional form of our equation system. This section is meant to provide details on how such lower dimensional representations of eq. (2.56)-(2.57) can be obtained. We anticipate that the result of the reduction will depend on how matter is distributed along the eliminated spatial dimension.

The naive way of carrying out the reduction is to simply drop all x_3 (x_2, x_3) partial derivatives to arrive at a two (one) dimensional version of eq. (2.56)-(2.57). This appears to be the common approach in low-dimensional studies on Structure Formation employing Fuzzy Dark Matter [82, 76, 51, 60, 31] and turns out to be true assuming we demand a *uniform* matter distribution along the neglected dimensions. The approach is equally applicable for $d = 1, 2$. One then arrives at the d-dimensional SP equation in which we retain Poisson's equation for the gravitational potential.

As we will see, maintaining Poisson's equation as field equation has implications on how gravity acts in lower dimensions because the periodic Green's function in eq. (2.64) depends on the dimensionality of the Laplace operator. Unfortunately, it is not possible to simply enforce a $1/r$-interaction kernel in one dimension. Even on finite domains will the singularity at the origin be too strong and will consequently yield an ill-defined convolution kernel. This is different for $d = 2$ where the volume element $\mathrm{d}V = r\mathrm{d}r\mathrm{d}\varphi$ cancels the singularity. Consequently, we ask whether a reduction procedure exists by which we *approximately* preserve the 3-dimensional interaction with only one spatial degree of freedom. This is realized by *strongly confining* matter along the dimension the evolution is observed. The result is the *(periodized) line adiabatic model* (P)LAM — a $(1+1)$-dimensional NLSE in which the long-range interaction will be modelled by a convolution-type potential. This potential is neither the solution to Poisson's equation nor can it be recast into a PDE form.

We already alluded to the equivalence of the PDE formulation of $(3+1)$-SP with the convolution-type NLSE (2.65). It turns out to be convenient to adopt the latter formulation for the following discussion as well, i.e. the starting point for any reduction procedure will be eq. (2.65) and a lower dimensional version of it will again be a NLSE involving a convolution-type nonlinearity. Thus, the overall form of eq. (2.65) will be preserved and what changes is the convolution kernel. For the convenience of the reader, but also to fix notation, we refer to Figure 2.2 in which all interaction kernels of section 2.3.1 and 2.3.2 together with their relations to each other are anticipated.

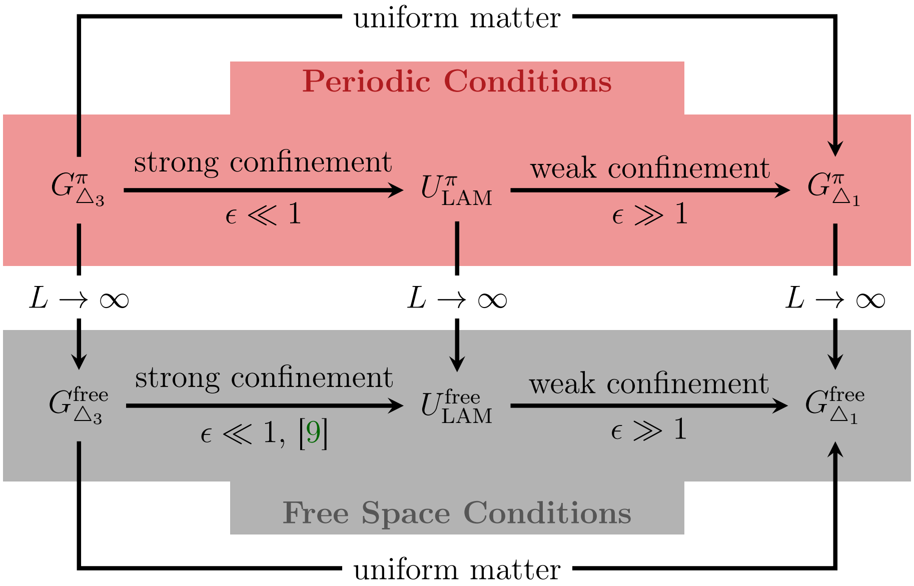

Figure 2.2: Overview of all interaction kernels appearing in section 2.3 as well as their relations. Green's function are denoted by a G, general convolution kernels with U. Boundary conditions are specified as superscript with π referring to periodic conditions. The subscript either specifies a differential operator (in the case of a Green's function) or the model name of the interaction. Under the confinement approach an effective one-dimensional reduction, say onto the x_3-direction, is achieved by reducing the confinement parameter ϵ, i.e. making the external potential in the orthogonal plane, say an harmonic-potential in x_1x_2-direction, steeper, see eq. (2.83).

Notation-wise, we denote Green's functions, i.e. point-source solution to PDEs, with G and give the associated differential operator as subscript. If an interaction kernel is not the fundamental solution to a PDE, it is denoted by U followed by the model name as subscript. To denote periodic boundary conditions, a π-superscript is used. Asymptotic conditions are denoted by a free-superscript.

2.3.1 Homogeneous Matter Sheets — $(1+1)$-SP

Let us focus on the $(3+1) \to (2+1)$ reduction for the time being.

From a cosmological perspective, the most natural way to reduce the spatial degrees of freedom is to insist that matter is homogeneously distributed in one dimension, say x_3, such that all gravitational forces cancel out in this direction and the potential V is constant along the x_3-direction.

Quantum mechanically, this ansatz motivates a factorization of the full fledged wave function $\psi(\boldsymbol{x},t)$ into a two-dimensional part $\psi_2(\boldsymbol{x}_\perp,t)$ and a plane wave eigenstate $\chi(x_3,t)$ of the Hamiltonian H_{x_3}:

$$\psi(\boldsymbol{x},t) = \chi(x_3,t)\psi_2(\boldsymbol{x}_\perp,t) \qquad \text{and} \tag{2.66}$$

$$H_{x_3}\chi = \left[-\frac{1}{2}\partial_{x_3}^2\right]\sqrt{L_3}e^{i(px_3-Et)} = E\chi \qquad \text{with} \qquad E = \frac{p^2}{2}\;. \tag{2.67}$$

Our objective is to determine the evolution equation of $\psi_2(\boldsymbol{x}_\perp,t)$. Inserting eq. (2.66) into eq. (2.65), using eq. (2.67), multiplying the result by χ^*, integrating over z and swapping the integration order leaves us with:

$$i\partial_t\psi_2 = \left[-\frac{1}{2}\triangle_\perp + \frac{a(t)}{L_3}\int_{\Omega_1\times\Omega_2}\mathrm{d}^2x_\perp\left(\int_{\Omega_3}\mathrm{d}z\int_{\Omega_3}\mathrm{d}z' G^\pi_{\triangle_3}(\boldsymbol{x},\boldsymbol{x}')\right)|\psi_2(\boldsymbol{x}'_\perp)|^2\right]\psi_2\;. \tag{2.68}$$

For the nonlocal term, the new periodic interaction kernel $U^\pi(\boldsymbol{x}_\perp,\boldsymbol{x}'_\perp)$ is:

$$U^\pi(\boldsymbol{x}_\perp,\boldsymbol{x}'_\perp) = \frac{1}{L_3}\int_{\Omega_3}\mathrm{d}z\int_{\Omega_3}\mathrm{d}z' G^\pi_{\triangle_3}(\boldsymbol{x},\boldsymbol{x}') \tag{2.69}$$

$$= \frac{1}{L_1L_2L_3^2}\sum_{\|\boldsymbol{n}_3\|>0}\frac{-1}{\boldsymbol{k}_3^2}e^{i\boldsymbol{k}_3\cdot(\boldsymbol{x}-\boldsymbol{x}')}\int_{\Omega_3}\mathrm{d}z\int_{\Omega_3}\mathrm{d}z' e^{i\boldsymbol{k}_3\cdot(\boldsymbol{x}-\boldsymbol{x}')}\;. \tag{2.70}$$

Let $\boldsymbol{k}_2$ and $\boldsymbol{n}_2$ be the first two components of $\boldsymbol{k}_3$ and $\boldsymbol{n}_3$. We split the series into $\sum_{\|\boldsymbol{n}_3\|>0} = \sum_{\|\boldsymbol{n}_2\|>0, n_{3i}=0} + \sum_{\|\boldsymbol{n}_2\|, n_{3i}\neq 0}$. The second sum vanishes because the integral in eq. (2.69) vanishes. For the first sum we get:

$$U^\pi(\boldsymbol{x}_\perp,\boldsymbol{x}'_\perp) = \frac{1}{L_1L_2}\sum_{\|\boldsymbol{n}_2\|>0}\frac{-1}{\boldsymbol{k}_2^2}e^{i\boldsymbol{k}_2\cdot(\boldsymbol{x}_\perp-\boldsymbol{x}'_\perp)}\;. \tag{2.71}$$

This is precisely the same as setting $n_{3i}=0$ and $L_3=1$ in eq. (2.64), i.e. considering the Laplace operator on a two dimensional domain. Hence:

$$U^\pi(\boldsymbol{x}_\perp,\boldsymbol{x}'_\perp) = G^\pi_{\triangle_2}(\boldsymbol{x}_\perp,\boldsymbol{x}'_\perp)\;. \tag{2.72}$$

By exactly the same reasoning, one can reduce to $d=1$ degrees of freedom. The periodic interaction kernel then reads:

$$U^\pi(x_1,x'_1) = G^\pi_{\triangle_1}(x_1,x'_1) = \frac{1}{L_1}\sum_{|n_1|>0}\frac{-1}{k_1^2}e^{ik_1(x_1-x'_1)}\;. \tag{2.73}$$

We arrive at the d-dimensional SP equation:

$$\boxed{i\partial_t\psi = \left[-\frac{1}{2}\triangle_\mathrm{d} + a(t)V\right]\psi, \quad \triangle_\mathrm{d}V = |\psi|^2-1\;.} \tag{2.74}$$

Eq. (2.74) is *equivalent* to the NLSE:

$$\boxed{i\partial_t\psi = \left[-\frac{1}{2}\triangle_d + a(t)\left(G^\pi_{\triangle_d} * |\psi|^2\right)\right]\psi \quad \boldsymbol{x}\in\Omega\;.} \tag{2.75}$$

On balance, one finds that by assuming a homogeneous matter distribution *Poisson's equation is preserved* but the point source potential, i.e. its Green's function changes.

So far, we're still lacking descriptive representations for $G^{\pi}_{\triangle_d}$. Starting from eq. (2.64) [59] derives the following periodic interaction kernels:

$$G^{\pi}_{\triangle_1}(x_1, x_1') = \frac{1}{2}|x_1 - x_1'| - \frac{1}{2}\left[\frac{(x_1 - x_1')^2}{L_1} + \frac{L_1}{6}\right] , \tag{2.76}$$

$$\begin{aligned} G^{\pi}_{\triangle_2}(\boldsymbol{x}_\perp, \boldsymbol{x}_\perp') = &\frac{1}{L_2} G^{\pi}_{\triangle_1}(x_1, x_1') \\ &+ \frac{1}{4\pi}\sum_{m\in\mathbb{Z}} \log\Bigg(1 - 2e^{-\frac{2\pi}{L_2}L_1\left|m + \frac{x_1 - x_1'}{L_1}\right|}\cos\left(\frac{2\pi}{L_2}(x_2 - x_2')\right) \\ &\qquad\qquad + e^{-\frac{4\pi}{L_2}L_1\left|m + \frac{x_1 - x_1'}{L_1}\right|}\Bigg) , \end{aligned} \tag{2.77}$$

$$\begin{aligned} G^{\pi}_{\triangle_3}(\boldsymbol{x}, \boldsymbol{x}') = &\frac{1}{L_3} G^{\pi}_{\triangle_2}(\boldsymbol{x}_\perp, \boldsymbol{x}_\perp') - \frac{1}{\pi L_3}\sum_{m=1}^{\infty}\Bigg\{\cos\left(\frac{2\pi m}{L_3}(x_3 - x_3')\right) \\ &\times \sum_{n,l\in\mathbb{Z}} K_0\left(\frac{2\pi m}{L_3}\sqrt{L_1^2\left(n + \frac{x_1 - x_1'}{L_1}\right)^2 + L_2^2\left(l + \frac{x_2 - x_2'}{L_2}\right)^2}\right)\Bigg\} , \end{aligned} \tag{2.78}$$

where K_0 denotes the 0th-modified Bessel function of the second kind. Realize the $(d+1)$-dimensional interaction kernel depends on the $d-$dimensional Green's function. Also note that we are only able to find a closed form expression for $d = 1$. For the convenience of the reader, Appendix A.1 sketches the derivation of eq. (2.76)-(2.78). We refer to [59] for more details.

Approaching Free Space Conditions It is instructive to consider the limiting behavior of these expressions for $\epsilon_i = \frac{|x_i - x_i'|}{L_i} \to 0$. This can be realized by either making the domain infinitely large, i.e. approach the free-space problem, or by moving source and field points ever closer together, i.e. consider the situation in which the domain boundaries are far away.

Clearly, for $d = 1$ we have (modulo an offset):

$$G^{\pi}_{\triangle_1}(x_1, x_1') \xrightarrow{\epsilon_1 \to 0} G^{\text{free}}_{\triangle_1}(x_1, x_1') = \frac{1}{2}|x_1 - x_1'| . \tag{2.79}$$

For $d = 2$, only the $m = 0$ term in eq. (2.77) contributes significantly as $\epsilon_{1,2} \to 0$. Expanding both the cosine and the exponential up to $\mathcal{O}(\epsilon^3)$ yields:

$$G^{\pi}_{\triangle_2}(\boldsymbol{x}_\perp, \boldsymbol{x}_\perp') \xrightarrow{\epsilon_{1,2} \to 0} G^{\text{free}}_{\triangle_2}(\boldsymbol{x}_\perp, \boldsymbol{x}_\perp') = \frac{1}{2\pi}\log|\boldsymbol{x}_\perp - \boldsymbol{x}_\perp'| . \tag{2.80}$$

For $d = 3$ we follow [59] and first take $\epsilon_{1,2} \to 0$ to obtain a mixed Green's function for two unconstrained and one periodic dimension. Similar to before, only $n = l = 0$

dominates in this limit since $K_0(x) \to 0$ for $x \to \infty$. Hence:

$$\begin{aligned} G^{\pi}_{\triangle_3}(\boldsymbol{x}, \boldsymbol{x}') &\xrightarrow{\epsilon_{1,2}\to 0} G^{\text{mixed}}_{\triangle_3}(\boldsymbol{x}, \boldsymbol{x}') \\ &= \frac{1}{2\pi L_3} \log |\boldsymbol{x}_\perp - \boldsymbol{x}'_\perp| \\ &\quad - \frac{1}{\pi L_3} \sum_{m=1}^{\infty} \cos\left(\frac{2\pi m}{L_3}(x_3 - x'_3)\right) K_0\left(\frac{2\pi m}{L_3}|\boldsymbol{x}_\perp - \boldsymbol{x}'_\perp|\right) \end{aligned} \tag{2.81}$$

Now take $\epsilon_3 \to 0$ by $L_3 \to \infty$. Then the Riemann sum in eq. (2.81) approaches an analytically solvable integral:

$$\begin{aligned} G^{\text{mixed}}_{\triangle_3}(\boldsymbol{x}, \boldsymbol{x}') &\xrightarrow{\epsilon_3\to 0} G^{\text{free}}_{\triangle_3}(\boldsymbol{x}, \boldsymbol{x}') \\ &= -\frac{1}{2\pi^2} \int_0^\infty \mathrm{d}k K_0\left(k|\boldsymbol{x}_\perp - \boldsymbol{x}'_\perp|\right) \cos\left(k(x_3 - x'_3)\right) \\ &= -\frac{1}{4\pi|\boldsymbol{x}|} \,. \end{aligned} \tag{2.82}$$

The limiting, free space, cases in eq. (2.79)-(2.82) reemphasize the argument made before that the nonlocal interaction changes as a function of dimension.

2.3.2 Strong Confinement — PLAM

Section 2.3.1 conducted the dimension reduction by assuming matter is maximally delocalized, i.e. uniformly distributed, in the subspace orthogonal to the direction in which we observe the dynamics.

Alternatively, we can trap matter by an external potential in the orthogonal subspace and control it's confinement via a small parameter $\epsilon < 1$. In the limit of infinitely strong confinement, $\epsilon = 0$, this leads to a lower-dimensional form of eq. (2.56). We will see this is *not* achievable with only one remaining spatial degree of freedom. However, strong confinement, $\epsilon \ll 1$, still yields an effective lower dimensional version of eq. (2.56).

This reduction procedure was thoroughly investigated in [9] for asymptotic boundary conditions resulting in the *surface adiabatic-* and *line adiabatic model* (LAM) in $d = 2$ and $d = 1$ dimensions respectively. We only focus on the $(3+1) \to (1+1)$ reduction and take the arguments of [9] as inspiration for developing a novel lower dimensional representation of eq. (2.65) — the *periodic line adiabatic model* (PLAM).

To this end, define $\boldsymbol{x}_\perp = (x_1\ x_2)^\intercal \in \mathbb{R}^2$ and introduce a confining potential,

$$V(\boldsymbol{x}_\perp) = \frac{1}{\epsilon^2} V\left(\frac{\boldsymbol{x}_\perp}{\epsilon}\right), \qquad \epsilon > 0 \,, \tag{2.83}$$

into the Hamiltonian of eq. (2.65). Notice that we do *not* impose periodic boundary conditions in x_1x_2-plane. Consequently, the interaction kernel we depart from is the *mixed*-conditions three dimensional Green's function (2.81) for which only the x_3-direction is periodic.

The Hamiltonian then reads:

$$H = H_{x_3} + H_{\perp}^{\epsilon} \quad \text{with} \tag{2.84}$$

$$H_{x_3} = -\frac{1}{2}\partial_{x_3}^2 + a(t)\left(G_{\triangle_3}^{\text{mixed}} * |\psi|^2\right) \,, \tag{2.85}$$

$$H_{\perp}^{\epsilon} = \frac{1}{\epsilon^2}\left[-\frac{1}{2}\triangle_{\tilde{\perp}} + V(\boldsymbol{x}_{\tilde{\perp}})\right] = \frac{1}{\epsilon^2}H_{\tilde{\perp}} \,, \tag{2.86}$$

with $\boldsymbol{x}_{\tilde{\perp}} = \boldsymbol{x}_{\perp}/\epsilon$. As done for the homogeneous case in section 2.3.1, consider the eigenstates, $\chi_k(\boldsymbol{x}_{\tilde{\perp}})$ of the orthogonal Hamiltonian $H_{\tilde{\perp}}$:

$$H_{\tilde{\perp}}\chi_k(\boldsymbol{x}_{\tilde{\perp}}) = \lambda_k\chi_k(\boldsymbol{x}_{\tilde{\perp}}) \,, \tag{2.87}$$

with $\|\chi_k\|_2 = 1$. This time, however, these eigenstates have a non-trivial spatial dependence. Once the set $\{\lambda_k, \chi_k\}$ is determined, rescaling yields normalized eigenstates χ_k^{ϵ} for $H_{\perp}^{\epsilon}$ as well:

$$H_{\perp}^{\epsilon}\chi_k^{\epsilon}(\boldsymbol{x}_{\perp}) = \lambda_k^{\epsilon}\chi_k^{\epsilon}(\boldsymbol{x}_{\perp}) \quad \text{with} \tag{2.88}$$

$$\lambda_k^{\epsilon} = \frac{1}{\epsilon^2}\lambda_k, \quad \chi_k^{\epsilon}\left(\boldsymbol{x}_{\perp}\right) = \frac{1}{\epsilon}\chi_k\left(\frac{\boldsymbol{x}_{\perp}}{\epsilon}\right) \,. \tag{2.89}$$

Now assume the orthogonal dynamics is set by the ground state $\chi_0^{\epsilon}(\boldsymbol{x}_{\perp}, t)$ independent of the evolution along the x_3-direction. We then have a factorization of the form:

$$\psi(\boldsymbol{x}, t) = \psi_1(x_3, t)\chi_0^{\epsilon}(\boldsymbol{x}_{\perp}, t) \tag{2.90}$$

and seek for an evolution equation of ψ_1 only. Following the steps of section 2.3.1 leaves us with an equation similar to eq. (2.68), but this time the new, one dimensional interaction kernel depends on the ground state $\chi_0^{\epsilon}(\boldsymbol{x}_{\perp}, t)$ and integration is performed over the entire x_1x_2-plane:

$$\begin{aligned}
U_{\text{LAM}}^{\pi}(x_3, x_3'; \epsilon) &= \int_{\mathbb{R}^2} \mathrm{d}^2x_{\perp} \int_{\mathbb{R}^2} \mathrm{d}^2x_{\perp}' G_{\triangle_3}^{\text{mixed}}(\boldsymbol{x}_{\perp}, x_3, \boldsymbol{x}_{\perp}', x_3')|\chi_0^{\epsilon}(\boldsymbol{x}_{\perp})|^2|\chi_0^{\epsilon}(\boldsymbol{x}_{\perp}')|^2 \\
&\overset{(2.81)}{=} \frac{1}{2\pi L_3}\int_{\mathbb{R}^2} \mathrm{d}^2x_{\perp} \int_{\mathbb{R}^2} \mathrm{d}^2x_{\perp}' \log|\boldsymbol{x}_{\perp} - \boldsymbol{x}_{\perp}'||\chi_0^{\epsilon}(\boldsymbol{x}_{\perp})|^2|\chi_0^{\epsilon}(\boldsymbol{x}_{\perp}')|^2 \\
&\quad - \frac{1}{\pi L_3}\sum_{m=1}^{\infty}\Bigg\{\cos\left(k_m(x_3 - x_3')\right) \\
&\quad \times \int_{\mathbb{R}^2} \mathrm{d}^2x_{\perp} \int_{\mathbb{R}^2} \mathrm{d}^2x_{\perp}' K_0\left(k_m|\boldsymbol{x}_{\perp} - \boldsymbol{x}_{\perp}'|\right)|\chi_0^{\epsilon}(\boldsymbol{x}_{\perp})|^2|\chi_0^{\epsilon}(\boldsymbol{x}_{\perp}')|^2\Bigg\}
\end{aligned}$$

with $k_m = \frac{2\pi m}{L_3}$. The first integral is finite and constitutes a physically irrelevant offset. Define $u_i = \epsilon^{-1}(\boldsymbol{x}_{\perp,i} - \boldsymbol{x}_{\perp,i}')$ and $v_i = \epsilon^{-1}(\boldsymbol{x}_{\perp,i} + \boldsymbol{x}_{\perp,i}')$ so that:

$$\begin{aligned}
U_{\text{LAM}}^{\pi}(x_3, x_3'; \epsilon) \overset{(2.89)}{=} -\frac{1}{4\pi L_3}\sum_{m=1}^{\infty}\Bigg\{&\cos\left(k_m(x_3 - x_3')\right)\int_{\mathbb{R}^2}\mathrm{d}^2u\int_{\mathbb{R}^2}\mathrm{d}^2v K_0\left(k_m\epsilon|\boldsymbol{u}|\right) \\
&\times \left|\chi_0\left(\frac{\boldsymbol{u}+\boldsymbol{v}}{2}\right)\right|^2\left|\chi_0\left(\frac{\boldsymbol{u}-\boldsymbol{v}}{2}\right)\right|^2\Bigg\} \,.
\end{aligned}$$

To make further progress a confining potential needs to be fixed. The canonical choice is a harmonic potential, [9]:

$$V(\boldsymbol{x}_\perp) = \frac{1}{2}|\boldsymbol{x}_\perp|^2 \qquad \text{and} \qquad \chi_0(\boldsymbol{x}_\perp) = \frac{1}{\sqrt{\pi}} e^{-\frac{|\boldsymbol{x}_\perp|^2}{2}} \ . \tag{2.91}$$

Thus, $U^\pi_{\mathrm{LAM}}(x_3, x_3'; \epsilon)$ reads:

$$\begin{aligned} U^\pi_{\mathrm{LAM}}(x_3, x_3') &\overset{(2.91)}{=} -\frac{1}{4\pi^3 L_3}\sum_{m=1}^{\infty} \cos\left(k_m(x_3 - x_3')\right) \int_{\mathbb{R}^2} \mathrm{d}^2 u \int_{\mathbb{R}^2} \mathrm{d}^2 v K_0\left(k_m \epsilon |\boldsymbol{u}|\right) e^{-\frac{|\boldsymbol{u}|^2 + |\boldsymbol{v}|^2}{2}} \\ &= -\frac{1}{\pi L_3}\sum_{m=1}^{\infty} \cos\left(k_m(x_3 - x_3')\right) \int_0^\infty \mathrm{d}u\, u K_0\left(k_m \epsilon u\right) e^{-\frac{u^2}{2}} \end{aligned}$$

The remaining integral can be brought into the following form: [36]:

$$U^\pi_{\mathrm{LAM}}(x_3, x_3'; \epsilon) = -\frac{1}{2\pi L_3}\sum_{m=1}^{\infty} e^{\frac{1}{2}k_m^2\epsilon^2} E_1\left(\frac{1}{2}k_m^2 \epsilon^2\right) \cos\left(k_m(x_3 - x_3')\right) \ , \tag{2.92}$$

where $E_1(x) = \int_1^\infty \mathrm{d}t \frac{e^{-tx}}{t}$ denotes the exponential integral. Eq. (2.93) is the PLAM Green's function and constitutes a Fourier series of an even function with vanishing DC mode:

$$U^\pi_{\mathrm{LAM}}(x_3, x_3'; \epsilon) = \frac{1}{L_3}\sum_{|m|>0} -\frac{1}{4\pi} e^{\frac{1}{2}k_m^2\epsilon^2} E_1\left(\frac{1}{2}k_m^2 \epsilon^2\right) e^{ik_m(x_3 - x_3')} \ . \tag{2.93}$$

The author is neither aware of (i) a function producing this type of spectrum nor (ii) an associated linear differential operator with a Green's function taking the form of eq. (2.93). Consequently, it is (i) not possible to invert the series in eq. (2.93) to a closed-form, real space representation and (ii) PLAM can only be represented as integro-NLSE:

$$i\partial_t \psi = \left[-\frac{1}{2}\partial_x^2 + a(t)\left(U^\pi_{\mathrm{LAM}} * |\psi|^2\right)\right]\psi \ , \quad x \in \Omega_1 \ . \tag{2.94}$$

Approaching Free Space Conditions As done in section 2.3.1, it is instructive to consider the free-space limit, $L_3 \to \infty$, for eq. (2.92) by transforming the Riemann sum into an integral over k. In accordance with the considerations of [9], we obtain:

$$U^\pi_{\mathrm{LAM}}(x_3, x_3'; \epsilon) \xrightarrow{L_3 \to \infty} U^{\mathrm{free}}_{\mathrm{LAM}}(x_3, x_3'; \epsilon) = -\frac{1}{\sqrt{32\pi}\epsilon} e^{\frac{(x_3 - x_3')^2}{2\epsilon^2}} \mathrm{Erfc}\left(\frac{|x_3 - x_3'|}{\sqrt{2}\epsilon}\right) \ , \tag{2.95}$$

with $\mathrm{Erfc}(x) = \frac{2}{\sqrt{\pi}}\int_x^\infty \mathrm{d}t e^{-t^2}$ as complementary error function.

To answer in which sense (P)LAM approximates the familiar $1/r$-interaction in $d = 1$, recall the asymptotic expansion of the complementary error function and truncate it after the first term,

$$\mathrm{Erfc}(|x|) \sim \frac{e^{-x^2}}{\sqrt{\pi}|x|} \quad \text{as} \quad |x| \to \infty \ , \tag{2.96}$$

implying:

$$U^{\pi}_{\mathrm{LAM}}(x_3, x_3'; \epsilon) \sim \frac{-1}{4\pi|x_3 - x_3'|} = G^{\mathrm{free}}_{\triangle_3}\Big|_{\boldsymbol{x}_\perp = 0} \tag{2.97}$$

at far field, $|x_3 - x_3'| \to \infty$. In other words, PLAM approaches the canonical gravitational interaction assuming a sufficiently large periodic domain *and* in the limit of large source-field separation.

Approaching the Weak/Strong Confinement Limit Additionally, one can study the limiting behavior of eq. (2.92) under (infinitely) strong or weak confinement. Of course, the most interesting situation is $\epsilon = 0$, i.e. infinitely strong confinement which would be equivalent to constraining the dynamics onto a d=2 manifold while retaining a $1/r^2$-force law. Unfortunately, $\lim_{x\to 0} E_1(x) = \infty$, implying there is no well behaved reduction for, $\epsilon = 0$. This result is in alignment with the free-space considerations of [9]. We note in passing that for $d = 2$, infinitely strong confinement and consequently a $1/r^2$-force law is in fact realizable and gives rise to the surface adiabatic model. Based on the introductory remarks of section 2.3, this is not surprising: If it is possible to directly implement a 1/r-interaction by hand, it should also be possible to smoothly approach the same convolution kernel by increasing the orthogonal confinement.

For $\epsilon \to \infty$ we employ the first term in the asymptotic expansion of the confluent hypergeometric function of the second kind, $U(a, b, x)$, [63]:

$$e^x E_1(x) = U(1, 1, x) \sim x^{-1} \; . \tag{2.98}$$

Therefore:

$$\begin{aligned} U^{\pi}_{\mathrm{LAM}}(x_3, x_3'; \epsilon) &= -\frac{1}{2\pi L_3} \sum_{m=1}^{\infty} U\left(1, 1, \frac{1}{2}k_m^2\epsilon^2\right) \cos\left(k_m(x_3 - x_3')\right) & (2.99) \\ &\sim -\frac{1}{2\pi L_3} \sum_{m=1}^{\infty} \frac{2}{\epsilon^2 k_m^2} \cos\left(k_m(x_3 - x_3')\right) \quad \text{as} \quad \epsilon \to \infty \; . & (2.100) \end{aligned}$$

Using the limit, [36]:

$$\sum_{m=1}^{\infty} \frac{\cos mx}{m^2} = \frac{\pi^2}{6} - \frac{\pi|x|}{2} + \frac{x^2}{4} \tag{2.101}$$

one arrives at:

$$U^{\pi}_{\mathrm{LAM}}(x_3, x_3'; \epsilon) \sim \frac{1}{2\pi\epsilon^2} G^{\pi}_{\triangle_1}(x_3, x_3') \quad \text{as} \quad \epsilon \to \infty \; . \tag{2.102}$$

In other words, under weak confinement, PLAM only approaches the uniform reduction kernel if one additionally rescales the coupling strength $a \to 2\pi\epsilon^2 a$. The same result holds true for free space conditions, i.e. LAM obeys asymptotically:

$$U^{\mathrm{free}}_{\mathrm{LAM}}(x_3, x_3'; \epsilon) \sim \frac{1}{2\pi\epsilon^2} G^{\mathrm{free}}_{\triangle_1}(x_3, x_3') \quad \text{as} \quad \epsilon \to \infty \; . \tag{2.103}$$

For all other finite values of $\epsilon > 0$, it is worth mentioning that eq. (2.93) yields a potential *free of any singularities.* In fact, it is easy to see this must be true: For large values of x we already had $U(1,1,x) \sim x^{-1}$. Moreover, one can check that for $x \to 0$ the spectrum can still be bounded by x^{-1}. Consequently the Fourier coefficients decay at most $\propto k_m^{-2}$ for $|m| > 0$ and *any* $\epsilon > 0$. $U^{\pi}_{\mathrm{LAM}}(x_3, x_3'; \epsilon)$ is then bounded by:

$$|U^{\pi}_{\mathrm{LAM}}(x_3, x_3'; \epsilon)| \leq c \left| \sum_{|m|>0} \frac{1}{k_m^2} e^{ik_m(x_3 - x_3')} \right| \propto |G^{\pi}_{\triangle_1}(x_3, x_3')| < \infty \ , \tag{2.104}$$

with c as constant depending on ϵ.

Figure 2.3 illustrates all periodic, one dimensional interaction kernels encountered in section 2.3. For the positive half-space we assume periodic boundary conditions and therefore show eq. (2.93) for various confinement strengths together with the Green's function of the Laplace operator in eq. (2.76). Note all these kernels have a vanishing mean. Taking $L \to \infty$ we arrive at the free-space interactions (2.79) and (2.95) depicted in the negative half-space.

A crucial aspect not mentioned yet is the *range* R of an symmetric interaction $U(\boldsymbol{x}, \boldsymbol{x}') = U(|x - x'|) = U(r)$. An intuitive way to define it, is to demand a particle at a distance R away from the potential source to be force free:

$$-\left.\partial_r U\right|_{r=R} \equiv 0 \ . \tag{2.105}$$

Unfortunately, eq. (2.105) is not practical as under periodic boundary conditions all considered symmetric kernels would have $r = L/2$ so that no kink exists at the domain boundary.

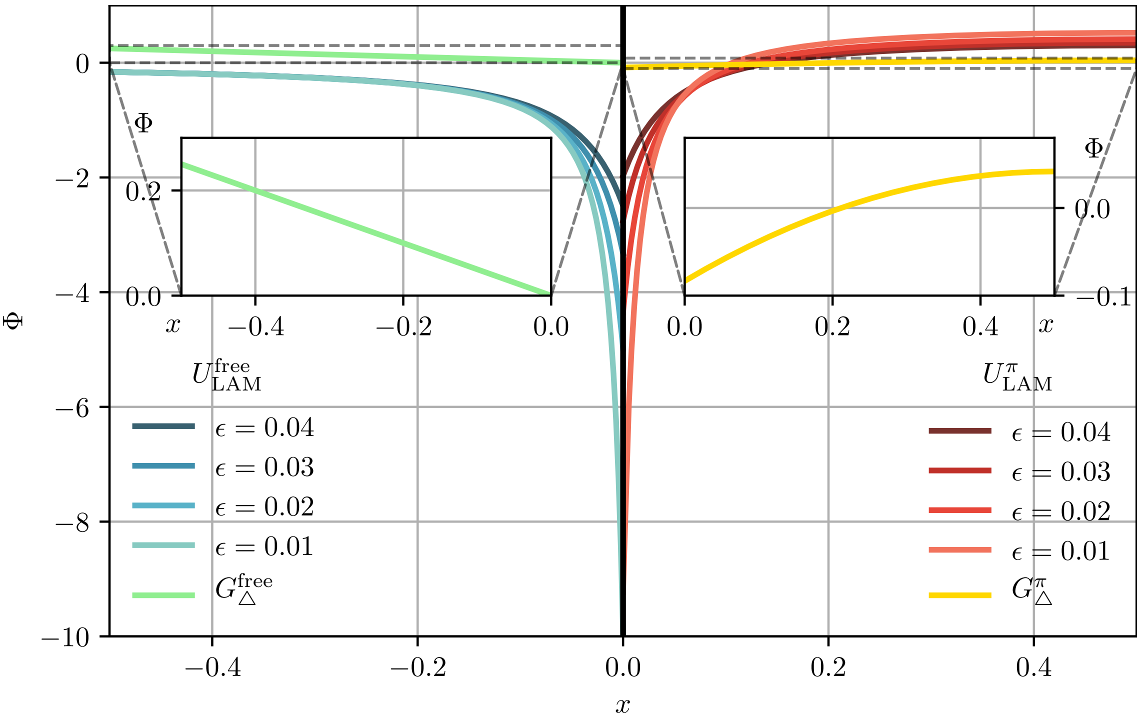

(a) $L = 1$. **Insets:** Zoom version of $G^{\mathrm{free}}_{\triangle_1}$ (left) and $G^{\pi}_{\triangle_1}$ (right).

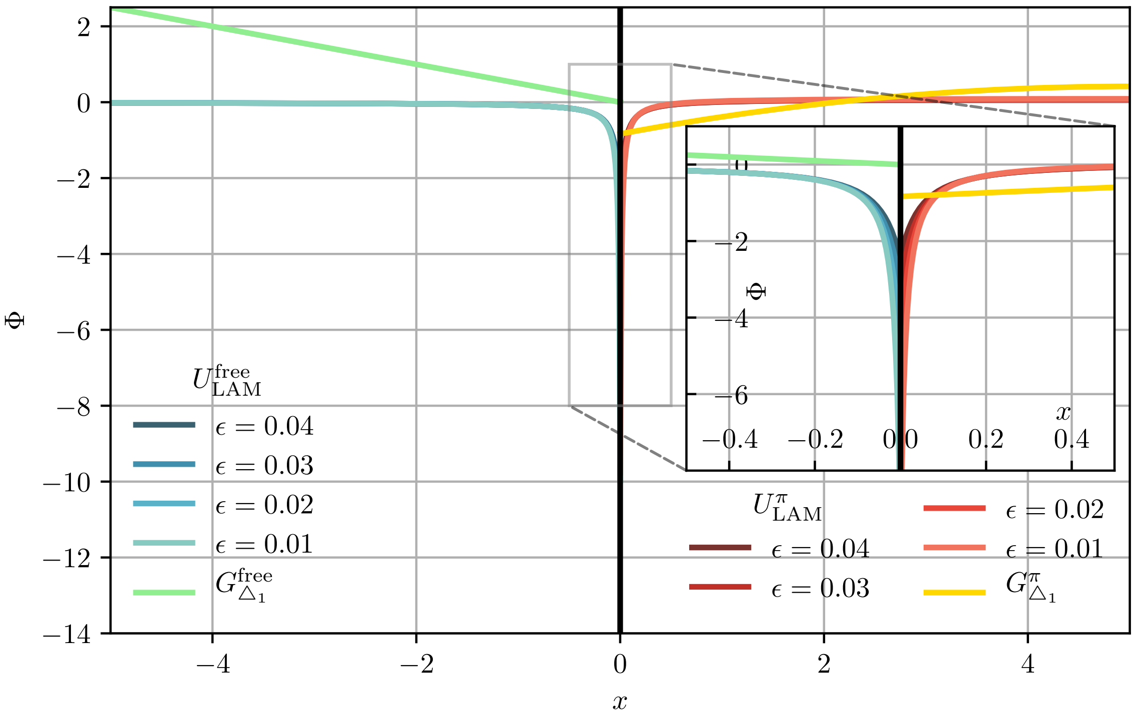

(b) $L = 10$. **Inset:** Zoom into the same region as Figure 2.3a.

Figure 2.3: Comparison of the point source potentials for a source at $x' = 0$ and two different periodic domain sizes L.
Positive half spaces: Periodic boundary conditions. We therefore show the PLAM kernel of eq. (2.93) (red) and the periodic Laplace Green's function (yellow) given in eq. (2.76).
Negative half spaces: Free space conditions, i.e. the limit of the positive half space as $L \to \infty$. Shown are the line adiabatic kernel (LAM) of eq. (2.95) (blue) and the free space Laplace Green's function (green) of eq. (2.79).

Revisit Figure 2.3 for clarification of this claim. Hence, it is more practical to define the interaction range R relative to the maximal force exerted by a point source generating a potential U:

$$\left| \partial_r U|_{r=R} \right| \equiv c \max_r \left(|\partial_r U| \right) \ , \tag{2.106}$$

where $c \ll 1$ denotes a constant, say $c = 10^{-2}$.

Figure 2.4 illustrates that the confined kernel (2.93) has a *finite range* smaller than L slowly approaching the free space range as $L \to \infty$. This is *not* the case for the one dimensional Poisson interaction (2.76) the range of which grows $\propto L$ and is infinite in the free-space case (2.79).

Additionally, we observe $\epsilon \propto R$ for PLAM. Thus, one can identify ϵ also as the parameter setting the interaction range. We get back to the importance of the interaction range in section 6.3.3.

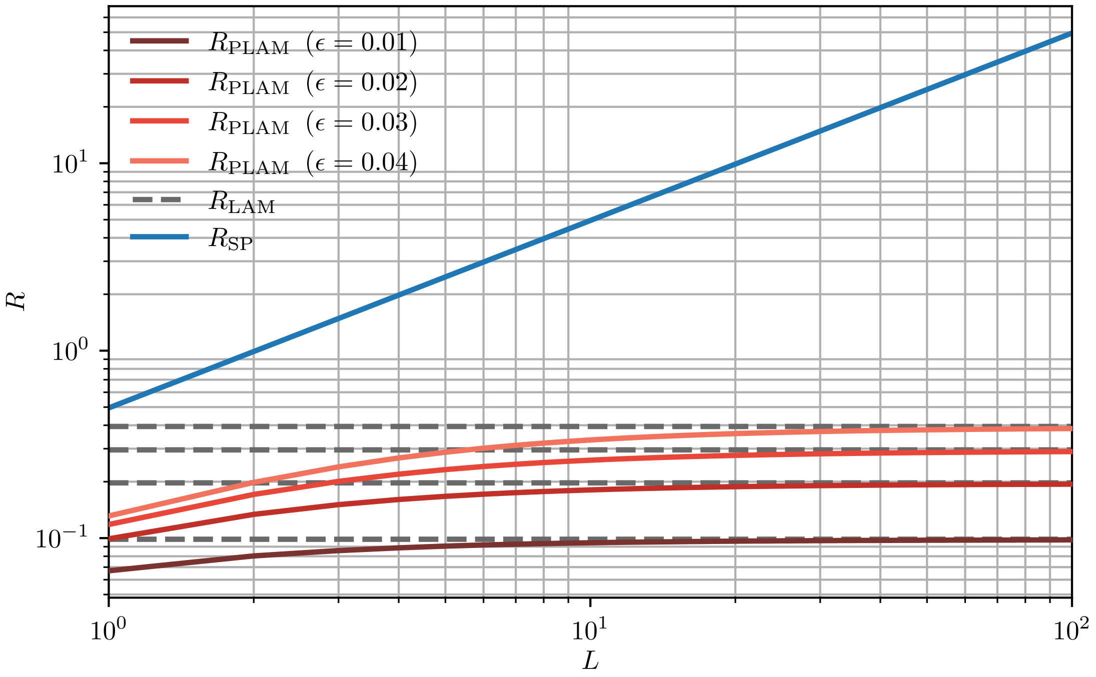

Figure 2.4: Interaction ranges, eq. (2.106) for PLAM and (1 + 1)-SP with $c = 10^{-2}$. ϵ chosen as in Figure 2.3. Dashed lines depict the corresponding *finite* range of the free space (LAM) limit. Notice how the Poisson interaction for (1 + 1)-SP is unbounded. Since $R_{\text{LAM}} \propto \epsilon$, one can interpret the confinement strength equally well as interaction range parameter.

2.4 Symmetries and Conserved Quantities

Section 2.3 illustrated that the specifics of the dimension reduction procedure only affects the form of the interaction kernel but not the form of the nonlinear Schrödinger equation. Hence a unified description for both one dimensional models is the NLSE for which the nonlocality is given by a convolution type interaction with symmetric, periodic kernel $U^\pi(|x|) = U^\pi(r)$:

$$i\partial_t \psi = \left[-\frac{1}{2}\partial_x^2 + a(t)\left(U^\pi * |\psi|^2\right)\right]\psi \ , \quad x \in \Omega_1 \ . \tag{2.107}$$

Naturally, we are interested in the conserved quantities of eq. (2.107), especially from a numerical perspective. A theoretical point of departure for deriving these is obtained by noting that eq. (2.107) has a Lagrangian structure, i.e. follows by taking the variation of the action:

$$\begin{aligned}\mathcal{S} &= \int \mathrm{d}t \int_{\Omega_1} \mathrm{d}x \mathcal{L}[\psi, \psi^*, \partial_x\psi, \partial_x\psi^*, t]) \\ &= \int \mathrm{d}t \int_{\Omega_1} \mathrm{d}x (i\psi^*\partial_t\psi - \mathcal{H}[\psi, \psi^*, \partial_x\psi, \partial_x\psi^*, t]) \ ,\end{aligned} \tag{2.108}$$

with the Hamiltonian density

$$\mathcal{H} = \frac{1}{2}\left(|\partial_x\psi|^2 + a(t)(U^\pi * |\psi|^2)|\psi|^2\right) \ . \tag{2.109}$$

Invoking Noether's theorem then yields *mass conservation*,

$$\frac{\mathrm{d}}{\mathrm{d}t}\left(\int_{\Omega_1}\mathrm{d}x|\psi(x,t)|^2\right)=0\;, \tag{2.110}$$

due to invariance of the action under global phase changes, $\psi(x,t)\to e^{i\varphi}\psi(x,t)$, and *momentum conservation*,

$$\frac{\mathrm{d}}{\mathrm{d}t}\left(-i\int_{\Omega_1}\mathrm{d}x\psi^*\partial_x\psi\right)=\frac{\mathrm{d}}{\mathrm{d}t}\left(\mathrm{Im}\int_{\Omega_1}\mathrm{d}x\psi\partial_x\psi^*\right)=0\;, \tag{2.111}$$

due to spatial translation invariance, $\psi(x,t)\to\psi(x-x',t)$ — a consequence of periodic boundary conditions *and* the symmetry of the interaction kernel. Moreover, eq. (2.108) is invariant under inertial frame changes of the form:

$$\psi(x,t)\to e^{i(vx-\frac{1}{2}v^2t)}\psi(x-vt,t) \tag{2.112}$$

and thus *conserves the galileian boost operator*, see [5].

If we consider a *static* space-time, i.e. $a(t)=\text{const.}$, then the action (2.108) is also time translation invariant, $\psi(x,t)\to\psi(x,t-t')$, and the *total energy*,

$$\begin{aligned}E&=\int_{\Omega_1}\mathrm{d}x\mathcal{H}[\psi,\psi^*,\partial_x\psi,\partial_x\psi^*,t]\\&=\frac{1}{2}\int_{\Omega_1}\mathrm{d}x|\partial_x\psi|^2+\frac{a}{2}\int_{\Omega_1}\mathrm{d}x\left(U^\pi*|\psi|^2\right)|\psi(x)|^2\equiv\langle T\rangle+\frac{a}{2}\langle V\rangle\;,\end{aligned} \tag{2.113}$$

is conserved as well. This is of course *not* true once we allow space-time to expand.

Most of these results are clear without taking a field theoretical point of view but instead stay in the quantum mechanical framework: Eq. (2.107) consititutes a Schrödinger equation free of complex dissipation terms. It therefore must be norm preserving. Recall this was not the case for proper coordinates in eq. (2.36). Moreover, under static space-time conditions we deal with a *closed* quantum system without any external, driving forces. Thus, the dynamics must be energy preserving. Once we allow space-time to expand, a driving force is added and energy conservation is lost. As we show in Appendix A.2, momentum conservation can also directly be obtained from eq. (2.107).

From the quantum mechanical point of view it is also clear that in the orthogonal plane of (1 + 1)-SP the dynamics is set by a free Schrödinger equation, cf. eq. (2.67), implying norm-, momentum and energy conservation immediately. The same holds true under confinement for which the orthogonal dynamics is governed by an harmonic Hamiltonian with potential (2.91).

Another important symmetry heavily used in the context of FDM, [67, 69, 71, 60] is the *scaling symmetry* of $(d+1)$-SP under *static space-time* conditions, i.e. $a(t)=a=\text{const.}$: If $\psi(\boldsymbol{x},t)$ solves eq. (2.75) then so does:

$$\widetilde{\psi}(\boldsymbol{x},t)=\lambda^2\psi(\lambda\boldsymbol{x},\lambda^2t)\;,\quad\lambda\in\mathbb{R}^+\;. \tag{2.114}$$

We emphasize this is true for any $d<3$ and under both free space *and* periodic boundary conditions. This can easily be confirmed by inserting one of the six possible kernels (2.76) - (2.80) or (2.82) into the d-dimensional SP equation (2.75). We refer to Appendix A.3 for the calculation.

Unfortunately, this scaling symmetry is *not* found for the (periodic) line adiabatic model, i.e. for kernels (2.92) or (2.95). Here the confinement strength ϵ introduces a novel length scale, the interaction range, into the problem. Consequently, one would have to rescale $\epsilon \to \epsilon/\lambda$ to make eq. (2.114) a valid solution of the NLSE. However, changing the interaction range means changing the physical system and we therefore conclude (P)LAM breaks the symmetry (2.114).

As a final remark we mention that in $(3 + 1)$ dimensions eq. (2.65) is also rotationally invariant implying *conservation of angular momentum.* This is useful as it allows a factorization of the wave function into a radial and angular part, just as for the hydrogen atom. The angular wave function will then be an eigenstate of the angular momentum operator whereas the radial part obeys a one-dimensional NLSE, giving us access to yet another lower dimensional representation of FDM in addition to $(1 + 1)$-SP and PLAM. The reader is referred to section 7.2.3 for more details.

Chapter 3

Fuzzy Dark Matter in the Linear Growth Regime

As we saw in chapter 2, the wave function ψ consists of a spatially homogeneous part and perturbations which source the gravitational potential Φ. Clearly, only these perturbations act as the seeds of all non-homogeneous structures we see in the universe today. Understanding their dynamics early on in the process of structure formation when fluctuations are small compared to the homogeneous background is the main objective of this chapter and vital for the generation of cosmological initial conditions.

The discussion follows mostly the standard practice for cold dark matter, e.g. [64, 23, 45]. However, we emphasize distinguishing aspects unique to FDM, e.g. [82, 20].

As in chapter 2, we depart from the three dimensional problem, i.e. FDM as modeled by $(3+1)$-SP, and start by characterizing small scale perturbation in a statistical sense both in the position and frequency space. Along the way we define the *linear matter power spectrum* as the key observable in the linear growth regime.

Understanding how the three dimensional power spectrum evolves in time will demand a rephrasing of eq. (2.39) into a hydrodynamical form as well as a *first order* stability analysis to identify gravitationally stable spatial scales. In contrast to CDM, not all scales turn out to be unstable but only those for which gravity dominates the intrinsic pressure of the perturbations. This pressure is *not* of kinetic origin like in ordinary fluids or gases but originates from Heisenberg's uncertainty principle. The result is a *sharp suppression of linear fluctuation power on scales smaller than the de-Broglie wavelength*, [41], of the zero spin boson our scalar field models. Following [41], we encapsulate this effect in a FDM *transfer function* which acts on the linearly rescaled CDM matter power spectrum.

Once the evolution of the $(3+1)$-FDM power spectrum is understood, we reduce its dimensionality to arrive at a lower dimensional fluctuation description used to generate cosmological initial conditions for $(1+1)$-SP. For implementation details, the reader is referred to [85].

3.1 Statistical Description of Fluctuation

Let us start by defining the *dark matter density contrast* $\delta(x,t)$ as the density fluctuation $\delta\rho(x,t)$ relative to the homogeneous background $\rho_m(t)$:

$$\delta(x,t) \equiv \frac{\delta\rho(x,t)}{\rho_m(t)} = \frac{\rho(x,t)}{\rho_m(t)} - 1 \ . \tag{3.1}$$

As remarked before, in the linear growth regime fluctuation are assumed to be small, so $\delta \ll 1$.

There is nothing unique about the primordial fluctuations from which our universe evolved from, so the exact form of $\delta(x,t)$ for $t \to 0$ is best understood as a realization of a particular type of stochastic process known as *Random Field.* Characterizing the statistical properties of the fluctuation field can be done in real space and in its reciprocal domain.

The discussion will concentrate on $\mathbb{R}^3$. Dimensional Reduction will be considered in section 3.3.1.

3.1.1 Statistics in Real Space - The Correlation Function

Giving a rigorous definition, [1], of a random field is cumbersome and not required for our purposes since we will work on discrete spatial grids later on. Therefore, we invoke the more practical approach reviewed in [10] and restrict ourselves to finitely many points in space.

Definition. *Let* $\{\boldsymbol{x}_m \in \mathbb{R}^3 | 1 \leq n \leq m < \infty\}$ *be an arbitrary, finite set of points in space. A Random Field* $F(\boldsymbol{x})$ *is then a set of random variables* $F(\boldsymbol{x}_m)$ *for which the probability of realizing a particular set is:*

$$p[F(\boldsymbol{x}_1), \ldots, F(\boldsymbol{x}_m)]\, dF(\boldsymbol{x}_1) \ldots dF(\boldsymbol{x}_m) \ . \tag{3.2}$$

A random field is homogeneous *if the joint probability* p *is invariant under translation* $\boldsymbol{y}$ *of all points:*

$$p\left[F(\boldsymbol{x}_1 + \boldsymbol{y}), \ldots, F(\boldsymbol{x}_m + \boldsymbol{y})\right] = p\left[F(\boldsymbol{x}_1), \ldots, F(\boldsymbol{x}_m)\right] \ . \tag{3.3}$$

A random field is isotropic *if the joint probability* p *is invariant under spatial rotations* $\boldsymbol{R}$ *of all points:*

$$p\left[F(\boldsymbol{R}\boldsymbol{x}_1), \ldots, F(\boldsymbol{R}\boldsymbol{x}_m)\right] = p\left[F(\boldsymbol{x}_1), \ldots, F(\boldsymbol{x}_m)\right] \ . \tag{3.4}$$

Most inflationary models predict the primordial density perturbation to be a *Gaussian Random Field* (GRF). In the discrete sense considered here, this means that all possible n-point joint probability densities are multivariate gaussian distributions:

$$p(\boldsymbol{\delta}) = \frac{1}{(2\pi \det \boldsymbol{\Sigma})^{3/2}} \exp\left[-\frac{1}{2}\left(\boldsymbol{\delta} - \langle\boldsymbol{\delta}\rangle\right)^{\intercal} \boldsymbol{\Sigma} \left(\boldsymbol{\delta} - \langle\boldsymbol{\delta}\rangle\right)\right] \tag{3.5}$$

with $\boldsymbol{\delta} = (\delta(\boldsymbol{x}_1)\dots\delta(\boldsymbol{x}_n)) \in \mathbb{R}^n$ as vector representation of the random set. $\boldsymbol{\Sigma}$ denotes the covariance matrix specified shortly.

Before this, however, consider the expectation value of the density contrast $\langle\delta\rangle$. Fortunately, for conditions valid in cosmology GRFs are in fact *ergodic*, see [1]. Therefore, the expectation value $\langle Q\rangle$ of a quantity $Q(x)$ can be computed via spatial averaging of a *single* realization:

$$\langle Q\rangle \overset{!}{=} \lim_{|\Omega|\to\infty}\langle Q\rangle_\Omega \equiv \lim_{|\Omega|\to\infty}\frac{1}{|\Omega|}\int_{|\Omega|}\mathrm{d}^3x Q(x)\ . \tag{3.6}$$

A direct consequence of this is by definition (3.1):

$$\langle\delta\rangle = 0\ . \tag{3.7}$$

Moreover, by ergodicity we have two estimators of the expectation value at hand for practical applications: Firstly, the arithmetic mean over an ensemble of realizations and secondly, a finite volume average over a single realization.

Coming back to eq. (3.5) now with vanishing $\langle\boldsymbol{\delta}\rangle$. In this case the covariance matrix $\boldsymbol{\Sigma}$ is just a sampling of the continuous *two-point correlation function* $\xi(\boldsymbol{x},\boldsymbol{x}')$:

$$\boldsymbol{\Sigma}_{ij} = \langle\delta(\boldsymbol{x}_i)\delta(\boldsymbol{x}_j)\rangle \equiv \xi(\boldsymbol{x}_i,\boldsymbol{x}_j)\ . \tag{3.8}$$

Next, assume the *cosmological principle* is satisfied in a statistical sense, that is we enforce statistical homogeneity and isotropy for the random field. Since GRFs are completely determined by the two-point correlation function, just as a gaussian distribution is completely fixed by its covariance, both homogeneity and isotropy translate into conditions on ξ. More concretely, if neither rotations nor translations are allowed to alter $\xi(\boldsymbol{x},\boldsymbol{x}')$, it can only be a function of spatial separation:

$$\xi(\boldsymbol{x},\boldsymbol{x}') = \xi(|\boldsymbol{x}-\boldsymbol{x}'|)\ . \tag{3.9}$$

3.1.2 Statistics in Reciprocal Space - The Power Spectrum

Obviously, the connection between real-space and its reciprocal k-space is the Fourier transform. We already introduced our convention for *bounded* domains in eq. (2.61) and eq. (2.62). For convenience, we restate them:

$$\hat{\delta}_{\boldsymbol{k}} = \int_{\Omega_3}\mathrm{d}^3x\delta(\boldsymbol{x})e^{-i\boldsymbol{k}\cdot\boldsymbol{x}}\ ,\qquad \delta(\boldsymbol{x}) = \frac{1}{L^3}\sum_{\boldsymbol{k}}\hat{\delta}_{\boldsymbol{k}}e^{i\boldsymbol{k}\cdot\boldsymbol{x}}\ , \tag{3.10}$$

assuming $L_1 = L_2 = L_3 = L$. Here, the inverse is just the Fourier series of δ and the sum runs over all vectors $\boldsymbol{k} = \frac{2\pi}{L}\cdot(i,j,k)^\intercal$ with $i,j,k \in \mathbb{Z}$.

For *unbounded* three dimensional domains the Fourier transform of a function $\delta(\boldsymbol{x})$ and its inverse are:

$$\hat{\delta}(\boldsymbol{k}) = \int_{\mathbb{R}^3}\mathrm{d}^3x\delta(\boldsymbol{x})e^{-i\boldsymbol{k}\cdot\boldsymbol{x}}\ ,\qquad \delta(\boldsymbol{x}) = \int_{\mathbb{R}^3}\frac{\mathrm{d}^3k}{(2\pi)^3}\hat{\delta}(\boldsymbol{k})e^{i\boldsymbol{k}\cdot\boldsymbol{x}}\ . \tag{3.11}$$

Consider now the *infinite* space Fourier transform of the correlation function under the assumption of statistical homogeneity and reality of δ, implying $\hat{\delta}(-\boldsymbol{k}) = \hat{\delta}^*(\boldsymbol{k})$:

$$\begin{aligned}\xi(\boldsymbol{x}, \boldsymbol{x}') &= \langle \delta(\boldsymbol{x}) \delta(\boldsymbol{x}') \rangle \\ &\overset{!}{=} \langle \delta(\boldsymbol{x}+\boldsymbol{y}) \delta(\boldsymbol{x}'+\boldsymbol{y}) \rangle && \text{(homogeneity)} \\ &= \int_{\mathbb{R}^3} \frac{\mathrm{d}^d k}{(2\pi)^3} \int_{\mathbb{R}^3} \frac{\mathrm{d}^d k'}{(2\pi)^3} \langle \hat{\delta}^*(\boldsymbol{k}) \hat{\delta}(\boldsymbol{k}') \rangle e^{-i\boldsymbol{k}\cdot\boldsymbol{x}} e^{i\boldsymbol{k}'\cdot\boldsymbol{x}'} e^{i(\boldsymbol{k}'-\boldsymbol{k})\cdot\boldsymbol{y}} && (\delta(\boldsymbol{x}) \in \mathbb{R}) \ .\end{aligned} \tag{3.12}$$

Notice the left hand side is independent of the arbitrary translation vector $\boldsymbol{y}$. Therefore, the integrand is only allowed to be non-zero if $\boldsymbol{k} = \boldsymbol{k}'$. To make this observation manifest, define the *continuous linear matter power spectrum* $P(\boldsymbol{k})$ via:

$$\langle \hat{\delta}^*(\boldsymbol{k}) \hat{\delta}(\boldsymbol{k}') \rangle \equiv (2\pi)^3 P(\boldsymbol{k}) \delta^D(\boldsymbol{k}' - \boldsymbol{k}) \tag{3.13}$$

and denote with δ^D the Dirac delta function.

Integration over k' then yields the statement of the *Wiener–Khinchin theorem*:

$$\xi(\boldsymbol{x}, \boldsymbol{x}') = \xi(\boldsymbol{x} - \boldsymbol{x}') = \int \frac{\mathrm{d}^d k}{(2\pi)^3} P(\boldsymbol{k}) e^{i\boldsymbol{k}\cdot(\boldsymbol{x}-\boldsymbol{x}')} \ . \tag{3.14}$$

The two-point correlation function is the Fourier transform of the power spectrum.

So far we only used homogeneity. Statistical isotropy demands the power spectrum do be only a function of the modulus of $\boldsymbol{k}$. Consequently, we can integrate out the angular dependence in eq. (3.14) to arrive at:

$$\xi(|\boldsymbol{x} - \boldsymbol{x}'|) = \xi(r) = \frac{1}{2\pi^2} \int_0^\infty \mathrm{d}k P(k) k^2 \frac{\sin kr}{kr} \tag{3.15}$$

and

$$P(|\boldsymbol{k}|) = P(k) = 4\pi \int_0^\infty \mathrm{d}r \xi(r) r^2 \frac{\sin kr}{kr} \tag{3.16}$$

respectively.

3.2 Time Evolution of the Matter Power Spectrum

As we noted before, all statistical properties of a GRF are encapsulated in the two-point correlation function or equivalently in the power spectrum. Higher order statistics such as the n-point correlation function vanish exactly. Thus, it suffices to determine the time evolution of $P(k, t)$ as long as we are in the linear regime with $\delta \ll 1$. Once we enter the nonlinear growth regime at $z \lessapprox 10$, we depart from a GRF. The random field then acquires non-gaussian features and higher order moments will be populated.

By definition of the power spectrum in eq. (3.13), it is apparent if we seek for the evolution of $P(k, t)$, we must understand how the density contrast evolves in the reciprocal domain. To this end, we start by bringing eq. (2.39) into a hydrodynamical form and subsequently linearize the emerging equations.

Note we start from a *dimensionfull* equation as opposed to the adimensional form (2.56). We do this to make contact with the existing literature but also to prepare for the dimensional analysis of $(1+1)$-SP in Appendix C.3.

3.2.1 The Quantum-Euler-Poisson Equation

The connection to hydrodynamics is established by means of the *Madelung transformation* [58]:

$$\psi(x,t) = \sqrt{\rho(x,t)} \exp\left(\frac{i}{\hbar} S(\boldsymbol{x},t)\right) , \tag{3.17}$$

which is inserted into (2.39) in order to find equations for both density ρ and phase S. The imaginary part then yields:

$$\partial_t \rho + \frac{1}{a} \nabla(\rho \boldsymbol{v}) = 0 , \tag{3.18}$$

which is just the continuity equation in comoving coordinates. To arrive at eq. (3.18), we also demanded that the *peculiar velocity* $\boldsymbol{v}$ is globally given as the gradient of the phase function:

$$\boldsymbol{v}(\boldsymbol{x},t) = \frac{1}{ma} \nabla S(\boldsymbol{x},t) . \tag{3.19}$$

Some remarks are in order. Firstly, note that the phase of our wave function acts as velocity potential. Consequently, the matter flow is *irrotational* as it is true for any conservative field:

$$\nabla \times \boldsymbol{v} = 0 . \tag{3.20}$$

Secondly, different conventions can be found in the literature concerning the type of velocity in which one chooses to write eq. (3.18) and subsequent equations. Here, we chose the *peculiar flow* as done in [74, 20]. Recall the peculiar flow $\boldsymbol{v}$ is the deviation from the Hubble flow and the total proper velocity $\dot{\boldsymbol{r}}$ is:

$$\dot{\boldsymbol{r}} = H\boldsymbol{r} + a\dot{\boldsymbol{x}} \equiv H\boldsymbol{r} + \boldsymbol{v} . \tag{3.21}$$

Another approach, e.g. [82, 76, 85], is to use the *conjugate velocity* $\boldsymbol{u}$ set via the wave function phase by

$$\boldsymbol{u}(\boldsymbol{x},t) \equiv \frac{1}{m}\frac{\mathrm{d}L}{\mathrm{d}\dot{\boldsymbol{x}}} = a^2 \dot{\boldsymbol{x}} = \frac{1}{m} \nabla S(\boldsymbol{x},t) , \tag{3.22}$$

with L as the Lagrange function of a classical particle, see [85].

Thirdly, using eq. (3.19) to compute the peculiar flow is somewhat cumbersome because of the phase jumps in $S(x,t)$ from $-\pi$ to π. One would have to unwrap the entire phase function before the gradient can be applied. Alternatively, one can bypass this inconvenience by extracting the peculiar flow directly from the wave function via:

$$\boldsymbol{v}(\boldsymbol{x},t) = \frac{1}{ma|\psi|^2} \mathrm{Im}\left(\psi^* \nabla \psi\right) \tag{3.23}$$

— a relation readily verified.

Back to the substitution of the Madelung representation (3.17) into the SP equation. From the real part we obtain an equation for the phase function:

$$\partial_t S + \frac{1}{2ma^2} \left(\nabla S\right)^2 = -m\Phi + \frac{\hbar^2}{2ma^2} \nabla \left(\frac{\triangle\sqrt{\rho}}{\sqrt{\rho}}\right) . \tag{3.24}$$

Next, take the gradient and use eq. (3.19) to find:

$$\partial_t \boldsymbol{v} + \frac{1}{2a} m \nabla \boldsymbol{v}^2 + H\boldsymbol{v} = -\frac{1}{a}\nabla\Phi + \frac{\hbar^2}{2m^2a^3}\nabla\left(\frac{\triangle\sqrt{\rho}}{\sqrt{\rho}}\right) . \tag{3.25}$$

Since $\boldsymbol{v}$ is irrotational, we have:

$$\frac{1}{2}\nabla\boldsymbol{v}^2 = (\boldsymbol{v}\cdot\nabla)\boldsymbol{v} + \boldsymbol{v}(\nabla\times\boldsymbol{v}) = (\boldsymbol{v}\cdot\nabla)\boldsymbol{v} . \tag{3.26}$$

In summary, eq. (3.17) turns the SP equation into the irrotational *Euler-Poisson* equations:

$$\begin{aligned} \partial_t\rho + \frac{1}{a}\nabla\cdot(\rho\boldsymbol{v}) &= 0 , \\ \partial_t\boldsymbol{v} + \frac{1}{a}(\boldsymbol{v}\cdot\nabla)\boldsymbol{v} + H\boldsymbol{v} &= -\frac{1}{a}\nabla\Phi + \frac{\hbar^2}{2m^2a^3}\nabla\left(\frac{\triangle\sqrt{\rho}}{\sqrt{\rho}}\right) , \\ \nabla\times\boldsymbol{v} &= 0 , \\ \triangle\Phi &= \frac{4\pi G}{a}\left(\rho - \rho_m\right) . \end{aligned} \tag{3.27}$$

Equation (3.27) provides a very intuitive picture for the dynamics of FDM in terms of pressure forces. Main driver of the gravitational instability is obviously the gravitational force $-\nabla\Phi$ which for CDM, i.e. in the limit $\hbar \to 0$, turns out to be the only force. This already hints at the result we will encounter in section 3.2.2: *CDM is dynamically unstable on all scales. FDM, on the other hand, allows for a stabilization against gravitational collapse due to the* quantum pressure*,*

$$p_Q = \frac{\hbar^2}{2m^2a^2}\left(\frac{\triangle\sqrt{\rho}}{\sqrt{\rho}}\right) . \tag{3.28}$$

Before we proceed, please note the Euler-Poisson equation in eq. (3.27) is *not* equivalent to the SP equation in eq. (2.39), see [77]. The argument is based on the fact that a well-defined wave function must be single-valued everywhere in its domain. Without any further constraints eq. (3.27) can only guarantee this to be true on simply connected domains C for which irrotationality implies:

$$\Gamma = \oint_{\partial C} v\cdot \mathrm{d}\boldsymbol{x} = \frac{1}{ma}\oint_{\partial C}\nabla S\cdot\mathrm{d}\boldsymbol{x} = 0 . \tag{3.29}$$

Unfortunately, in regions of destructive interference it is quite common for the wave function to develop points with $\psi = 0$, therefore rendering the phase function S ill-defined. Once these pathological points are taken out of the domain it is not simply connected anymore and $\boldsymbol{v}$ cannot *globally* be represented as a gradient field. That said, for any curve γ, not necessarily enclosing a simply connected subset, we must have:

$$\Gamma = \oint_\gamma \boldsymbol{v}\cdot\mathrm{d}\boldsymbol{x} = \frac{1}{ma}\oint_\gamma\nabla S\cdot\mathrm{d}\boldsymbol{x} \overset{!}{=} \frac{\hbar}{ma}\cdot 2\pi j , \quad j\in\mathbb{Z}\, n \tag{3.30}$$

in order to guarantee single-valueness of ψ.

Fortunately, in the linear regime where $\delta \ll 1$ essentially guarantees that pathological points don't exist, it is perfectly fine to use eq.(3.27) and not to worry about the condition (3.30).

By contrast, it is insufficient to evolve FDM by means of eq. (3.27) with standard fluid dynamics codes. Additionally, one must check whether the quantization condition (3.30) is satisfied. We refer to [54, 84] for a discussion on how this affects the results of standard fluid solvers, attempting to integrate FDM by merely incorporating eq. (3.28) as an additional pressure.

3.2.2 Stability Analysis and Growth Factors

With the hydrodynamical equations at hand, proceed by setting:

$$\rho(\boldsymbol{x}, t) = \rho_m(1 - \delta(\boldsymbol{x}, t)) \ , \tag{3.31}$$

substitute into eq. (3.27) and drop all quadratic terms of small quantities. This includes terms of order $\mathcal{O}(\boldsymbol{v}^2)$ and $\mathcal{O}(\delta \cdot \boldsymbol{v})$ as well. Realize ρ_m in eq. (3.31) is a comoving density and hence constant in time. The linearization is straight forward and yields:

$$\partial_t \delta + \frac{1}{a} \nabla \cdot \boldsymbol{v} = 0 \ , \tag{3.32}$$

$$\partial_t \boldsymbol{v} + H \boldsymbol{v} = -\frac{1}{a} \nabla \Phi + \frac{\hbar^2}{4 m^2 a^3} \nabla \triangle \delta \ , \tag{3.33}$$

$$\triangle \Phi = \frac{4\pi G}{a} \delta \ . \tag{3.34}$$

At this stage we are only concerned with the evolution of δ. Thus, eliminate the velocity by taking the combination $\nabla \cdot$ (3.33) $- \, a\partial_t$ (3.32) and insert eq. (3.34) into the result:

$$\partial_t^2 \delta + 2H \partial_t \delta = \frac{4\pi G \rho_m}{a^3} \delta - \frac{\hbar^2}{4 m^2 a^4} \triangle \triangle \delta \ . \tag{3.35}$$

Upon Fourier transformation, we arrive at:

$$\ddot{\hat{\delta}}(k, t) + 2H(t) \dot{\hat{\delta}}(k, t) + \left(\frac{\hbar^2 k^4}{4 m^2 a^4} - \frac{4\pi G \rho_m}{a^3} \right) \hat{\delta}(k, t) = 0 \ , \tag{3.36}$$

where dots denote total derivatives with respect to cosmic time.

Note that no mode coupling occurs meaning all perturbations evolve *independently.* Concerning the power spectrum, we conclude no power is transferred from large to small scales, or vice versa, as long as eq. (3.36) is valid.

For each mode k, eq. (3.36) is a harmonic oscillator with time dependent dampening $H(t)$ and frequency:

$$\omega(k, t) = \sqrt{\frac{\hbar^2 k^4}{4 m^2 a^4} - \frac{4\pi G \rho_m}{a^3}} \ . \tag{3.37}$$

From here two insightful cases can be considered.

Cold Dark Matter The behavior of CDM, i.e. $\hbar = 0$, is that of a classical, pressure-less fluid. In this limit, ω is purely imaginary which implies instability on all scales.

To determine how modes grow, set $\hbar = 0$ and choose the scale factor a as time parameter instead of cosmic time t. This takes eq. (3.36) to:

$$\hat{\delta}''(k,a) + \frac{2}{a}\hat{\delta}'(k,a) - \frac{3\Omega_m}{2a^5E^2(a)}\hat{\delta}(k,a) = 0 \ , \tag{3.38}$$

or equivalently as given in [23]:

$$\hat{\delta}''(k,a) + \left(\frac{3}{a} + \frac{\mathrm{d}\log H}{\mathrm{d}a}\right)\hat{\delta}'(k,a) - \frac{3\Omega_m}{2a^5E^2(a)}\hat{\delta}(k,a) = 0 \ , \tag{3.39}$$

where we denote $f' \equiv \frac{\mathrm{d}f}{\mathrm{d}a}$ and interpret $E(a)$ as Hubble constant normalized to unity at present time, cf. eq.(2.26).

Since the coefficients of eq. (3.39) are independent of k, we can separate out the dependence of $\hat{\delta}$ on k by setting $\hat{\delta}(k,a) = D(a)\hat{\delta}(k;a_{\text{start}})$. Physically, this implies CDM perturbations do not just grow independently but also *identically* in the linear regime.

Inserting the separation ansatz and confining ourselves to *flat, radiation-free* FLRW models with $1 = \Omega_m + \Omega_\Lambda$ this equation has the *exact*, growing solution, [23]:

$$D(a) = \frac{5}{2}\Omega_m E(a)\int_0^a \frac{\mathrm{d}a'}{a'^3E(a)^3} \tag{3.40}$$

$$\overset{[12]}{=} \frac{5}{6}B_x\left(\frac{5}{6},\frac{2}{3}\right)\left(\frac{\Omega_m}{\Omega_\Lambda}\right)^{\frac{1}{3}}\sqrt{1+\frac{\Omega_m}{\Omega_\Lambda a^3}} \quad \text{with} \quad x = \frac{\Omega_\Lambda}{E^2(a)} \tag{3.41}$$

and $B_x(a,b) = \int_0^x \mathrm{d}u u^{a-1}(1-u)^{b-1}$ as incomplete Beta function. The latter representation proofs to be convenient for numerical purposes as specialize algorithms exist for evaluating $B_x(a,b)$. Figure 3.1 illustrates the *linear growth factor* $D(a)$. One commonly normalizes its value to a reference time z_i such as present time, $z = 0$:

$$D_{a_i}(a) \equiv \frac{D(a)}{D(a_i)} \ . \tag{3.42}$$

Fuzzy Dark Matter For $\hbar \neq 0$ the condition $\omega = 0$ defines a time-dependent, critical spatial scale, the *comoving Jeans scale* $\lambda_J = 2\pi/k_J$ below which quantum pressure counteracts gravity and perturbation do not collapse under their own gravitational force. We find:

$$k_J(a) = \left(\frac{16\pi G\rho_m m^2 a}{\hbar^2}\right)^{\frac{1}{4}} \propto a^{\frac{1}{4}} \ , \quad \lambda_J(a) = \pi^{\frac{3}{4}}\left(\frac{\hbar}{m}\right)^{\frac{1}{2}}(G\rho_m a)^{-\frac{1}{4}} \propto a^{-\frac{1}{4}} \tag{3.43}$$

and write:

$$\ddot{\hat{\delta}}(k,t) + 2H(t)\dot{\hat{\delta}}(k,t) - \frac{4\pi G\rho_m}{a^3}\left[1-\left(\frac{k}{k_J(a)}\right)^4\right]\hat{\delta}(k,t) = 0 \ . \tag{3.44}$$

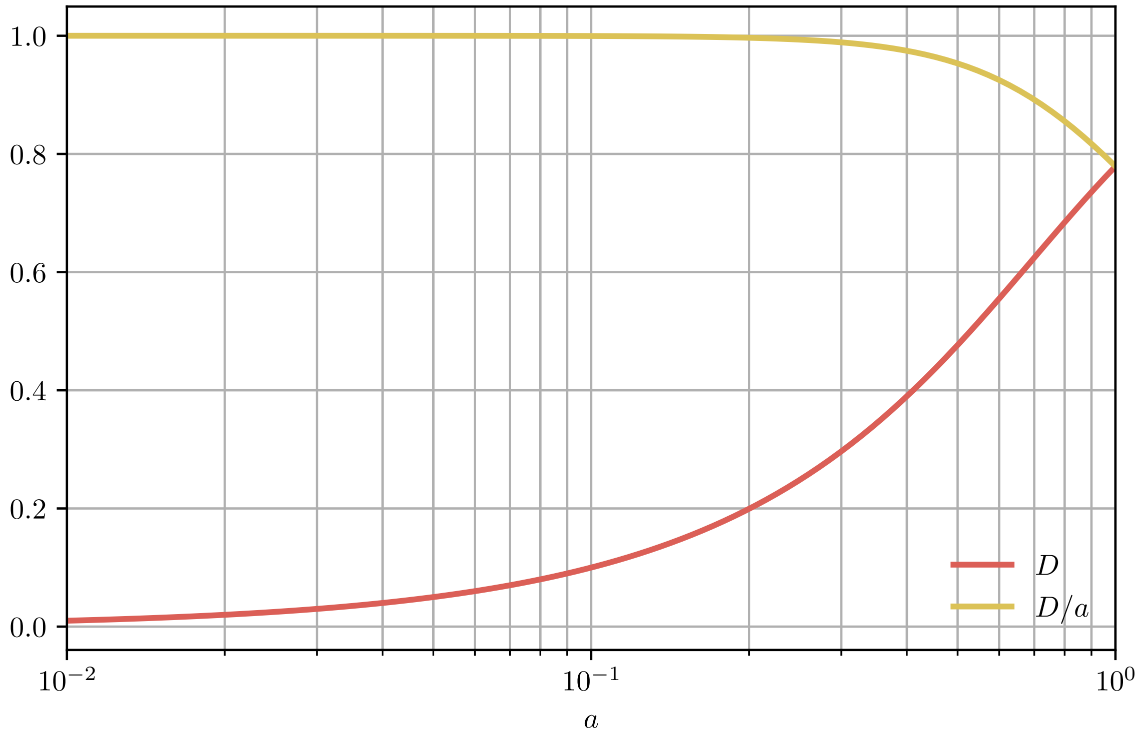

Figure 3.1: Linear CDM growth factor $D(a)$, i.e. eq. (3.40). Notice how the ration $D(a)/a$ is unity for small values of a.

Intuitively, the Jeans scale can be understood as a consequence of Heisenberg's uncertainty principle. To see this, consider the uncertainty between *proper* position σ_r and the *proper*, peculiar velocity σ_v,

$$m\sigma_r\sigma_v = am\sigma_x\sigma_v \simeq \hbar \; , \tag{3.45}$$

and remember its relation to the *comoving* position:

$$\sigma_r = a\sigma_x \; . \tag{3.46}$$

In hydrodynamic terms the flow uncertainty σ_v can be interpreted as a velocity dispersion and a simple way to estimate it is to consider the velocity of a particle trapped inside a gravitational well of a matter distribution with mean density ρ_m. For such a particle we have:

$$\sigma_v \propto r \cdot \sqrt{G\rho_m a^{-3}} = ax \cdot \sqrt{G\rho_m a^{-3}} \; , \tag{3.47}$$

with $\left(G\rho_m a^{-3}\right)^{-1/2}$ as the free-fall time scale. It then follows:

$$\sigma_x \simeq \frac{\hbar}{am\sigma_v} = \frac{\hbar}{mx\sqrt{G\rho_m a}} \; . \tag{3.48}$$

Setting $x = \sigma_x$ yields eq. (3.43) up to a numerical constant.

The interpretation then is that the source of the quantum pressure is Heisenberg's uncertainty principle which induces an increasing velocity dispersion in the FDM condensate once particles are confined to a space region that is comparable to the *comoving de-Broglie* $\lambda_{dB} \propto \sigma_x$, [41].

It is also possible to get a rough order of magnitude estimate for the boson mass m. Set $a = 1$ and demand the uncertainty principle to be effective on galactic scales, say $\lambda_{dB} \approx 1\,\mathrm{kpc}$. Furthermore, assume a dark matter velocity of $v \approx 100\,\mathrm{kms}^{-1}$ consistent with a typical velocity dispersion in galaxies. Then $m \approx 10^{-22}\,\mathrm{eV}$ and such miniscule boson masses are in fact characteristic for FDM, [41].

From the explicit dependence of eq. (3.44) on k it is apparent that FDM modes will evolve independently but *differently* as opposed to CDM. In principle one would have to find a solution of eq. (3.44) which depends parametrically on k. The author is not aware of a solution with the same generality as eq. (3.40) for CDM. Nevertheless, two insightful limits are worth mentioning.

Firstly, for an *Einstein-de-Sitter universe* (EdS), i.e. when:

$$a = \left(\frac{t}{t_0}\right)^{2/3}, \quad H = 2/3t^{-1}, \quad \text{and} \quad \rho_m = (6\pi G t_0^2)^{-1}\,, \tag{3.49}$$

eq.(3.36) can be solved *exactly.* This situation is interesting as our canonical flat FLRW universe is accurately approximated by EdS at high redshifts of $1000 > z > \mathcal{O}(1)$. The growing solution reads, [82, 20, 54]:

$$\hat{\delta}(k, a) \propto \frac{1}{a^{\frac{1}{4}}} J_{-\frac{5}{2}}\left(\sqrt{6}\frac{k^2}{k_J(a)^2}\right)\,, \tag{3.50}$$

with $J_n(x)$ as n^{th} Bessel function of the first kind.

We illustrate eq. (3.50) in Figure 3.2 which reproduces our arguments made before: Modes with $k > k_J(a)$ are stabilized by the quantum pressure and oscillate in time whereas scales with $k < k_J(a)$ are dominated by gravity and quickly leave the linear growth regime.

Secondly, for modes satisfying $k \ll k_J$ eq. (3.44) reduces to the CDM case and we conclude on sufficiently large scales compared to the Jeans wavelength CDM and FDM grow identically as set by the linear growth factor (3.40). This will become important in section 5.2.2.

By now the reader may be convinced that the quantum pressure (3.28) always opposes gravity and should therefore leave a sharp imprint even in the power spectrum dominated by non-linear dynamics. As already noted by [41, 54], *this is not true.* Realize the arguments above are only valid up to *first order* in δ. In fact, by keeping higher order terms in the expansion of eq. (3.28), one already identifies the second order correction to amplify the gravitational instability of a perturbation:

$$p_Q = \frac{\hbar^2}{4m^2a^2}\left(\triangle\delta - \left[\frac{1}{2}\delta\,\triangle\delta + \frac{1}{4}\triangle\left(\delta^2\right)\right]\right) + \mathcal{O}(\delta^3)\,. \tag{3.51}$$

Consequently, the Jeans stability is a purely linear notion and only suppresses power of *linearly* evolving scales with $k > k_J$. This does of course note imply Heisenberg's principle looses its importance in the nonlinear regime. In fact, section 5.2.1 we will argue suppression imprints in the nonlinear power spectrum can be quantitatively understood as consequence of the cosmic-scale uncertainty in x and k.

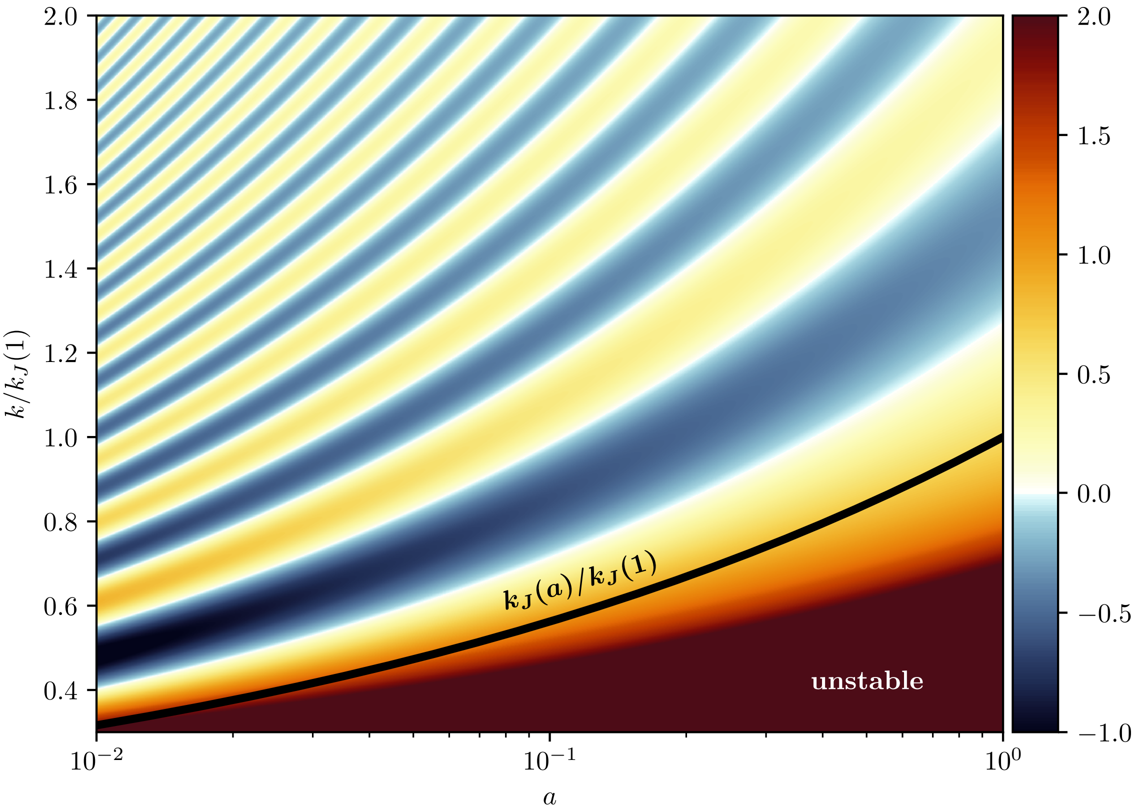

Figure 3.2: Growth behavior of a FDM perturbation in an Einstein-de-Sitter universe as a function of scale factor and spatial scale, cf. eq. (3.50). Wave numbers are normalized to the critical wave number at present time, $k_J(1)$. As one can see, modes k above the black stability line oscillate in time. This changes once the time-dependent Jeans scale passes k. After this point the perturbation enters the unstable, graviationally dominated evolution and quickly leaves the linear regime.

3.2.3 Transfer Functions

At this point we succeeded in understanding how the entire CDM spectrum and the large scale part of the FDM spectrum evolve in linear approximation. Unfortunately, eq. (3.36) is only valid for a universe free of radiation and in which matter can be approximated as *non-relativistic* fluid. Adding radiation allows for baryon-photon interactions such as Thompson scattering. These interactions are significant during radiation domination when baryons where tightly coupled to the relativistic photon fluid. We also note radiation pressure has a stabilizing effect on perturbations and that expansion was slower during radiation domination impacting the growth rate of all density constituents in general. All this effects leave observable imprints on the present day matter power spectrum.

The full fledged analysis is beyond the scope of this thesis. We refer to [23, 45] for an in depth discussion. In short, one is required to solve a coupled system of linearized Boltzmann equations for baryons, dark matter and radiation under space-time expansion. Publicly available codes such as `CAMB`, [53], exist performing exactly this task. One of the key quantities computed by these codes is the CDM *transfer function* $T(k)$. $T(k)$ encapsulates all pre-matter domination physics by representing the enhancement or suppression of mode $\hat{\delta}(k)$ relative to the large scale limit $k \to 0$, [45]:

$$T^2(k) \equiv \frac{\langle|\hat{\delta}(k, a=1)|^2\rangle}{\langle|\hat{\delta}(k, a\to 0)|^2\rangle} \Bigg/ \frac{\langle|\hat{\delta}(0, a=1)|^2\rangle}{\langle|\hat{\delta}(0, a\to 0)|^2\rangle} \; . \tag{3.52}$$

Now, choose a red shift z^* large enough such that all scales of interest are still linear and denote the primordial power spectrum $P_{\mathrm{prim}}(k)$. The present day, linear CDM matter power then takes the form:

$$P^L_{\mathrm{CDM}}(k) \propto D^2_{a^*}(1) T^2(k) P_{\mathrm{prim}}(k) \; . \tag{3.53}$$

Three remarks are in order. Firstly, eq. (3.53) is of course not identical to the measurable present day matter power spectrum $P_{\mathrm{CDM}}(k)$ which developed non-linear features at high k. That said, eq. (3.53) has practical relevance as it can be used to construct linear spectra at $a = a_{\mathrm{start}}$ from which CDM simulations can depart:

$$P^L_{\mathrm{CDM}}(k, a_{\mathrm{start}}) = D^2_1(a_{\mathrm{start}}) P^L_{\mathrm{CDM}}(k) \; . \tag{3.54}$$

One then compares the nonlinear simulation results with $P_{\mathrm{CDM}}(k)$.

Secondly, the normalization of the matter power spectrum must be measured.

Thirdly, the form of the primordial spectrum was left unspecified. One usually employs a *Harrison-Zeldovich spectrum*, $P_{\mathrm{prim}}(k) \propto k$, to ensure scale-invariance of perturbations in the gravitational potential Φ, [45].

As discussed in section 3.2.2, the evolution of the FDM matter power spectrum is expected to follow CDM for modes $k \ll k_J$. On the other hand, for perturbations larger than k_J a modification to the linear CDM matter power spectrum is required. [41] proposes to encode these changes in yet another transfer function:

$$T_{\mathrm{FDM}}(k) = \frac{\cos(x^3)}{1+x^8} \quad \text{with} \quad x = 1.61 \cdot \left(\frac{m}{10^{-22}\mathrm{eV}}\right)^{\frac{1}{18}} \frac{k}{k_{\mathrm{Jeq}}} \tag{3.55}$$

and $k_{\mathrm{Jeq}} = 9 \cdot \left(\frac{m}{10^{-22}\mathrm{eV}}\right)^{1/2} \mathrm{Mpc}^{-1}$ as Jeans scale at matter-radiation equality. In alignment with our expectation, T_{FDM} quickly approaches unity below k_{Jeq}. With this additional modification the linear FDM matter power spectrum at simulation start time a_{start} reads:

$$P^L_{\mathrm{FDM}}(k, a_{\mathrm{start}}) = D^2_1(a_{\mathrm{start}}) T^2_{\mathrm{FDM}}(k) P^L_{\mathrm{CDM}}(k) \; . \tag{3.56}$$

Figure 3.3 illustrates how the CDM-FDM transition (red) and the linear rescaling (yellow) affect the present day, linear CDM matter power spectrum (black). We also anticipate the dimension reduction (green) from three to one spatial dimension discussed in section 3.3.1. The steep power law suppression introduced by the FDM transfer function leads to a smoothing of initial density contrast compared to CDM. This is illustrated in Figure 5.2.

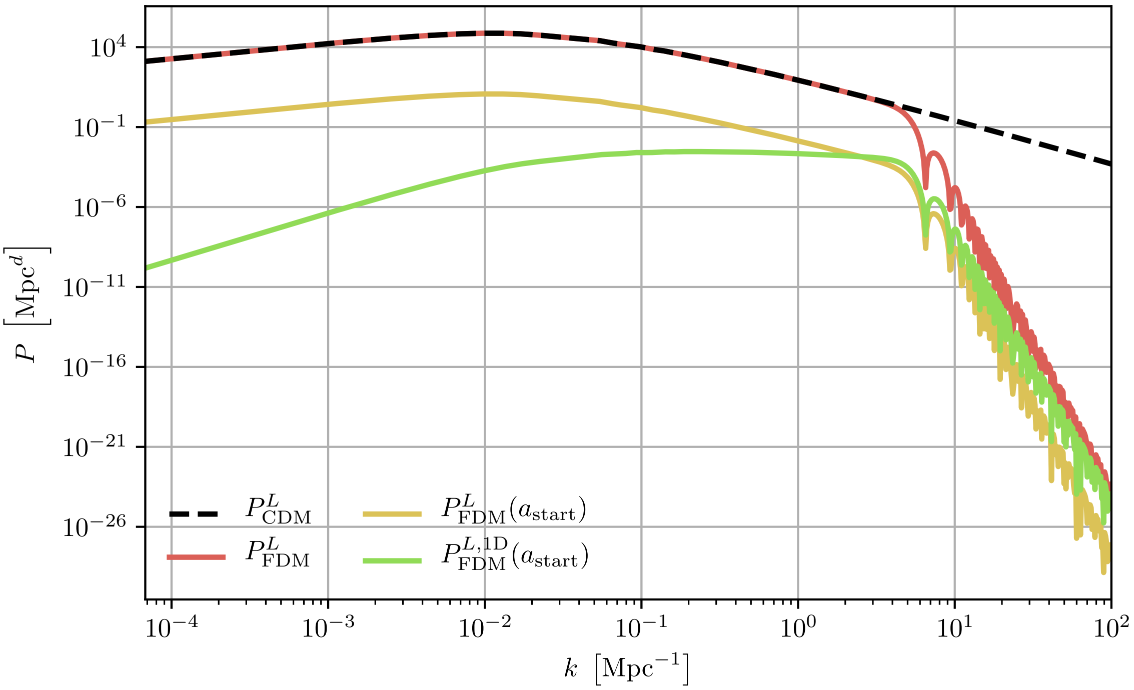

Figure 3.3: Comparison of different matter power spectra. **Black**: linear, CDM matter power spectrum at present time. **Red**: FDM matter power spectrum at present time **Yellow**: FDM matter power spectrum at $z = 100$ according to eq. (3.56) **Green**: FDM spectrum at $z = 100$ reduced to one dimension by applying eq. (3.62).

3.3 Initial Conditions for $(1 + 1)$ SP

The forgoing discussion contains almost all the necessary ingredients to construct cosmological initial conditions for $(1 + 1)$-SP. In this section we tie up loose ends.

Since $\delta \ll 1$ the hydrodynamic picture is applicable and we can represent the initial $(1 + 1)$-SP wave function via Madelung's representation, cf. eq. (3.17):

$$\psi(x, a_{\mathrm{start}}) = \sqrt{\rho_m(1 + \delta(x, a_{\mathrm{start}})} \exp\left(i\frac{S(x, a_{\mathrm{start}})}{\hbar}\right) . \tag{3.57}$$

Hence, one is required to construct an initial density contrast and phase function.

3.3.1 Initial Density Contrast

To construct the initial density contrast, we need a reduction procedure mapping the three dimensional FDM spectrum in eq. (3.56) to $d = 1$ degrees of freedom.

To this end, we adopt our previous approach in [86] and depart from the one dimensional correlation function $\xi^{1\mathrm{D}}(x, x')$. By the same arguments which lead to eq. (3.14) in $d = 3$, it is related to the $d = 1$ matter power spectrum by an infinite space Fourier transform:

$$\xi^{1\mathrm{D}}(x, x') = \frac{1}{2\pi} \int_{\mathbb{R}} \mathrm{d}k P^{1\mathrm{D}}(k) e^{ik(x-x')} . \tag{3.58}$$

Next, set $x = x'$ to arrive at the variance of the fluctuation field:

$$\left(\sigma^{1\mathrm{D}}\right)^2 = \xi^{1\mathrm{D}}(x,x) = \frac{1}{2\pi}\int_{\mathbb{R}} \mathrm{d}k P^{1\mathrm{D}}(k) = \frac{1}{\pi}\int_0^\infty \mathrm{d}k P^{1\mathrm{D}}(k) \;, \tag{3.59}$$

being uniform in space. For the last equality we used isotropy, or equivalently evenness, of $P^{1\mathrm{D}}(k)$.

In $d = 3$ one finds, cf. eq. (3.15) with $r = 0$:

$$\left(\sigma^{3\mathrm{D}}\right)^2 = \frac{1}{2\pi^2}\int_0^\infty \mathrm{d}k P^{3\mathrm{D}}(k) k^2 \;. \tag{3.60}$$

Demanding the variance to be independent of the number of dimensions, i.e. $(\sigma^{1\mathrm{D}})^2 = (\sigma^{3\mathrm{D}})^2$, yields a simple relation between both power spectra:

$$P^{1\mathrm{D}}(k) = \frac{k^2}{2\pi} P^{3\mathrm{D}}(k) \;. \tag{3.61}$$

In total, the one dimensional, linear FDM matter spectrum at $a = a_{\mathrm{start}}$ is:

$$P^{L,1\mathrm{D}}_{\mathrm{FDM}}(k, a_{\mathrm{start}}) = \frac{k^2}{2\pi} D_0^2(a_{\mathrm{start}}) T^2_{\mathrm{FDM}}(k) P^L_{\mathrm{CDM}}(k) \;. \tag{3.62}$$

However, careful attention must be paid as this spectrum assumes an *unbounded* domain. To adjust it to a *bounded* periodic domain of size L, we rederive the matter power spectrum akin to eq. (3.12) but this time using the series in eq. (3.10) instead of the Fourier integral in eq. (3.11). By the same arguments as for eq. (3.12) we arrive at:

$$\begin{aligned}
\xi(x,x') = \langle \delta(x)\delta(x')\rangle &\overset{!}{=} \langle \delta(x+y)\delta(x'+y)\rangle && \text{(homogeneity)}\\
&= \frac{1}{L^2}\sum_{k,k'} \langle \hat{\delta}'_k \hat{\delta}_k\rangle e^{ikx} e^{ik'x'} e^{i(k+k')y} \\
&= \frac{1}{L^2}\sum_{k} \langle \hat{\delta}_{-k} \hat{\delta}_k\rangle e^{ik(x-x')} && \text{(LHS independent of } y)\\
&= \frac{1}{L^2}\sum_{k} \langle \hat{\delta}^*_k \hat{\delta}_k\rangle e^{ik(x-x')} && (\delta(x) \in \mathbb{R})
\end{aligned} \tag{3.63}$$

and consequently:

$$\xi(x,x') = \xi(x-x') = \frac{1}{L}\sum_k P(k) e^{ik(x-x')} \quad \text{with} \quad P(k) \equiv \frac{1}{L}\langle |\hat{\delta}_k|^2\rangle \tag{3.64}$$

which is the *finite* domain, lower dimensional analogue to eq. (3.14) including an additional factor of L^{-1}. Combining eq. (3.62) with eq. (3.64) yields an expression for the *second moment* of the k-space modulus of $\hat{\delta}_k$:

$$\langle |\hat{\delta}_k|^2\rangle(a_{\mathrm{start}}) = L P^{L,1\mathrm{D}}_{\mathrm{FDM}}(k, a_{\mathrm{start}}) = L\frac{k^2}{2\pi} D_0^2(a_{\mathrm{start}}) T^2_{\mathrm{FDM}}(k) P^L_{\mathrm{CDM}}(k) \;. \tag{3.65}$$

Notice that in addition to eq. (3.7) we have $\langle |\hat{\delta}_0|^2\rangle = 0$. This is crucial as it guarantees *every realization* of $\delta(x)$ and not just its ensemble average $\langle \delta \rangle$ to have a vanishing

DC-mode. As discussed in section 2.2.2, this was the condition for Poisson's equation to be well defined.

It remains to be shown how a single realization, $\delta(x)$, of a GRF obeying eq. (3.65) is generated. As noted in [10], for a GRF to be homogeneous means its Fourier modes are (i) mutually independent (ii) have random phases and (iii) Rayleigh-distributed moduli.

(i) implies we can concentrate on each mode individually. Let's decompose $\hat{\delta}_k$ into modulus and phase:

$$\hat{\delta}_k = |\delta_k| e^{i\varphi_k} \ . \tag{3.66}$$

By (ii) and (iii) the probability of realizing such a $\hat{\delta}_k$ then is:

$$p(|\hat{\delta}_k|, \varphi_k) \mathrm{d}|\hat{\delta}_k| \mathrm{d}\varphi_k = \frac{|\hat{\delta}_k|}{\sigma^2(k)} \exp\left(-\frac{|\hat{\delta}_k|^2}{2\sigma(k)^2}\right) \mathrm{d}|\hat{\delta}_k| \frac{\mathrm{d}\varphi_k}{2\pi} \ . \tag{3.67}$$

To determine the yet unknown function $\sigma^2(k)$ we compute the second moment of eq. (3.67):

$$\langle|\hat{\delta}_k|^2\rangle = \int_0^\infty \mathrm{d}|\hat{\delta}_k| |\hat{\delta}_k|^2 \frac{|\hat{\delta}_k|}{\sigma^2(k)} \exp\left(-\frac{|\hat{\delta}_k|^2}{2\sigma(k)^2}\right) = 2\sigma^2(k) \ . \tag{3.68}$$

Now substitute eq. (3.65) and solve for $\sigma^2(k)$ to arrive at:

$$\sigma^2(k, a_{\text{start}}) = \frac{L}{2} P^{L,1\text{D}}_{\text{FDM}}(k, a_{\text{start}}) = \frac{L}{2} \frac{k^2}{2\pi} D_0^2(a_{\text{start}}) T^2_{\text{FDM}}(k) P^L_{\text{CDM}}(k) \ . \tag{3.69}$$

On balance, the following steps must be undertaken to construct $\delta(x, a_{\text{start}})$:

1. Compute the present day, linear CDM matter power spectrum $P^L_{\text{CDM}}(k)$ via `CAMB`, please see discussion around eq. (3.53). This must be done only once.
2. Apply eq. (3.69) to get $\sigma^2(k)$. By doing so we adjusted CDM to FDM, rescaled to a_{start}, reduced the dimensionality to $d = 1$ and truncated the domain to a periodic box of size L.
3. For each mode k, represented on a *discrete* grid, cf. section 4.2, use $\sigma^2(k)$ to draw a Rayleigh-distributed modulus $|\hat{\delta}_k|$ and uniform phase φ. The result is a discrete coefficient vector $\hat{\boldsymbol{\delta}}(a_{\text{start}})$ representing the realization in k-space.
4. Apply an inverse Fourier transform to arrive at $\delta(x, a_{\text{start}})$ on a discrete uniform grid.

The reader is referred to Figure 5.2 for an example of the end result of these steps.

3.3.2 Initial Phase

We seek for a relation between the initial phase function and the density contrast. As explained in section 3.2.2, modes with $k \ll k_J(a)$ follow the CDM fluctuation growth. Since T_{FDM} suppresses modes with $k > k_J(a)$ we simply assume in the following that early on, i.e for $z \approx 100$, the full FDM spectrum evolves according to the CDM growth factor (3.40). Under this simplification, all modes evolve identically such that in x-space:

$$\delta(x, a) = D_{a_\text{start}}(a)\delta(x, a_\text{start}) \; . \tag{3.70}$$

The time derivative at $a(t_\text{start}) = a_\text{start}$ then reads:

$$\partial_t \delta(x, t) = H(a_\text{start}) \frac{a_\text{start}}{D(a_\text{start})} \delta(x, a_\text{start}) \frac{\mathrm{d}D(a)}{\mathrm{d}a} \bigg|_{a_\text{start}} \; . \tag{3.71}$$

By Figure 3.1 it is clear that for $a_\text{start} \approx 10^{-2}$ both the derivative and $\frac{a_\text{start}}{D(a_\text{start})}$ are unity and therefore:

$$\partial_t \delta(x, t) = H(a_\text{start})\delta(x, a_\text{start}) \; . \tag{3.72}$$

Now insert this result into the linearized continuity eq. (3.32) for $d = 1$, i.e.:

$$\partial_x v(x, a_\text{start}) = -a_\text{start} H(a_\text{start})\delta(x, a_\text{start}) \; , \tag{3.73}$$

and use the definition of the peculiar flow (3.19) to find:

$$\partial_x^2 S(x, a_\text{start}) = -m a_\text{start}^2 H(a_\text{start})\delta(x, a_\text{start}) \; . \tag{3.74}$$

Hence, once the initial density is known, solving eq. (3.74) yields the initial phase. Again, we refer to Figure 5.2 for a visualization of an exemplary initial phase function.

Chapter 4

Numerical Considerations

After deriving the dynamical equations of FDM in chapter 2 and analyzing the behaviour of small scale fluctuations in the linear growth regime in chapter 3, we present the necessary numerical tools to extend the dynamical study of $(1+1)$ FDM deeply into the nonlinear growth regime, cf. chapter 5 and 6. Main purpose of this chapter is twofold: (i) present numerical procedures for computing the collective, non-local interaction potentials of SP and PLAM and (ii) devise integration methods for the non-local, non-linear Schrödinger equation (2.107).

We embark by stating general challenges involved in the integration of FDM and continue with a brief survey of existing approaches to simulating FDM by means of the $(d+1)$-Schrödinger-Poisson equation.

Due to the periodic nature of the problem, a *pseudospectral* approach involving Fourier-basis functions is a well established and highly accurate method of discretizing the NLSE (2.107) in the spatial domain. Since its non-local interaction potential is of convolution-type, application of the *convolution theorem* yields a general approach to computing the gravitational potential for SP and under strong confinement for PLAM.

The result of the spatial discretization will be a N-dimensional ordinary differential equation (ODE) for the values of the wave function on a uniform grid of N grid sites. Integration of this ODE is performed by the *operator splitting* technique. More precisely, we present a simple extension of the well known second order Strang splitting scheme applicable as approximation to the full fledged time-evolution operator of eq. (2.107) for both static and expanding background cosmologies.

We demonstrate the effectiveness and convergence of the numerical approach by a detailed convergence analysis for unstable synthetic initial conditions in the sense of chapter 3 in Appendix B.2. Main results of this analysis will be summarized in the main text.

4.1 Numerical Challenges and Existing Methods

Let us return to our original conventions 2.52 and restate the equation to solve:

$$i\partial_t\psi(x,t) = \left[-\frac{1}{2}\partial_x^2 + a(t)\left(U^\pi * |\psi|^2\right)\right]\psi(x,t) \quad x\in\Omega=[0,L] \tag{4.1}$$

$$\begin{aligned}\psi(0,t) &= \psi(L,t)\\ \partial_x\psi(0,t) &= \partial_x\psi(L,t)\end{aligned} \tag{4.2}$$

$$\psi(x,0) = \psi_0(x) \quad \text{with} \quad \int_\Omega \mathrm{d}x|\psi_0|^2 = L \tag{4.3}$$

with the interaction kernel U^π given as:

$$U^\pi(x,x') = \begin{cases} \frac{1}{L}\sum_{|m|>0} -\frac{1}{k_m^2}e^{ik_m(x-x')} = \frac{1}{2}|x-x'| - \frac{1}{2}\left[\frac{(x-x')^2}{L}+\frac{L}{6}\right] & (1+1)\ \text{SP} \\ \frac{1}{L}\sum_{|m|>0} -\frac{1}{4\pi}e^{\frac{1}{2}k_m^2\epsilon^2}E_1\left(\frac{1}{2}k_m^2\epsilon^2\right)e^{ik_m(x-x')} & \text{PLAM}\end{cases}. \tag{4.4}$$

As mentioned before, eq. (4.1) constitutes a non-local, non-linear Schrödinger equation with explicitly time-dependent, non-autonomous, Hamiltonian. It is especially the latter two properties which pose a challenge to the numerical integration: After spatial discretization, whatever form it may take, one arrives at a semi-discrete version of eq. (4.1) of the type:

$$i\partial_t\boldsymbol{\Psi}(t) = \hat{H}(|\boldsymbol{\Psi}|^2,t)\boldsymbol{\Psi} \tag{4.5}$$

with discrete Hamiltonian $\hat{H}$ and a vector of wave function coefficients $\boldsymbol{\Psi}$. Obviously, the exact form of both objects depends on the discretization and will be specified in section 4.2.

At this stage it suffices to see that non-linearities induce a (large) system of nonlinear equations in eq. (4.5). Such a system needs to be solved at every time step in an iterative fashion rendering most methods unusable already for small problem sizes.

The explicit time dependence of $\hat{H}$, on the other hand, makes the structure of the exact time evolution operator $\hat{U}(t,t')$ complicated due to the non-commutativity of $\hat{H}$ for $t\neq t'$. This is already true for linear problems. Consequently, one is required to find an efficient approximation, $\hat{\mathcal{U}}$, to the time ordered evolution operator $\hat{U}$:

$$\hat{U}(t,t') = \hat{\mathcal{T}}\left(\exp\int_t^{t'}\mathrm{d}s\hat{H}(s)\right) \approx \hat{\mathcal{U}}(t,t')\ . \tag{4.6}$$

Moreover, a non-autonomous Hamiltonian makes the dynamics non-energy preserving, depriving us of an important constant of motion by which we can assess the stability and convergence of a candidate method.

All these numerical obstacles concern primarily the temporal discratization and are independent of the exact type of nonlinear interaction or the dimensionality of the domain Ω. It is therefore instructive to survey existing methods for FDM employing the $(d+1)$-dimensional SP equation.

The authors of [81] and [51] consider SP for $d = 1, 2$ spatial degrees of freedom in an expanding FLRW universe. The time integration in these works are of Crank-Nicolson/Cayley type, an implicit finite-difference scheme to approximate eq. (4.6) which is second order in time and manifestly unitary. The gravitational potential is computed with a Fourier-based solver for Poisson's equation. As discussed above, the implicit nature of Cayley's method requires the solution of multiple linear systems per step. In fact, we employed a predictor corrector version of Cayley's method in [85, 49] and found unfavourable behavior of the integrator for dynamic $a(t)$.

[71] investigated the dynamics of core mergers under (3+1) FDM by incorporating the wave function as an additional scalar field into the Eulerian hydrodynamics code `Nyx`, [2]. Time integration is then performed by the classic 4^{th}-order Runge-Kutta method. This all purpose integrator enjoys great reputation due to it's ease of implementation and favorable accuracy at comparably low cost. Unfortunately, it does not respect the special structure of eq. (4.1), in particular it's unitarity. Consequently, norm conservation is only satisfied up to 10^{-3}. Also note that [71] does not consider an expanding space-time, but instead sets $a = 1$.

In [60] a second order Strang-type splitting approach is employed and combined with a Fourier pseudospectral discretization akin to the well known Leapfrog method for N-body problems. This integrator is manifestly unitary, easy to implement and reasonably accurate. Although [60] only considers a static space-time, we will see that their approach can readily be extended to the non-autonomous problem with no additional cost.

An inherent problem of all grid based approaches is the vast disparity of spatial scales found in truely cosmological simulations. These range from 100 Mpc boxes down to galactic cores of kpc-size — 5 orders of magnitude! Therefore, if one wants to stay in the Eulerian, i.e. grid based, framework then *adaptive meshes* are indispensable for high resolution simulations in $d = 3$ dimensions. To this end, [67] developed `GAMER`, [68] — an adaptive mesh refinement (AMR) framework suited for FDM. Combined with an operator splitting technique, [67] is arguably the state-of-the-art approach for the full fledged $(3 + 1)$ dimensional simulation of FDM.

Although not considered here, a first step towards relaxing the rigidity of the uniform grid approach which does not come with the implementation complexity of full fledged AMR is to expand ψ in a spatially localized basis such as B-splines, [18].

We refer to [84] for further comparisons, in particular for the applicability of the *smoothed particle hydrodynamics* approach to FDM.

4.2 Spatial Discretization

Since eq. (4.1) is considered on a periodic domain and only contains second derivatives in space, expansion of ψ in a finite-dimensional Fourier-basis is a natural way to discretize eq. (4.1). Let N denote an even positive integer. We then have:

$$\psi(x,t) = \frac{1}{L}\sum_{l=-N/2}^{N/2-1} \widehat{\psi}_l(t) e^{ik_l x}, \quad k_l = \frac{2\pi}{L} l \tag{4.7}$$

and time-dependent coefficients:

$$\widehat{\psi}_l(t) = \int_0^L \mathrm{d}x \psi(x,t) e^{-ik_l x} \; . \tag{4.8}$$

Assuming the continuous dynamics of $\psi(x,t)$ is p-times continuously differentiable, periodic function, $\psi(x,t) \in C^p_\pi(\Omega)$, then the expansion coefficients of eq. (4.7) decay as $|\widehat{\psi}_k| \sim k^{-p}$ and therefore provide an accurate approximation to the complete Fourier series. For smooth $\psi(x,t) \in C^\infty(\Omega)$ we achieve spectral convergence, i.e. faster than any polynomial.

Now, substitute expansion (4.7) into eq. (4.1), multiply by $e^{-ik_m x}$ and integrate over the entire domain to arrive at:

$$i\partial_t \widehat{\psi}_m(t) = \frac{k_m^2}{2}\widehat{\psi}_m(t) + \frac{a(t)}{L} \sum_{l=-N/2}^{N/2-1} \widehat{\psi}_l(t) \widehat{(U^\pi * |\psi|^2)}_{m-l} \; . \tag{4.9}$$

Two obstacles are apparent. Firstly, since the wave function is unknown we obviously cannot precompute the coefficient integral in eq. (4.8). Therefore, we resort to numerical quadrature and discretize the spatial domain as well. By choosing the same number of grid points as for the reciprocal domain in eq. (4.7), we obtain a uniform mesh with grid sites on which we evaluate the wave function and the non-linear potential:

$$x_j = \Delta x \cdot j, \quad j = 0, \ldots, N-1, \quad \Delta x = \frac{L}{N} \tag{4.10}$$

$$\psi_j(t) \equiv \psi(x_j, t) \quad V_j(t) \equiv (U^\pi * |\psi|^2)(x_j, t) \; . \tag{4.11}$$

The coefficient integral (4.8) is then approximated by the trapezodial rule. Under normal circumstances this would be an inadequate choice for the evaluation of proper integrals. However, under periodic conditions and the aforementioned smoothness assumption on ψ it holds:

$$\widehat{\psi}_l(t) = \int_0^L \mathrm{d}x \psi(x,t) e^{-ik_l x} = \frac{L}{N}\sum_{j=0}^{N-1} \psi_j(t) e^{-ik_l x_j} + \mathcal{O}\left(\Delta x^p\right) \equiv L\widetilde{\psi}_l(t) + \mathcal{O}\left(\Delta x^p\right) \tag{4.12}$$

as one can verify by the *Euler-Maclaurin summation formula*, [63]. Up to a constant prefactor, the reader will recognize eq. (4.12) as the *discrete Fourier transform* (DFT). The expansion (4.7) evaluated at the uniform grid sites x_j now reads:

$$\psi(x_j, t) = \sum_{l=-N/2}^{N/2-1} \widetilde{\psi}_l(t) e^{ik_l x_j} = \psi_j(t) \tag{4.13}$$

and eq. (4.9) is approximated as:

$$i\partial_t \widetilde{\psi}_m(t) = \frac{k_m^2}{2}\widetilde{\psi}_m(t) + a(t) \sum_{l=-N/2}^{N/2-1} \widetilde{\psi}_l(t) \widetilde{V}_{m-l}(t) \; . \tag{4.14}$$

The second obstacle still present in eq. (4.14) is the discrete convolution in the potential term. To get rid of it, we retransform into real space by multiplying with $e^{ik_m x_j}$ and summation over all modes.

Let $\odot$ denote the Hadamard product, i.e. component-wise multiplication. This yields:

$$i\partial_t \boldsymbol{\Psi}(t) = \hat{H}(t)\boldsymbol{\Psi}(t) = \left[\mathcal{F}^{-1}\left(\frac{\boldsymbol{k}^2}{2}\odot\right)\mathcal{F} + a(t)\boldsymbol{V}(|\boldsymbol{\Psi}(t)|^2)\odot\right]\boldsymbol{\Psi}(t) \tag{4.15}$$

for which we defined $(\boldsymbol{\Psi})_j = \psi_j$, $\boldsymbol{k}^2 = \boldsymbol{k}\odot\boldsymbol{k}$, $|\boldsymbol{\Psi}|^2 = \boldsymbol{\Psi}\odot\boldsymbol{\Psi}^*$, $\left(V(|\boldsymbol{\Psi}|^2)\right)_j = V_j$ and introduced the DFT operators:

$$\begin{aligned} \mathcal{F} : \mathbb{C}^N &\longrightarrow \mathbb{C}^N & \mathcal{F}^{-1} : \mathbb{C}^N &\longrightarrow \mathbb{C}^N \\ \boldsymbol{\Psi} &\longmapsto \mathcal{F}\boldsymbol{\Psi} = \frac{1}{N}\exp(-i\boldsymbol{k}\cdot\boldsymbol{x}^\intercal)\boldsymbol{\Psi} & \widetilde{\boldsymbol{\Psi}} &\longmapsto \mathcal{F}^{-1}\widetilde{\boldsymbol{\Psi}} = \exp(i\boldsymbol{x}\cdot\boldsymbol{k}^\intercal)\widetilde{\boldsymbol{\Psi}} \end{aligned} \tag{4.16}$$

with *component-wise* exponentiation followed by a matrix-vector product.

Next, we construct the vector $\boldsymbol{V}(|\boldsymbol{\Psi}(t)|^2)$. Omitting the time argument, its components are given by:

$$V_j = V(x_j) \overset{(4.11)}{=} \int_0^L \mathrm{d}x' U^\pi(|x_j - x'|)|\psi(x')|^2 \tag{4.17}$$

into which we insert the truncated and approximated Fourier series of $|\psi|^2$ akin to eq. (4.13) and the series of the interaction kernel with coefficients $\widehat{U}^\pi_n$. A simple calculation reveals the statement of the *convolution theorem*:

$$V(x_j) = \sum_{\substack{n=-N/2\\ n\neq 0}}^{N/2-1} \widetilde{|\psi|^2}_n \widehat{U^\pi}_n e^{ik_n x_j} \tag{4.18}$$

If we define $\widehat{U^\pi}_0 = 0$ then (4.18) is equivalent to an inverse DCT. Hence, we can return to the vector notation of eq. (4.15) and write:

$$\boldsymbol{V}(|\boldsymbol{\Psi}(t)|^2) = \mathcal{F}^{-1}\left(\widehat{\boldsymbol{U}^\pi}\odot\right)\mathcal{F}(|\boldsymbol{\Psi}(t)|^2) \tag{4.19}$$

with kernel coefficient vector:

$$(\widehat{\boldsymbol{U}^\pi})_n = \widehat{U^\pi}_n \overset{(4.4)}{=} \begin{cases} 0 & k = 0 \\ -\frac{1}{k_n^2} & k \neq 0 \quad (1+1)\text{ SP} \\ -\frac{1}{4\pi}U(1,1,\frac{1}{2}k_n^2\epsilon^2) & k \neq 0 \quad \text{PLAM} \end{cases} . \tag{4.20}$$

$U(a,b,x) = e^x E_1(x)$ denotes the *conflluent hypergeometric function of the second kind*, [63], and introducing it has practical relevance since computing the product $e^{x^2}E_1(x^2)$ will only succeed for small values of x. Already for moderate values of $x \sim 10$ floating point overflow occurs due to the leading exponential function. Hence, it is required to use specialized algorithms, [30], for $U(a,b,x)$ to calculate the interaction vector.

This completes the spatial discretization step, the result of which is an ordinary differential equation for the values of the wave function on the equidistant x-grid:

$$i\partial_t \mathbf{\Psi}(t) = \hat{H}(t)\mathbf{\Psi}(t) = \left[\mathcal{F}^{-1}\left(\frac{\boldsymbol{k}^2}{2}\odot\right)\mathcal{F} + a(t)\boldsymbol{V}(|\mathbf{\Psi}(t)|^2)\odot\right]\mathbf{\Psi}(t) \tag{4.21}$$

$$= \left[\mathcal{F}^{-1}\left(\frac{\boldsymbol{k}^2}{2}\odot\right)\mathcal{F} + a(t)\left(\mathcal{F}^{-1}\left(\widehat{\boldsymbol{U}^{\pi}}\odot\right)\mathcal{F}(|\mathbf{\Psi}(t)|^2)\right)\odot\right]\mathbf{\Psi}(t)\,. \tag{4.22}$$

Naïvely computing $\hat{H}\mathbf{\Psi}$ requires three component-wise vector multiplications and one vector addition both of $\mathcal{O}(N)$ complexity. Moreover, application of the DFT operators amounts to a total of four matrix-vector products with $\mathcal{O}(N^2)$ arithmetic steps. Fortunately, the matrix-vector product can be accelerated by means of a *fast Fourier transform* (FFT). This reduces the overall computational work to $\mathcal{O}(N\log N)$.

4.3 Time Integration

In this section we focus on finding an adequate approximation $\hat{\mathcal{U}}(t_0, t_0 + \Delta t)$ to the time evolution operator (4.6). To keep to scope of the discussion reasonable, we only highlight key ideas and refer to Appendix B.1 for more details.

The problem at hand is approached in two steps: First, we consider the autonomous, non-expanding case. Second, we generalize to the fully time-dependent problem.

4.3.1 Integration in a Static Space Time

The ODE to integrate reads:

$$i\partial_t \mathbf{\Psi}(t) = \left[\hat{H}_K + \hat{H}_V(t)\right]\mathbf{\Psi}(t) = \left[\mathcal{F}^{-1}\left(\frac{\boldsymbol{k}^2}{2}\odot\right)\mathcal{F} + a\boldsymbol{V}(|\mathbf{\Psi}(t)|^2)\odot\right]\mathbf{\Psi}(t) \tag{4.23}$$

where we introduced the kinetic and potential sub-Hamiltonian. Interestingly, if each subproblems is analyzed independently, i.e.:

$$i\partial_t \mathbf{\Psi}(t) = \mathcal{F}^{-1}\left(\frac{\boldsymbol{k}^2}{2}\odot\right)\mathcal{F}\mathbf{\Psi}(t) \tag{4.24}$$

$$i\partial_t \mathbf{\Psi}(t) = a\boldsymbol{V}(|\mathbf{\Psi}(t)|^2)\odot\mathbf{\Psi}(t) \tag{4.25}$$

we can find *exact* time evolution operators $\hat{U}_{K/V}$ respectively. This is trivial for the kinetic subproblem. Denote $\hat{U}_K(t_0, t_0+\Delta t) \equiv \hat{U}_K(\Delta t)$:

$$\hat{U}_K(\Delta t) = \exp\left(-i\frac{\boldsymbol{k}^2}{2}\Delta t\right)\,. \tag{4.26}$$

For the potential subproblem we realize since $\boldsymbol{V}$ is real, eq. (4.25) conserves $|\mathbf{\Psi}|^2$:

$$\frac{\mathrm{d}}{\mathrm{d}t}\left(|\mathbf{\Psi}|^2\right) \overset{(4.25)}{=} 0 \tag{4.27}$$

and the potential sub-Hamiltonian of eq. (4.25) is therefore *time-independent*:

$$i\partial_t \boldsymbol{\Psi}(t) = a\boldsymbol{V}(|\boldsymbol{\Psi}(t_0)|^2) \odot \boldsymbol{\Psi}(t) \ . \tag{4.28}$$

Consequently, no time-ordering problem occurs and the evolution operator $\hat{U}_V$ follows by simple integration. In abbreviated notation, we have:

$$\hat{U}_V(\Delta t) = \exp\left(-ia\boldsymbol{V}(|\boldsymbol{\Psi}(t_0)|^2)\Delta t\right) \ . \tag{4.29}$$

So far, no approximation was made. This changes, once we employ the idea of *operator splitting* to combine the exact evolutionary maps $\hat{U}_{K/V}$ in such a way that they approximate the full fledged operator $\hat{U}_{K+V}$.

In general, a s-stage splitting of order $\mathcal{O}(\Delta t^p)$ takes the form, [72]:

$$\begin{aligned} \hat{U}_{K+V}(\Delta t) &= \hat{\mathcal{U}}_{K+V}(\Delta t) + \mathcal{O}(\Delta t^{p+1}) \\ &= \hat{U}_K(b_{s+1}\Delta t) \circ \hat{U}_V(a_s\Delta t) \circ \hat{U}_K(b_s\Delta t) \\ &\qquad \circ \cdots \circ \hat{U}_K(b_2\Delta t) \circ \hat{U}_V(a_1\Delta t) \circ \hat{U}_K(b_1\Delta t) + \mathcal{O}(\Delta t^{p+1}) \end{aligned} \tag{4.30}$$

with splitting coefficients $\{a_i\}_{i=1,\dots,s}$ and $\{b_i\}_{i=1,\dots,s+1}$ and $\circ$ as composition operation. A plethora of possible splittings exist, each of which defined by a particular set of a_i's and b_i's. Here, we pick a rather simple representative known as second order *Strang splitting* $\mathcal{S}^{[2]}$:

$$\begin{aligned} \hat{U}_{K+V}(\Delta t) &= \mathcal{S}^{[2]}(\Delta t) + \mathcal{O}(\Delta t^3) \\ &= \hat{U}_K\left(\frac{1}{2}\Delta t\right) \circ \hat{U}_V\left(\Delta t\right) \circ \hat{U}_K\left(\frac{1}{2}\Delta t\right) + \mathcal{O}(\Delta t^3) \end{aligned} \ . \tag{4.31}$$

For more information consult Appendix B.1 or [27, 72].

A couple of remarks are in order: Firstly, $\mathcal{S}^{[2]}$ satisfies $a_i = a_{s+1-i}$ and $b_i = b_{s+2-i}$ and is therefore *time-symmetric*. Moreover, since the composition of unitary maps is unitary, $\mathcal{S}^{[2]}$ is *norm-preserving* by design. Unfortunately, it cannot conserve the total energy (2.113) exactly. This can be understood as follows: If one would recast the composition of eq. (4.31) into a single operator exponential by means of the *Baker-Campbell-Hausdorff formula*, we could read of the Hamiltonian which $\mathcal{S}^{[2]}$ integrates exactly. The result would take the form, [72]:

$$\hat{H}_{\mathcal{S}^{[2]}} = \hat{H}_{K+V} + \Delta t^2 H_{\text{error}} + \mathcal{O}\left(\Delta t^4\right) \tag{4.32}$$

with H_{error} consisting of nested commutators. Importantly, the dynamics under $\hat{H}_{\mathcal{S}^{[2]}}$ is still energy preserving, but the numerically conserved energy only coincides with the FDM energy (2.113) up to second order.

At last we draw attention to the *first-same-as-last* (FSAL) property, $b_{s+1} = b_1$, in eq. (4.31). Due to FSAL, one can omit application of the first operator in time-step n by enlarging $\Delta t \to 2\Delta t$ for application of the last evolution map in step $n-1$. This saves one FFT per time-increment.

4.3.2 Integration in an Expanding Space Time

Once we allow space time to expand the sub-Hamiltonian $\hat{H}_V$ *does* become explicitly time dependent:

$$i\partial_t \boldsymbol{\Psi}(t) = a(t)\boldsymbol{V}(|\boldsymbol{\Psi}(t_0)|^2) \odot \boldsymbol{\Psi}(t) \tag{4.33}$$

and the evolution operator $\hat{U}_V(\Delta t)$ cannot be written as:

$$\hat{U}_V(\Delta t) \neq \exp\left(-i\int_{t_0}^{t_0+\Delta t} \mathrm{d}s\hat{H}(s)\right) \tag{4.34}$$

due to the non-commutativity $\left[\hat{H}_K(t_0), \hat{H}_K(t_0+\Delta t)\right] \neq 0$.

Multiple strategies exist for dealing with this problem. For the extension of $\mathcal{S}^{[2]}$ we invoke the *Magnus expansion*, [16], stating $\hat{U}_V(\Delta t)$ can be written as operator exponential of a formal series of hermitian operators $\hat{\Omega}_k(t)$:

$$\hat{U}_V(\Delta t) = \exp\left(-i\sum_{k=1}^{\infty}\hat{\Omega}_k(\Delta t)\right) \tag{4.35}$$

where the first two terms read:

$$\hat{\Omega}_1(\Delta t) = \int_{t_0}^{t_0+\Delta t} \mathrm{d}t_1 \hat{H}_V(t_1) \tag{4.36}$$

$$\hat{\Omega}_2(\Delta t) = \frac{1}{2}\int_{t_0}^{t_0+\Delta t} \mathrm{d}t_1 \int_{t_0}^{t_1} \mathrm{d}t_2 \left[\hat{H}_V(t_1), \hat{H}_V(t_2)\right] . \tag{4.37}$$

An important property of eq. (4.35) is that any finite truncation

$$\hat{U}_V(\Delta t) = \exp\left(-i\sum_{k=1}^{N}\hat{\Omega}_k(\Delta t)\right) + \mathcal{O}(\Delta t^{r+1}) \tag{4.38}$$

yields a unitary operator, [16]. Therefore, Magnus-based integrators are norm preserving by design.

Since $\mathcal{S}^{[2]}$ is of order $p = 2$, there is no point in approximating $\hat{U}_V(\Delta t)$ by a truncation of the type (4.38) that is of order $r > 2$, as the overall order will be $\min(p, r)$. It therefore suffices to use the first term in Magnus and approximate the remaining integral by means of the midpoint method. We arrive at:

$$\hat{U}_V(\Delta t) = \hat{\mathcal{U}}_V(\Delta t) + \mathcal{O}(\Delta t^3) = \exp\left[-ia\left(\frac{\Delta t}{2}\right)\boldsymbol{V}(|\boldsymbol{\Psi}|(t_0)|^2)\Delta t\right] + \mathcal{O}(\Delta t^3) . \tag{4.39}$$

Substituting $\hat{\mathcal{U}}_V(\Delta t)$ for $\hat{U}_V(\Delta t)$ in the splitting (4.31) for $\mathcal{S}^{[2]}$ yields the second order Strang-Magnus splitting $\mathcal{SM}^{[2]}$. Compared to $\mathcal{S}^{[2]}$ *no additional cost* is required to compute $\mathcal{SM}^{[2]}$.

This concludes the extension to the non-autonomous case. Apart from specifying the procedure to compute $a(t)$ nothing is left to be done for the integration of FDM. For the latter we recall it's differential definition in eq. (2.53). $a(t)$ then follows by numerical integration of $\frac{\mathrm{d}t}{\mathrm{d}a}$ and subsequent inversion of the result. Storing the result makes it possible to "compute" the scale factor for any value of t in $\mathcal{O}(1)$ steps by interpolating between precomputed values. We refer to [85, 86] for further informations.

We note in passing that the author recently implemented a promising higher order splitting applicable in the non-autonomous case. Although it is *not* used for integrating FDM in this work, we give more details about it in Appendix B.1 as reference for future works.

4.4 Convergence and Stability

In Appendix B.2 an extensive study concerning the convergence and stability as a function of the spatio-temporal grid parameters $\{N, \Delta t\}$ is conducted. We summarize the main results of the analysis for completeness sake but encourage the reader to consider Appendix B.2 for more information about the methodology.

Dominance of the Temporal Error Our tests show once enough Fourier modes N are used in the expansion of ψ so that the spectrum $|\hat{\psi}_k|^2$ is well resolved, there is no numerical benefit in adding additional grid points. To be more precise, the error metric ϵ used to assess convergence is independent of N in the range of considered grid point numbers and changing N therefore has no observable effect on convergence or stability of the integration. This statement is true for both $(1+1)$-SP and PLAM examined in static or expanding space-times.

In fact, for static (1+1)-SP this result is not surprising as existence and uniqueness results, [43], guarantee smooth initial conditions to stay smooth. The Fourier expansion is therefore expected to converge rapidly.

Behavior of the Temporal Error For both reduction models and both expansion scenarios second order scaling of the error metric can be confirmed, $\epsilon \propto \Delta t^2$. Concerning stability, a distinction has to be made:

Under static space-time conditions, an investigation of the evolution of the numerical error as a function of time $\epsilon(t)$ reveals stability of $\mathcal{S}^{[2]}$ for SP and PLAM. More precisely, we find $\epsilon \propto t$. For $(1+1)$-SP a rigorous stability analysis under evolution of $\mathcal{S}^{[2]}$ exists, [56], and its predictions are confirmed by our implementation.

Adding expansion to the evolution induces a exponentially growing error in $\mathcal{SM}^{[2]}$ at low redshifts, $z < 10$. This is true for both reduction models. For sufficiently small time steps, say $\Delta t < 10^{-4}$, the error increases to a still reasonable magnitude. Hence, we deem the simplistic, first order Magnus approach to be effective.

Let's recapitulate. $\mathcal{SM}^{[2]}$, the approximation to the exact time evolution operator, in combination with the pseudospectral Fourier discretization of section 4.2 is an easily implemented, explicit method that provides second-order accuracy in time and spectral accuracy in space. Since $\mathcal{SM}^{[2]}$ approximates the non-autonomous, potential sub-problem by truncating its associated Magnus expansion and subsequently combines it with the exact evolution operator of the kinetic sub-problem via a composition, the entire integrator is unitary by construction. Furthermore, under static space-time conditions, i.e. $a = 1$, it is unconditionally stable and preserves both energy and total momentum well, see section 6.3 and 6.4. Approximate momentum conservation is also achieved for a dynamic space-time.

The main numerical problem remaining is its exponentially growing error under expanding space-time conditions. At this stage, we combat this issue by decreasing the temporal step size to $\Delta t \approx 10^{-5}$. In the light of the spectral convergence in space this does not seem like a substantial obstacle — after all there is no *numerical* constraint on the choice of N. Unfortunately, section 5.2.2 will reveal that there is in fact a *physical* constraint on Δx. In short, it turns out to important to resolve the entire spectrum of ψ, and not just the scales one is interested in, otherwise the large scale dynamics is systematically affected. It is this combination of a numerical constraint on Δt and a physical one on Δx that restricts us to grids with $N = 2^{20}$ and $\Delta t = 2 \cdot 10^{-5}$ implying typical simulation run times of $T = 60$ h, see section 5.1.

Chapter 5

Fuzzy Dark Matter in the Nonlinear Growth Regime

After investigation of the linear FDM evolution in chapter 3 and the numerical preparations of chapter 4, we attempt to integrate a cosmological gaussian random field with $(1+1)$-SP deeply into the nonlinear growth regime. We stress that all results presented in this chapter are obtained for $(1+1)$-SP, i.e. the reduction model *without* confinement in the transversal plane.

Over the course of chapter 2-4 a number of physical and numerical parameters were introduced, their exact values, however, were mostly left unspecified. Thus, we begin with a brief discussion on how and why we set the numerical value of certain parameters.

Next, an in depth analysis of the matter power spectrum evolution is carried out revealing intriguing physical and systematic effects. More precisely, we find the importance of the cosmic-scale uncertainty principle to carry over from linear theory inducing a sharp suppression of nonlinear matter power on scales comparable to the de-Broglie wavelength of the FDM condensate.

On large scales a CDM-like perturbation growth, akin to eq. (3.40), is confirmed for most of the integration time. At late evolution stages, however, this correspondence breaks down and one finds (i) an unphysical growth suppression in the matter power spectrum as well as (ii) a phase of mode de-correlation in the k-space correlation matrix. Reasons for this systematic effect, in particular its connection to the small scale suppression effect are explored.

Turning to x-space evolution, special attention is drawn to the issue of attaining a qualitatively identical asymptotic state for $(1+1)$-SP as it is realized for FDM under $(3+1)$-SP. In the later, stable density structures known as *solitons* emerge which act as dynamical attractor for the $(3+1)$-SP evolution. Although such unique states exist for $(1+1)$-SP, see chapter 6, our analysis indicates they are not realized under the cosmological conditions of the present chapter, i.e. GRF initial conditions and FLRW background cosmology. This failure motivates the exploration of PLAM as an alternative low-dimensional analogue of $(3+1)$-SP which we compare to $(1+1)$-SP in chapter 6.

5.1 Parameter Choices and Experimental Setup

A physically reasonable simulation setup entails many parameters, some of which can not be chosen independently but are intertwined to some degree. In this section the employed parameter set is presented and justified.

For the background expansion, we choose a flat FLRW universe with total mass density of $\Omega_m = \Omega_{\mathrm{DM}} + \Omega_{\mathrm{baryon}} = 0.3$ and a present day Hubble constant $H_0 = 68\ \frac{\mathrm{km}}{\mathrm{sMpc}}$, comparable with recent measurements, [22]. The integration is initialized at $z = 100$ which is well inside the linear growth regime for all scales of interest.

To justify this claim, the reader is reminded that linearity breaks down once $\delta \lessapprox 1$. Ignore the influence of the real space correlation function $\xi(r > 0)$ for the moment and focus on on-diagonal elements only. The initial density contrast can then be understood as a single draw from a zero mean, N-variate normal distribution with spatially uniform variance given by eq. (3.59). Under these simplified circumstances one can identify the nonlinear length scale, $l_{\mathrm{NL}} = \frac{2\pi}{k_{\mathrm{NL}}}$, by demanding, cf. (3.59):

$$1 \overset{!}{=} \xi^{1\mathrm{D}}(0) = \sigma^2(a) = \frac{1}{\pi} \int_0^{k_{\mathrm{NL}}} \mathrm{d}k P^{L,1\mathrm{D}}_{\mathrm{FDM}}(k, a) \tag{5.1}$$

and $P^{L,1\mathrm{D}}_{\mathrm{FDM}}(k, a)$ given by eq. (3.62).

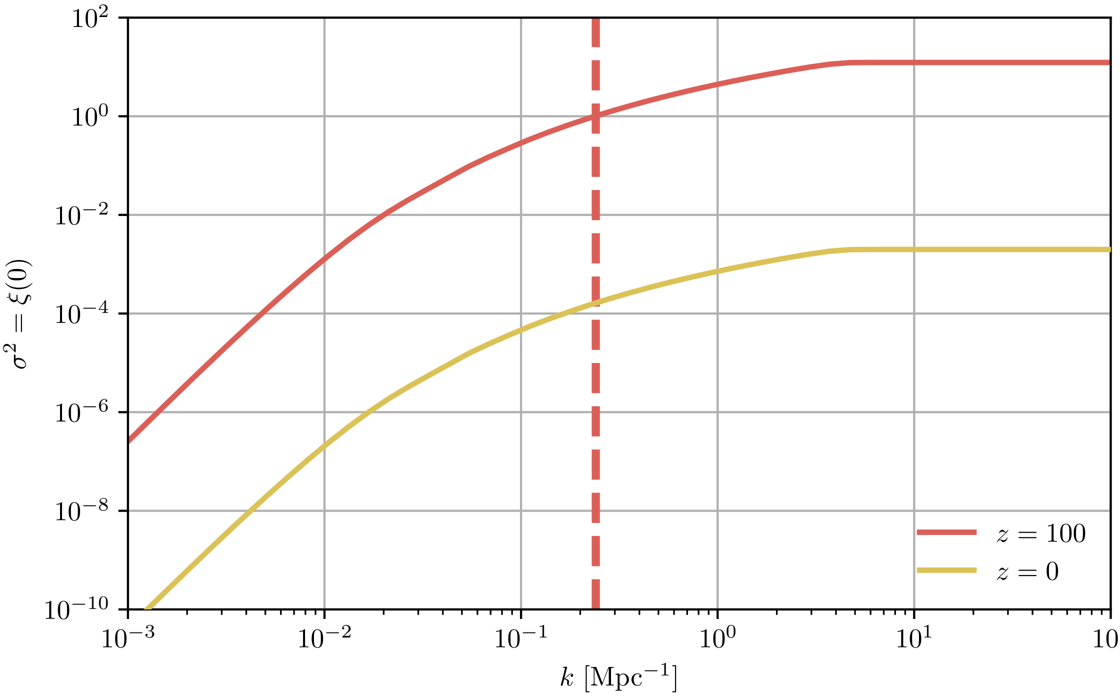

Figure 5.1: Linear FDM fluctuation variance as a function of spectral content, cf. eq. (5.1). At $z = 100$ integration of the entire spectrum yields a variance of $\sigma^2 \approx 2 \times 10^{-3}$. The entire spectrum is therefore still linearly evolving. On the other hand, at $z = 0$ linearity breaks down past $k_{\mathrm{NL}} \approx 0.24\ \mathrm{Mpc}^{-1}$ (red dashed line) and we expect to see nonlinear behavior in the matter power spectrum on spatial scales smaller than $2\pi/k_{\mathrm{NL}}$.

Figure 5.1 visualizes the right hand side integral at $z = 100$ (red) and $z = 0$ (yellow) as a function of its upper integration limit. In both cases, allowing for more spectral modes first increases the linear FDM fluctuation variance until the strong suppression of the FDM transfer function (3.55) leads to a quick saturation at $k \approx 4\ \mathrm{Mpc}^{-1}$. Notably, the final value for $z = 100$ is $\sigma^2 \approx 2 \times 10^{-3}$. Consequently, we draw the initial density field from a gaussian with variance significantly smaller than unity implying linear theory is applicable.

On the other hand, naively extending linear theory up to $z = 0$ produces a fluctuation variance that exceeds unity at $k_{\mathrm{NL}} \approx 0.24\ \mathrm{Mpc}^{-1}$ or equivalently $l_{\mathrm{NL}} \approx 26$ Mpc. Scales larger than l_{NL} are expected to be linear until present day, wheres scales with $k > k_{\mathrm{NL}}$ should be ruled by a nonlinear evolution.

We repeat that this simple argument only focuses on the real space variance but excludes the non-zero, off-diagonal elements of the full, real space covariance matrix. Nevertheless, the result is in good alignment with the structure of the *nonlinear*, three dimensional, present day matter power spectrum from CDM simulations. Here, one identifies scales with $k_{\mathrm{NL}} > 0.2\ \mathrm{Mpc}^{-1}$ to be nonlinearly modified. The good correspondence is of course no surprise as the dimension reduction of the matter power spectrum, section 3.3.1, was build around the idea of a dimension independent fluctuation variance.

Having identified the linear scales at present time also allows us to choose a domain size L such that the largest representable mode, $\frac{2\pi}{L}$, is still linear at $z = 0$. Doing so makes it possible to compare it's evolution with the CDM growth factor in eq. (3.40) which it is required to obey, cf. section 3.2.2. This is an important sanity check for the integration process and will give us valuable inside into systematic problems associated with the numerical evolution of FDM.

Obviously, one wants to set L as large as possible. However, a large L induces a reduction of the largest (Nyquist) frequency $k_{\max} = \frac{\pi}{\Delta x}$ if the number of spatial points N is not increased accordingly. Increasing N is obviously paid with an increase in computation time. Unfortunately, it is a priori not clear how the wave function spectrum $|\hat{\psi}_k|^2$ will evolve and consequently how large $k_{\max}$ must be in order to resolve all features of the density field. We investigate this in more detail in section 5.2.1 and its consequences on the large scale evolution in section 5.2.2.

That said, a good compromise between resolution and runtime is $L = 50\ \mathrm{Mpc}^{-1}$ and $N = 2^{20} = 1048576$ yielding a uniform spatial resolution of $\Delta x \approx 50$pc. Combining this with a fixed temporal step size of $\Delta t = 2 \cdot 10^{-5}$ implies good convergence, see B.2, and manageable single-realization run times of $T_1 = 60$h. [1] Further increasing the resolution Δx or box size L is not possible at this point due to implementational limitations as well as resource and time constraints. The possibility of a dynamic time increment and implications on the runtime are discussed in section 5.2.2.

---

[1] The current implementation is AVX-512 vectorized and delegates FFT and linear algebra steps to the highly optimized Intel MKL. The runtime T_1 was measured under single threaded operation. Shared memory parallelization was also tested and achieved an additional speed up of $T_N \approx T_1/N$ with N as the number of spanned threads. Simulations were conducted on compute nodes of the bwUniCluster2 using Intel Xeon Gold 6230 CPUs. The memory footprint of a single threaded process was measured as roughly 200 MByte.

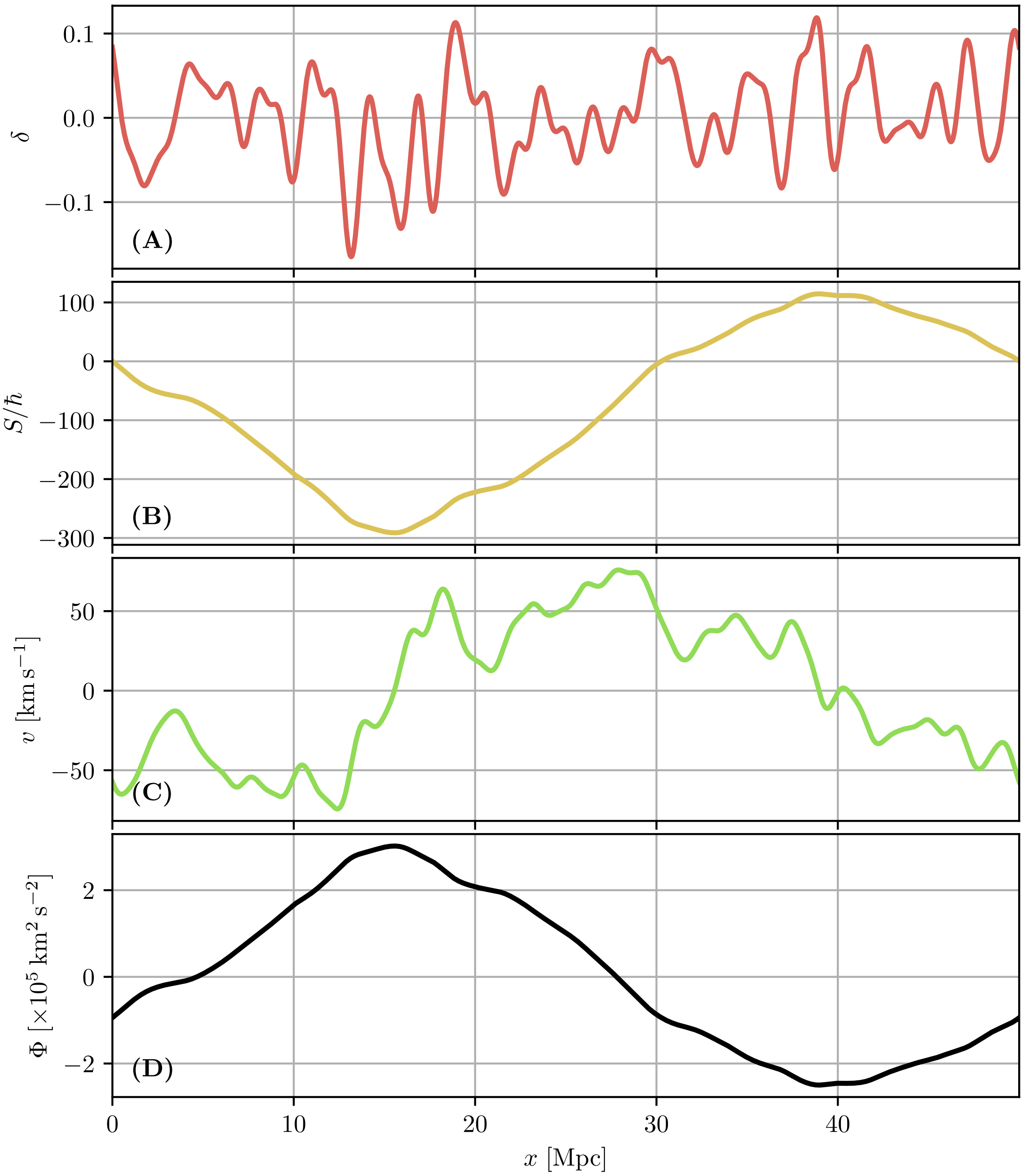

Figure 5.2: Exemplary cosmological initial conditions at $z = 100$ in a comoving box of $L = 50$ Mpc and $N = 2^{19}$ spatial points. **(A)**: Density contrast. **(B)**: Phase of the initial wave function, eq.(3.74). **(C)**: Peculiar velocity, eq. (3.23). **(D)**: Gravitational potential.

Based on the convergence and stability discussion of section 4.4 the reader cannot anticipate the physical necessity of such an excessive resolution at this point. We refer to section 5.2.1 for an explanation.

For the FDM mass, we adopt $m = 5 \cdot 10^{-23}$ eV which is slightly smaller than what was numerically deduced in [67] by fitting the ground state density of $(3+1)$-SP, cf. section 6.2, to the mass distribution of the dwarf spherical galaxy Fornax. The chosen boson mass is compatible with the cosmological parameter constraints derived in [40], where a lower bound of $m > 10^{-24}$ eV based on CMB temperature anisotropies is established. On the other hand, it is in marginal tension with the upper bound of $m < 4 \cdot 10^{-23}$ eV inferred from fitting the luminosity-averaged velocity dispersion of dwarf spherical galaxies, [35], or the lower bound of $m > 10^{-21}$ eV following from measurements of the Lyman-α forest flux power spectrum, [44]. It should be clear from these, partially contradictory, bounds that the discussion on the FDM mass is by no means settled and will require higher resolution numerical investigations in the future. That said, we do not attempt to give high precision results anyways and therefore deem a mass of $m \approx 10^{-22}$ eV to be acceptable.

As all quantities of interest, such as the matter power spectrum or the real-space correlation function, are properties of an *ensemble* one is required to approximate expectation values of the latter. Unfortunately, ergodicity breaks down once δ develops non-gaussian features meaning it is *not* enough to spatially average a single realization. Instead we are required to estimate the ensemble average by taking the arithmetic over a set of realizations of size $\mathcal{N}$. In general $\mathcal{N}$ cannot be to large. We choose to limit our considerations to $\mathcal{N} = 100$ realizations in order to limit the required computational effort. The total ensemble computation time then amounts to 6000 CPU hours.

By following the steps outlined in section 3.3, one arrives at the initial conditions depicted in Figure 5.2. Here two aspects are worth mentioning. Firstly, note the smoothness of the density contrast in **(A)** — a consequence of the sharp power suppression mediated by the FDM transfer function for scales larger than k_{Jeq}, eq. (3.55).

Secondly, the gravitational potential shown in **(D)** proves to be a lot smoother and less spiky as one might expect by comparison with the density field in **(A)**. This is the consequence of the long range behavior of the periodic Poisson kernel $G^{\pi}_{\triangle_1}$, eq. (2.76), effectively smoothing out the small scale features of the density contrast from which it is sourced. In fact, the initial phase function in **(B)** shows the same slowly varying behavior as Φ which is not surprising as it obeys a Poisson-type equation, eq. (3.74), as well.

Recall from the discussion in section 2.3 that the range R of $G^{\pi}_{\triangle_1}$ was $R \approx L/2$. We therefore expect only the half-box-averaged behavior of δ to affect the structure of Φ or S. This is readily verified: Overdensities in δ are somewhat more often to find in the interval $25\,\mathrm{Mpc} \leq x \leq 50\,\mathrm{Mpc}$, hence a gravitational trough at $x \leq 40\,\mathrm{Mpc}$, whereas the initial density contrast in $5\,\mathrm{Mpc} \leq x \leq 25\,\mathrm{Mpc}$ is negative on average, thus forming a ridge in Φ at $x \leq 15\,\mathrm{Mpc}$. This results in the sinusoidal shape of Φ and S. We get back to the potential smoothing of $(1+1)$-SP in section 6.3.3.

5.2 Evolution in Reciprocal Space

Let us begin by investigating the evolution of the one dimensional FDM matter power spectrum $P^{\mathrm{1D}}_{\mathrm{FDM}}$ as a function of the redshift. For this consult Figure 5.3 illustrating $P^{\mathrm{1D}}_{\mathrm{FDM}}$ at various stages of the integration up to $z = 0$.

Here, the black, dashed spectrum represents $P^{L,\mathrm{1D}}_{\mathrm{FDM}}$, i.e. the linear FDM spectrum used to construct the initial conditions. All remaining spectra are depicted together with their respective 1σ-confidence interval (shaded areas) which we determined as error of the arithmetic mean.

Generally, one finds small scale power to emerge quickly from the numerical noise at 10^{-30}. In the process a sharp power cut off develops traveling to ever smaller scales, i.e. larger k, as the evolution progresses.

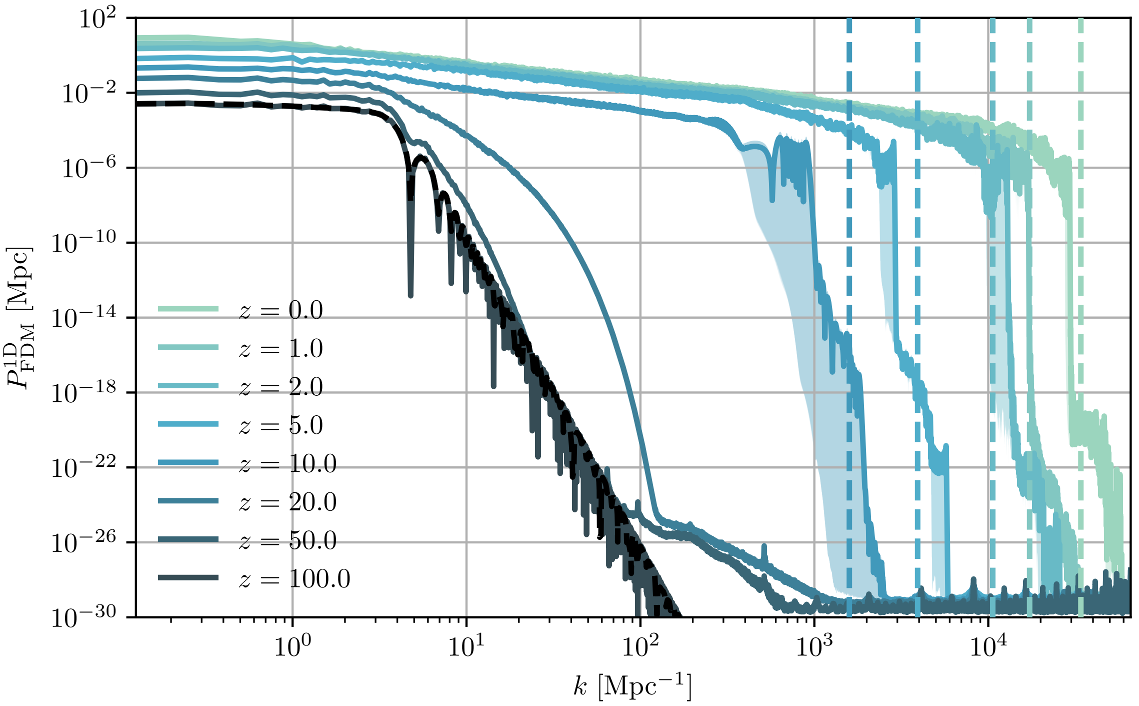

Figure 5.3: One dimensional FDM matter power spectrum as a function of redshift estimated from $\mathcal{N} = 100$ realizations. The shaded regions represents the 1σ-confidence interval and the black, dashed line depicts the linear spectrum $P_{\mathrm{FDM}}^{L,\mathrm{1D}}$ of eq. (3.62) used for the sampling process of the initial conditions in Figure 5.2. Colored, vertical dashed lines illustrate the dynamical Heisenberg/de-Broglie scale which we infer from the velocity dispersion of the peculiar flow — the hydrodynamic analogue to the quantum uncertainty — and Heisenberg's uncertainty principle. Consult section 5.2.1 for more information.

Simultaneously, one observes an overall increase in power, mostly pronounced on large scales, i.e. small k and based on the discussion of section 3.2.2 we expect this power growth to be governed by the CDM growth function in eq. (3.40). Both aspects, i.e. the sharp small scale suppression and the large scale growth are analyzed in the following.

5.2.1 Small Scale Suppression — The Heisenberg Scale

We already saw in the context of linear theory, section 3.2.2, how the uncertainty principle gave rise to the Jeans scale below which gravitational collapse was quantum mechanically suppressed. It is therefore natural to conjecture that the uncertainty principle leads to an equivalent effect in the nonlinear regime.

To test this hypothesis, we set in accordance with section 3.2.2:

$$\sigma_r \simeq \frac{\hbar}{m\sigma_v} \tag{5.2}$$

Remember this relation is in *proper* coordinates. The velocity dispersion on the scale of the comoving box is then estimated via:

$$\sigma_v = \sqrt{\langle v^2 \rangle_L - \langle v \rangle_L^2} \tag{5.3}$$

where $\langle . \rangle_L$ denotes a spatial average, v follows from eq. (3.23) and σ_r as *proper* spatial uncertainty. Figure 5.4 shows the arithmetic mean of σ_v and σ_r over all $\mathcal{N}$ realizations together with their respective 1σ confidence intervals.

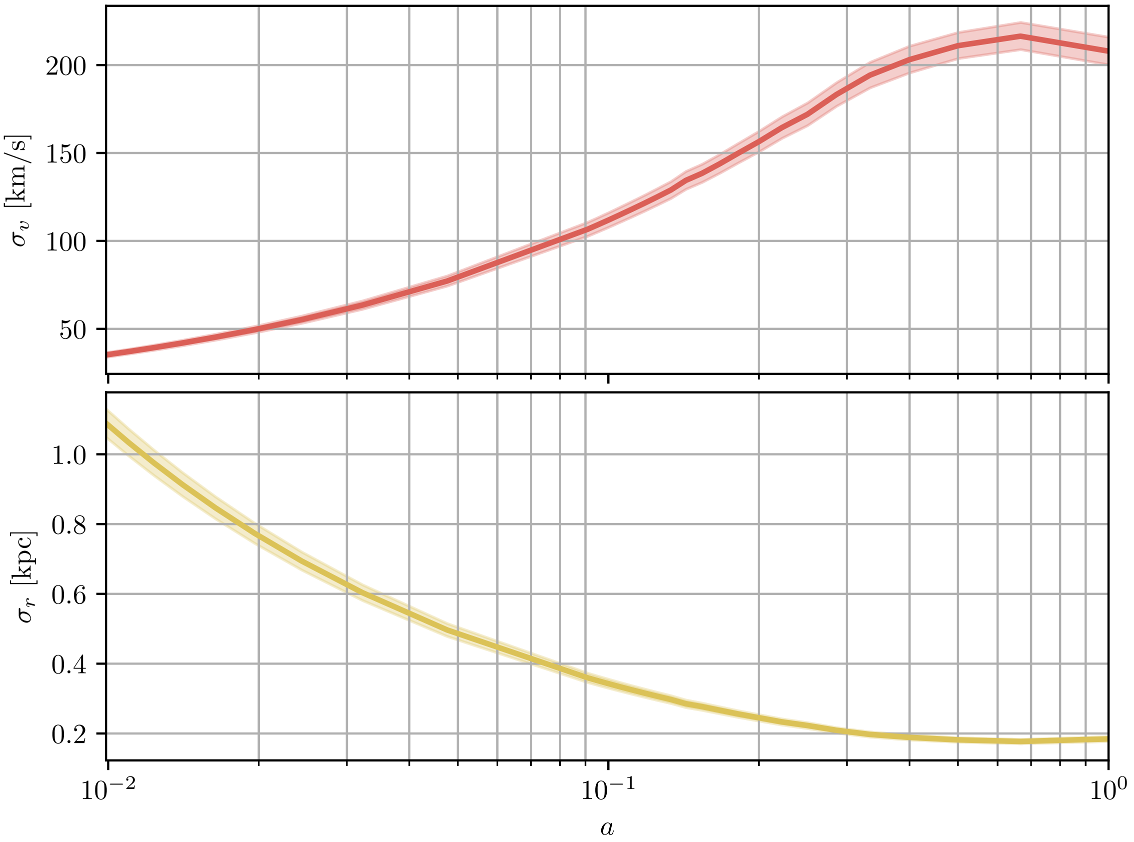

Figure 5.4: Estimated expectation value of the peculiar velocity dispersion σ_v and induced proper spatial uncertainty σ_r, eq. (5.2). The behavior of both quantities follows our expectation: As time progresses, matter accumulates in the gravitational wells, therefore getting more localized in space. The system responds to this increased spatial localization by an increase in the velocity uncertainty, i.e. a repulsion in the reciprocal space.

We find numerical values of the velocity uncertainty which are in fact compatible with generic galaxy dispersion velocities in (3+1) dimensions and the behavior of both quantities follows our expectation: As time progresses, matter accumulates in the gravitational wells, therefore getting more localized in space. The system responds to this increased spatial localization by an increase in the velocity uncertainty, i.e. a repulsion in the reciprocal space. The saturation in the velocity dispersion around $\sigma_v = 210\,\mathrm{km\,s}^{-1}$ may be an indicator for reaching the system's equilibrium configuration. However, in light of the systematic effects encountered in section 5.2.2 it may also be an indicator for the finite velocity resolution of the uniform spatio-temporal grid $\{\Delta t, \Delta x\}$.

Defining the *comoving* reciprocal scale $k_{\sigma_x} = \frac{2\pi}{\sigma_r/a}$, one arrives at the dashed, vertical lines of Figure 5.3. These yield a reasonable estimate for the cutoff wave number discussed before and we conclude that the uncertainty principle is responsible for the matter power suppression in the nonlinear regime.

5.2.2 Large Scale Growth

To assess how large scales evolve compared to CDM, we normalize the nonlinear matter power spectrum of Figure 5.3 to the prediction of the linear CDM theory, i.e. analyze the ratio $P^{\mathrm{1D}}_{\mathrm{FDM}}(k,z)/P^{L,\mathrm{1D}}_{\mathrm{FDM}}(k,z)$ and take the linearly evolved spectrum $P^{L,\mathrm{1D}}_{\mathrm{FDM}}(k,z)$ from eq. (3.62).

Figure 5.5 depicts the normalized spectrum for modes $k < 10$ Mpc^{-1}. Here, three aspects are important.

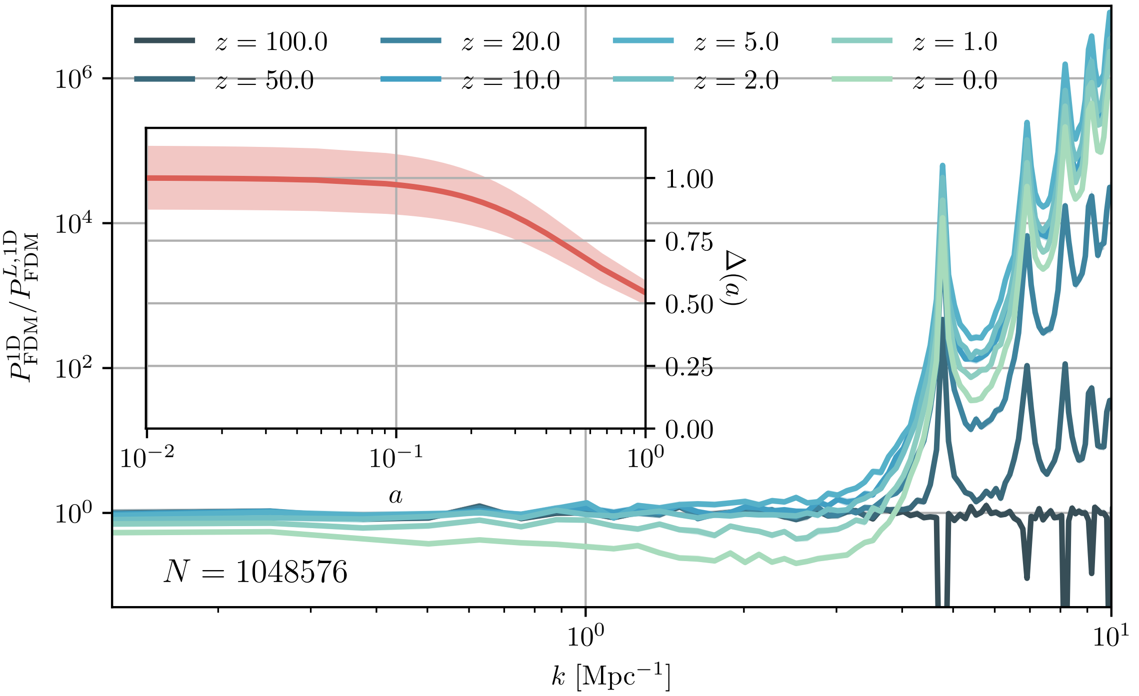

Figure 5.5: Comparison between the large scale FDM spectrum and linear theory. Linear theory is valid at redshift z if the ratio $\Delta = P^{\mathrm{1D}}_{\mathrm{FDM}}/P^{L,\mathrm{1D}}_{\mathrm{FDM}}$ approaches unity for $k \to k_{\mathrm{min}}$. **Inset**: Power loss of k_{min} compared to linear theory.

Firstly, matter power is massively enhanced compared to linear theory for mid-sized scales. This is the result of the nonlinear evolution. Non-linear evolution also explains the emerging peak structure: Recall the heuristic FDM transfer function in eq. (3.55) has multiple roots where the linear spectrum vanishes exactly. Although our uniform k-grid never hits such a root exactly, it still includes points close to them. These appear as dips in the initial, normalized spectrum at $z = 100$. If linear theory were correct, these dips should persist to exist for later times, yet nonlinear dynamics enhances the spectral power close to these roots and therefore turns dips into peaks.

Secondly, if linear theory were correct on the largest scales until redshift z, the corresponding normalized spectrum should converge to unity as $k \to k_{\mathrm{min}}$. Interestingly, we observe a loss of power as the integration approaches $z = 0$. The inset in Figure 5.5 analyzes this effect in more detail for $k = k_{\mathrm{min}}$ by means of:

$$\Delta(a) = \frac{1}{D^2_{a_{\mathrm{start}}}(a)} \frac{P^{\mathrm{1D}}_{\mathrm{FDM}}(k_{\mathrm{min}}, a)}{P^{\mathrm{1D}}_{\mathrm{FDM}}(k_{\mathrm{min}}, a_{\mathrm{start}})} \tag{5.4}$$

and its respective 1σ-confidence interval. As in section 3.2.2, $D^2_{a_{\mathrm{start}}}(a)$ denotes the linear CDM growth factor normalized to unity at $a = a_{\mathrm{start}}$. The inset indicates a power loss of about 45%.

The large scale power loss effect was also reported in [54] for $d = 3$ dimensions and recently analyzed in more detail for $d = 1, 2$ degrees of freedom by [32]. Both works identify an insufficient resolution of the Heisenberg- or (up to a factor of 2π) de-Broglie scale to be the main source of this systematic effect. Verifying this claim is simple. One can either reduce the boson mass, [54], while keeping all other parameters fixed or decrease the number of spatial nodes N, [32]. The latter saves computation time which is why we reduce the discussion to this approach. Figure 5.6 illustrates the large scale growth for $N = 2^{15}$ points. Clearly the suppression effect is strongly enhanced and power drops to less than 10% of what linear theory predicts at present time.

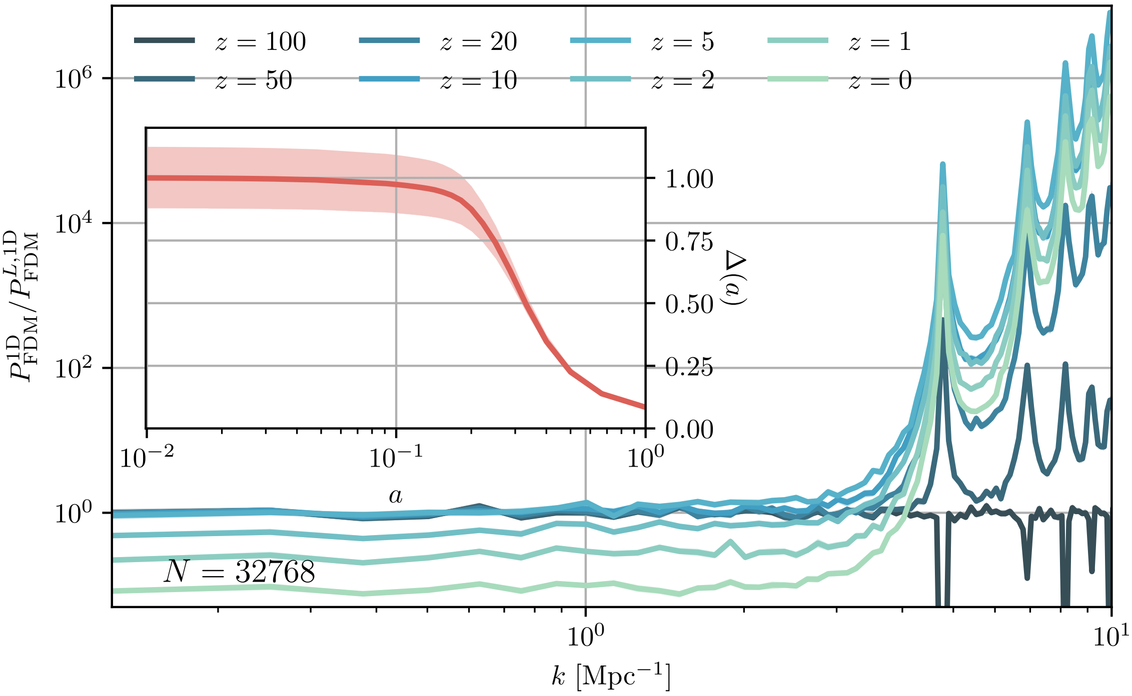

Figure 5.6: Comparison between the large scale FDM spectrum and linear theory in a $L = 50$ Mpc box with only $N = 2^{15}$ points. Note how at late times a loss of power on the largest scale induces a power reduction for the entire spectrum. **Inset**: Power loss of k_{min} compared to linear theory.

Understanding this systematic effect on an intuitive level is straight forward: Let us return to the linearized continuity equation (3.73) and transform it into k-space:

$$\hat{v}_k = \frac{iaH(a)}{k}\hat{\delta}_k \; . \tag{5.5}$$

Now, consulting Figure 3.3 shows that the linear, one dimensional FDM spectrum $P^{L,1\mathrm{D}}_{\mathrm{FDM}}$ is nearly white noise, i.e. uniform, for $0.1\ \mathrm{Mpc}^{-1} \leq k \leq 5\ \mathrm{Mpc}^{-1}$ implying $\hat{\delta}_k$ is drawn from a gaussian distribution with approximately constant variance σ_k^2. It is therefore valid to assume $\hat{\delta}_k$ is approximately constant as $k \to k_{\mathrm{min}}$. However, $\hat{v}_k$ increases in the same limit as it behaves $\propto k^{-1}$. *Thus large scales are associated with high peculiar velocities.* Velocities, on the other hand, are encoded in the phase of the wave function and if the uniform grid is not capable of resolving the phase function up to the largest physical velocity associated with the Heisenberg/de-Broglie scale $k_{\sigma_x} \propto \frac{am\sigma_v}{\hbar}$ the integration systematically underestimates the flow of large scale modes. Hence, we fail to follow the large scale evolution correctly and find *FDM simulations to be extremely demanding in terms of spatial resolution. It is not enough to resolve the length scales of interest. Additionally, one must ensure that the Heisenberg/de-Broglie scale is resolved which is typically significantly smaller.* This only reemphasizes the urgent need of a spatially adaptive discretization such as the B-spline approach, [18], or non-uniform FFTs. Note that CDM simulations or FDM-SPH (smoother particle hydrodynamics) codes typically satisfy this resolution constrained implicitly. This is plausible due to the Lagrangian nature of their formulation: One follows the trajectories of a fixed number of (fluid) particles instead of a field on a fixed uniform grid. Combined with a adjustable step size, this implies no velocity resolution limit for N-body or FDM-SPH codes.

That said, our $N = 2^{15}$-ensemble clearly supports the resolution arguments made in [54, 32] but it does not explain the origin of the power loss for $N = 2^{20}$ for which Figure 5.3 proves that the Heisenberg scale is well resolved. One possible explanation is the size of the periodic box. Realize $k_{\mathrm{min}} = 0.126\ \mathrm{Mpc}^{-1}$ is according to Figure 5.1 with $\sigma^2(k_{\mathrm{min}}) = 0.48$ already dangerously close to leaving the linear regime at $z = 0$. One should therefore expect deviations from the linear growth function anyways. Furthermore, an insufficient time step size might be a source of errors. Appendix B.2 illustrated the sensitivity of the integration on Δt, especially for late times where an expanding background cosmology induces exponentially growing errors. Hence, it is only natural to assume that decreasing Δt alleviates the power loss effect. Unfortunately, as $\Delta x = \frac{L}{N}$ is essentially fixed by the Heisenberg scale and L cannot be made significantly smaller without k_{min} leaving the linear regime, there is no immediate way to reduce N while decreasing Δt to (i) keep computation times within reasonable bounds and (ii) check the impact on Δt on the power loss without violating the Heisenberg scale or the box size linearity constrained. Application of the fourth order splitting scheme presented in section B.1 might be a sensible path forward. We leave further investigations to future works.

Thirdly, the systematic loss effect does not just influence small k but leads to an unphysical reduction of matter power on all scales, cf. Figure, 5.6. This makes the assessment of nonlinear growth somewhat complicated. [32] proposes to simply rescale the final spectrum by the loss experienced for small k. However, it is also noted that "the extent to which this naive rescaling captures nonlinear growth is unclear", [32]. In fact, we will see in section 5.2.3 how the power loss problem leads to a *decorrelation of nonlinear modes* and it is clear that the proposed rescaling will never resolve this issue. We refrain of imposing any artificial corrections on our results at this point

Let us close this section by mentioning that [32] achieves a power loss of only 10% in a one dimensional domain of $L = 1$ Gpc/h with only $N = 2^{17}$ spatial points. At first sight, it seems that the integration results presented here are inferior. This is conclusion is premature. [32] considers $(d+1)$-SP in the framework of the *Schrödinger method* (SM), cf. section 2.2, and therefore interprets $\hbar$ as a free model parameter. Converting their employed phase space resolution yields a boson mass of $m \approx 10^{-26}$ eV implying a Heisenberg scale σ_x which is three orders of magnitude larger compared to the boson mass used in this work. Consequently there is more freedom in tweaking L and N until the resolution constraint is violated.

Furthermore, the authors of [32] do not follow the same procedure of generating cosmological initial conditions as outlined in section 3.3. In particular, the moduli $|\hat{\delta}_k|$ are not drawn from a Rayleigh distribution but taken as:

$$|\hat{\delta}_k(a_{\text{start}})| = \sqrt{L P^{L,\text{1D}}_{\text{CDM}}(a_{\text{start}}, k)}\ .$$

Only phases are randomly drawn. This reduces the sampling variance significantly but is not strictly correct.

We also emphasize (i) the equivalence of the dimension reduction procedure in eq. (3.61) but (ii) the application of the CDM spectrum when using SM as oppose to the FDM version of eq. (3.62). An interesting consequence of this is the missing small scale power suppression in the initial conditions which nevertheless will arise during the time integration as the governing equation is still $(d+1)$-SP. In that sense, power suppression below σ_x is not an intriguing physical effect in the context of SM but must be interpreted as a systematic error.

At last, it should be noted that integration scheme of [32] is essentially equivalent to $\mathcal{SM}^{[2]}$ with the additional property of being time adaptive. In practice, the time step Δt is adapted by demanding a constant phase change θ_{max} in each unitary evolution operator,

$$\Delta t = \min\left(\frac{4\Delta x^2}{\pi^2}, \frac{1}{a \max_x |V|}\right) \times \theta_{\text{max}}\ ,$$

an approach which proves to be quite popular in the FDM literature, e.g. [71, 60] and many others. Usually the quadratic nature of the kinetic condition makes it more stringent than the potential phase limiter. Inserting our parameters for $\theta_{\text{max}} = 0.1$ yields a miniscule step size of $\Delta t = 10^{-7}$, implying single realization run times of 500 days!

5.2.3 Nonlinear Mode Coupling

Another intriguing property of the nonlinear growth regime is mode coupling. Recall from section 3.2.2 that both CDM and FDM perturbation modes evolve independently as long as $\delta \ll 1$. The difference between both dark matter models then lies in how these independent modes evolve. For CDM *all* modes behave indentically and obey eq. (3.40) whereas FDM modes evolve differently depending on the wave number k. Once we leave the linear regime, structures form by gravitational collapse on large scales resulting transferring matter power to smaller scales. Here we expect to find strong correlation between these small scale modes.

To investigate how these correlations emerge, we compute the unbiased estimator $C(k_i, k_j)$ of the *matter power covariance matrix* over $\mathcal{N}$ realizations,

$$C(k_l, k_m) = \frac{1}{\mathcal{N}-1} \sum_{i=1}^{\mathcal{N}} \left(\bar{P}_i(k_l) - \bar{P}(k_l)\right) \left(\bar{P}_i(k_m) - \bar{P}(k_m)\right) , \quad \bar{P}(k) = \frac{1}{\mathcal{N}} \sum_{i=1}^{\mathcal{N}} \bar{P}_i(k) \ . \tag{5.6}$$

Importantly, $\bar{P}(k)$ in eq. (5.6) is *not* the same power spectrum illustrated in Figure 5.3 but a re-binned version of it. More precisely, one chooses a new bin size $\Delta k' = K \cdot \Delta k$ with K as even positive integer and then averages over all K modes inside the new bin centered at k_j. Hence, the re-binned spectrum of realization i reads:

$$\bar{P}_i(k_j) = \frac{L}{K} \sum_{l=1}^{K} |\hat{\delta}_{i,j+l-\frac{K}{2}}|^2 \ . \tag{5.7}$$

and is sometimes coined the *band power spectrum*. Purpose of this re-binning is to reduce the scatter of the single realization spectrum. This is especially important in $d = 1$ dimensions where a bin of Δk contains $N(k) = 1$ mode. Compare this with $d = 3$ where one averages over radial shells with $N(k) \propto 4\pi k^2$ modes. Evidently, this leads to a significantly reduced sampling variance compared to $d = 1$ which we could only combat by drastically increasing the number of realizations $\mathcal{N}$.

In the following $K = 4$ was chosen leaving us with $N(k) = 4$ modes per bin. This seems rather small — and it is — but the correlation structure is most interesting at low k where one expects a linear-to-nonlinear transition region. Increasing K to say $K \approx \mathcal{O}(10 - 100)$ would certainly increase the signal-to-noise ratio but also leave us with a very limited number of modes in the large scale regime. The only way to increase the resolution, and therefore allow larger K, is to decrease $k_{\text{min}} \propto L^{-1}$ itself. As outlined in the foregoing discussion, this has implications on the required number of spatial points in order to satisfy the resolution conditions at high-k and quickly becomes unwieldy.

After normalization of eq. (5.6) we arrive at the *correlation matrix*:

$$R(k_l, k_m) = \frac{C(k_l, k_m)}{\sqrt{C(k_l, k_l) C(k_m, k_m)}} \tag{5.8}$$

the elements of which are confined to $-1 \leq R(k_l, k_m) \leq 1$.

Consult Figure 5.7 for the evolution of the correlation matrix in the $N = 2^{20}$-ensemble. The evolution starts from a uncorrelated, diagonal state at $z = 100$ and evolves into a highly correlated configuration most pronounced at $z = 10$. As one expects, small scales are affected first by nonlinear mode coupling, cf. $z = 50$, and the correlated regime than expands to ever smaller, originally linearly evolving k over the course of the integration.

Interestingly, past $z = 10$, the ensemble undergoes a de-correlation phase during which large off diagonal elements reduce in magnitude. Although some nonlinear

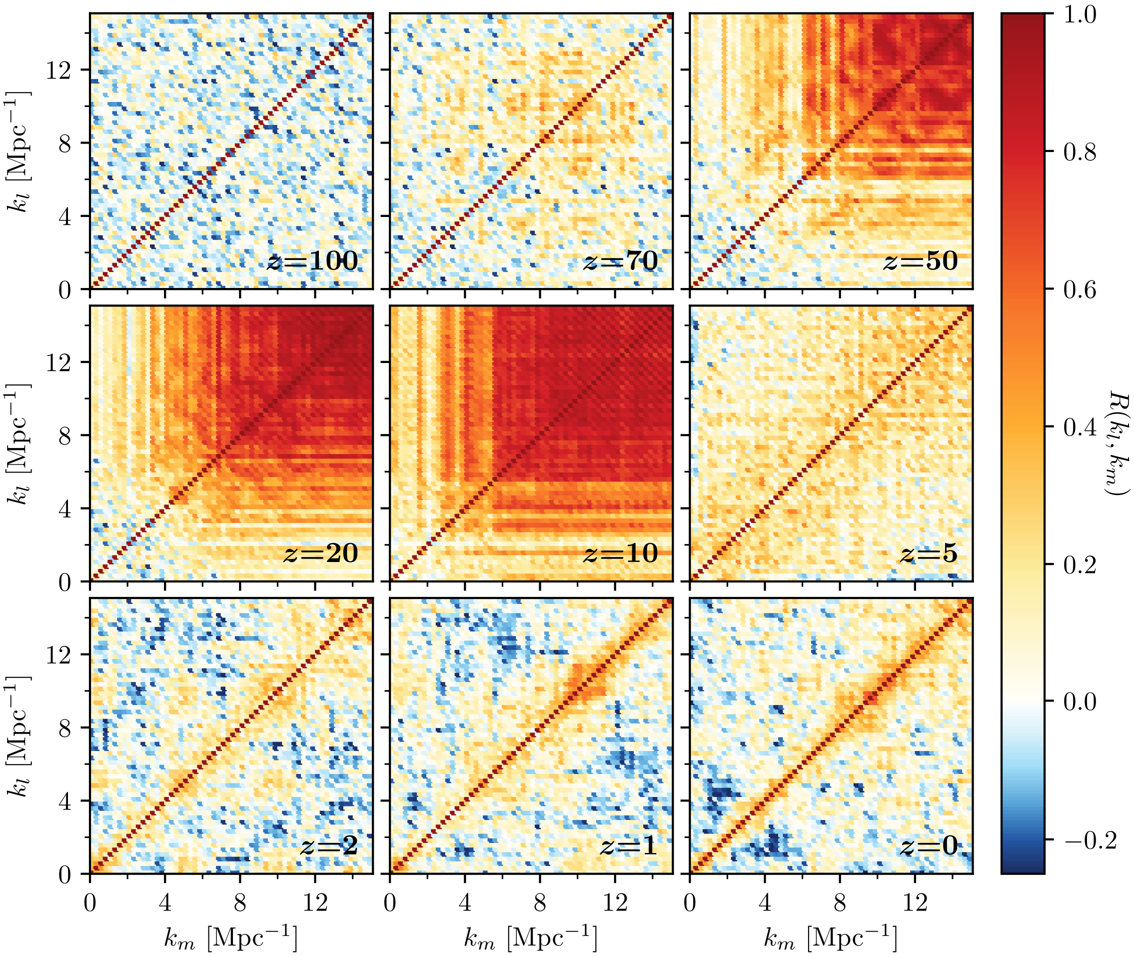

Figure 5.7: Evolution of the matter band power correlation matrix, eq. (5.8) for $N = 2^{20}$ spatial points and $\mathcal{N} = 100$ realizations for large to mid-sized scales. Notice the unphysical de-correlation of modes past $z < 10$

imprints remain close to the diagonal and at large k, the correlation matrix is again close to its initial diagonal form when the integration reaches present time. This second evolution phase is obviously unphysical and with the Heisenberg scale being well resolved we suspect the insufficient temporal resolution already mentioned in section 5.2.2 to be the dominant source of errors.

5.3 Evolution in Real Space

In section 5.2 special attention was put on temporal evolution of ensemble properties in k-space. We now turn the focus to the evolution in real, comoving space. This entails an investigation of conjugate observable of the matter power spectrum — the two-point correlation function $\xi(r)$ — and the spatial structure of the dark matter clusters present at $z = 0$.

5.3.1 Correlation Function

The real space correlation function $\xi(r)$ and the matter power spectrum $P(k)$ form a Fourier transformation pair, cf. eq. (3.58). Thus, no new physics is encapsulated in $\xi(r)$ and we are therefore somewhat brief in its analysis. Nevertheless, it is interesting to see how (i) presumably large correlations at small distances and late times change as one moves to larger scales as well as (ii) how the uncertainty principle presents itself on cosmic scales.

For this, we turn the attention to Figure 5.8 depicting $\xi(r)$ alongside its 1σ-confidence interval at different stages in the integration. Here, spatial correlations show a logarithmic decay of increasing slope as the integration approaches $z = 0$. Additionally, the uncertainty principle induces an upper bound on the correlation function which is quickly reached by $\xi(r)$ once we pass the comoving Heisenberg/de-Broglie scale σ_x depicted as dashed lines in Figure 5.8.

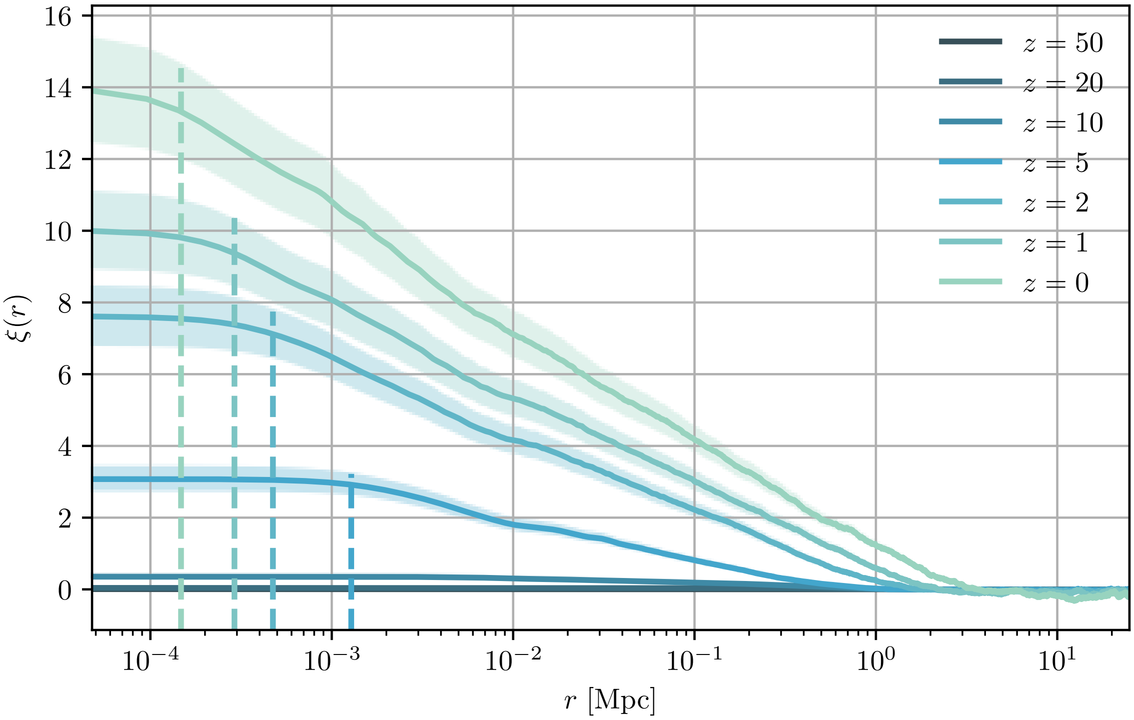

Figure 5.8: One dimensional correlation function $\xi(r)$ as a function of redshift. Dashed, vertical lines show the Heisenberg/de-Broglie scale σ_x below which spatial correlations are damped.

An intriguing regime for studying $\xi(r)$ in $d = 3$ dimensional CDM studies is the baryonic acoustic oscillation (BAO) scale at roughly $r = 100$ Mpc/h. Since the dimension reduction of the initial conditions used in this work is found by a local rescaling of $P^{3\mathrm{D}}(k)$ and the FDM transfer function leaves modes below $k < 1\ \mathrm{Mpc}^{-1}$ unaltered, BAOs are still present in the $d = 1$ FDM power spectrum. Unfortunately, the employed box size too small to probe this regime. One would have to quadruple L, and most likely N, in order to increase the domain of $\xi(r)$ sufficiently. Once next generation numerics, i.e. B-spline discretization plus $\mathcal{BM}^{[4]}$ integration, see Appendix B.1, are implemented and tested this should be one of the first physical studies carried out in the future as one expects FDM to approach CDM on such large scales. We note in passing that the authors of [32] conducted a numerical study designed to probe the BAO regime in the context of Schrödinger's method and found good correspondence for $(2+1)$- and $(3+1)$-SP with the three dimensional CDM correlation function.

5.3.2 Failure of $(1+1)$-SP in Reaching the Soliton State

We close this chapter by investigating the spatial structure of the gravitationally bound objects present at $z = 0$. To give the reader a sense of how these structures emerge from the fluctuation field consider Figure 5.9, depicting the spatio-temporal evolution of $|\psi|^2$ and departing from the initial conditions of Figure 5.2. Also illustrated are fixed time snapshots of $|\psi|^2 = \delta + 1$ and the gravitational potential Φ. Realize the latter is *not* the interaction potential V present in the NLSE. Their relation is given in eq. (2.55) and includes, apart from a dimensional constant, an additional factor of $a(t)^{-1}$.

Now, from the spatio-temporal evolution of $|\psi|^2$ it is evident that overdense regions grow independently from each other until late in the evolution. Past $z = 10$ this changes when the most massive matter clusters attract their smaller satellites and merge into a single gravitationally bound matter clump, which we identify as dark matter halo in the following discussion. The late time evolution is depicted in the zoom inset of Figure 5.9.

Comparing the potentials Φ at $z = 70$ and $z = 10$ shows only marginal differences. This is the result of the long interaction range inherent to the convolution kernel $G^{\pi}_{\triangle_1}$ making V and consequently Φ somewhat insensitive to the exact matter distribution. Only later on, when $\delta \sim 100$, do we observe noteworthy changes in the shape of the gravitational potential.

An interesting consequence of this observation is that evolution under $(1+1)$-SP is essentially a linear problem for most of the integration time, i.e. it would be enough to relax the recomputation of V from every integration step to every n^{th}-step early on. One then gradually decreases n back to $n = 1$ once the density contrast becomes large and the computation of a self consistent potential regains its importance, especially at late times when the scale factor magnifies any inconsistencies in V.

Arguably, the most compelling property of FDM in $d = 3$ dimensions, i.e. evolution of the scalar field under $(3+1)$-SP, is the existence of flat density cores at the center of the emerging dark matter halos. These so called *solitons* provide a natural solution to a number of problems associated with the small scale crises of CDM like the "cusp-core-problem", see chapter 1. In fact, curious physical properties, such as invariance under mutual, *nonlinear* interaction, can be associated with this stable matter configuration. We postpone an in depth discussion until section 6.2 and only mention here that a FDM soliton exist for $(1+1)$-SP as well.

Numerical considerations of $(3+1)$-SP, e.g. [38, 37, 67, 71, 60], identify the soliton state as a dynamical attractor in the evolution of FDM. More precisely, overdense regions collapse under their self-gravity and in the process radiate away excess matter. The result of this process, sometimes dubbed *gravitational cooling*, is a relaxed matter distribution in which a solitonic core is immersed in a "sea of fluctuations".

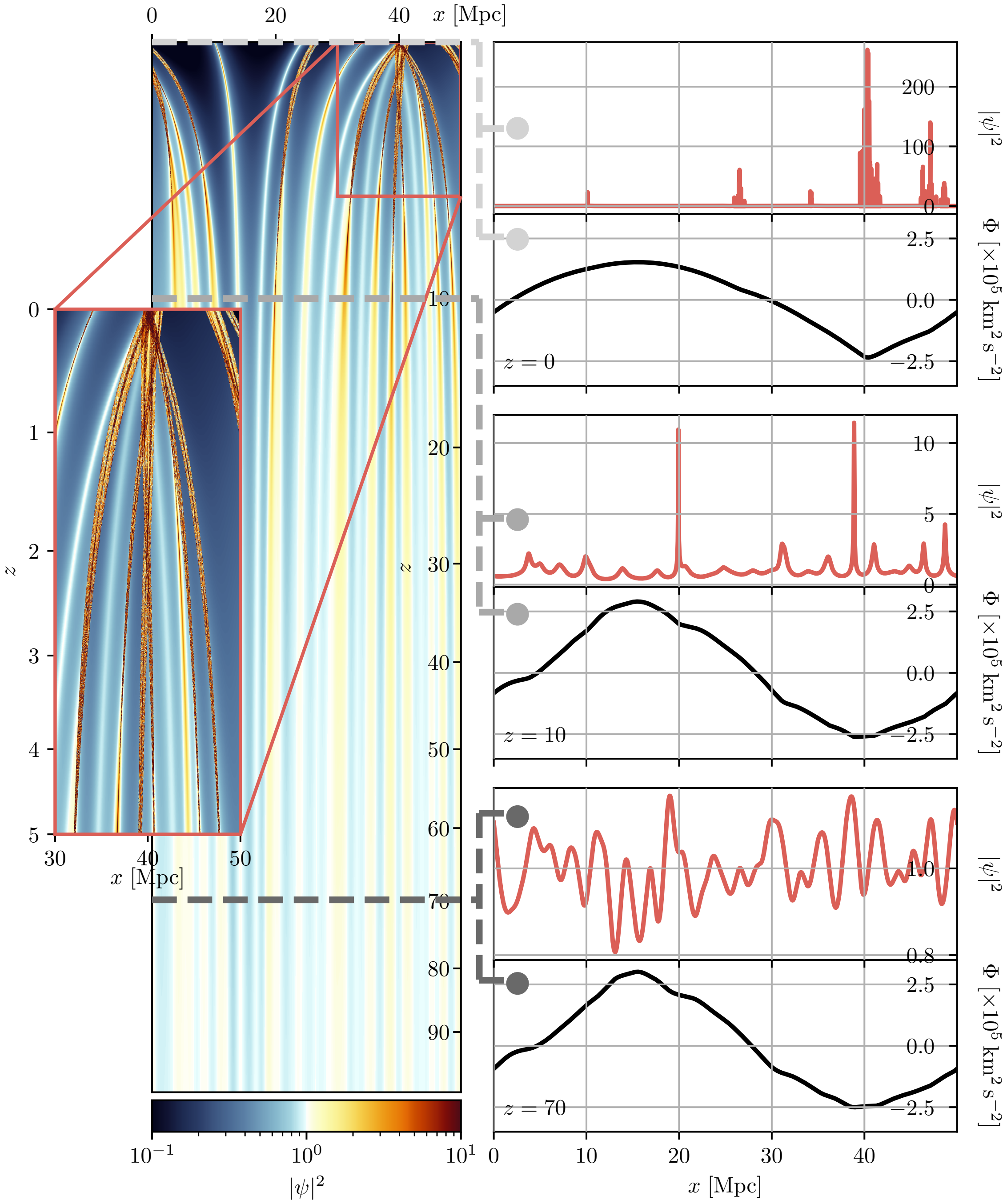

Figure 5.9: Exemplary spatio-temporal evolution of the realization with initial conditions depicted in Figure 5.2. **Left, Inset**: Temporal evolution of $|\psi|^2$. The density was clipped to $0.1 \leq |\psi|^2 \leq 10$. **Right**: Three snapshots of the matter density (**red**) and gravitational potential Φ (**black**). Notice (i) the smoothness and (ii) similarity of Φ at $z = 70$ and $z = 10$. (i) is a consequence of the large interaction range of $U^{\pi}_{\triangle_1}$ so that only the averaged behavior of $|\psi|^2$ on the scale of the box matters for Φ. (ii) is and indicator for the quasi-linearity of the evolution until $z \approx 10$.

Naturally, one wants to know if solitons are also realized in only one spatial dimension assuming the simple dimension reduction procedure of section 2.3.1 leading up to $(1+1)$-SP.

Since $(3+1)$-SP forms a soliton in *every* halo, we start our search with the realization shown in Figure 5.9 and extract from it the medium-sized halo around the mass peak at $x = 26$ Mpc. Let us denote this cluster as $\mathcal{C}$. Note we do not choose the highest-mass structure at $x = 40$ Mpc since the spatio-temporal evolution in Figure 5.9 indicates it to be in the midst of a merger with its satellites. One should therefore expect disturbances of the equilibrium mass distribution anyways. The $\mathcal{C}$-cluster, on the other hand, evolved comparatively isolated and should consequently be closer to the sought after asymptotic state at $z = 0$.

To check this hypothesis, we compare the soliton density $|\varphi_{\mathrm{GS}}|^2$ of mass M_{GS}, cf. section 6.2.1, with $|\psi|^2$ in the halo core region. This is achieved by exploiting the scaling symmetry of $(1+1)$-SP, eq. (2.114), according to which knowledge of φ_{GS} grants access to an entire family of solitons $\varphi_{\mathrm{GS}}(x;\lambda)$ differing in their mass $M_{\mathrm{GS}}(\lambda)$:

$$\begin{aligned} \rho_{\mathrm{GS}}(\lambda) &= |\varphi_{\mathrm{GS}}(x;\lambda)|^2 = \lambda^4 |\varphi_{\mathrm{GS}}(\lambda x)|^2 \ , \quad \lambda \in \mathbb{R}^+ \ , \\ M_{\mathrm{GS}}(\lambda) &= \int_\Omega \mathrm{d}x |\varphi_{\mathrm{GS}}(x,\lambda)|^2 \ . \end{aligned} \tag{5.9}$$

We get back to this in section 6.2.2.

However, as the spatial distribution of $\mathcal{C}$ indicates, Figure 5.10A, a real space fit is essentially impossible given the highly oscillating nature of $|\psi|^2$. Thus we transform the density to k-space in the hope to achieve at least a partial spectral separation of fluctuations and potential soliton, a strategy also employed in chapter 6. The k-space analogue of the one parameter family (5.9) reads:

$$|\hat{\rho}_{\mathrm{GS}}(k;\lambda)| = \lambda^3 |\hat{\rho}_{\mathrm{GS}}(\lambda^{-1}k)| \tag{5.10}$$

where intermediate values of k not part of the uniform k-grid follow from linear interpolation.

Consider Figure 5.10B, depicting the spectral distribution of cluster $\mathcal{C}$, i.e. $\rho_{\mathcal{C}}(x)$, alongside a selection of spectral soliton profiles. Even without a proper fit the failure of $(1+1)$-SP to produce two well separated components, namely soliton and random fluctuations, is evident. More precisely, the distribution of $\mathcal{C}$ is to wide and fluctuates too strongly on all scales. Above $k > 3 \cdot 10^3$ Mpc^{-1} a k^{-1}-decay is found — an numerical artefact of the rather crude cluster extraction. Closer inspection of $|\psi|^2$ reveals a jump discontinuity across the truncated box of Figure 5.10. Hence $\rho_{\mathcal{C}}(x) \in C^1_\pi$ only and according to the discussion of section 4.2 this directly implies $|\widehat{(\rho_{\mathcal{C}})}_k| \sim k^{-1}$ as $k \to \infty$. We reiterate this deficiency is only present in $\rho_{\mathcal{C}}$ and *not* in ρ.

The exemplary analysis of Figure 5.10 was repeated for a number of realizations all of which with identical result: *Solitons, if present under* $(1+1)$*-SP, are far less pronounced and, at best, compete in magnitude with the fluctuation component the in the late time matter configuration.* This is qualitatively different to $(3+1)$-SP where the solitonic core is a distinctive feature in every dark matter halo.

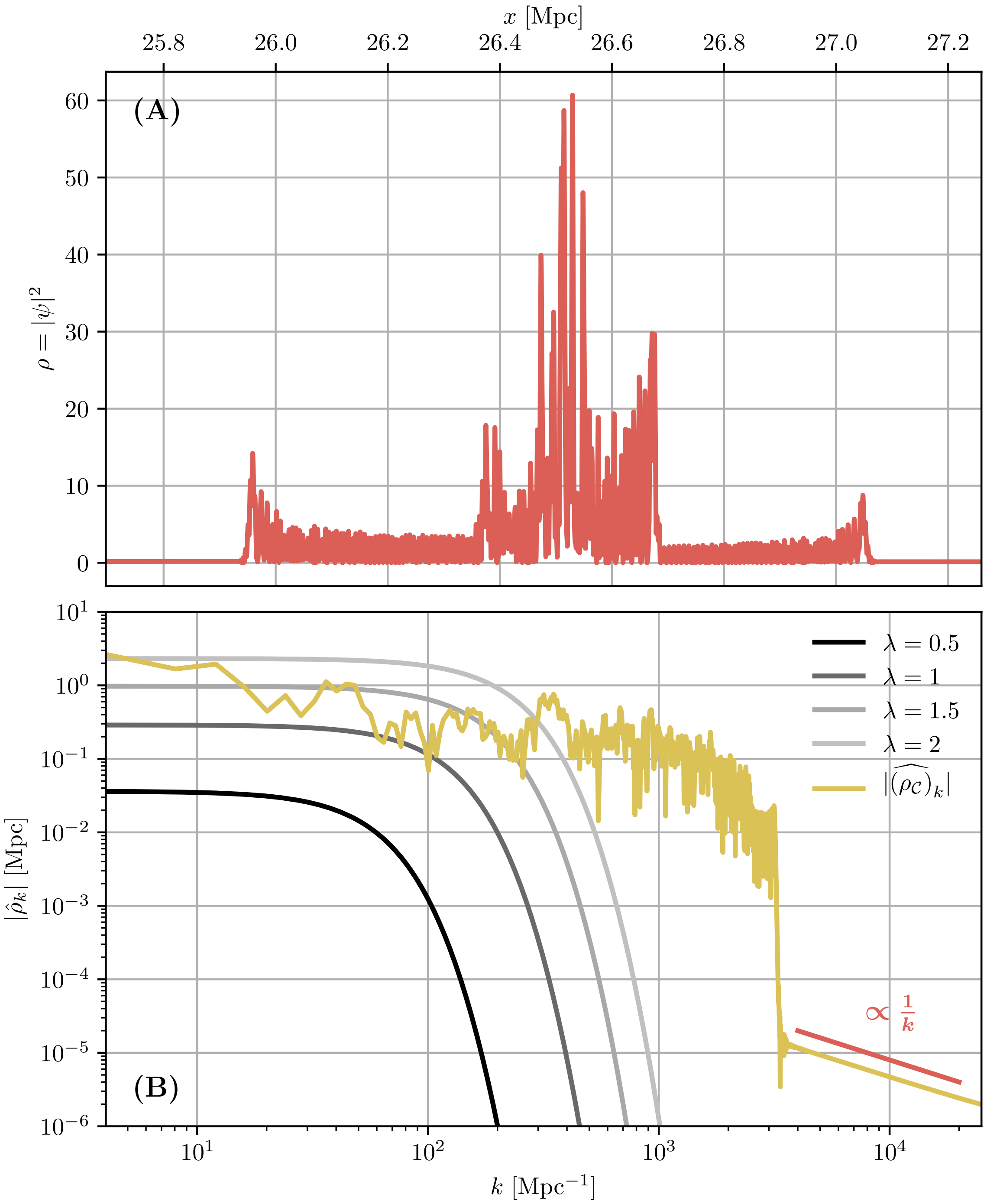

Figure 5.10: Spatial and spectral structure of the matter cluster $\mathcal{C}$ at $x = 26.5$ Mpc also illustrated in Figure 5.9. **(A)**: Spatial distribution of $\rho = |\psi|^2$. The highly fluctuating nature makes a sensible fit in x-space impossible. **(B)**: Spectral composition $|\hat{\rho}_k|$ of cluster $\mathcal{C}$ (yellow) and different mass solitons (black-gray) given by eq. (5.9). The reference soliton, $\varphi_{\text{GS}}(x; 1)$ has *adimensional* mass of $M = L = 10$. For conversion see Figure 2.1.

Note we do not exclude the possibility of a naturally emerging $(1+1)$-SP soliton at this stage. It's spectral structure might still become visible in the distribution of $|\hat{\rho}_k|$ once the fluctuations are suppressed. To this end, consider now the entire ensemble, extract from each realization i a cluster $\mathcal{C}_i$, treat $\mathcal{C}_i$ as separate solution to $(1+1)$-SP and thus use the scaling symmetry to homogenize the individual bounding boxes of size L_i, see eq. (6.35). In practice, we choose the arithmetic mean of all L_i as common domain. At last, take the average of all rescaled clusters.

This procedure is based on the assumption that fluctuations inside each cluster are random, i.e. have no special structure and no spatial correlation which is preserved across realizations. Note a naive time averaging of a single realization would be conceptionally wrong since the ergodic hypothesis is not applicable in the nonlinear regime. Moreover, the scale factor changes rapidly close to $z = 0$ implying one would average over physically quite different situations.

Although simple in theory, the practical execution is cumbersome as we want to exclude clusters akin to the massive structure in the inset of Figure 5.9 undergoing a not yet completed merger at $z = 0$. These clusters are most likely out of equilibrium and would induce systematic effects in the spectral composition of $|\hat{\rho}_k|$. Therefore only clusters with approximate spatial symmetry, as in Figure 5.9A are included in the analysis. Unfortunately, these need to be identified by hand which is why we limit ourselves to only $\mathcal{N} = 25$ individual clusters.

Figure 5.11 illustrates the obtained mean spectrum $|\hat{\rho}_k|$ and multiple $(1+1)$-SP solitons. Although, fluctuation are now significantly reduced compared to the single realization of Figure 5.10, there is still no reasonable correspondence between experimental data and any soliton profile. *We conclude a direct analogue to the asymptotic state of $(3+1)$-SP is not realized by $(1+1)$-SP under sound cosmological conditions, neither in a single realization nor in the ensemble sense.*

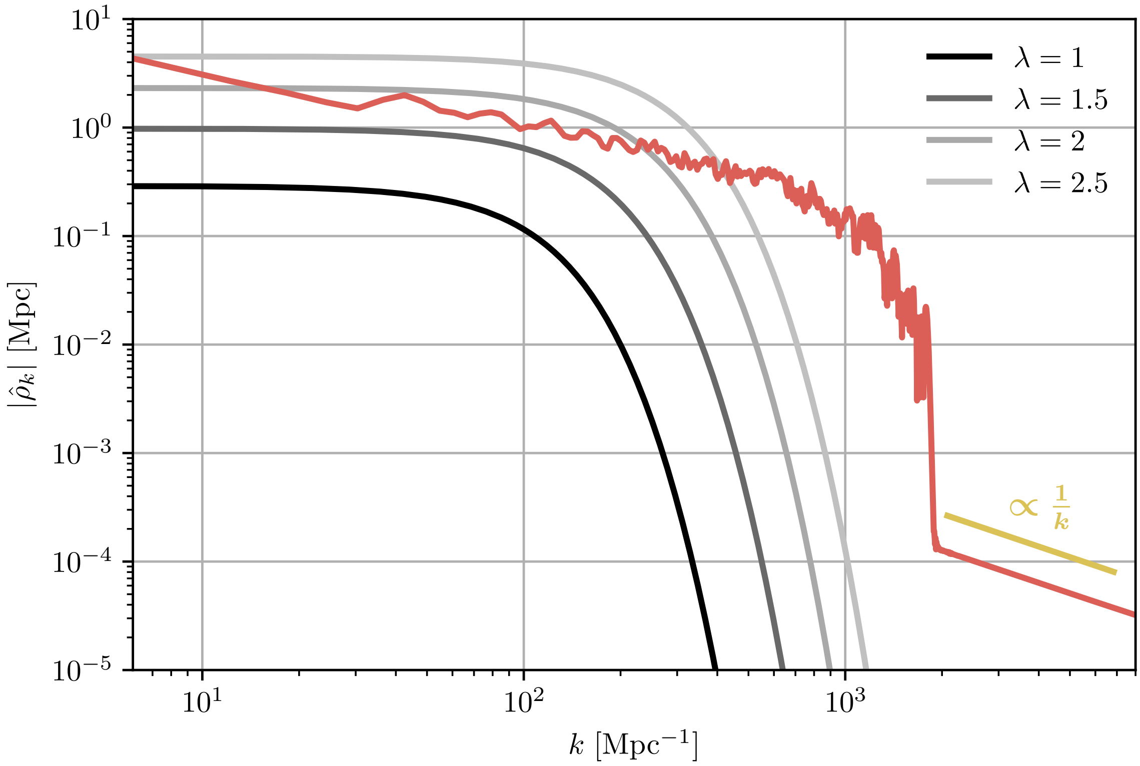

Figure 5.11: Spatial and spectral structure of the *mean* matter cluster and its 1σ-confidence interval obtained from averaging over $\mathcal{N} = 25$ individual clusters each of which was taken from a different realization of the $N = 2^{20}$, $\mathcal{N} = 100$ ensemble. Again, very poor correspondence with the $(1+1)$-SP soliton is found (gray lines).

Clearly, the presented analysis is by no means exhaustive. For instance, the reported failure of $(1+1)$-SP to form a soliton might very well be a problem of the length of integration time. In fact, we already saw in Figure 5.9 how long it took the system to form nonlinear structures in the first place. A working hypothesis is therefore that the relaxation time-scale for $(1+1)$-SP is simply larger than the expansion time from $z = 100$ to $z = 0$. These and more aspects will be thoroughly explored in chapter 6.

Chapter 6

Asymptotic Dynamics

Chapter 5 revealed that, contrary to $(3+1)$-dimensional SP equation, the naively reduced $(1+1)$-SP system is not capable of relaxing into a asymptotic equilibrium configuration characterized by collapsed density structures in which a solitonic core is embedded in a "sea of fluctuations".

Purpose of this chapter is to investigate why $(1+1)$-SP fails to do so and if the asymptotic dynamics is altered once we perform the dimension reduction by strongly confining matter in the orthogonal plane. The problem is approached as follows:

We first attempt to characterize the asymptotic state more precisely. This includes an in-depth discussion on potential types of equilibria FDM relaxes into. In this context, a dynamical equilibrium, in the sense of the *quantum virial theorem*, and a *thermal equilibirium*, in the sense of maximal entropy are introduced alongside observables which measure if the system has virialized or thermalized. Special attention will be drawn to the role of periodic boundary conditions.

Next, the nature of the solitonic ground state for (1+1)-FDM with and without confinement is explored in detail. This includes a rephrasing of the stationary version of eq. (4.1) as nonlinear optimization problem and the exposition of a physically motivated numerical procedure, Appendix C.2, capable of generating these ground states. Analytical arguments based on the *hydrostatic equilibrium* and numerical studies are used to identify the *mass-size-relation* and the *solitonic* nature of the FDM ground state for $(1+1)$-SP and PLAM.

We then return to numerical collapse studies, this time however, in a more controlled setting compared to chapter 5. In the spirit of [71, 60], artificial initial conditions without space-time expansion are investigated first. Under these conditions the confinement approach turns out to be capable in generating a single solitonic core after sufficiently long integration time, whereas $(1+1)$-SP still fails to attain the expected asymptotic state. We attempt to explain this disparity by comparing the interaction range with the ground state size of both reduction models. Moreover, our results indicate that irrespective of the dimension reduction approach the long term dynamics is best understood as a thermalization process maximizing the entropy of the system.

By reintroducing space-time expansion, we neither find $(1+1)$-SP nor PLAM to be fully thermalized at present time $z = 0$. Nevertheless, the spectrum of ψ under strong confinement is still close to its ground state for $a = 1$.

6.1 Relaxation Processes and Equilibrium States

It is a priori not clear what mechanism drives FDM into its asymptotic equilibrium state let alone what type of equilibrium is attained. Moreover, it may be just the emerging density core, or even the total density field including its fluctuations, reaching this ominous equilibrium. At this stage, without further theoretical insight, only data can give us a hint. We therefore broaden the discussion and consider two types of equilibria.

6.1.1 Quantum Virial Equilibrium

It is a well known fact from classical physics that any *bounded* dynamics obeys the classical virial theorem, [34]. It is derived by taking the time derivative of $G = px$, using Newton's axioms and performing a time-averaging,

$$2(T)_\infty - (x\partial_x V)_\infty = 0, \tag{6.1}$$

with T as total kinetic energy of a system of N particles and

$$(A)_t = \frac{1}{t}\int_0^t \mathrm{d}t' A(t), \quad (A)_\infty = \lim_{t\to\infty}\left(\frac{1}{t}\int_0^t \mathrm{d}t' A(t')\right) . \tag{6.2}$$

Realize eq. (6.1) only holds in the limit $t \to \infty$. Notable exceptions from this are *stationary* or *T-periodic* particle configuration which obey eq. (6.1) already for arbitrary finite $t > T$.

Eq. (6.1) proves to be an extremely handy tool in astrophysics and it is reasonable to seek for a corresponding result in quantum mechanics. Relaxation into *virial equilibirum*, i.e. the regime where the quantum analogue of eq. (6.1) is (approximately) satisfied, is then to be understood as a consequence of the evolution under Schrödinger's equation. That said, any finite quantum system would virialize in the limit $t \to \infty$.

Interestingly, a quantum virial theorem exists and was first derived for *stationary states* by Fock, [29]. The most general form akin to eq. (6.1) and also applicable for non-stationary problems is based on *Ehrenfest's theorem* for which the textbook version reads:

Theorem (Ehrenfest's Theorem, [25])**.** *Let $\mathcal{H} = L_2(\mathbb{R})$ be the Hilbert space of interest, $\hat{G}(t)$ an hermitian operator and $\hat{H}$ the Hamiltonian. Then the evolution of its expectation value is:*

$$\frac{\mathrm{d}}{\mathrm{d}t}\left\langle \hat{G}(t)\right\rangle = -i\left\langle\psi\right|\left[\hat{G},\hat{H}\right]\left|\psi\right\rangle + \langle\psi|\partial_t\hat{G}|\psi\rangle \ . \tag{6.3}$$

Unfortunately, eq. (6.3) is incomplete for operators $\hat{G}$ for which $\hat{G}\psi \notin \mathrm{Dom}(\hat{H})$, rendering the commutator in eq. (6.3) meaningless. It is easily seen that this situation occurs in the present context for $\hat{G} = \hat{x}$ and periodic domains, i.e. when:

$$\mathcal{H} = \{\psi \in L_2(\Omega) \mid \psi(0) = \psi(L), \partial_x\psi(0) = \partial_x\psi(L)\} \tag{6.4}$$

since $\hat{x}\psi = x\psi$ is not periodic anymore, [3].

To see how Ehrenfest's theorem needs to be extended, e.g. [28, 50], we take the total time derivative of $\langle \hat{G} \rangle$ and use Schrödingers equation to find:

$$\frac{\mathrm{d}}{\mathrm{d}t} \left\langle \hat{G}(t) \right\rangle = \langle \psi | \partial_t \hat{G} | \psi \rangle + i \left\langle \hat{H}\psi \middle| \hat{G} \left| \psi \right\rangle - i \left\langle \psi \right| \hat{G}\hat{H} \left| \psi \right\rangle \right. . \tag{6.5}$$

Notice how we *do not* use the familiar self-adjointness of $\hat{H}$ in the second term to form a commutator with the third term — self-adjointness only holds on the domain of $\hat{H}$ but here we allow $\hat{G}\psi \notin \mathrm{Dom}(\hat{H})$. However, we can always take the adjoint of $\hat{H}$ and insert a zero to write:

$$\frac{\mathrm{d}}{\mathrm{d}t} \left\langle \hat{G}(t) \right\rangle = \langle \psi | \partial_t \hat{G} | \psi \rangle - i \langle \psi | \left[\hat{G}, \hat{H} \right] | \psi \rangle + i \langle \psi | \hat{H}^\dagger \hat{G} - \hat{H}\hat{G} | \psi \rangle \ . \tag{6.6}$$

The last term constitutes a correction term to the standard Ehrenfest theorem and measures the degree to which $\hat{H}$ is not self-adjoint anymore once we allow it to act on $\hat{G} |\psi\rangle \equiv |\varphi\rangle$.

Computing the correction term with the Hamiltonian of eq. (4.1) under periodic boundary conditions is straight forward. One finds:

$$B \equiv i \langle \psi | \hat{H}^\dagger \hat{G} - \hat{H}\hat{G} | \psi \rangle = -\frac{i}{2} \left(\partial_x \psi^* \varphi - \psi^* \partial_x \varphi \right) \Big|_0^L \ . \tag{6.7}$$

The quantum virial theorem then follows by considering a quantized version of $G = px$ in the extended formulation of the Ehrenfest theorem. Since $\hat{x}$ and $\hat{p}$ are non-commutative, one typically takes the symmetric version $\hat{G} = \frac{1}{2}(\hat{p}\hat{x} + \hat{x}\hat{p})$ as starting point. However, it holds:

$$\frac{\mathrm{d}}{\mathrm{d}t} \langle \hat{x}\hat{p} \rangle = \frac{\mathrm{d}}{\mathrm{d}t} \left(\langle \hat{p}\hat{x} \rangle + i \right) = \frac{\mathrm{d}}{\mathrm{d}t} \langle \hat{p}\hat{x} \rangle \tag{6.8}$$

which is why we set $\hat{G} = \hat{p}\hat{x}$ to arrive at:

$$\begin{aligned} \frac{\mathrm{d}}{\mathrm{d}t} \left\langle \hat{G} \right\rangle &= -i \langle \psi | \left[\hat{G}, \hat{H} \right] | \psi \rangle + B \\ &= 2 \langle T \rangle - a(t) \langle x \partial_x V \rangle + \frac{L}{2} \left(\psi^*(0,t) \partial_x^2 \psi(0,t) - |\partial_x \psi(0,t)|^2 \right) \ , \end{aligned} \tag{6.9}$$

where the boundary term B follows trivially from eq. (6.7). For the evaluation of the commutator expectation value we refer to Appendix C.1.

Now, if ψ is a *stationary* state then $\left\langle \hat{G} \right\rangle$ is constant in time. This directly yields the stationary quantum virial theorem under periodic boundary conditions:

$$0 = 2 \langle T \rangle - a \langle x \partial_x V \rangle + \frac{L}{2} \left(\psi^*(0,t) \partial_x^2 \psi(0,t) - |\partial_x \psi(0,t)|^2 \right) \ . \tag{6.10}$$

A particularly import stationary state that satisfies eq. (6.10) is the ground state. Eq. (6.10) was also found in [80] by integrating the stationary Schrödinger equation directly.

On the other hand, if ψ has a non-trivial time dependence, we time-average according to eq. (6.2) and take $t \to \infty$:

$$\begin{aligned}\lim_{t\to\infty}\frac{1}{t}\left[\left\langle\hat{G}\right\rangle(t)-\left\langle\hat{G}\right\rangle(0)\right] &= 2\left(\langle T\rangle\right)_\infty-\left(a(t)\left\langle x\partial_x V\right\rangle\right)_\infty \\ &+\left(\frac{L}{2}\left(\psi^*(0,t)\partial_x^2\psi(0,t)-\left|\partial_x\psi(0,t)\right|^2\right)\right)_\infty .\end{aligned} \tag{6.11}$$

Assuming $\left\langle\hat{G}\right\rangle$ is bounded, one arrives at the *time-dependent* quantum virial theorem under periodic boundary conditions:

$$0=2\left(\langle T\rangle\right)_\infty-\left(a(t)\left\langle x\partial_x V\right\rangle\right)_\infty+\left(\frac{L}{2}\left(\psi^*(0,t)\partial_x^2\psi(0,t)-\left|\partial_x\psi(0,t)\right|^2\right)\right)_\infty . \tag{6.12}$$

Strictly speaking, eq. (6.12) only holds for $t \to \infty$. However, for practical purposes we may consider the finite time average and interpret the system to be virialized once eq. (6.12) is approximately satisfied.

6.1.2 Thermal Equilibirum

Following section 6.1.1 we take our motivation from classical N-Body physics. In the classical CDM paradigm, dark matter is assumed to be collionless due to the humongous number of particles involved, thereby rendering a dynamical relaxation based on two-body interactions ineffective — at least on time-scales comparable to the age of the universe, [45]. On the other hand, dark matter halos turn out to be of relative universal shape, [61], suggesting their evolution ends in some sort of asymptotic equilibrium configuration. Naturally, if two-body interaction cannot explain this relaxation process one must ask what mechanism replaces it. The very same problem is known from stellar systems such as elliptical galaxies.

In the seminal work [57], it was shown while a fan-out of particle trajectories in phase space leads to an entropy preserving filamentation of the *fine-grained* Vlasov phase space distribution, a *coarse-grained* version of the latter does in fact attain a quasi-stationary state. This process is called *violent relaxation* and it is expected that the final, coarse-grained phase space distribution maximizes entropy and the relaxation process should then be understood as a consequence of thermodynamics.

To adopt this idea for FDM a phase space description is required. Luckily, this is the central task of *Schrödinger's Method*, [81, 76, 51], mentioned in section 2.2.1. One first associates the wave function ψ with a fine-grained phase space distribution $f_W(x,k)$ known as *Wigner distribution*,

$$f_W(x,k)=\frac{1}{2\pi}\int_\Omega \mathrm{d}x'\psi\left(x-\frac{x'}{2}\right)\psi^*\left(x+\frac{x'}{2}\right)e^{ikx'}, \tag{6.13}$$

and subsequently performs a coarse graining of $f_W(x,k)$ by smoothing it with a bivariate gaussian. This yields *Husimi's distribution*:

$$f_H(x,k)=\frac{1}{2\pi\sigma_x\sigma_k}\int_\Omega\frac{\mathrm{d}x'\mathrm{d}k'}{2\pi}e^{-\frac{(x-x')^2}{2\sigma_x^2}}e^{-\frac{(k-k')^2}{2\sigma_k^2}}f_W(x',k') . \tag{6.14}$$

The relation between the smoothing scales σ_x and σ_k is set according to Heisenberg's uncertainty principle, $\sigma_x \sigma_k = \frac{1}{2}$, to guarantee positiveness of eq. (6.14), [19]. We then use *Wehrl's entropy*, [78],

$$S_H = S[f_H] = -\frac{1}{2\pi} \int_\Omega \mathrm{d}x\mathrm{d}k f_H(x,k) \log f_H(x,k), \tag{6.15}$$

as our entropy functional. Thermalization is completed once S_H attains its maximum value.

6.2 The FDM Groundstate

We expect the central region of a collapsed density structure to contain a stable core matching the density distribution of the FDM ground state, e.g. [37, 67, 69, 71, 60].

In this section we give details on how the ground states of $(1+1)$-SP and PLAM can be obtained and what properties they satisfy. For instance, we already saw that any stationary state is in virial equilibrium according to eq. (6.10) irrespective of the form of the interaction.

6.2.1 Construction of the $(1+1)$-FDM Ground State

Let us set $a = \text{const}$. Mathematically, the ground state $\varphi(x)$ of eq. (4.1) with mass M is defined as:

$$\begin{aligned}\varphi_{\mathrm{GS}} &= \underset{\varphi \in S}{\operatorname{argmin}}\, E[\varphi] = \underset{\varphi \in S}{\operatorname{argmin}} \{T[\varphi] + V[\varphi]\} \\ &= \underset{\varphi \in S}{\operatorname{argmin}} \left\{ \frac{1}{2} \int_{\Omega_1} \mathrm{d}x |\partial_x \psi|^2 + \frac{a}{2} \int_{\Omega_1} \mathrm{d}x \left(U^\pi * |\psi|^2\right) |\psi(x)|^2 \right\}\end{aligned} \tag{6.16}$$

with the set of admissible functions:

$$S = \left\{ \varphi \mid \int_\Omega \mathrm{d}x |\varphi|^2 = M \right\} . \tag{6.17}$$

Eq. (6.16) constitutes a constrained, nonlinear, non-convex, minimization problem. Under free-space conditions for SP, i.e. when $U = G_{\triangle_1}^{\mathrm{free}}$, [21] proves existence of a unique, real, symmetric and always positive minimizer. We tacitly assume this to be true under periodic conditions for both SP and PLAM as well. The idea is then to find critical points φ_c of eq. (6.16) and check if φ_c has roots in the domain. If not, we set $\varphi_{\mathrm{GS}} = \varphi_c$.

To find critical points of the energy functional we perform a standard gradient descent with time τ as continuous descent parameter. Thus, we account for the normalization constrained by introducing a Lagrange multiplier $\mu(\tau)$ and descent along the "grand canonical energy":

$$\partial_\tau \varphi = -\frac{1}{2} \frac{\delta}{\delta \varphi} E_{\mathrm{GC}}[\varphi] = -\frac{1}{2} \frac{\delta}{\delta \varphi} \left(E[\varphi] + \mu(\tau) N[\varphi]\right), \quad N[\varphi] = \int_\Omega \mathrm{d}x \varphi^2 . \tag{6.18}$$

Note we have infinitely many normalization constraints, one for every τ. Consequently, μ needs to be a function of the descent parameter.

Taking the functional derivative of the kinetic part $T[\varphi]$ and the mass functional $N[\varphi]$ is straight forward. For the potential part, we find:

$$\begin{aligned}\delta V[\varphi,h] &= \left.\frac{\mathrm{d}}{\mathrm{d}\epsilon}\right|_{\epsilon=0} V[\varphi+\epsilon h] \\ &= a\int_\Omega \mathrm{d}x \int_\Omega \mathrm{d}x' h(x)\varphi(x)U^\pi(|x-x'|)\varphi^2(x') \\ &\qquad\qquad + a\int_\Omega \mathrm{d}x \int_\Omega \mathrm{d}x' \varphi^2(x)U^\pi(|x-x'|)h(x')\varphi(x') \ .\end{aligned} \tag{6.19}$$

Upon interchanging $x \leftrightarrow x'$ in the last integral and exploiting the symmetry of the convolution kernel, one finds:

$$\begin{aligned}\delta V[\varphi,h] &= \int_\Omega \mathrm{d}x \int_\Omega \mathrm{d}x' h(x)\cdot 2a\varphi(x)U^\pi(|x-x'|)\varphi^2(x') \\ &= \int_\Omega \mathrm{d}x h(x)\cdot 2a\varphi(x)\left(U^\pi * \varphi^2\right)(x) = \int_\Omega \mathrm{d}x h(x)\frac{\delta V}{\delta\varphi} \ .\end{aligned} \tag{6.20}$$

In total, eq. (6.18) yields the equation of the *continuous normalized gradient flow*:

$$\partial_\tau\varphi = \frac{1}{2}\partial_x^2\varphi - a(U^\pi * \varphi^2)\varphi + \mu(\tau)\varphi \ . \tag{6.21}$$

Eq. (6.21) is norm-preserving, $\frac{\mathrm{d}}{\mathrm{d}\tau}\left(\|\varphi\|_2\right) = 0$, by construction. Thus, by multiplying with φ, integrating over Ω and using Leibniz' integral rule we find:

$$\int_\Omega \varphi\partial_t\varphi = \frac{1}{\|\varphi\|_2}\frac{\mathrm{d}}{\mathrm{d}\tau}\left(\|\varphi\|_2\right) \overset{!}{=} 0 = \int_\Omega \mathrm{d}x\left\{\frac{1}{2}\varphi\partial_x^2\varphi - a(U^\pi * \varphi^2)\varphi^2\right\} + \mu(\tau)\|\varphi\|_2^2 \ . \tag{6.22}$$

Upon partial integration, we obtain the value of the Lagrange multiplier along the descent path:

$$\mu(\tau) = \frac{1}{\|\varphi\|_2^2}\int_\Omega \mathrm{d}x\left\{\frac{1}{2}(\partial_x\varphi)^2 + a(U^\pi * \varphi^2)\varphi^2\right\} \ . \tag{6.23}$$

This closes eq. (6.21). In Appendix C.2, a simple numerical method is devised to solve eq. (6.21) and eq. (6.23), giving us access to the ground state wave function for $(1+1)$-SP and PLAM.

Let us now assume the descent was successful such that at τ^* the descent led us to the global minimum $E_{\mathrm{GS}} = E[\varphi_{\mathrm{GS}}]$ and Lagrange multiplier $\mu_{\mathrm{GS}} \equiv \mu(\tau^*)$. At this point $\left.\partial_\tau\varphi\right|_{\tau=\tau^*} = 0$ and eq. (6.21) therefore reduces to:

$$\mu_{\mathrm{GS}}\varphi_{\mathrm{GS}} = \left[-\frac{1}{2}\partial_x^2 + a(U^\pi * \varphi_{\mathrm{GS}}^2)\right]\varphi_{\mathrm{GS}} \ . \tag{6.24}$$

We recognize this nonlinear eigenvalue problem as the stationary Schrödinger equation. Clearly, one would have arrived at the same result by bringing ψ_{GS} into stationary form, i.e. $\psi_{\mathrm{GS}}(x,t) = \varphi_{\mathrm{GS}}(x)e^{-i\mu_{\mathrm{GS}}t}$ and inserting into the time-dependent problem (4.1). However, the optimization approach gives us additional inside into the physical nature of the eigenvalue. In this formulation the eigenvalue coincides with the Lagrange multiplier which in turn can be interpreted as the change of E_{GS} induced by a change in the total mass. To see this, recall the total Lagrange functional of the constrained optimization problem:

$$L[\varphi, \mu(t)] = E_{\mathrm{GC}}[\varphi] - \mu(t)M = E[\varphi] + \mu(t)(N[\varphi] - M) \tag{6.25}$$

which at the global minimum reduces to:

$$L[\varphi_{\mathrm{GS}}, \mu_{\mathrm{GS}}] = E_{\mathrm{GS}} \tag{6.26}$$

since φ_{GS} satisfies the constraint.

Let us parametrize the global minimum, i.e. have $E_{\mathrm{GS}}(M)$, $\mu_{\mathrm{GS}}(M)$ and $\varphi_{\mathrm{GS}}(M)$. Taking the total derivative of E_{GS} wrt. M then yields:

$$\frac{\mathrm{d}E_{\mathrm{GS}}}{\mathrm{d}M} = \frac{\mathrm{d}L[\varphi_{\mathrm{GS}}; \mu_{\mathrm{GS}}]}{\mathrm{d}M} = \frac{\delta L}{\delta \varphi_{\mathrm{GS}}}\frac{\mathrm{d}\varphi_{\mathrm{GS}}}{\mathrm{d}M} + \frac{\partial L}{\partial \mu_{\mathrm{GS}}}\frac{\mathrm{d}\mu_{\mathrm{GS}}}{\mathrm{d}M} + \frac{\partial L}{\partial M}\ . \tag{6.27}$$

The first two terms vanish because $\mu_{\mathrm{GS}}(M)$ and $E_{\mathrm{GS}}(M)$ represent the global minimum for all M by construction. Hence, we are left with:

$$\frac{\mathrm{d}E_{\mathrm{GS}}}{\mathrm{d}M} = \frac{\partial L}{\partial M} = -\mu_{\mathrm{GS}} \tag{6.28}$$

which is essentially the *chemical potential.*

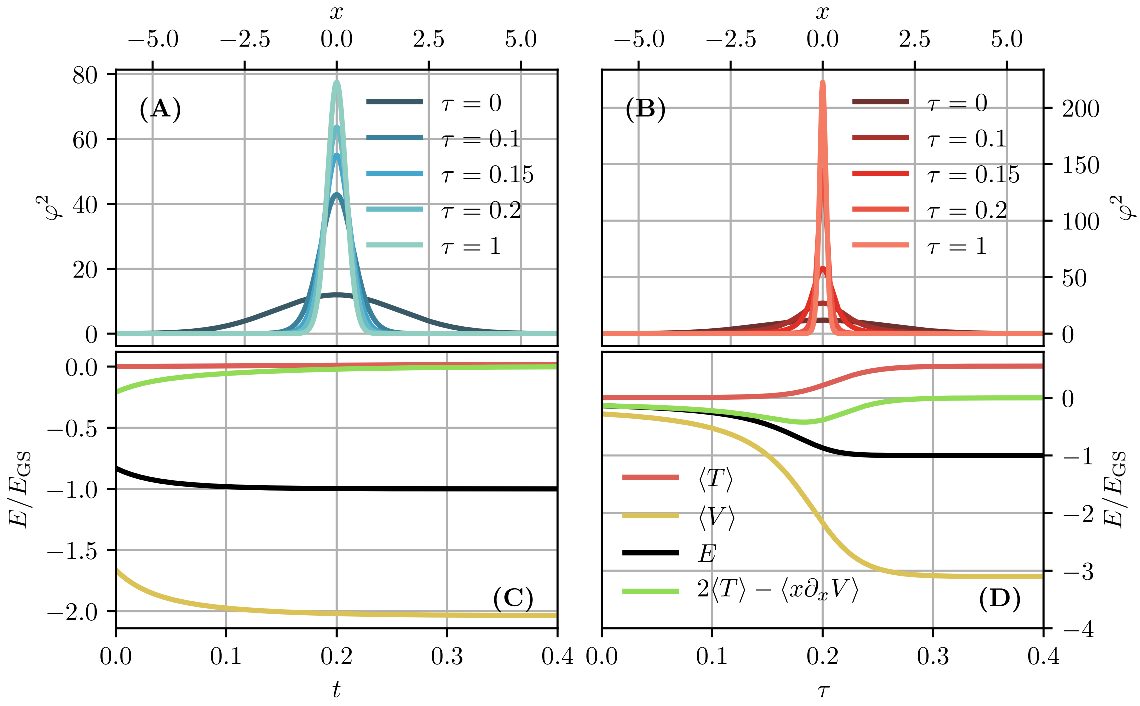

Figure 6.1: Evolution of densities and energies during gradient descent for both reduction models and a ground state mass of $M_{\mathrm{GS}} = 50$ and $a = 1$. **(A)** depicts different densities for $(1+1)$-SP. **(B)** illustrates the same situation under strong confinement (PLAM) with $\epsilon = 10^{-2}$. **(C/D)** show the energy evolution for $(1+1)$-SP, **(C)**, and PLAM, **(D)**, respectively. Both models realize an energy minimum with an all positive density. Moreover the green line in **(C/D)** indicates both reduction models satisfy the stationary virial theorem (6.10) without the boundary term — a consequence of φ_{GS}'s exponential decay.

Figure 6.1 compares the results of an exemplary energy descent for $(1+1)$-SP and PLAM assuming a ground-state mass of $M_{\text{GS}} = 50$ and $a = 1$. Evidently, confining matter in the transversal direction, i.e. PLAM, leads to a narrower ground state compared to the $(1+1)$-SP ground state containing the same total mass. We quantify this import observation in section 6.2.2.

As we mentioned in section 6.1.1 but also saw explicitly in the forgoing discussion on the ground-state, φ_{GS} is, like any critical point of $E[\varphi]$, a stationary state. Therefore, φ_{GS} is in virial equilibrium given by eq. (6.10). As Figure 6.1 illustrates, this is true for both reduction models even without the boundary term B of eq. (6.7). The reason is quite simple: φ_{GS} decays exponentially fast in space implying B to be negligible.

6.2.2 Properties of the $(1+1)$-FDM Ground State

So far we identified the virial equilibrium as a property of the FDM ground state which holds true independent of the exact form of the long-range interaction. Here, we want to draw attention to multiple other important characteristics of φ_{GS}. As before we set $a = \text{const}$.

Hydrostatic Equilibrium Following the hydrodynamic considerations of chapter 3 for $(3+1)$-SP, it is easy to find identical results for one spatial degree of freedom only. On balance, application of Madelung's transformation reveals a one dimensional Euler equation akin to eq. (3.27) and valid for both $(1+1)$-SP and PLAM. However, further progress can be made since φ_{GS} is stationary and therefore has vanishing velocity, $v = 0$. Thence, eq. (3.27) reduces to the equation of *hydrostatic equilibrium* in which the quantum pressure force balances gravity to avoid further collapse. In one spatial dimension this force equilibrium reads:

$$m\partial_x \Phi = \frac{\hbar^2}{2ma^2}\partial_x \left(\frac{\partial_x^2 \sqrt{\rho_{\text{GS}}}}{\sqrt{\rho_{\text{GS}}}} \right) . \tag{6.29}$$

We return to this dimensionfull equation shortly. For now, apply the unit convention (2.52) to find:

$$-F_G \equiv \partial_x V = \frac{1}{2a^2}\partial_x \left(\frac{\partial_x^2 \sqrt{\varphi_{\text{GS}}^2}}{\sqrt{\varphi_{\text{GS}}^2}} \right) \equiv F_Q . \tag{6.30}$$

Figure 6.2 compares the gravitational force F_G and the quantum pressure force F_Q across the density of the ground state generated in Figure 6.1. We find excellent agreement with eq. (6.30).

Mass-Size Relation Another interesting question one can ask is how the spatial extent R_{GS} of the ground state depends on its total mass M_{GS}. For $(1+1)$-SP this can be answered in two different ways, either by application of the scaling symmetry (2.114) or by dimensional arguments. Here only the former is shown but the reader is encouraged to consult Appendix C.3 for the attractive [1] derivation based on a simple dimensional analysis for the hydrostatic equilibrium condition (6.29).

---

[1] at least in the eyes of the author

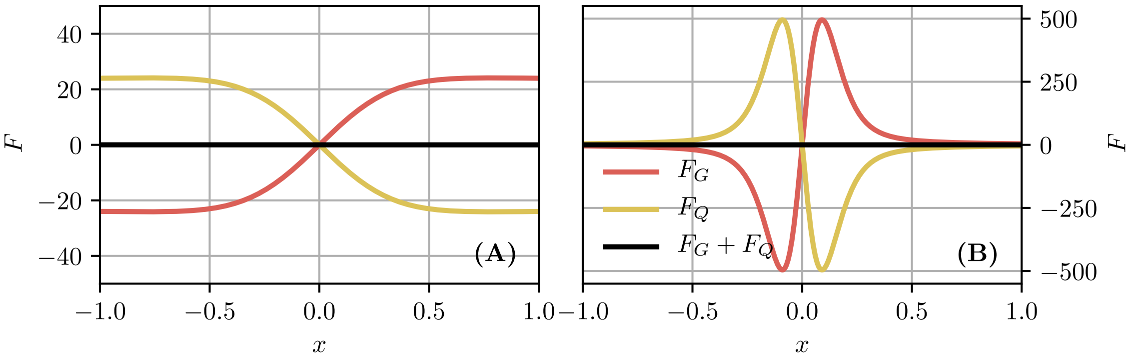

Figure 6.2: Force comparison according to eq. (6.30) across the extent of the ground states generated in Figure 6.1. **(A)** $(1+1)$-SP and **(B)** PLAM.

Back to the objective of deducing the relation $R_{\mathrm{GS}}(M_{\mathrm{GS}})$. We start by defining the ground state's spatial extent R_{GS} by:

$$\Delta \cdot M_{\mathrm{GS}} = \int_{-R_{\mathrm{GS}}}^{R_{\mathrm{GS}}} \mathrm{d}x \varphi_{GS}(x)^2 \tag{6.31}$$

with Δ as numerical constant close to unity, say $\Delta = 0.99$. Consider now two ground states $\varphi^2_{\mathrm{GS}}(x)$ and $\widetilde{\varphi}^2_{\mathrm{GS}}(x;\lambda)$ related by a scale transformation of magnitude λ. Their respective ranges are set by the conditions

$$\Delta \cdot M_{\mathrm{GS}} = \int_{-R_{\mathrm{GS}}}^{R_{\mathrm{GS}}} \mathrm{d}x \varphi^2_{GS}(x) \quad \text{and} \tag{6.32}$$

$$\Delta \cdot \widetilde{M}_{\mathrm{GS}} = \int_{-\tilde{R}_{\mathrm{GS}}}^{\tilde{R}_{\mathrm{GS}}} \mathrm{d}x \widetilde{\varphi}^2_{GS}(x;\lambda) \overset{(2.114)}{=} \lambda^4 \int_{-\tilde{R}_{\mathrm{GS}}}^{\tilde{R}_{\mathrm{GS}}} \mathrm{d}x \varphi^2_{GS}(\lambda x) \,. \tag{6.33}$$

Now perform the transformation $x' = x/\lambda$ in the second condition to find:

$$\Delta \cdot \widetilde{M}_{\mathrm{GS}} = \lambda^3 \int_{-\tilde{R}_{\mathrm{GS}}/\lambda}^{\tilde{R}_{\mathrm{GS}}/\lambda} \mathrm{d}x' \varphi^2_{GS}(x') \,. \tag{6.34}$$

If we identify the integration limits in this expression with the spatial extent of the unscaled state $\varphi_{\mathrm{GS}}(x)$ it follows:

$$\widetilde{R}_{\mathrm{GS}} = \lambda^{-1} R_{\mathrm{GS}}, \quad \widetilde{M}_{\mathrm{GS}} = \lambda^3 M_{\mathrm{GS}} \,. \tag{6.35}$$

and consequently

$$\frac{R'_{\mathrm{GS}}}{R_{\mathrm{GS}}} = \left(\frac{M_{\mathrm{GS}}}{M'_{\mathrm{GS}}}\right)^{\frac{1}{3}} \quad \Rightarrow \quad R_{\mathrm{GS}} \propto M_{\mathrm{GS}}^{-\frac{1}{3}} \tag{6.36}$$

which is the sought after mass-size relation.

Consider Figure 6.3 for the numerical results assessing the validity of eq. (6.36). To arrive at the data shown, we computed the $(1+1)$-SP ground state with total masses ranging from $M_{\mathrm{GS}} = 10 - 1000$. The associated range R_{GS} was found by numerical quadrature of $\varphi^2_{\mathrm{GS}}/M_{\mathrm{GS}}$ up to the 99 percentile. Our numerical results suggest:

$$R_{\mathrm{GS,SP}} = 2.83 \cdot M_{\mathrm{GS}}^{-0.34} \tag{6.37}$$

which is in good agreement with the arguments above.

For PLAM the situation is considerably more difficult as (i) the scaling symmetry (2.114) is not satisfied and (ii) no closed form expression is available for the second derivate of the gravitational potential Φ. An extension of our analysis, in particular Appendix C.3, is therefore not immediate and we investigate the ground state mass-size relation for PLAM only numerically. Again a power-law is found:

$$R_{\mathrm{GS,PLAM}} = 4.91 \cdot M_{\mathrm{GS}}^{-0.72} \quad (\epsilon = 10^{-2}) \ . \tag{6.38}$$

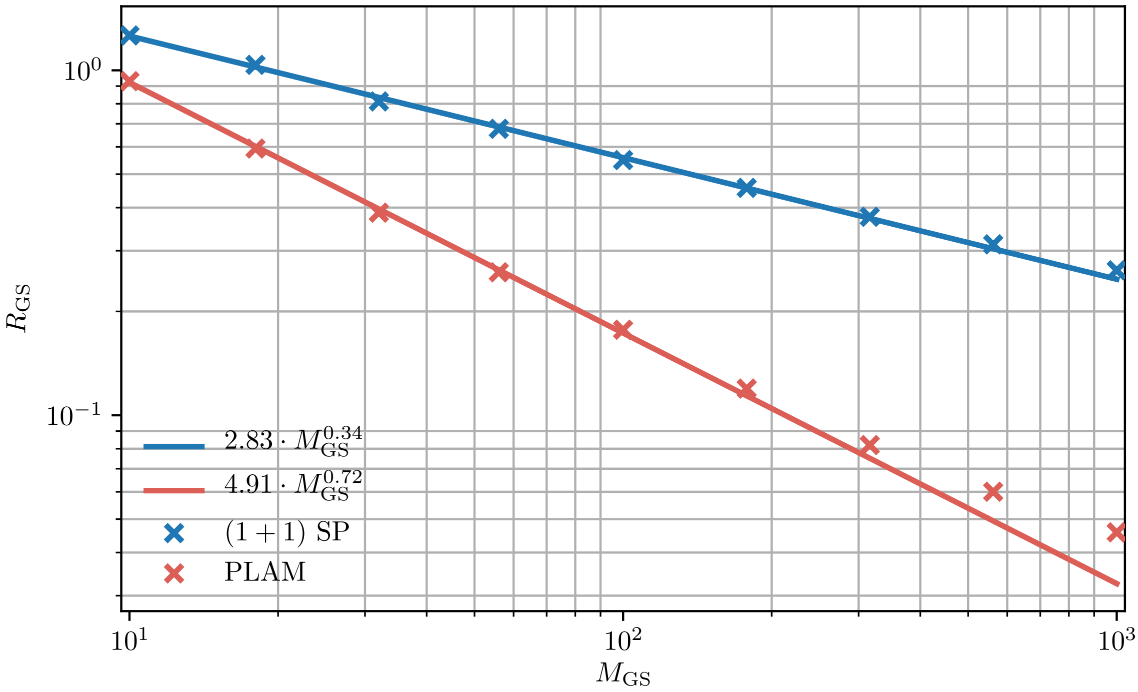

Figure 6.3: Ground state mass-size relation for $(1+1)$-SP (blue) and PLAM (red) for $\epsilon = 10^{-2}$. The numerical result for $(1+1)$-SP is in good agreement with the considerations following a dimensional analysis.

Soliton Behavior The term *soliton* tends to be a loaded notion. Here, we mean a nonlinear wave which is (i) stationary, i.e. has a time-independent envelope $|\psi|^2$, and (ii) preserves it's form in interactions with other solitons.

Property (i) clearly holds for the FDM ground state. Testing (ii) is done by conducting a collision study with the two ground-states generated in Figure 6.1. To this end, we place two equal mass ground states into a domain of size $L = 2M_{\mathrm{GS}} = 100$ and boost each one to velocity $v = 2\pi$ and $-v$ respectively, cf. section 2.4 and [71]:

$$\psi_0(x) = \varphi_{\mathrm{GS}}\left(x + \frac{L}{4}\right) e^{ivx} + \varphi_{\mathrm{GS}}\left(x - \frac{L}{4}\right) e^{-ivx} \ . \tag{6.39}$$

Figure 6.4 illustrates the result for both reduction models. During the interaction strong interference patterns emerge at the point of collision. However, once both ground-states passed through each other, the post-collision density is still remarkably close to the initial matter distribution. Realize this behavior is highly non-trivial as the evolution is nonlinear.

We conclude property (ii) is satisfied and we will use the term ground state and soliton interchangeably and furthermore set $M_\mathrm{S} \equiv M_\mathrm{GS}$ and $R_\mathrm{S} \equiv R_\mathrm{GS}$.

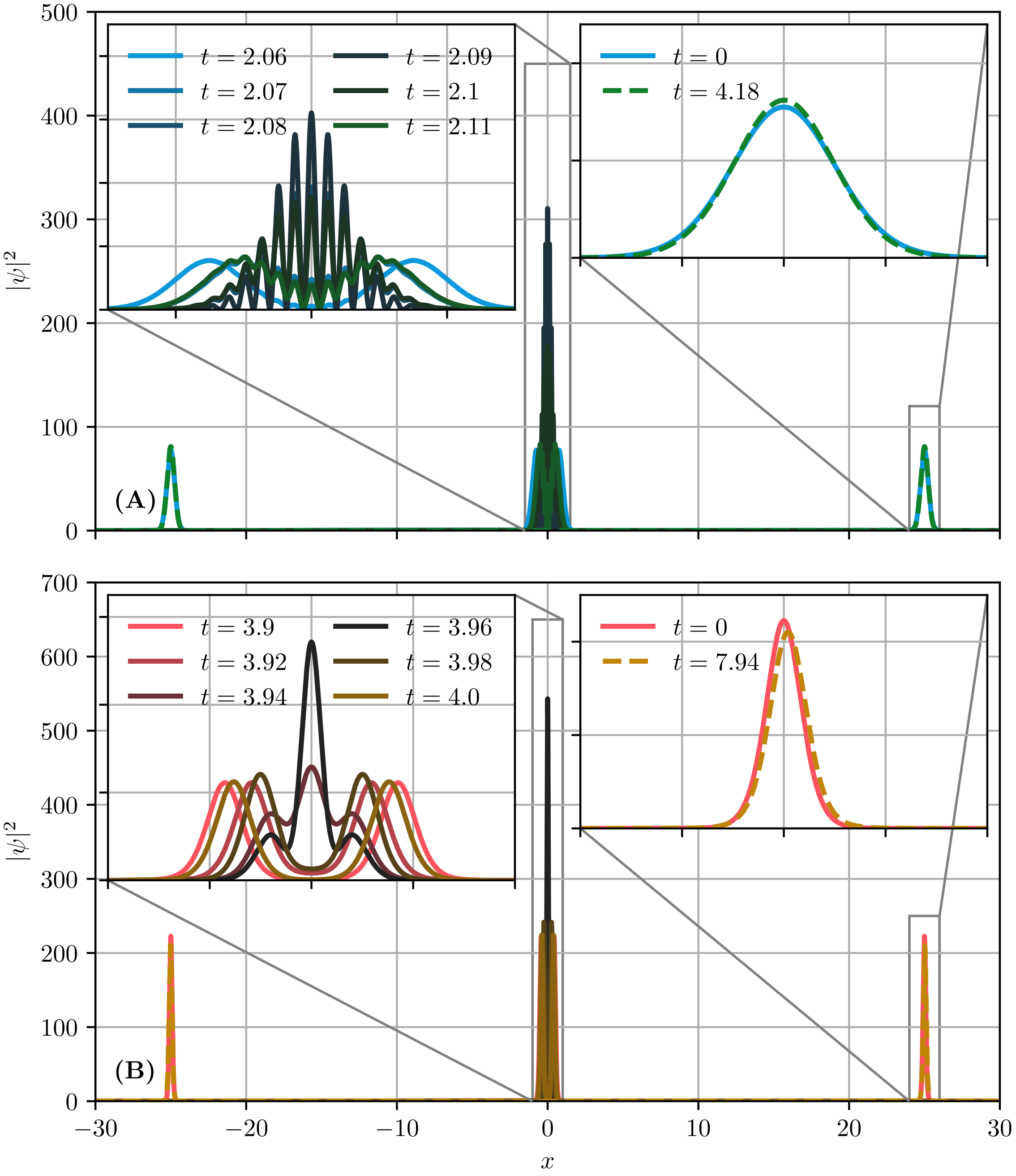

Figure 6.4: Equal mass ground state collision in (1 + 1)-SP **(A)** and PLAM **(B)**. In both models, the ground states interfere at $x = 0$ but retain their shape once they passed through each other. The emerging interference patterns are shown in the **left insets**. Comparison between the initial and final state is illustrated in the **right insets**. These show good correspondence and we conclude ground state-ground state collisions are form-preserving despite the nonlinear interaction. This is the defining property of a soliton.

6.3 Static Space-Time Dynamics

As explained in the beginning of this chapter, we investigate the long term dynamics of both reduction approaches under simplified conditions.

Concerning the choice of initial conditions, chapter 5.3 already showed how the existence of *multiple* overdense regions in the initial conditions leads to *multiple* high density structures at late times which in a subsequent evolutionary phase undergo mergers. Especially late time mergers complicate the dynamics unnecessarily as they drive clusters out of equilibirum therefore increasing the required integration time to re-relax into the asymptotic state. Naturally one, wants to minimize the integration time to keep numerical errors under control, especially when the nonlinear coupling constant is large. In this light, we choose to use artificial initial conditions with a single spatially localized overdense reason as oppose to spatially delocalized cosmological initial conditions.

More precisely, this section sets $a = 1$, assumes a zero initial peculiar velocity and a gaussian initial density:

$$|\psi_0(x)|^2 = \mathcal{N} e^{-\frac{x^2}{2\sigma^2}}, \qquad \mathrm{Arg}[\varphi_0(x)] = 0 \ , \tag{6.40}$$

where the normalization constant $\mathcal{N}$ is determined numerically. The width of the gaussian is chosen based on the stability considerations of section 3.2.2. Strictly speaking, these only apply for $(d+1)$-SP and not for PLAM. However, our focus does not lie on exactly picking the critical length scale under confinement below which matter is quantum mechanically stabilized. Instead getting a rough idea of the size of this length scale is enough and we assume the $(d+1)$-SP Jeans wavelength λ_J to be a reasonable guess for PLAM as well. We then exceed λ_J significantly to make sure collapse really happens in both models. That said, set:

$$\sigma = 6 \cdot \frac{\lambda_J(a=1)}{2\pi} = 6 \cdot \frac{\sqrt{2}\pi}{2\pi} \approx 4.24 \ . \tag{6.41}$$

To assure periodicity of the initial conditions up to floating point precision, the box size is chosen as $L = 30 \cdot \sigma \approx 127.28$.

6.3.1 $(1+1)$-Schrödinger-Poisson

Figure 6.5 illustrates the collapse under $(1+1)$-SP. The collapse proceeds violently in the beginning of the simulation but results in a spatio-temporal evolution of $|\psi|^2$, **(D)**, which develops no new features past $t \approx 10$.

As expected the total energy (2.113) is preserved, cf. **(E)**, and we find the system to both virialize according to eq. (6.12), **(F)**, and thermalize **(G)**.

Notably, the boundary term in eq. (6.12) does not play a role in achieving virial equilibrium. This is clear from considering the time evolution of $|\psi|^2$: Under $(1+1)$-SP no excess matter is ejected from the collapse site towards the boundaries. Hence, ψ and its derivatives persist to be small at $x = 0$ and $x = L$.

The entropy evolution reveals eq. (6.15) not to be a strictly increasing function which one might intuitively expect from *Boltzmann's H-theorem*. However, this is

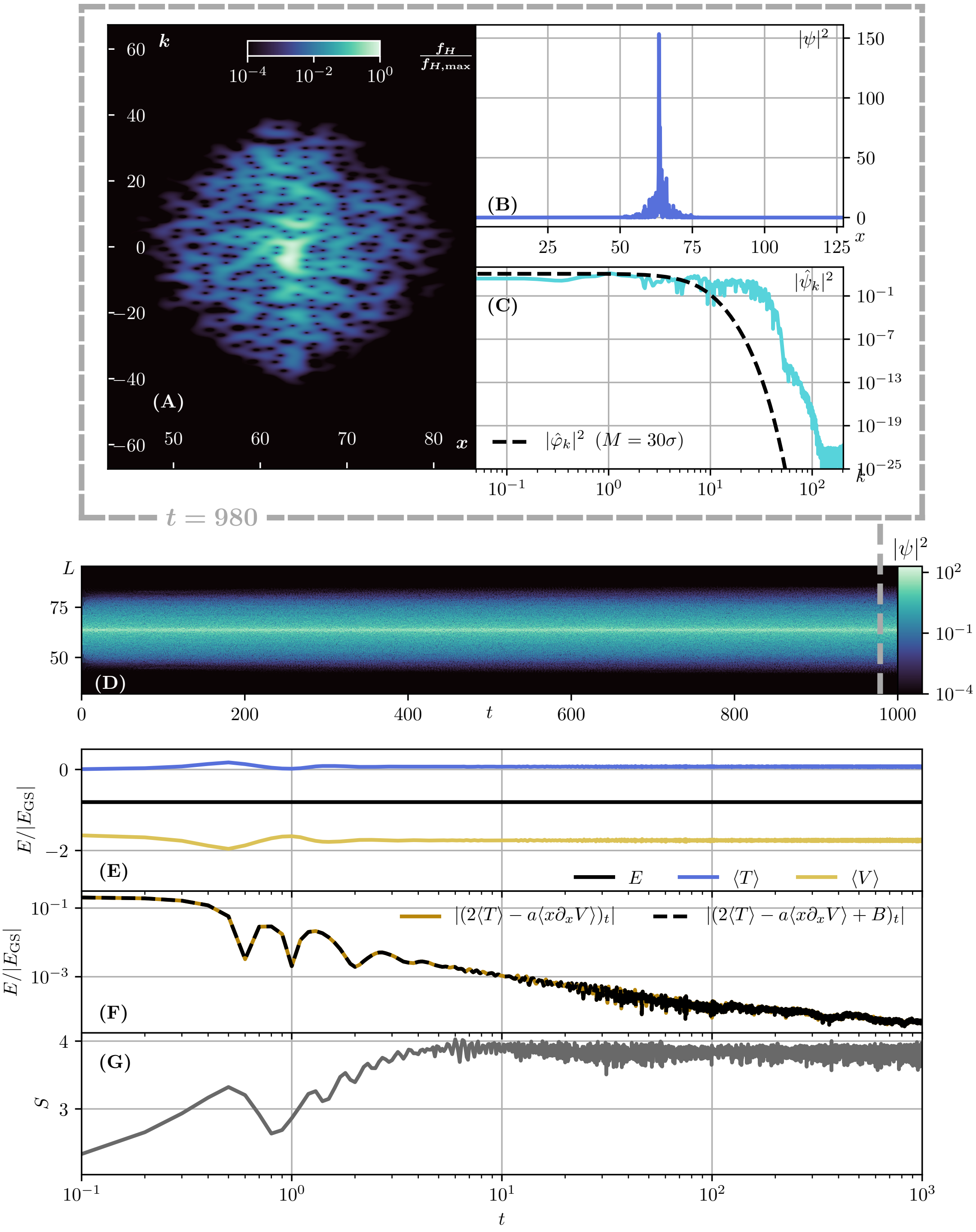

Figure 6.5: Collapse of gaussian initial conditions (6.40) under $(1+1)$-SP for $a = 1$ in multiple observables. **(A)**: Husimi's phase space distribution (6.14) at $t = 980$. **(B/C)**: matter density $|\psi|^2$ and spectrum $|\hat{\psi}_k|^2$ at $t = 980$. **(D)**: spatio-temporal evolution of $|\psi|^2$. Only a zoomed interval around the collapse center is shown. **(E)**: total, kinetic and potential energies as a function of integration time. **(F)**: deviation from the virial theorem (6.12). **(G)**: Entropy evolution, cf. eq. (6.15). All energies in **(E/F)** have been normalized to a $(1+1)$-SP ground state of mass $M_{\mathrm{S}} = L = 30\sigma$, the spectrum of which is shown as dashed black line in **(C)**. Also note the logarithmic time axis in **(E)**-**(G)**

acceptable as the H-theorem only applies for ideal, collisional dynamics, which is not the case here. Although strict monotony is not achieved, Wehrl's entropy is still maximized during the evolution.

Comparing virialization with the thermalization process indicates that the entropy $S(t)$ is a better suited measure to assess whether the relaxation of the total system is completed: As we mentioned before, the physically observable density $|\psi|^2$ does not develop new features after a few collapse cycles and therefore attains its asymptotic state already at $t = 10$. This is clearly reflected in the entropy evolution but not in the deviation from the virial equilibrium in **(G)**. A natural question is then how the thermalization time scale depends on the system parameters, in particular the nonlinear coupling strength a. We come back to this point shortly.

The asymptotic state is visualized in **(A)**-**(C)**. In real space, **(B)**, $|\psi|^2$ develops a central peak surrounded by strong fluctuations. Everything is quickly oscillating, both spatially and temporally, and far from a stationary state. Also note the unphysical asymmetry of the density distribution. This asymmetry originates from tiny numerical errors adding up over the long integration time until the spatial symmetry around the origin is broken. In **(C)** we compare the asymptotic spectrum $|\hat{\psi}|^2$ with an exemplary soliton spectrum $|\hat{\varphi}|^2$ of mass $M_{\mathrm{S}} = 30\sigma$. Clearly, $|\hat{\psi}|^2$ is heavily distorted compared to $|\hat{\varphi}|^2$. Thus, $(1+1)$-SP failed to relax into a single solitonic core even under the simplified conditions studied here. This result is in alignment with our previous study in [86].

Although $(1+1)$-SP fails to attain the sought after asymptotic FDM state there is still something to be learned about the long term density distribution. After all, the Wigner-Weyl formalism establishes a connection between $(1+1)$-SP and a smoothed, classical phase space distribution governed by Vlasov-like dynamics. Thus, the complementary, classical view point suggests to compare the results of $(1+1)$-SP with predictions for one-dimensional gravitating collisionless systems, in particular density profile models for dark matter haloes.

The Navarro-Frenk-White (NFW) profiles, [61] with $\rho_{\mathrm{NFW}}(|\boldsymbol{x}|) \propto |\boldsymbol{x}|^{-1}(|\boldsymbol{x}|+\alpha)^{-2}$ is the canonical choice for the spherically averaged halo mass density in $d = 3$ dimensions. For the $d = 1$ situation at hand [13] observed how the process of violent relaxation drives the system towards power-law densities $\rho(|x|) \propto |x|^{-\gamma}$ with $\gamma \simeq 0.5$. Inspired by Einasto's profile [26], the authors of [70] extended this by an exponential suppression factor dominant past a cut-off radius r_0. Following [70], we therefore expect:

$$\bar{\rho}(x) \propto |x|^{-\gamma} \exp\left(-\left(\frac{r}{r_0}\right)^{2-\gamma}\right) . \tag{6.42}$$

Importantly, $\bar{\rho}(x) \neq |\psi|^2$: Realize we reentered the framework of Schrödinger's method by expecting eq. (6.42) — a classical prediction — to be a good model for the dark matter density encoded in $|\psi|^2$. As noted before, the Schrödinger-to-Vlasov mapping is only accurate for Husimi's distribution $f_H(x, k)$, i.e. a *smoothed* phase space distributions, and statistical moments of it, see [76]. Consequently, it is the marginal distribution, or 0^{th}-order moment,

$$\bar{\rho}(x) \equiv \frac{1}{2\pi} \int_{\Omega} \mathrm{d}k f_H(x, k) \overset{[51]}{=} \frac{1}{\sqrt{2\pi}\sigma} e^{-\frac{x^2}{2\sigma_x^2}} * |\psi|^2 , \tag{6.43}$$

which must be compared to eq. (6.42). To spare us the necessity of choosing the smoothing scale σ_x we consider the integrated halo mass $M(r)$ rather than the mass density directly. That said, one expects:

$$\frac{M(r)}{M_{\mathrm{tot}}} = -\frac{r_0^{1-\gamma}}{M_{\mathrm{tot}}(2-\gamma)^2}\left[\Gamma\left(\frac{1}{\gamma-2}\right) + (2-\gamma)\Gamma\left(1+\frac{1}{\gamma-2}, \left(\frac{r}{r_0}\right)^{2-\gamma}\right)\right] \tag{6.44}$$

with $\Gamma(x)$ and $\Gamma(x, y)$ denoting the (incomplete) Gamma function.

Figure 6.6 illustrates the integrated mass of the final time density $|\psi|^2$ from Figure 6.5 together with a fit of eq. (6.44). The correspondence is convincing and similar results were obtained by [31, 86]. Although the best fit value of $\gamma = 0.58$ is slightly too large with respect to the classical findings of [13, 70], it should be emphasized that the analysis is also somewhat crude. For more reliable results an ensemble of simulations should be considered.

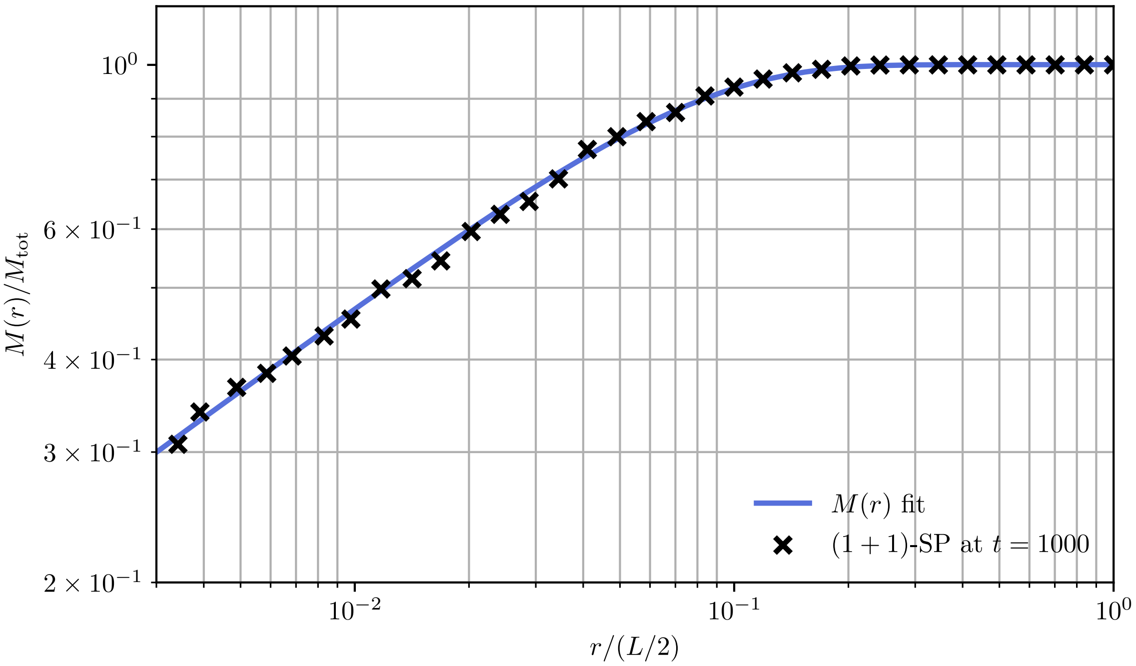

Figure 6.6: Comparison of the final integrated mass under $(1+1)$-SP and the classical prediction, eq. (6.44), for one dimensional, collisionless, self-gravitating systems

Before proceeding with PLAM, let us return to the thermalization time t_{th} and investigate its dependence on the coupling strength a. To this end, we rerun the experiment of Figure 6.5 for different values of a and extract t_{th} from the entropy evolution by computing the final entropy S_{final} as time average in $990 \le t \le 1000$ and demanding $S(t_{\mathrm{th}}) = S_{\mathrm{final}}$.

Consult Figure 6.7 for a comparison of all entropy curves with the red dots designating the individual thermalization points. Also included is the case $a = 0$ for which eq. (4.1) reduces to the free Schrödinger equation. An analytical solution exists in this scenario and one can compute the entropy exactly:

$$\begin{aligned} S_{\mathrm{free}} = S[f_{\mathrm{free}}] = \frac{\sigma_x|\Omega|}{\sigma|f|}\frac{1}{\sqrt{\mathrm{Re}[\Omega]\,(1-\mathrm{Re}[\Omega])}}\left(1-\log\frac{2\sigma_x|\Omega|}{\sigma|f|}\right) \quad \text{with} \\ \Omega = \frac{1}{1+\frac{\sigma_x^2}{\sigma^2 f}}, \quad f = 1+\frac{it}{2\sigma^2}\,. \end{aligned} \tag{6.45}$$

The good agreement between eq. (6.45) and the numerical data (black crosses) is reassuring.

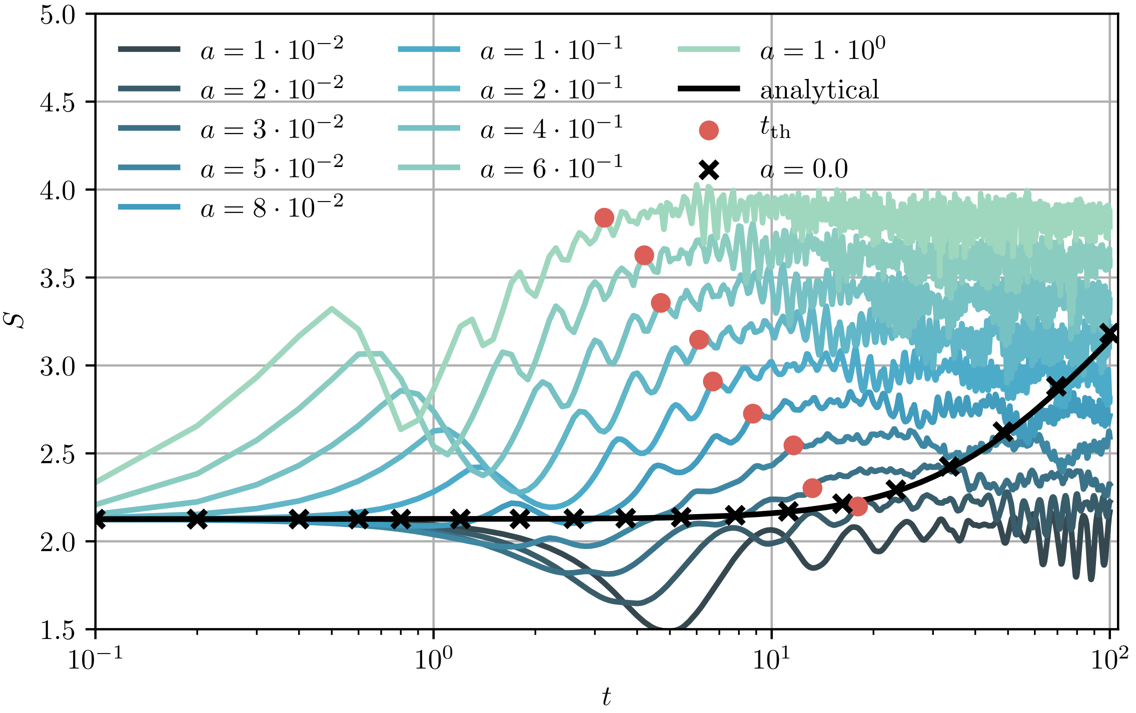

Figure 6.7: Entropy evolution under (1+1)-SP for different values of the coupling strength a. Red dots designate the extracted thermalization time found by demanding $S(t_{\mathrm{th}}) = S_{\mathrm{final}}$. The final value S_{final} corresponds to the average value of the entropy in the interval $990 \leq t \leq 1000$. Averaging is required as Wehrl's entropy is not a strictly monotonically increasing function as known from classical, collisionless gases but instead shows oscillations on top of its saturated, final value. The solid black line corresponds to the entropy function of the free Schrödinger equation given in eq. (6.45).

Plotting t_{th} as a function of the coupling strength, Figure 6.8, reveals a power law dependence over two orders of magnitude:

$$t_{\mathrm{th}}(a) = 3.01 \cdot a^{-0.43} \tag{6.46}$$

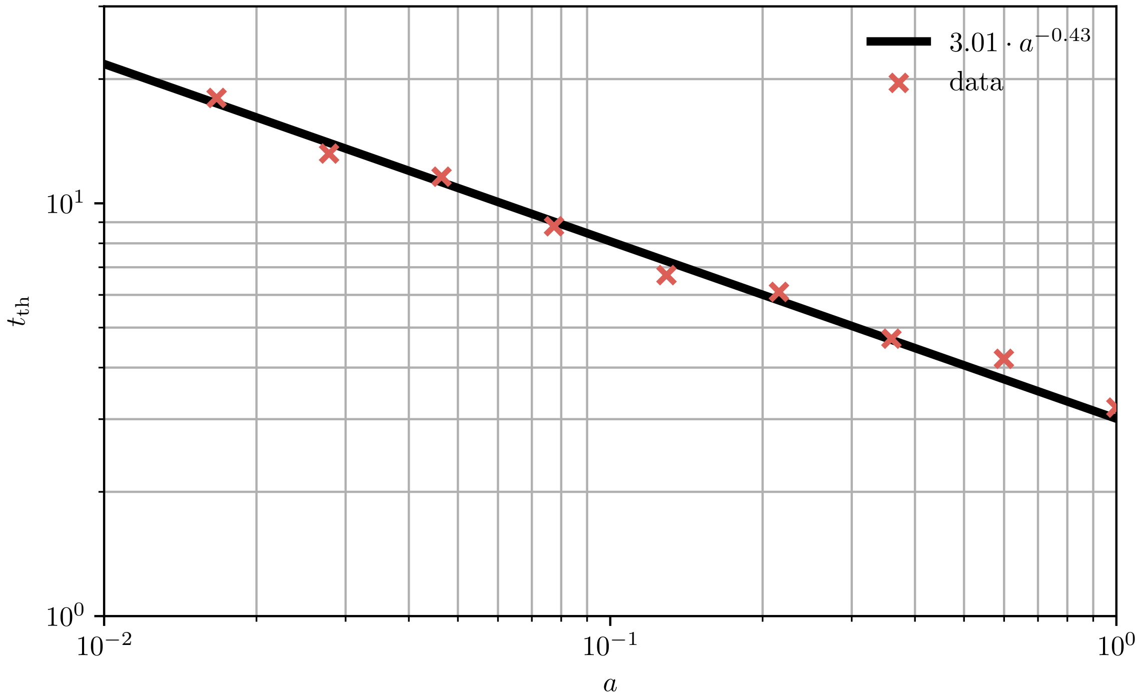

Figure 6.8: Thermalization time of $(1+1)$-SP as a function of the coupling strength a.

6.3.2 PLAM

Next, we turn our attention to PLAM and rerun the experiment of section 6.3.1. This requires us to choose a confinement strength ϵ. Since we are interested in a lower dimensional approximation of $(3+1)$-SP, it is evident to investigate the strong confinement regime, $\epsilon \ll 1$. Other than this, no conditions are imposed on ϵ leaving some arbitrariness in its numerical value. The results reported below were obtained for $\epsilon = 10^{-2}$. Additional tests were conducted for $\epsilon = 10^{-1}$ yielding qualitatively similar results.

Turning to Figure 6.9 proves PLAM dynamics to be significantly different from $(1+1)$-SP. Firstly, the spatio-temporal density evolution in **(D)** illustrates that soon after integration starts the gravitational collapse leads to an emission of excess matter towards the boundaries. These matter lumps organize into a stable solitonic form and collide, or more precisely pass through each other, at the boundaries at $t \approx 100$. Around the same time, the earliest emitted matter chunks re-collide with the central soliton. A slight, most likely numerically induced, difference in their velocity breaks the symmetry of the problem, resulting in a drift of the high-mass soliton originally situated at the box center. From this point forward, the dynamics is characterized by multiple soliton-soliton interactions of different mass ratios. We find, the highest mass soliton to slowly consume lower mass solitons until only a single one remains. At the same time, the background fluctuations increase in magnitude up to $\mathcal{O}(1)$ until the end of the integration.

The background fluctuation growth is also nicely visible in the phase space distribution **(A)**-**(C)**. Here multiple, ovally shaped soliton distribution are embedded into the background matter field which slowly broadens in momentum direction over the course of the integration. At $t = 990$ a single stable core immersed in a "sea of fluctuations" remains.

The energy evolution in **(E)** also follows our expectations. As the background is not expanding, the total energy must be conserved which is readily verified by our data (black line). In general, we observe a slow but steady conversion from potential energy $\langle V \rangle$ into kinetic energy $\langle T \rangle$. This is plausible since the main contributor to the kinetic energy is the emerging fluctuation field. Remember that $\langle T \rangle$ depends on the gradient of the wave function which obviously increases if higher amplitude fluctuations are present. Peaks in the energy evolution, such as at $t = 650$, are associated with soliton-soliton collisions.

Figures **(F)**-**(G)** show, as in the case of $(1+1)$-SP, how the system slowly approaches the expected virial and thermal equilibrium. This time, however, achieving virialization hinges on the boundary contribution B in eq. (6.12), simply because significant mass travels across the boundary over the course of the integration. *Please note that without the correction term, the dynamics would depart from virial equilibrium.* Also note that the way we follow the virialization process is still not perfect. For instance, the sudden jump in

$$|(2\langle T \rangle - a\langle x\partial_x V \rangle + B)_t|$$

at $t = 250$ is of course unphysical. Comparing with **(D)** reveals how matter is moving across the boundary at this point, which constitutes a sudden change for the boundary term. To account for these sudden changes, one would have to increase the temporal resolution with which the time-average integral in eq. (6.2) is computed. However, one doesn't know in advance when these critical points will occur. All of these problems can of course be addressed, but we refrain from doing so at this point as we already identified the entropy to be better suited metric to assess relaxation.

This is again true in the present case, cf. **(G)**. Compared to $(1+1)$-SP entropy increases very slowly up to $t = 850$ after which only one soliton is present.

Two open question remain. Firstly, we tacitly called the final state to be a ground-state soliton. It remains to be shown this is the case. Secondly, the spatio-temporal evolution of $|\psi|^2$ proves that these (supposedly) solitonic cores are quite mobile. Hence, one must ask if the total momentum is actually preserved. Both aspects are addressed in Figure 6.10, where we compare the spectrum of $|\hat{\psi}|^2$ at $t = 1000$ with the spectrum of the best matching soliton and show momentum conservation up to 1 part 1000.

It should be noted that Figure 6.10 is *not* a fit but follows from manual adjustment. Since (P)LAM has no scaling symmetry akin to eq. (2.114) for $(1+1)$-SP, a simple rescaling of a reference ground state to a best fitting core mass is not possible. In practice, the soliton mass was manually tweaked under the constraints (i) of a good correspondence of $|\hat{\psi}_k|^2$ with $|\hat{\varphi}_k|^2$ and (ii) $E_{\text{tot}}/|E_{\text{GS}}| > -1$.

Obviously, one can rerun the simulation with different standard deviations of the initial gaussian, and therefore different total masses, to check if the dynamics changes qualitatively. It turns out this is not the case. In all conducted studies, the behavior is identical to Figure 6.9: Multiple solitons get emitted during the first collapse which then merge into a single core after sufficiently long integration time. At the same time the fluctuating background increases in magnitude. Figure 6.11 depicts the asymptotic spectra of simulation runs with $\sigma' = 2/3\sigma$ and $\sigma'' = 1/3\sigma$.

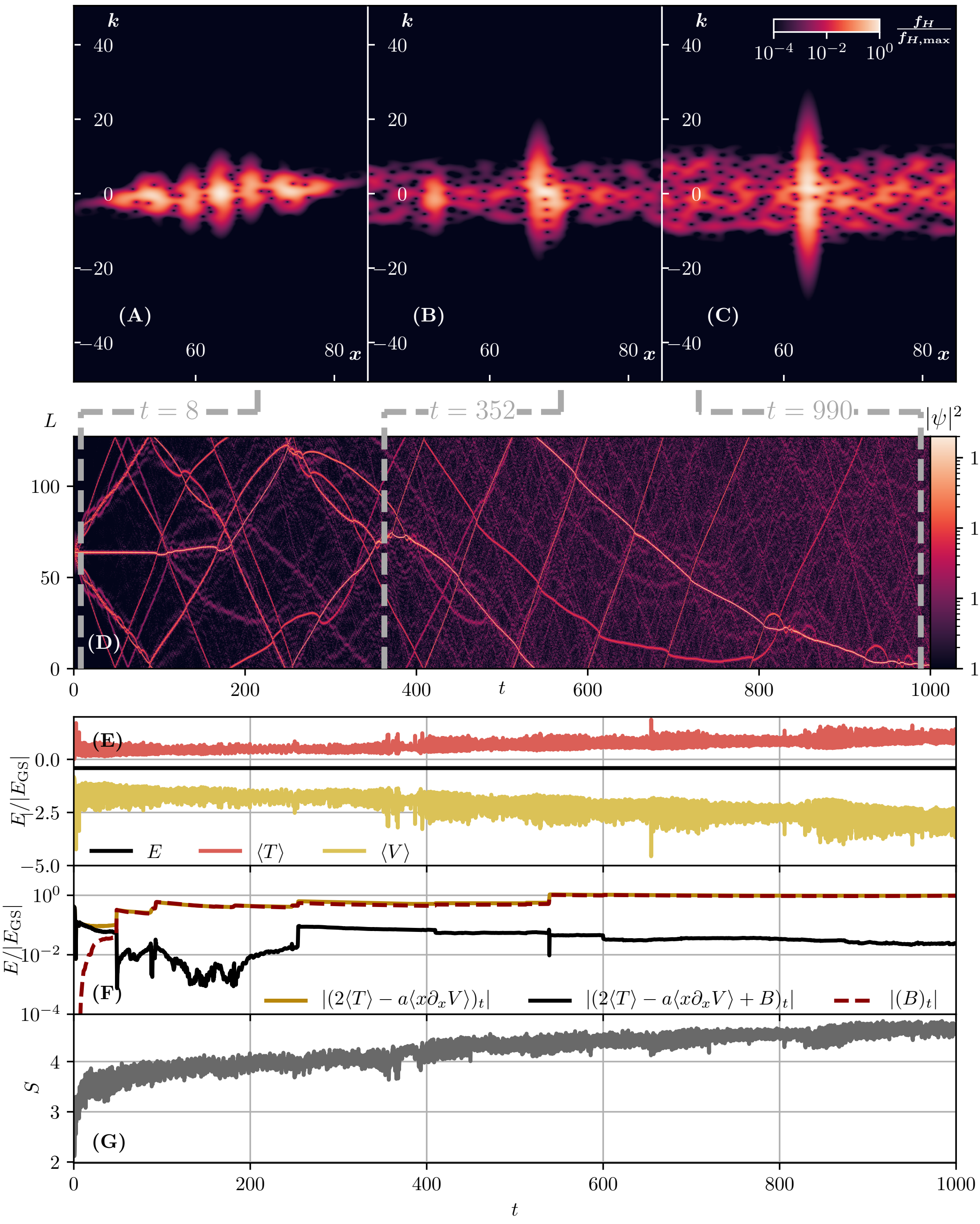

Figure 6.9: Collapse of gaussian initial conditions (6.40) under strong confinement with confinement strength $\epsilon = 0.01$ for $a = 1$ in multiple observables. **(A)-(C)**: Husimi's phase space distribution (6.14) at $t = 8, 352, 990$ respectively. The distribution at $t = 990$ has been re-centered at the origin for convenience. **(D)**: Spatio-temporal evolution of $|\psi|^2$. Compared to Figure 6.5C the entire spatial domain is shown. Notice how multiple solitons merge into one while the fluctuating background increases in magnitude up to $\mathcal{O}(1)$ **(E)**: total, kinetic and potential energies as a function of integration time. **(F)**: deviation from the virial theorem (6.12). Without addition of the boundary term, the system would depart from virial equilibirum. **(G)**: Entropy evolution, cf. eq. (6.15). All energies in **(E/F)** have been normalized to a PLAM ground state of mass $M_S = 50$, cf. Figure 6.10. Also note the linear time axis in **(E)-(G)** compared Figure 6.5E-G.

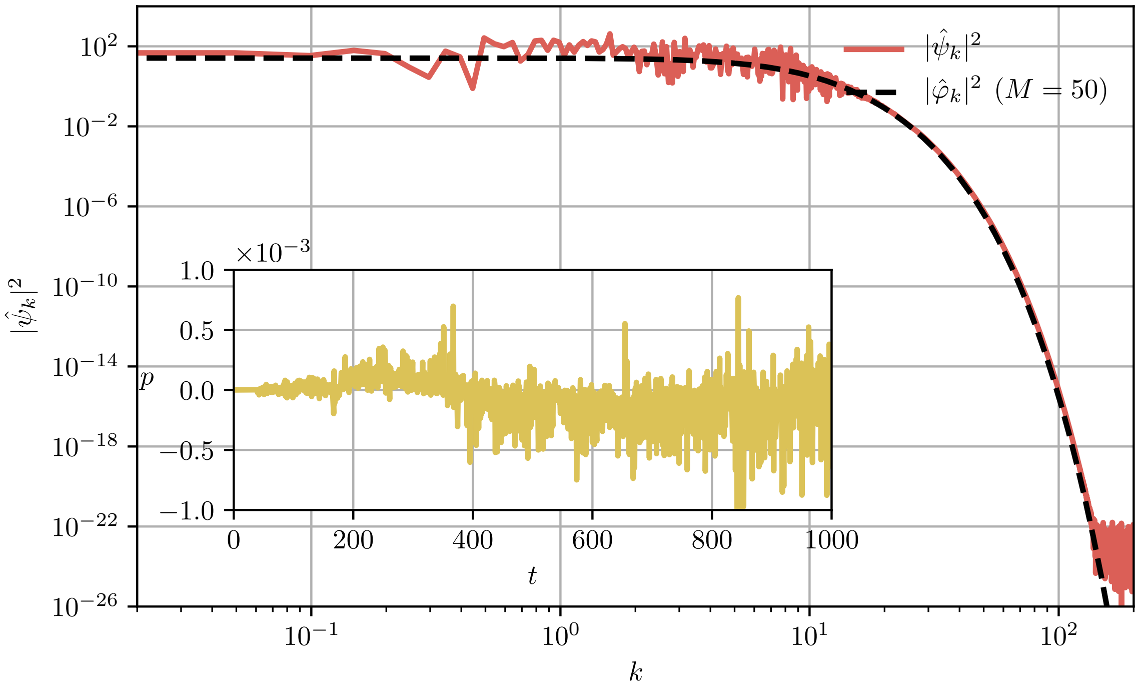

Figure 6.10: Spectrum of the last PLAM wave function at $t = 1000$ together with a ground state of mass $M_\mathrm{S} = 50$. This ground state was also used for the energy normalization in Figure 6.9. Background fluctuations show up as spectral disturbances below $k \leq 10$. Given the extremely long integration time, which is roughly 50 times as long as for cosmological considerations, we deem this to be a formidable result. Inset: Momentum conservation according to eq. (2.111) is satisfied up to $\Delta p = 10^{-3}$.

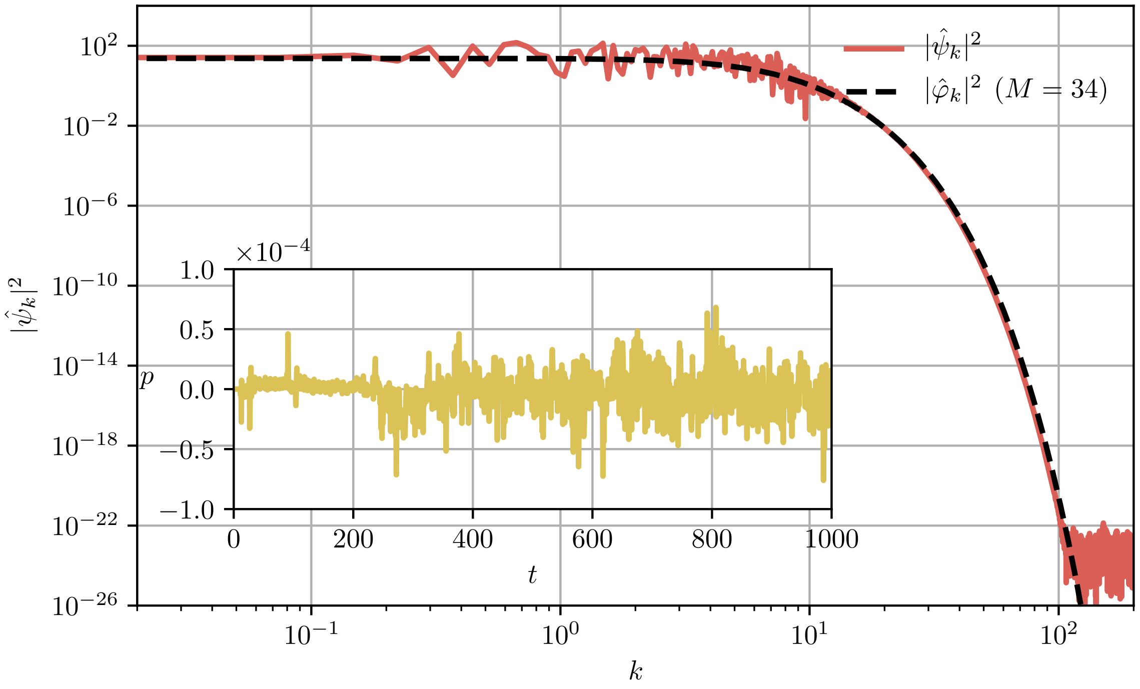

(a) $\sigma' = 2/3\sigma$

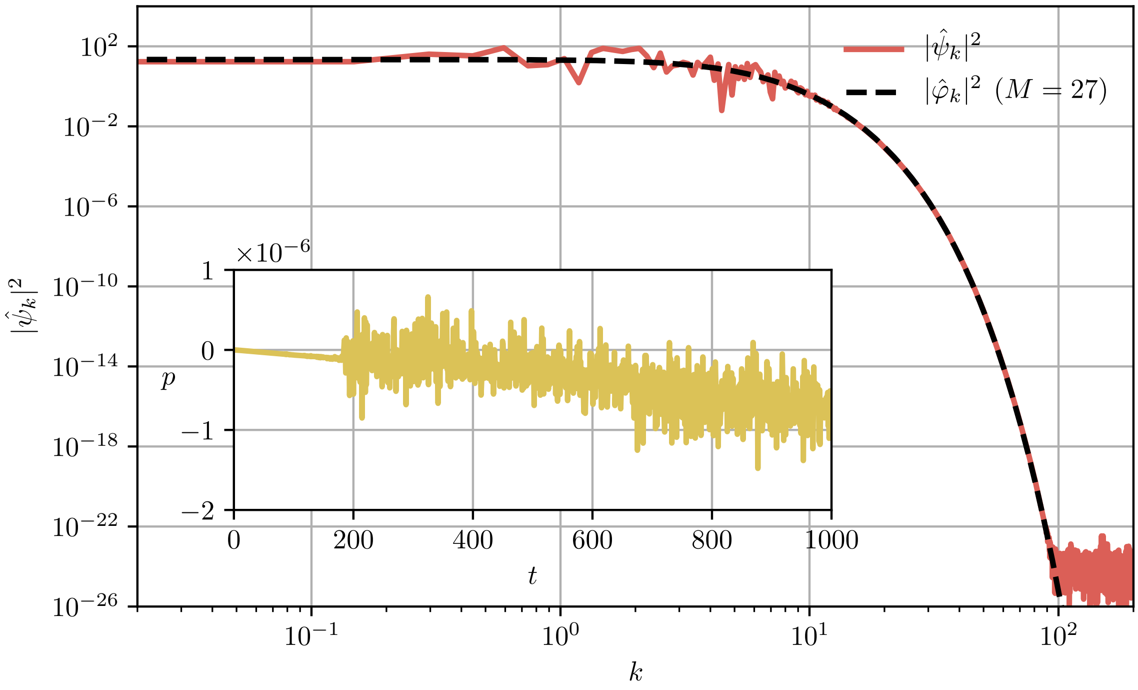

(b) $\sigma'' = 1/3\sigma$

Figure 6.11: Asymptotic PLAM spectra at $t = 1000$ together with best matching ground state for smaller total mass inside the domain compared to Figure 6.10. Insets show momentum conservation.

6.3.3 Self-Organization Processes in Nonlinear Dynamics

The observed self organization principle of $(1+1)$-FDM under strong confinement is not new. In fact, [83] already showed how for a large class of focusing, *local* nonlinearity's of the NLSE perturbed uniform initial conditions have a single soliton as dynamical attractor. More precisely, the perturbed initial conditions develop a number of small mass solitons which subsequently merge into a single high-mass soliton at late times. This phenomenon was coined *soliton turbulence* and it was argued it is "thermodynamically favorable" for the system to develop in this particular way.

The authors of [46] later put these findings on more theoretical grounds by developing a statistical theory around a mean-field approximation of the nonlinear Hamiltonian and the *maximum entropy principle*.

More recently, the problem of *nonlocal* interactions was considered in the context of nonlinear optics by [65]. Numerical and analytical arguments showed that the dynamics is mainly driven by the ratio between the interaction range R and the soliton size R_S. This is quite intuitive: If the interaction range is too large, matter far away from a potential soliton, but still within interaction range, contributes significantly to the convolution integral. Consequently, the delicate potential required to form a soliton get's averaged out by the surrounding fluctuations. Hence, we expect soliton-turbulence-like behavior for $R_\mathrm{S} > R$. For the opposite case $R_\mathrm{S} < R$, [65] found the system to organize "into a spatially localized incoherent structure" coined *incoherent soliton*. Their results resemble our findings of section 6.3.1.

To check if we can associate the PLAM and $(1+1)$-SP dynamics to the soliton turbulence regime $R_{\mathrm{S}} > R$ or the incoherent soliton regime $R_{\mathrm{S}} < R$ we combine the data of Figure 2.4 with the mass-size relation of Figure 6.3. Figure 6.12 illustrates the situation for $(1+1)$-SP.

Here, two regimes need to be distinguished. Up to $M_{\mathrm{S}} = L \approx 3.5$ the size of the soliton is larger then half the domain size. This would violate the periodicity of ψ and is therefore not realized. Above this minimum mass the linearly growing interaction range of the $(1+1)$-SP interaction kernel dominates the SP-soliton size. Following [65], we expect the generation of incoherent solitons and the results of section 6.3.1 support this claim.

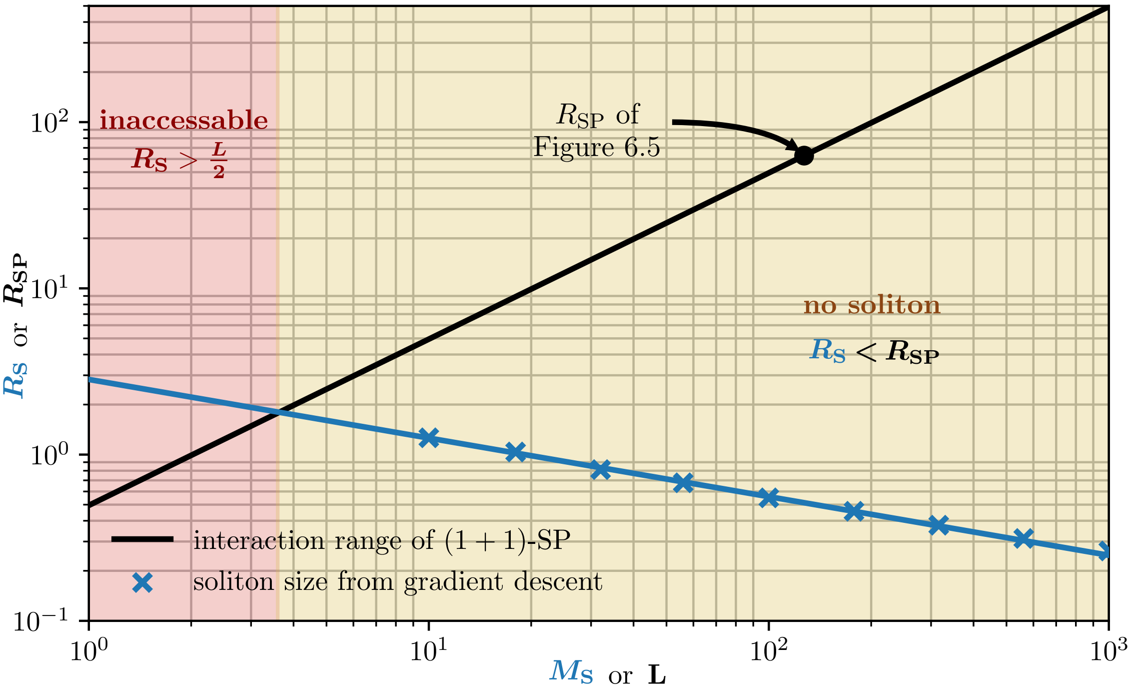

Figure 6.12: Comparison of the relations $R_{\mathrm{S}}(M_{\mathrm{S}})$ (blue line), i.e. the mass-size relation of the ground state soliton of $(1+1)$-SP, and $R_{\mathrm{SP}}(L)$ (black line), i.e. the interaction range of $(1+1)$-SP as a function of the box size L. Blue crosses correspond to the numerically determined soliton sizes of Figure 6.3. Choosing a box size L implies a particular interaction range R_{SP}. For instance, choosing $L \approx 127$, as done for Figure 6.5, yields $R_{\mathrm{SP}} \approx 65$ found at the location of the black arrow. Since there is no soliton of size $R_{\mathrm{S}} > 65$, we expect the gravitational potential of any potential soliton to get averaged away due the convolution with the surrounding matter field. The region for which $R_{\mathrm{S}} > R_{\mathrm{SP}}$ would be satisfied (red) is inconsistent with the periodicity of the domain, i.e. the soliton would be larger than the box.

The situation changes under strong confinement shown in Figure 6.13. Here the interaction range is bounded by it's *finite* free space limit of $\lim_{L\to\infty} R_{\mathrm{PLAM}} = R_{\mathrm{LAM}} \approx 0.1$. This allows for an intermediate soliton mass regime which is consistent with soliton turbulence requirement formulated by [65]. The confined systems of Figure 6.10 and 6.11 then organize into solitons with final masses satisfying $R_S/R_{\mathrm{PLAM}} = 3-5$.

By the above reasoning PLAM should also allow for incoherent soliton dynamics (yellow part of Figure 6.13). We tested this by increasing the total box mass well into this regime. Note this does not mean the system is forced to generate a single incoherent soliton of mass $M_{\rm S} \approx L$ for large enough t. It is still possible to form lower mass ground states within the soliton turbulence regime and have more matter bound in the fluctuating background. By rerunning the experiment of section 6.3.2 we again find soliton turbulence. More investigation is required but it seems if the system is able to form both solitonic cores or incoherent solitons the former is favored.

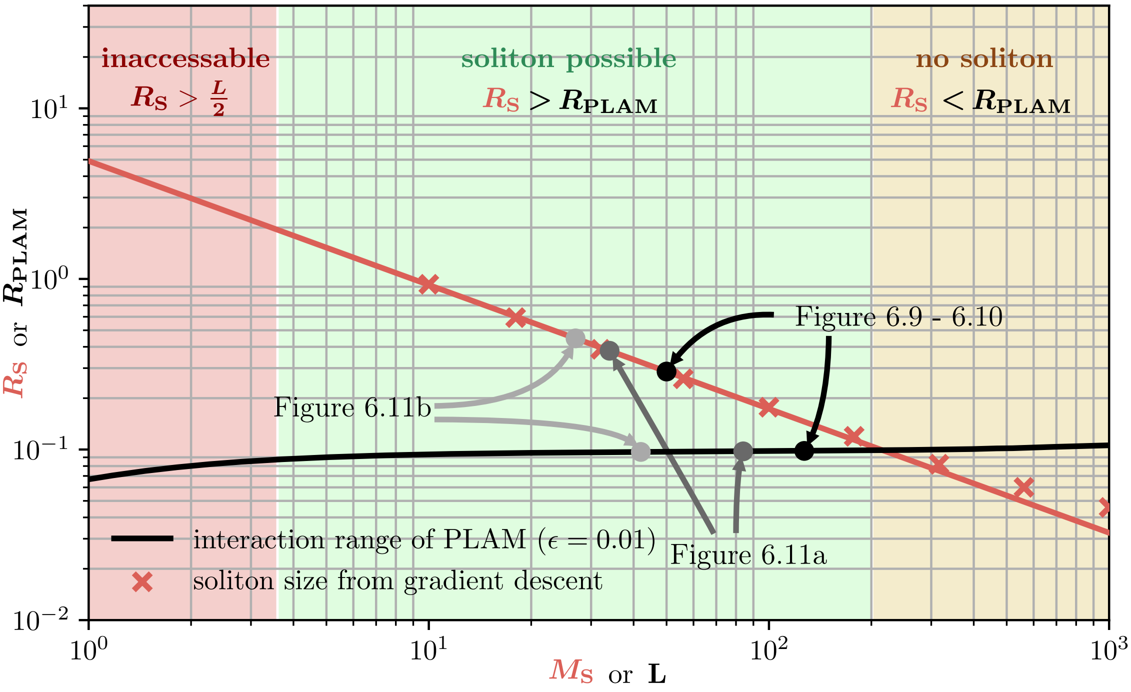

Figure 6.13: Comparison of the relations $R_{\rm S}(M_{\rm S})$ (red line), i.e. the mass-size relation of the ground state soliton of PLAM in eq. (2.106), and $R_{\rm PLAM}(L)$ (black line), i.e. the interaction range of PLAM as a function of the box size L, eq. (6.38). Red crosses correspond to the numerically determined soliton sizes of Figure 6.3. In contrast to Figure 6.12, we find domain sizes which are consistent with the boundary conditions *and* satisfy $R_{\rm S} > R_{\rm PLAM}$. Here soliton turbulence is achievable. For instance, consider the situation of Figure 6.9 (black dots) where a $L \approx 127$ domain induces an interaction range of $R_{\rm PLAM} \approx 0.1$. Given this situation, the analysis of Figure 6.10 identified a final soliton of mass $M_{\rm S} = 50$ implying $R_{\rm S} = 0.3$ by eq. (6.38). Hence, $R_{\rm S}/R_{\rm PLAM} = 3$ as one expects for "soliton turbulence".

6.4 Expanding Space-Time Dynamics

We now allow space-time to expand. Although the exact dynamics leading to the asymptotic configuration of the system might be different, the arguments of section 6.3.3 stay intact and one should not expect changes in the final, thermalized states of $(1+1)$-SP and PLAM if attained.

The "if attained" qualification becomes clear once we realize that the, now time-dependent, coupling strength $a(t)$ is small, i.e $a \ll 1$, for a significant portion of the integration time. We already saw for $(1+1)$-SP how a small coupling strength implies longer relaxation times, cf. Figure 6.8, and since thermalization in PLAM at $a = 1$ took long anyways, cf. Figure 6.9G, we should not expect fully relaxed matter configurations.

To assure comparability with the static space-time discussion in section 6.3, the same initial conditions are employed. By choosing a reasonable starting redshift of $z = 100$, these still proof to be gravitationally unstable:

$$\sigma_J = \frac{\lambda_J(z = 100)}{2\pi} = 2.24 < \sigma = 4.24 \tag{6.47}$$

and collapse should set in right away, however, less violent as for $a = 1$.

6.4.1 $(1+1)$-Schrödinger-Poisson

Figure 6.14 depicts the collapse under $(1+1)$-SP. The less violent collapse allows to clearly distinguish recurring phases in the evolution. Focusing on the spatio-temporal density evolution in **(D)**, we find central matter to contract until $z = 70$ when the core region reaches its peak density. The system responds to this event by pushing matter outward while at the same time outer matter is still flowing towards the center. Unfortunately, the interaction range is too large so that expelled density clumps return to the center around $z = 20$, superposing with yet another "radiation wave" which originated from the second core collapse at $z = 36$. These phases recur in ever smaller time intervals and are confined to a region in space of decreasing size. Also note that the total energy in **(E)** is not a conserved quantity anymore, see section 2.4.

Virialization, **(F)**, reaches a plateau around $z = 20$ and is potentially the limit of our finite resolution numerics. Again, the boundary term is insignificant since no matter travels across the domain boundaries.

Concerning thermalization, **(G)**, we find an increase in entropy after the first collapse which gets superposed by oscillations past $z = 20$. Since these oscillations still show a growing baseline for $z \leq 10$ we deem the thermalization process to be not fully completed.

For assessment of the (almost) asymptotic state, turn to Figure 6.15 in which the final spectrum at $z = 0$ is compared with a $M_{\mathrm{S}} = L$ $(1+1)$-SP ground state for $a = 1$. In alignment with Figure 6.5, we find significant distortions from the smoothly decaying soliton spectrum. This is reassuring given that the interaction range is unaltered under space-time expansion and should therefore still dominate the spatial extent of the soliton.

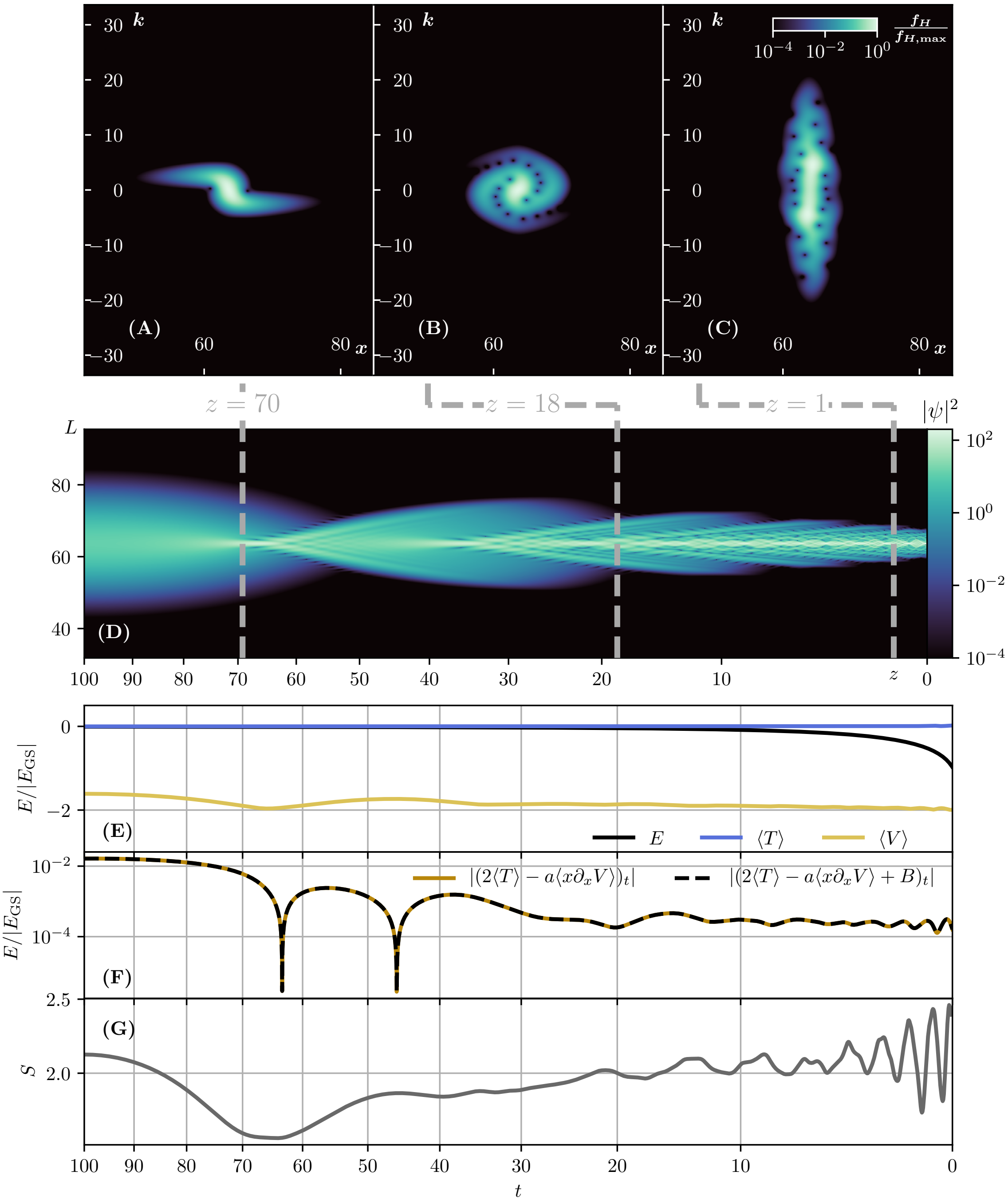

Figure 6.14: Collapse of gaussian initial conditions (6.40) under $(1+1)$-SP in a FLRW universe with $\Omega_m = 0.3$, $\Omega_\Lambda = 1 - \Omega_m$ illustrated in multiple observables. **(A)-(C)**: Husimi's phase space distribution (6.14) at $z = 70$ (first collapse), $z = 18$ and $z = 1$. **(D)**: Spatio-temporal evolution of $|\psi|^2$. Only a zoomed interval around the collapse center is shown. **(E)**: total, kinetic and potential energies as a function of integration time. Note how total energy is not conserved anymore. **(F)**: deviation from the virial theorem (6.12). **(G)**: Entropy evolution, cf. eq. (6.15). All energies in **(E/F)** have been normalized to a $(1+1)$-SP ground state of mass $M_{\mathrm{S}} = L = 30\sigma$, cf. Figure 6.15.

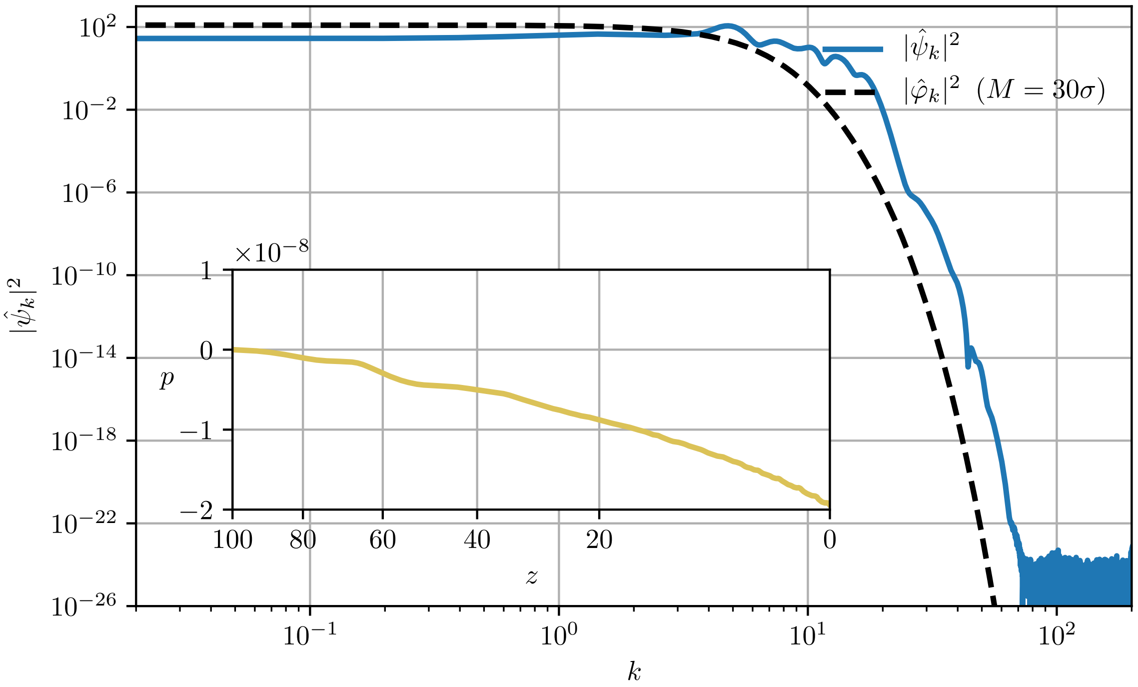

Figure 6.15: Final $(1+1)$-SP spectrum at $z = 0$ together with total mass ground state. Inset shows momentum conservation.

6.4.2 PLAM

Redoing the same experiment for PLAM with $\epsilon = 10^{-2}$ yields Figure 6.16. The time to first collapse is considerably longer compared to $(1+1)$-SP and is reached at $z = 18$. Notice how in the evolution of $|\psi|^2$ outer matter at $x = 50$ or $x = 70$ is essentially untouched throughout the integration time, contrary to the overall contraction observed in 6.14. This is a clear imprint of the small interaction range under confinement due to which no significant attracting force acts on the outer regions of the initial gaussian.

Similar to $(1+1)$-SP, each core collapse leads to an emission of matter radiation. Interestingly, and contrary to the static space-time evolution under confinement, this excess matter does not organize into outward traveling solitons but is more comparable to small scale oscillations.

As was the case for $(1+1)$-SP, virialization cannot be improved past the first couple of core collapse cycles and the entropy evolution indicates only partial thermalization at $z = 0$. One should therefore not expect to find a perfect solitonic core in the domain center. Interestingly, the correspondence of the same $M_\mathrm{S} = 50$ PLAM ground state already used under static conditions in Figure 6.10 matches the final spectrum at $z = 0$ still quite nicely. We show this comparison in Figure 6.17. The momentum evolution in Figure 6.10 also indicates that with the soliton-soliton interactions gone, the total momentum is well better preserved compared to the static case.

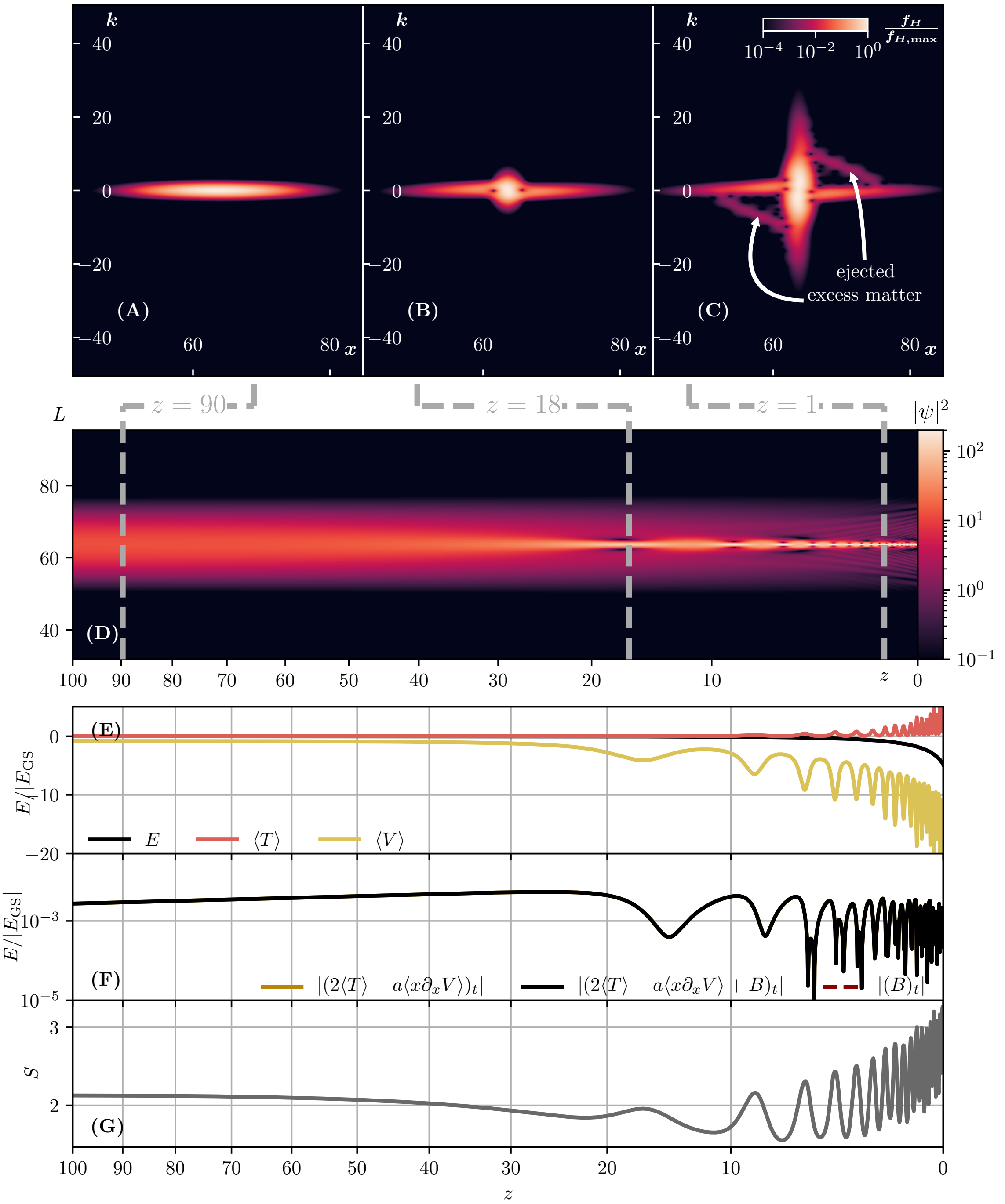

Figure 6.16: Collapse of gaussian initial conditions (6.40) under PLAM for $\epsilon = 10^{-2}$ in a FLRW universe with $\Omega_m = 0.3$, $\Omega_\Lambda = 1 - \Omega_m$ illustrated in multiple observables. **(A)-(C)**: Husimi's phase space distribution (6.14) at $z = 70$ (first collapse), $z = 18$ and $z = 1$. **(D)**: Spatio-temporal evolution of $|\psi|^2$. Only a zoomed interval around the collapse center is shown. **(E)**: total, kinetic and potential energies as a function of integration time. Note how total energy is not conserved anymore. **(F)**: deviation from the virial theorem (6.12). **(G)**: Entropy evolution, cf. eq. (6.15). All energies in **(E/F)** have been normalized to a PLAM ground state of mass $M_S = 50$, cf. Figure 6.17.

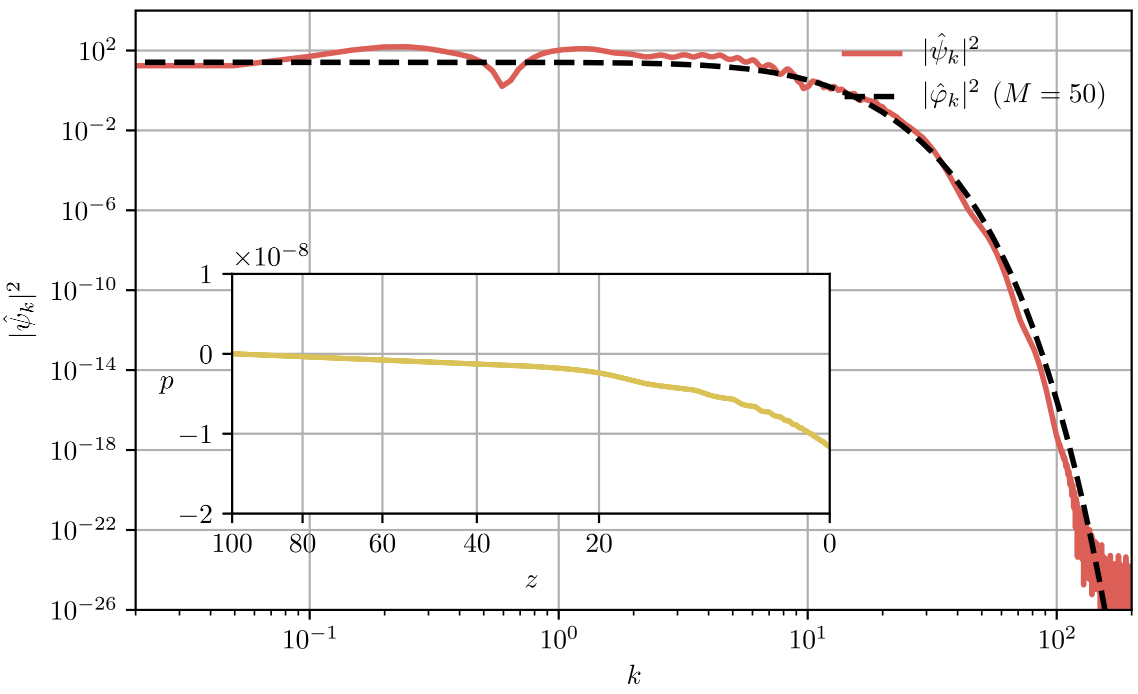

Figure 6.17: Final PLAM spectrum at $z = 0$ together with the same soliton spectrum already used in Figure 6.10. Although thermalization is clearly not completed according to Figure 6.16G the correspondence between both spectra is good.

Chapter 7

Conclusion and Perspectives

"It is finished!"

—Jesus Christ

7.1 Summary of Results

Purpose of this thesis was to investigate to what extend lower-dimensional representations of $(3+1)$-FDM can be employed to map three dimensional phenomena to only one spatial degree of freedom while benefiting from the significantly higher resolution achievable in $(1+1)$-dimensions.

We found the lower dimensional representation of FDM depends on how matter is organized in the orthogonal subspace. Whereas a uniform matter distribution yields the standard $(1+1)$-SP equation, strong confinement lead to the novel PLAM reduction which behaves at far field identical to the canonical $1/r$-interaction known from $(3+1)$-SP. $(1+1)$-SP, on the other hand, underlies an infinite range interaction inducing constant particle-particle forces independent of the spatial separation. In both cases the nonlocal, nonlinear Schrödinger equation (NLSE) with convolution type interaction term allowed for a unified description of both reduction models. Symmetries, in particular $(d+1)$-SP's scaling symmetry were revisited and discussed.

Contrasting FDM and CDM in linear theory emphasized the importance of Heisenberg's uncertainty principle which gave rise to a natural stabilization mechanism against gravitational collapse of overdense matter perturbations. In the hydrodynamic Madelung picture of FDM this stabilization mechanism can be understood as a quantum pressure term due to which the system reacts with an increased velocity dispersion once matter is to strongly confined in x-space. On the other hand, the dynamics on scales significantly larger than the stabilization length — the comoving Jeans scale — is expected to follow predictions of linear CDM theory, in particular the applicability of the linear growth function.

Extending the analysis to the highly nonlinear regime demanded us to formulate a unified numerical method applicable for both reduction models under arbitrary background cosmologies. In this context, numerical challenges associated with the non-autonomous, nonlocal NLSE, especially the explicit time dependence and the nonlinear interaction, were emphasized and possible solutions shown. A combination of exponential operator splitting and Magnus series truncation yielded $\mathcal{SM}^{[2]}$, a second-order, explicit approximation to the full fledged time evolution operator. Appendix B.2 analyses its convergence and stability in detail. Furthermore, Appendix B.1 introduces a promising fourth order scheme for future works.

Investigation of a high-resolution ensemble of cosmological simulations under $(1+1)$-SP revealed a number of interesting physical and systematic effects.

Firstly, as one would expect, Heisenberg's uncertainty principle remains important even under nonlinear evolution and is responsible for a sharp suppression of matter power below a time-dependent spatial scale. By evaluating the velocity dispersion of the FDM matter distribution this scale could be identified and was found to be in good agreement with the large k-behavior of the matter power spectrum.

Secondly, large scale modes grow identically to the CDM prediction for most of the integration time. For small redshifts, however, an unphysical power suppression was observed and its connection to the Heisenberg/de-Broglie scale discussed. On balance, FDM proofs to be extremely demanding in terms of spatial resolution and one typically needs to resolve distances far below the scales of interest to obtain reliable results — an observation which implies significant numerical problems for $d > 1$ simulations. Nevertheless, even if all features are spatially resolved, there is still a significant loss of power which we conjectured to be a result of an insufficient box size and an inappropriate time increment. Further work is required to obtain control over this systematic effect which also showed up in the mode correlation matrix as a phase of de-correlation at small z.

Thirdly, the real-space ensemble evolution indicated the failure of $(1+1)$-SP to realize the most prominent feature of $(3+1)$-SP, i.e. the existence of a asymptotic soliton state. We emphasize a soliton does exist for $(1+1)$-SP but it is not attained under real time evolution neither per realisation nor in a statistical sense.

To understand why $(1+1)$-SP fails to realize a lower dimensional analogue of the $(3+1)$-FDM asymptotic state and how PLAM behaves in this respect a thorough numerical study under simplified conditions, i.e. artificial, cold initial conditions and simplified background cosmologies, was conducted. In this context, adherence to the quantum virial theorem and the maximum entropy principle were discussed as possible relaxation mechanism. Moreover, we extended the formulation of the former to periodic domain conditions.

Irrespective of the considered reduction model or the expansion behavior of the background, we observed the system to maximize the entropy S associated with Husimi's phasespace distribution. Once S is close to saturation no new features emerge in the FDM wave function indicating the arrival in the asymptotic equilibrium state. That said, the attained equilibrium configuration is quite different for (1+1)-SP and PLAM.

In accordance with the aforementioned cosmological simulations $(1+1)$-SP still fails to realize the sought after FDM soliton. Instead, a strongly oscillating halo structure is found with an integrated mass function well described by classical CDM predictions. In contrast, FDM does attain a final soliton state. More precisely, after first collapse one observes FDM to organize into multiple stable solitons which subsequently merge into a single high-mass soliton through multiple soliton-soliton interactions of different mass ratios. Simultaneously, a delocalized radiation field emerges embedding the final soliton.

Inspired by considerations in nonlinear optics, we argued the essentially infinite range of the $(1+1)$-SP interaction kernel to be responsible for the discrepancy in the equilibrium configurations. In general, one can only generate solitons if the range R of the non-local interaction is smaller than the spatial extent of the soliton R_{S}. If this condition is violated, it is not possible for the potential soliton to feel its intricate confining potential due to smoothing behavior of the convolution-type interaction in the NLSE. In fact, we found the condition $R_{\mathrm{S}} > R$ to be violated for all conceivable scenarios under $(1+1)$-SP resulting in "incoherent soliton" dynamics. PLAM, however, satisfies $R_{\mathrm{S}} > R$ for a wide range of periodic domain sizes. Consequently, the system follows "turbulent soliton dynamics" and organizes itself into a final high-mass structure with $R_{\mathrm{S}}/R \approx 3-5$. These findings keep their validity even under flat space FLRW expansion although the thermalization processes cannot be fully completed in the given integration time.

7.2 Future Extensions

Evidently, the physical problem and its numerical treatment, as it was discussed in this thesis, are by no means exhausted and the possibilities for further investigations and optimizations are rather diverse. A short overview is given below.

7.2.1 Next Generation Numerics

As discussed in the cosmological context of chapter 5 but also more abstractly in Appendix B.2 $\mathcal{SM}^{[2]}$, i.e. the approximation of the time evolution operator, struggles to approximate the true evolution under space-time expansion past $z = 10$. Retaining it as integrator means choosing extremely small time increments which quickly becomes intractable especially for large problems. A possible path forward is the application of $\mathcal{BM}^{[4]}$, i.e. the optimized fourth order scheme presented in Appendix B.1. In fact, preliminary results in Appendix B.2 indicate it to be superior compared to $\mathcal{SM}^{[2]}$.

Another interesting extension might be to partially embed a lower order splitting into $\mathcal{BM}^{[4]}$, see [6], therefore gaining access to a cheap error estimate per time step with which the time increment can be adjusted dynamically.

We also note $\mathcal{BM}^{[4]}$ circumvents the difficulties of an explicitly time dependent Hamiltonian by promoting time to an additional *dependent* variable akin to the spatial coordinate. This has to be contrasted with $\mathcal{SM}^{[2]}$'s approach of truncating and approximating the Magnus expansion of the time evolution operator. Although mathematically sound, extensive tests will be required to assess if $\mathcal{BM}^{[4]}$'s simple approach is competitive with higher order approximations of Magnus' expansion. In the light of [14] we conjecture this might not be the case.

Concerning the spatial discretization, the aforementioned high-resolution demand of FDM makes a spatially non-uniform grid almost a necessity. This is especially true if one wants to achieve cosmological scale simulations with $d > 1$ dimensions.

A variety of approaches to achieve non-uniform grids are conceivable. For instance, the seminal work of [67] employed a sophisticated adaptive mesh refinement (AMR) technique.

We already alluded to the possibility of using B-splines in the main text. B-splines constitute finite support polynomials allowing a fast and accurate computation of expansion coefficients by means of gaussian quadrature, see [18]. One then expands the wave function in this localized basis and achieves higher spatial resolution by either increasing the number of basis functions or more importantly stretching and compressing the individual supports of each spline. This can of course be done adaptively throughout the integration. To assess where higher spatial resolution is required [67] employed a refinement technique of the finite element (FEM) approach, [55], and since a B-spline discretization is conceptionally close to FEM we believe the very same approach can also be used.

At last, application of nonuniform FFTs (NUFFTs) is worth mentioning since it (i) requires the least implementational effort, therefore minimizing surface area for potential bugs, and (ii) implements periodic boundary conditions by construction. In fact, the implementation of the present work is essentially compatible with NUFFTs. The only additional work required would be to devise a spatial node placement strategy akin to (or maybe exactly as) [55] for FEM. Also note that FFTs in the present work contribute the most expensive part of the integration step. This stays valid for NUFFTs as well which are typically implemented by a series of uniform FFTs. Since FFTs are a standard problem in scientific computing, off-the-shelf routines exist for shared/distributed memory parallelization or even accelerator cards such as GPUs. That said, the NUFFT approach should also scale to large problems with rather limited effort.

7.2.2 Nonlocal NLSE as Distinct Physical Problem

Although somewhat artificial from a cosmological perspective, the results of this thesis should have made clear that the NLSE with a nonlocal interaction term is an intriguing physical system in its own right and thus worth exploring.

Of particular interest are interaction models which allow for a free adjustment of their interaction range, such as PLAM, and we conjecture to find a dynamical phase transition from the regime of incoherent soliton dynamics to a phase of standard soliton turbulence. Recall only the latter was probed in this work by demanding strong confinement in order to realize an effective $(1+1)$-reduction of FDM.

It might also be worth adding a local nonlinearity $\propto |\psi|^2$ to the Hamiltonian and then study the transition between local and non-local interaction dominance.

From a theoretical point of view it is desirable to understand the thermalization aspect of the long term dynamics. It was remarked before that a statistical theory for the NLSE and a class of *local* interactions already exists. Naturally, one can ask if these arguments can be extended to the nonlocal case as well.

7.2.3 Towards $(3+1)$-FDM — Spherical Symmetry

Obviously the ultimate goal is to conduct cosmological simulations of $(3+1)$-FDM — a formidable task. A first conceptional step is to impose additional symmetries on the $(3+1)$ wave function $\psi(\boldsymbol{x},t)$ and its self-consistent potential $V(\boldsymbol{x},t)$, in particular spherical symmetry, which allows us to implement a $1/r$-interaction with an effectively one dimensional model. The following discussion closely follows the arguments presented in [24].

First note under spherical symmetry only the azimuthal and polar direction are periodic whereas the radial distance should be geometrically unconstrained. Our point of departure is therefore the nonlocal NLSE with the *free space* three dimensional Laplace Green's function on an *unbounded domain*:

$$i\partial_t\psi = \left[-\frac{1}{2}\triangle + a(t)\left(G^{\mathrm{free}}_{\triangle_3} * |\psi|^2\right)\right]\psi\ , \qquad x \in \mathbb{R}^3\ . \tag{7.1}$$

Assuming $\psi(\boldsymbol{x},t) = \psi(r,t)$ and $V(\boldsymbol{x},t) = V(r,t)$ this is *equivalent* to the PDE representation:

$$\begin{aligned} i\partial_t\psi &= \left[-\frac{1}{2r^2}\frac{\partial}{\partial r}\left(r^2\frac{\partial}{\partial r}\right) + a(t)V[|\psi|^2]\right]\psi\ , \\ \frac{1}{r^2}\frac{\partial}{\partial r}\left(r^2\frac{\partial V}{\partial r}\right) &= |\psi|^2\ , \end{aligned} \qquad r \in \mathbb{R}^+\backslash\{0\} \tag{7.2}$$

supplemented with asymptotic boundary conditions:

$$\partial_r\psi(0,t) = \partial_r V(0,t) = 0\ , \quad \lim_{r\to\infty}\psi(r,t) = 0\ , \quad \lim_{r\to\infty} rV(r,t) = \frac{1}{4\pi}\ . \tag{7.3}$$

Here the first two conditions enforce regularity at the origin. We emphasize the radial Poisson equation in eq. (7.2) is well defined without further compatibility conditions. This was not the case under periodic conditions, see discussion around eq. (2.62). Consequently, the normalization of the wave function can be freely chosen.

To transform eq. (7.2) into a more familiar form define:

$$\xi(r,t) = 2\sqrt{\pi}r\psi(r,t)\ , \qquad U(r,t) = 4\pi rV(r,t)\ , \tag{7.4}$$

recasting eq. (7.2) into:

$$\begin{aligned} i\partial_t\xi &= \left[-\frac{1}{2}\partial_r^2 + \frac{a(t)}{4\pi r}U(|\xi|^2)\right]\xi\ , \\ \partial_r^2 U &= \frac{1}{r}|\xi|^2\ , \end{aligned} \qquad r \in \mathbb{R}^+\backslash\{0\} \tag{7.5}$$

alongside:

$$\xi(0,t) = U(0,t) = 0, \quad \lim_{r\to\infty}\xi(r,t) = 0, \quad \lim_{r\to\infty}U(r,t) = 1\ . \tag{7.6}$$

Once eq. (7.5) is solved for ξ and U the original wave function ψ and potential V follow from inversion of eq. (7.4) for $r > 0$ and the first derivative of ξ and U at $r = 0$:

$$\psi(r,t) = \frac{1}{2\sqrt{\pi}}\begin{cases}\frac{\xi(r,t)}{r} & r > 0 \\ \partial_r\xi(r,t) & r = 0\end{cases}, \qquad V(r,t) = \frac{1}{4\pi}\begin{cases}\frac{U(r)}{r,t} & r > 0 \\ \partial_r U(r,t) & r = 0\end{cases}, \tag{7.7}$$

where validity of the second case is readily seen by taking the derivative of eq. (7.4).

For practical purposes eq. (7.5) is truncated on a finite domain $\Omega = (0, R)$ and $r = R$ is interpreted as spatial infinity. Thus the free space conditions in eq. (7.6) become *inhomogeneous* Dirichlet conditions:

$$\xi(0,t) = U(0,t) = 0, \quad \xi(R,t) = 0, \quad U(R,t) = 1 \; . \tag{7.8}$$

From a numerical perspective it is beneficial to work with *homogeneous* Dirichlet boundaries as this allows for a sine-pseudospectral spatial discretization which implements the boundary conditions naturally. Hence, [24] proposes the homogenization:

$$\bar{U}(r,t) = U(r,t) - \frac{r}{R} \; , \qquad r \in \bar{\Omega} \; . \tag{7.9}$$

The radial, truncated, coupled PDE system then takes the form:

$$\begin{aligned} i\partial_t \xi &= \left[-\frac{1}{2}\partial_r^2 + a(t) \left(\frac{1}{4\pi r}\bar{U}(|\xi|^2) + \frac{1}{4\pi R} \right) \right] \xi \; , \\ \partial_r^2 \bar{U} &= \frac{1}{r}|\xi|^2 \qquad \text{with} \end{aligned} \qquad x \in \Omega \tag{7.10}$$

$$\xi(0,t) = U(0,t) = 0, \quad \xi(R,t) = \bar{U}(R,t) = 0 \; . \tag{7.11}$$

For the sake of brevity further informations on the sine-pseudospectral discretization are omitted, see [24].

In principle $\mathcal{SM}^{[2]}$ is directly applicable for integrating eq. (7.10). However, to avoid matter radiation from travelling to $r = R$, potentially inducing reflection artefacts within the integration time, it is customary to add a static but complex absorbing potential $\varphi(r)$ to the Hamiltonian:

$$\begin{aligned} i\partial_t \xi &= \left[-\frac{1}{2}\partial_r^2 + a(t) \left(\frac{1}{4\pi r}\bar{U}(|\xi|^2) + \frac{1}{4\pi R} \right) - \frac{i}{2}\varphi(r) \right] \xi \; , \\ \varphi(r) &= \frac{\Phi}{2} \left[\tanh\left(\frac{1}{\Delta}(r - r_s) \right) + 1 \right] \Theta(r - r_p) \; , \end{aligned} \qquad x \in \Omega \; , \tag{7.12}$$

where the Heaviside function $\Theta(x)$ forbids any matter absorption inside the physical domain $\Omega_p = (0, r_p) \equiv (0, 4/5R)$. r_s denotes the radius at which φ drops to its half-amplitude value $\Phi/2$. We set r_s based on the numerical value of the absorption width Δ, i.e. $r_s = r_p + 5\Delta$.

Back to the modification of $\mathcal{SM}^{[2]}$, in particular the potential subproblem contributing one evolution operator to the splitting method:

$$i\partial_t \xi = \left[a(t) \left(\frac{1}{4\pi r}\bar{U}\left[|\xi|^2\right] + \frac{1}{4\pi R} \right) - \frac{i}{2}\varphi(r) \right] \xi \; . \tag{7.13}$$

Recall for $\Phi = 0$ this equation could be solved *exactly* since $|\xi|^2$ was a conserved quantity. This is not true anymore and we have:

$$\frac{\mathrm{d}}{\mathrm{d}t}|\xi|^2 = -\varphi(x)|\xi|^2 \qquad \Rightarrow \qquad |\xi|^2 = |\xi_0|^2 e^{-\varphi(x)t} \tag{7.14}$$

and

$$\hat{\mathcal{U}}_U(\Delta t) = \exp\left(-i\int_t^{\Delta t} \mathrm{d}t' a(t') \left\{\frac{1}{4\pi r}\bar{U}\left[|\xi(t)|^2 e^{-\varphi(x)t'}\right] + \frac{1}{4\pi R}\right\} - \frac{\varphi(x)}{2}\Delta t\right) \tag{7.15}$$

as first term truncation of the Magnus expansion for the exact operator $\hat{U}_U(\Delta t)$. Following the arguments of section 4.3 this is approximated by the midpoint method:

$$\hat{\mathcal{U}}_U(\Delta t) = \exp\left(-i\Delta t a\left(\frac{t+\Delta t}{2}\right)\left\{\frac{1}{4\pi r}\bar{U}\left[|\xi(t)|^2 e^{-\varphi(x)\frac{t+\Delta t}{2}}\right] + \frac{1}{4\pi R}\right\} - \frac{\Delta t}{2}\varphi(x)\right) \tag{7.16}$$

completing the required modification of $\mathcal{SM}^{[2]}$. Note the exponential attenuation of ξ due to the last term in eq. (7.16).

Clearly, one can now depart for an in depth analysis of the radial model for various initial conditions, parameter choices and expansion models. Here, only preliminary result for static space-time conditions, i.e. $a = 1$, and an ensemble of different gaussians varying in variance and mass are reported.

Figure 7.1 depicts the early evolutionary stages of the same mass and equal variance gaussian used for the (1+1)-SP and PLAM analysis in Figure 6.5 and 6.9 respectively. Around $t = 10$ the initial matter distribution is only slightly perturbed by small scale oscillations traveling outward. This effect magnifies considerably at $t \approx 20$ when a continuous flux of matter has widened the spatial matter distribution up to the absorption region (black). The delocalized distribution is then used by radiation waves as propagation medium. Note Figure 7.1 depicts $r^2|\psi|^2$ to combat the effect of geometrical dilution.

At last, Figure 7.2 investigates the asymptotic state of an ensemble of $\mathcal{N} = 20$ gaussians of different mass and variance. The data reported was obtained by rescaling the final matter densities at $t = 100$ by application of eq. (2.114) to a common peak density at $r = 0$ and subsequently taking the arithmetic mean.

The resulting matter distribution clearly shows a core-halo structure with a core region well described by a $(3+1)$-SP soliton (black, dashed line) and an approximate NFW halo profile $\propto r^{-3}$. In fact, this turns out to be true not just for the entire ensemble but for each individual realisation. The halo distribution shows mid-sized distortions from a perfect power law and we conjecture this is the result of reflection effects at the absorbing potential. More investigation will be required to assess this behavior.

Nevertheless, the preliminary results are satisfactory and in good alignment with the full $(3+1)$-dimensional phenomenology. That said, imposing radial symmetry deprives the system of a potentially important relaxation mechanism, namely the emission of quantum vortices, [60]. These should carry away turbulent kinetic energy and, due to subsequent emission of ever smaller vortices, implement an energy cascade very much like it is known from Kolmogorov's turbulence theory. Allowing the system to form such vortices could potentially decrease the thermalization time. This is especially important for expanding space-time conditions for which the integration time is roughly five times smaller compared to the static scenario investigated in Figure 7.2.

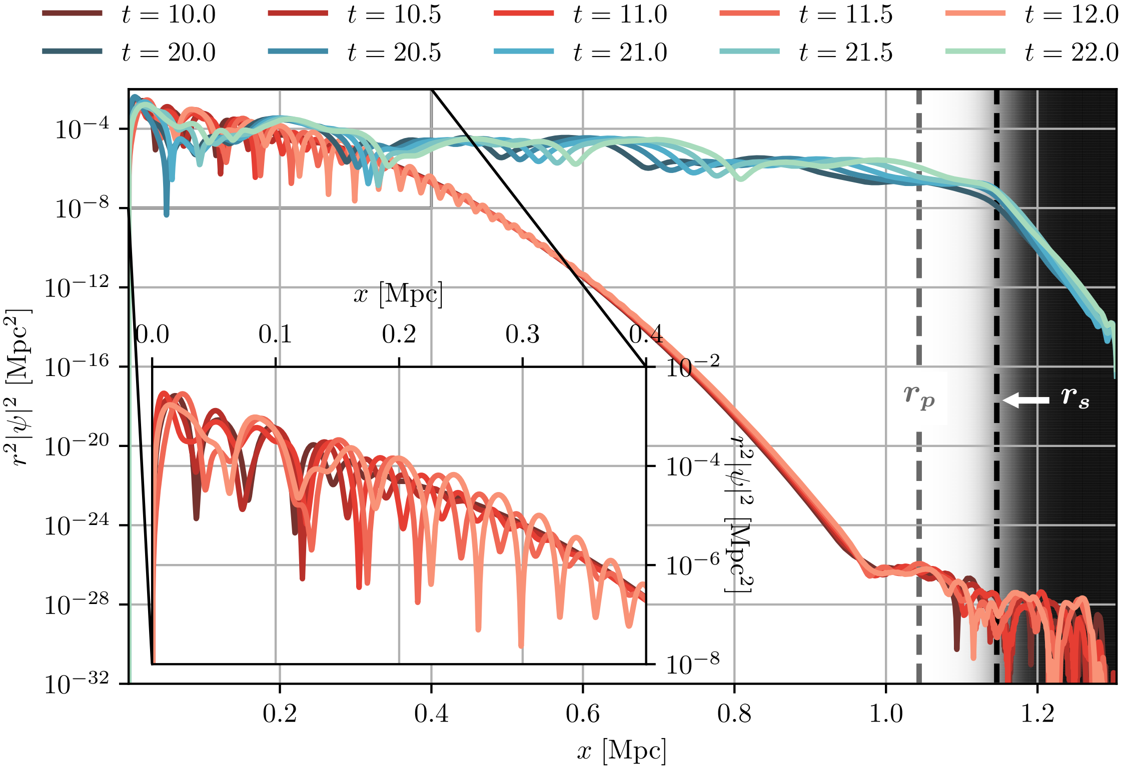

Figure 7.1: Gravitational cooling for the gaussian initial conditions of Figure 6.5 and Figure 6.9. Note how matter waves propagate outward until they experience exponential absorption past r_s.

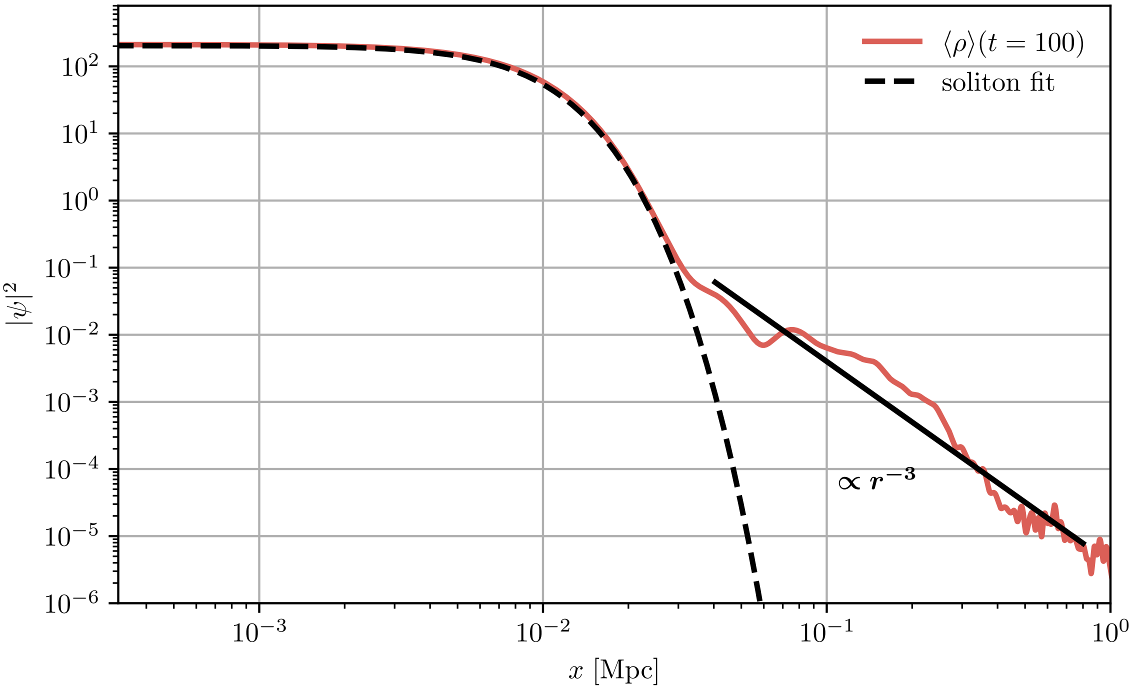

Figure 7.2: Final average density of $\mathcal{N} = 20$ gaussian initial conditions of different masses and widths rescaled by eq. (2.114). The distinct FDM core-halo structure is apparent.

Appendix A

Fuzzy Dark Matter from First Principles

A.1 Derivation of Periodic Greens Functions

We sketch the derivation of the Green's functions (2.76) - (2.78). For more details consult [59]. The starting point is eq. (2.64):

$$G^{\pi}_{\triangle_3}(\boldsymbol{x}, \boldsymbol{x}') = \frac{1}{L_1 L_2 L_3} \sum_{\|\boldsymbol{n}_3\|>0} \frac{-1}{\boldsymbol{k}_3^2} e^{i\boldsymbol{k}_3\cdot(\boldsymbol{x}-\boldsymbol{x}')} \,, \tag{A.1}$$

with $\boldsymbol{n}_3 = (n, m, l)^\intercal \in \mathbb{Z}^3$, $\boldsymbol{k}_3 \in \mathbb{R}^3$, $(k_3)_i = \frac{2\pi}{L_i}(\boldsymbol{n}_3)_i$ and $\Omega = [0, L_1] \times [0, L_2] \times [0, L_3]$. The series excludes $\boldsymbol{n}_3 = (0, 0, 0)^\intercal$. We first note the spectrum is spherical symmetric around $\boldsymbol{k}_3 = 0$. Therefore, expand the exponentials in terms of trigonometric functions, carry out the product and drop all factors involving a sin-function. The last step follows by symmetry if summed over all of $\mathbb{Z}^3$. One finds:

$$\begin{aligned} G^{\pi}_{\triangle_3}(\boldsymbol{x}, \boldsymbol{x}') = \frac{8}{L_1 L_2 L_3} \sum_{n=0}^{\infty}\sum_{m=0}^{\infty}\sum_{l=0}^{\infty} \Bigg\{ & \frac{-\gamma_{nml}}{k_n^2 + k_m^2 + k_l^2} \\ & \times \cos\left(k_n(x_1 - x_1')\right) \cos\left(k_m(x_2 - x_2')\right) \cos\left(k_l(x_3 - x_3')\right) \Bigg\} \end{aligned} \tag{A.2}$$

and

$$\gamma_{nml} = \begin{cases} 0 & n = m = l = 0 \\ \frac{1}{4} & n = m = 0 \lor n = l = 0 \lor m = l = 0 \\ \frac{1}{2} & n = 0 \lor m = 0 \lor l = 0 \\ 1 & \text{otherwise} \end{cases} \,. \tag{A.3}$$

One Dimensional Kernel Set $L_2 = L_3 = 1$ and $m = l = 0$. Eq. (A.2) then reduces to

$$G^{\pi}_{\triangle_1}(x_1, x_1') = \frac{2}{L_1} \sum_{n=1}^{\infty} \frac{-1}{k_n^2} \cos\left(k_n(x_1 - x_1')\right) \,. \tag{A.4}$$

Using the limit, [36]:

$$\sum_{n=1}^{\infty} \frac{\cos nx}{n^2} = \frac{\pi^2}{6} - \frac{\pi|x|}{2} + \frac{x^2}{4} \,, \tag{A.5}$$

with $x = \frac{2\pi}{L_1}(x_1 - x_1')$ one arrives at:

$$G^{\pi}_{\triangle_1}(x_1, x_1') = \frac{1}{2}|x_1 - x_1'| - \frac{1}{2}\left[\frac{(x_1 - x_1')^2}{L_1} + \frac{L_1}{6}\right] \ . \tag{A.6}$$

Two Dimensional Kernel Set $L_3 = 1$ and $l = 0$. Eq. (A.2) then reduces to:

$$G^{\pi}_{\triangle_2}(\boldsymbol{x}_\perp, \boldsymbol{x}_\perp') = \frac{8}{L_1 L_2}\sum_{n=0}^{\infty}\sum_{m=0}^{\infty}\frac{-\gamma_{nm0}}{k_n^2 + k_m^2}\cos\left(k_n(x_1 - x_1')\right)\cos\left(k_m(x_2 - x_2')\right) \ , \tag{A.7}$$

where $\boldsymbol{x}_\perp = (x_1, x_2, 0)^\intercal$. Now, split the double series into a contribution with $m = 0$ and a remainder series, use the definition of γ_{nm0} and exploit symmetry to arrive at:

$$\begin{aligned} G^{\pi}_{\triangle_2}(\boldsymbol{x}_\perp, \boldsymbol{x}_\perp') = &\frac{2}{L_1 L_2}\sum_{n=1}^{\infty}\frac{-1}{k_n^2}\cos\left(k_n(x_1 - x_1')\right) \\ &- \frac{2}{L_1 L_2}\sum_{m=1}^{\infty}\cos\left(k_m(x_2 - x_2')\right)\sum_{n\in\mathbb{Z}}\frac{1}{k_n^2 + k_m^2}\cos\left(k_n(x_1 - x_1')\right) \end{aligned} \tag{A.8}$$

$$\begin{aligned} = &\frac{1}{L_2}G^{\pi}_{\triangle_1}(x_1, x_1') \\ &- \frac{2}{L_1 L_2}\sum_{m=1}^{\infty}\cos\left(k_m(x_2 - x_2')\right)\sum_{n\in\mathbb{Z}}\frac{1}{k_n^2 + k_m^2}\cos\left(k_n(x_1 - x_1')\right) \end{aligned} \ . \tag{A.9}$$

Recall for functions $f : \mathbb{R} \to \mathbb{R}$ which are sufficiently smooth and decay quickly, e.g $\lim_{x\to\infty}(1 + x)^2\left(|f''(x)| + |f'(x)|\right) = 0$, *Poisson's summation formula* (PSF) is applicable. For *symmetric* $f(t)$ the PSF reads:

$$\sum_{n\in\mathbb{Z}} f(n)\cos(Tn) = \sum_{N\in\mathbb{Z}}\int_{-\infty}^{\infty}\mathrm{d}t f(t)\cos(t(2\pi N + T)) \ . \tag{A.10}$$

The inner series over $\mathbb{Z}$ in eq. (A.9) can be recast into this form if one sets:

$$T = \frac{2\pi}{L_1}(x_1 - x_1') \quad \text{and} \quad f(t) = \frac{L_1^2}{2\pi^2}\frac{1}{\left(\frac{L_1}{L_2}m\right)^2 + t^2} \ . \tag{A.11}$$

Moreover, it holds:

$$\int_{-\infty}^{\infty}\mathrm{d}t\frac{\cos(ta)}{b^2 + t^2} = \frac{\pi}{b}e^{-b|a|} \ , \tag{A.12}$$

so that with $a = 2\pi N + T$ and $b = \frac{L_1}{L_2}m$ the series takes the form:

$$\sum_{n\in\mathbb{Z}}\frac{1}{k_n^2 + k_m^2}\cos\left(k_n(x_1 - x_1')\right) = \frac{L_1 L_2}{4\pi m}\sum_{N\in\mathbb{Z}} e^{-k_m|NL_1 + x_1 - x_1'|} \tag{A.13}$$

and consequently:

$$G^{\pi}_{\triangle_2}(\boldsymbol{x}_\perp, \boldsymbol{x}_\perp') = \frac{1}{L_2}G^{\pi}_{\triangle_1}(x_1, x_1') - \frac{1}{2\pi}\sum_{n\in\mathbb{Z}}\sum_{m=1}^{\infty}\frac{e^{-k_m|NL_1 + x_1 - x_1'|}}{m}\cos\left(k_m(x_2 - x_2')\right) \ . \tag{A.14}$$

Now recall the series expansion of the complex, natural logarithm and take its real part:

$$\mathrm{Re}\left[\log(1-z)\right] \overset{|z|<1}{=} -\sum_{m=1}^{\infty}\frac{\mathrm{Re}\left[z^m\right]}{m} = -\sum_{m=1}^{\infty}\frac{|z|^m}{m}\cos\left(m\mathrm{Arg}[z]\right)\ . \tag{A.15}$$

By identification with eq. (A.14), it must hold:

$$|z| = e^{-\frac{2\pi}{L_2}|NL_1+x_1-x_1'|} < 1, \qquad \mathrm{Arg}[z] = \frac{2\pi}{L_2}(x_2-x_2')\ . \tag{A.16}$$

On the other hand:

$$\mathrm{Re}\left[\log(1-z)\right] = \frac{1}{2}\left[\log(1-z)+\log(1-z^*)\right] = \frac{1}{2}\log\left(1-2\mathrm{Re}[z]+|z|^2\right)\ . \tag{A.17}$$

Collecting these results and inserting them into eq. (A.14) yields:

$$\begin{aligned} G^{\pi}_{\triangle_2}(\boldsymbol{x}_\perp,\boldsymbol{x}'_\perp) &= \frac{1}{L_2}G^{\pi}_{\triangle_1}(x_1,x_1') \\ &\quad + \frac{1}{4\pi}\sum_{N\in\mathbb{Z}}\log\Bigg(1-2e^{-\frac{2\pi}{L_2}\left|NL_1+x_1-x_1'\right|}\cos\left(\frac{2\pi}{L_2}(x_2-x_2')\right) \\ &\qquad + e^{-\frac{4\pi}{L_2}\left|NL_1+x_1-x_1'\right|}\Bigg)\ . \end{aligned} \tag{A.18}$$

Three Dimensional Kernel No initial simplifications are possible for $d=3$ and we need to work with eq. (A.2) directly. In analogy with the treatment for $d=2$, split the l-sum into a $l=0$ and $l>0$ contribution, use γ_{nml} as well as the symmetry of the spectrum in the remainder series to extend the latter over all of $\mathbb{Z}$:

$$\begin{aligned} G^{\pi}_{\triangle_3}(\boldsymbol{x},\boldsymbol{x}') = \frac{8}{L_1L_2L_3}\sum_{n=0}^{\infty}\sum_{m=0}^{\infty}\sum_{l=0}^{\infty}\Bigg\{&\frac{-\gamma_{nml}}{k_n^2+k_m^2+k_l^2} \\ &\times\cos\left(k_n(x_1-x_1')\right)\cos\left(k_m(x_2-x_2')\right)\cos\left(k_l(x_3-x_3')\right)\Bigg\} \end{aligned} \tag{A.19}$$

$$\begin{aligned} = \frac{1}{L_3}G^{\pi}_{\triangle_2}(\boldsymbol{x}_\perp,\boldsymbol{x}'_\perp) - \frac{2}{L_1L_2L_3}\sum_{l=1}^{\infty}\cos\left(k_l(x_3-x_3')\right)\Bigg\{& \\ \times\sum_{m\in\mathbb{Z}}\cos\left(k_m(x_2-x_2')\right)\sum_{n\in\mathbb{Z}}\frac{1}{k_n^2+k_m^2+k_l^2}\cos\left(k_n(x_1-x_1')\right)&\Bigg\}\ . \end{aligned} \tag{A.20}$$

Applying the PSF, eq. (A.10), to the innermost series and carrying out the same integral already found for $d=2$ yields:

$$\sum_{n\in\mathbb{Z}}\frac{1}{k_n^2+k_m^2+k_l^2}\cos\left(k_n(x_1-x_1')\right) = \frac{L_1}{2}\sum_{N\in\mathbb{Z}}\frac{e^{-|NL_1+x-x'|\sqrt{k_l^2+k_m^2}}}{\sqrt{k_l^2+k_m^2}}\ . \tag{A.21}$$

The bracket term in eq. (A.20) becomes:

$$\begin{aligned}&\sum_{m\in\mathbb{Z}}\cos\left(k_m(x_2-x_2')\right)\sum_{n\in\mathbb{Z}}\frac{1}{k_n^2+k_m^2+k_l^2}\cos\left(k_n(x_1-x_1')\right)\\&=\frac{L_1}{2}\sum_{m\in\mathbb{Z}}\cos\left(k_m(x_2-x_2')\right)\sum_{N\in\mathbb{Z}}\frac{e^{-|NL_1+x-x'|\sqrt{k_l^2+k_m^2}}}{\sqrt{k_l^2+k_m^2}}\,,\end{aligned}\tag{A.22}$$

which is yet again of PSF-type — this time however with:

$$T=\frac{2\pi}{L_2}(x_2-x_2')\quad\text{and}\quad f(t)=\frac{L_2}{2\pi}\sum_{N\in\mathbb{Z}}\frac{\exp\left(-\frac{2\pi}{L_2}|NL_1+x-x'|\sqrt{\left(\frac{L_2}{L_3}l\right)^2+t^2}\right)}{\sqrt{\left(\frac{L_2}{L_3}l\right)^2+t^2}}\,.\tag{A.23}$$

That said, eq. (A.22) is recast into:

$$\begin{aligned}&\frac{L_1}{2}\sum_{m\in\mathbb{Z}}\cos\left(k_m(x_2-x_2')\right)\sum_{N\in\mathbb{Z}}\frac{e^{-|NL_1+x-x'|\sqrt{k_l^2+k_m^2}}}{\sqrt{k_l^2+k_m^2}}\\&=\frac{L_1L_2}{4\pi}\sum_{N\in\mathbb{Z}}\sum_{M\in\mathbb{Z}}\int_{-\infty}^{\infty}\mathrm{d}t\frac{e^{-B\sqrt{A^2+t^2}}}{\sqrt{A^2+t^2}}\cos\left(tC(M)\right)\end{aligned}\tag{A.24}$$

with:

$$A=\frac{L_2}{L_3}l,\quad B=\frac{2\pi}{L_2}|NL_1+x-x'|,\quad C(M)=2\pi M+T\,.\tag{A.25}$$

The remaining integral is solved by, [36]:

$$\int_{-\infty}^{\infty}\mathrm{d}t\frac{e^{-B\sqrt{A^2+t^2}}}{\sqrt{A^2+t^2}}\cos\left(tC(M)\right)=2K_0\left(A\sqrt{B^2+C(M)^2}\right)\,.\tag{A.26}$$

Collecting results and plugging everything into eq. (A.20) completes the derivation for the $d=3$ Laplace kernel:

$$\begin{aligned}G^{\pi}_{\triangle_3}(\boldsymbol{x},\boldsymbol{x}')=\frac{1}{L_3}G^{\pi}_{\triangle_2}(\boldsymbol{x}_\perp,\boldsymbol{x}'_\perp)-\frac{1}{\pi L_3}\sum_{k=1}^{\infty}\Bigg\{&\cos\left(\frac{2\pi}{L_3}(x_3-x_3')\right)\\\times\sum_{M,N\in\mathbb{Z}}&K_0\left(\frac{2\pi}{L_3}l\sqrt{(NL_1+x_1-x_1')^2+(ML_2+x_2-x_2')^2}\right)\Bigg\}\,.\end{aligned}\tag{A.27}$$

A.2 Momentum Conservation of $(1+1)$ Fuzzy Dark Matter

The task is to show

$$\frac{\mathrm{d}}{\mathrm{d}t}P(t)\equiv\frac{\mathrm{d}}{\mathrm{d}t}\left(\mathrm{Im}\int_\Omega\mathrm{d}x\psi^*\partial_x\psi\right)=0\,.\tag{A.28}$$

We start from eq. (2.107), multiply by $x\partial_x\psi^*$, integrate over the periodic domain and take the imaginary part. This yields:

$$\overbrace{\mathrm{Im}\left(\int_\Omega \mathrm{d}x\partial_t\psi\partial_x\psi^*\right)}^{I_1} - \mathrm{Im}\left(\overbrace{\frac{i}{2}\int_\Omega \mathrm{d}x\partial_x^2\psi\partial_x\psi^*}^{I_2}\right) \\ + \underbrace{\mathrm{Im}\left(ia(t)\int_\Omega \mathrm{d}x(U^\pi * |\psi|^2)\partial_x\psi^*\psi\right)}_{I_3} = 0 \ . \tag{A.29}$$

Consider the second integral first. By partial integration we have:

$$I_2 = \frac{i}{2}\int_\Omega \mathrm{d}x\partial_x^2\psi\partial_x\psi^* = \underbrace{\frac{i}{2}\partial_x\psi\partial_x\psi^*\Big|_0^L}_{=0 \text{ (PBC)}} - \frac{i}{2}\int_\Omega \mathrm{d}x\partial_x\psi\partial_x^2\psi^* \ . \tag{A.30}$$

The left hand side is the complex conjugate of the right hand side, hence it is real and taking the imaginary part makes it vanish.

Now, investigate the third integral:

$$\begin{aligned} I_3 &= \mathrm{Im}\left(ia(t)\int_\Omega \mathrm{d}x(U^\pi * |\psi|^2)\partial_x\psi^*\psi\right) \\ &= \mathrm{Re}\left(a(t)\int_\Omega \mathrm{d}x(U^\pi * |\psi|^2)\partial_x\psi^*\psi\right) \\ &= \frac{a(t)}{2}\int_\Omega \mathrm{d}x\partial_x\left(|\psi|^2\right)\int_\Omega \mathrm{d}x' U^\pi(|x-x'|)|\psi(x')|^2 \ . \end{aligned} \tag{A.31}$$

Use the product rule the express the integrand as an overall derivative plus a correction term:

$$\partial_x\left(|\psi|^2\right)\int_\Omega \mathrm{d}x' U^\pi(|x-x'|)|\psi(x')|^2 = \partial_x\left(|\psi|^2\int_\Omega \mathrm{d}x' U^\pi(|x-x'|)|\psi(x')|^2\right) \\ - |\psi|^2\int_\Omega \mathrm{d}x' U^\pi(|x-x'|)\partial'_x\left(|\psi(x')|^2\right) \ . \tag{A.32}$$

To arrive at this result, we used the convolution property $\partial_x(f*g) = \partial_x f * g = f * \partial_x g$.

Substitute eq. (A.32) into eq. (A.31). The first term then vanishes due to periodic boundary conditions. What remains is:

$$I_3 = -\frac{a(t)}{2}\int_\Omega \mathrm{d}x|\psi(x)|^2\int_\Omega \mathrm{d}x' U^\pi(|x-x'|)\partial'_x\left(|\psi(x')|^2\right) \ . \tag{A.33}$$

Swap the integration order and use the symmetry of the interaction kernel:

$$\begin{aligned} I_3 &= -\frac{a(t)}{2}\int_\Omega \mathrm{d}x'\partial'_x\left(|\psi(x')|^2\right)\int_\Omega \mathrm{d}x U^\pi(|x-x'|)|\psi(x)|^2 \\ &= -\frac{a(t)}{2}\int_\Omega \mathrm{d}x'\partial'_x\left(|\psi(x')|^2\right)\int_\Omega \mathrm{d}x U^\pi(|x'-x|)|\psi(x)|^2 \\ &= -I_3 \ . \end{aligned} \tag{A.34}$$

We conclude the third integral is zero as well. At last, dissect I_1:

$$\mathrm{Im}\left(\int_\Omega \mathrm{d}x \partial_t\psi\partial_x\psi^*\right) = \frac{\mathrm{d}}{\mathrm{d}t}P(t) - \underbrace{\mathrm{Im}\left(\int_\Omega \mathrm{d}x\psi\partial_t\partial_x\psi^*\right)}_{I_4} \ . \tag{A.35}$$

What remains to be shown is $I_4 = 0$. For this we insert the NLSE (2.107) to find:

$$I_4 = -\frac{1}{2}\mathrm{Re}\left(\int_\Omega \mathrm{d}x\psi\partial_x^3\psi^*\right) + I_3 = -\frac{1}{2}\mathrm{Re}\left(\int_\Omega \mathrm{d}x\psi\partial_x^3\psi^*\right) \ . \tag{A.36}$$

Performing three successive partial integration on the remaining integral term reveals $I_4 = -I_4$ which concludes the proof.

A.3 Scaling Symmetry

We aim to proof the scaling symmetry,

$$\widetilde{\psi}(\boldsymbol{x}, t) = \lambda^2\psi(\lambda\boldsymbol{x}, \lambda^2 t) \quad \lambda \in \mathbb{R}^+, \tag{A.37}$$

of the NLSE,

$$i\partial_t\psi = \left[-\frac{1}{2}\triangle_d + a\left(G^{\pi/\mathrm{free}}_{\triangle_d} * |\psi|^2\right)\right]\psi \quad \boldsymbol{x} \in \Omega, \tag{A.38}$$

for Poisson interactions (2.76) - (2.80) and (2.82).

The left-hand side of eq. (2.75) and the kinetic part of the Hamiltonian are trivial to transform:

$$i\partial_t\left(\lambda^2\psi(\lambda\boldsymbol{x}, \lambda^2 t)\right) = \lambda^4 \cdot i\partial_{\tilde{t}}\psi(\tilde{\boldsymbol{x}}, \tilde{t}) \tag{A.39}$$

$$-\frac{1}{2}\triangle_d\left(\lambda^2\psi(\lambda\boldsymbol{x}, \lambda^2 t)\right) = -\lambda^4 \cdot \frac{1}{2}\tilde{\triangle}_d\psi(\tilde{\boldsymbol{x}}, \tilde{t}) \tag{A.40}$$

with $\tilde{t} = \lambda^2 t$, $\tilde{\boldsymbol{x}} = \lambda\boldsymbol{x}$ and $\tilde{\triangle}_d = \partial_{\tilde{x}_i}\partial^{\tilde{x}_i}$. For the d-dimensional convolution term, we first have in general:

$$\begin{aligned}\left(G^{\pi/\mathrm{free}}_{\triangle_d} * |\tilde{\psi}|^2\right)\tilde{\psi} &= \lambda^6\psi(\tilde{\boldsymbol{x}}, \tilde{t})\int_{\frac{\Omega_d}{\lambda}/\mathbb{R}^d} \mathrm{d}^d x' G^{\pi/\mathrm{free}}_{\triangle_d}(\boldsymbol{x}, \boldsymbol{x}')|\psi(\lambda\boldsymbol{x}')|^2 \\ &= \lambda^{6-d}\psi(\tilde{\boldsymbol{x}}, \tilde{t})\int_{\Omega_d/\mathbb{R}^d} \mathrm{d}^d x'' G^{\pi/\mathrm{free}}_{\triangle_d}\left(\boldsymbol{x}, \frac{\boldsymbol{x}''}{\lambda}\right)|\psi(\boldsymbol{x}'')|^2 \ .\end{aligned} \tag{A.41}$$

What remains to be shown is:

$$G^{\pi/\mathrm{free}}_{\triangle_d}\left(\boldsymbol{x}, \frac{\boldsymbol{x}''}{\lambda}\right) = \lambda^{d-2}G^{\pi/\mathrm{free}}_{\triangle_d}(\lambda\boldsymbol{x}, \boldsymbol{x}'') \ , \tag{A.42}$$

so that

$$\left(G^{\pi/\mathrm{free}}_{\triangle_d} * |\tilde{\psi}|^2\right)\tilde{\psi} = \lambda^4 \cdot \left(G^{\pi/\mathrm{free}}_{\triangle_d} * |\psi|^2\right)(\tilde{\boldsymbol{x}})\psi(\tilde{\boldsymbol{x}}, \tilde{t}) \ . \tag{A.43}$$

It is trivial to see this is true for free space kernels in $d = 1, 3$. In $d = 2$ we have:

$$G^{\mathrm{free}}_{\triangle_2}\left(\boldsymbol{x}, \frac{\boldsymbol{x}''}{\lambda}\right) = \frac{1}{2\pi}\log\left(\left|\boldsymbol{x} - \frac{\boldsymbol{x}''}{\lambda}\right|\right) = \frac{1}{2\pi}\log(|\lambda\boldsymbol{x} - \boldsymbol{x}''|) - \frac{1}{2\pi}\log(\lambda) \ . \tag{A.44}$$

The second term is a physically irrelevant offset which can be dropped. The first term is in the required form to satisfy the symmetry.

For periodic conditions we note in addition to eq. (A.37) one must also rescale the domain according to $\tilde{L}_i = L_i/\lambda$ to assure periodicity of $\tilde{\psi}$ on $\tilde{\Omega}_i = [0, \tilde{L}_1] \times \cdots \times [0, \tilde{L}_i]$. Substituting this new domain size in the kernel expressions (2.76) - (2.78) yields the validity of eq. (A.42) by direct computation.

Appendix B

Numerical Considerations

B.1 An Augmented Fourth Order Scheme

We give additional information on how method coefficients are obtained and discuss a higher order splitting scheme put forward by [15]. Assume the autonomous situation of section 4.3.1 and recall the form of a general s-stage splitting:

$$\begin{aligned}\hat{U}_{K+V}(\Delta t) &= \hat{\mathcal{U}}_{K+V}(\Delta t) + \mathcal{O}(\Delta t^{p+1}) \\ &\equiv \hat{U}_K(b_{s+1}\Delta t) \circ \hat{U}_V(a_s\Delta t) \circ \hat{U}_K(b_s\Delta t) \\ &\qquad \circ \cdots \circ \hat{U}_K(b_2\Delta t) \circ \hat{U}_V(a_1\Delta t) \circ \hat{U}_K(b_1\Delta t) + \mathcal{O}(\Delta t^{p+1}) \ ,\end{aligned} \tag{B.1}$$

with splitting coefficients $\{a_i\}_{i=1,\ldots,s}$ and $\{b_i\}_{i=1,\ldots,s+1}$ and $\circ$ as composition operation. The procedure of obtaining a methods coefficients, [27, 72], is somewhat technical and employs the formal calculus of *Lie derivatives* and *Lie transformations*. This is necessary because of the nonlinear nature of $\hat{U}_V$. In a nutshell, one can associate exponentials of differential operators with both the true evolution operator $\hat{U}_{K+V}$ and its approximation $\hat{\mathcal{U}}_{K+V}$:

$$\hat{U}_{K+V}(\Delta t) = e^{\Delta t L_{K+V}} = e^{\Delta t (L_K + L_V)} \tag{B.2}$$

$$\hat{\mathcal{U}}_{K+V}(\Delta t) = e^{b_1 \Delta t L_K} e^{a_1 \Delta t L_V} \ldots e^{a_s \Delta t L_K} e^{b_{s+1} \Delta t L_V} \ , \tag{B.3}$$

where $L_{K/V}$ denotes the Lie derivative of the time dependent vector field $\hat{H}_K \mathbf{\Psi}(t)$ and $\hat{H}_V\left[\mathbf{\Psi}(t)\right]$ respectively. Note the reversal of the coefficients in eq. (B.3) compared to eq. (B.1). Understanding how $L_{K/V}$ is defined and how it behaves is not essential at this point.

The idea is then to iteratively apply the BCH-formula to the right hand side of eq. (B.3) to arrive at an operator $e^{F(\Delta t)}$ which can be compared with the right hand side of eq. (B.2). For instance, for a $s = 2$ stage method one finds up to second order in Δt:

$$F(\Delta t) = \Delta t \left(p_1(a_i) L_V + p_2(b_i) L_K\right) + \Delta t^2 p_3(a_i, b_i)[L_V, L_K] + \mathcal{O}(\Delta t^3) \ , \tag{B.4}$$

with polynomials:

$$p_1(a_1) = a_1, \quad p_2(b_1, b_2) = b_1 + b_2 \quad p_3(a_1, b_1, b_2) = \frac{1}{2} p_1(a_1) p_2(b_1, b_2) - b_1 a_1 \ . \tag{B.5}$$

From comparison with eq. (B.2) we get:

$$p_1 = p_2 = 1, \quad p_3 = 0 \qquad \Rightarrow \qquad b_1 = b_2 = \frac{1}{2} \quad \text{and} \quad a_1 = 1\ , \tag{B.6}$$

which the reader will recognize as the method coefficients of Strang's splitting $\mathcal{S}^{[2]}$.

This exemplifies the general procedure: Expand the combined s-stage BCH-exponent up to order $p+1$ and solve a system of polynomial equations, the so called order conditions, to obtain the method coefficient.

Contrary to the case of $\mathcal{S}^{[2]}$, it is of course possible to have $s > p$. One then arrives at a overdetermined system of equations and consequently a solution space of the polynomial equations with dimension $d > 1$. Probing this space for optimal coefficients that minimize the leading error term is a non-trivial task. The authors of [15] conducted such an analysis in a systematic way and found the coefficients of a 6-stage-4th-order method which we denote $\mathcal{BM}^{[4]}$. It is defined in Table B.1.

$\hat{\mathcal{U}}$	splitting coefficients	
$\mathcal{S}^{[2]}$	$a_1 = 1$	$b_1 = b_2 = 0.5$
$\mathcal{BM}^{[4]}$	$a_1 = a_6 = 0.209515106613361891$	$b_1 = b_7 = 0.0792036964311954608$
	$a_2 = a_5 = -0.143851773179818077$	$b_2 = b_6 = 0.353172906049773948$
	$a_3 = a_4 = 0.434336666566456186$	$b_3 = b_5 = -0.0420650803577191948$
		$b_4 = 0.219376955753499572$

Table B.1: Splitting coefficients of the integrators $\mathcal{S}^{[2]}$ and $\mathcal{BM}^{[4]}$.

As in the case of $\mathcal{S}^{[2]}$, the integrator $\mathcal{BM}^{[4]}$ is time-symmetric, unitary and satisfies the FSAL property.

Extending $\mathcal{BM}^{[4]}$ to the non-autonomous situation appears problematic at first sight because retaining order $p = 4$ would require taking Magnus up to higher order *and* solving the remaining integrals up to order $p = 4$. Higher oder terms contain nested commutators, increasing the complexity of the problem considerably. Fortunately, there is a trick, [66], to circumvent the explicit time dependence in eq. (4.33) all together. For this we go back to the unsplitted problem (4.21) and augment it by an auxiliary dependent variable τ:

$$\partial_t \begin{pmatrix} i\mathbf{\Psi}(t) \\ \tau \end{pmatrix} = \begin{pmatrix} \left[\hat{H}_K + \hat{H}_V(\tau)\right] \mathbf{\Psi}(t) \\ 1 \end{pmatrix} . \tag{B.7}$$

Clearly, because $\frac{\mathrm{d}\tau}{\mathrm{d}t} = 1 \Rightarrow \tau = t$, eq. (B.7) is *equivalent* to eq. (4.21). Now separate eq. (B.7) as:

$$\partial_t \begin{pmatrix} i\mathbf{\Psi}(t) \\ \tau \end{pmatrix} = \begin{pmatrix} \hat{H}_K \mathbf{\Psi}(t) \\ 1 \end{pmatrix} + \begin{pmatrix} \hat{H}_V(\tau)\mathbf{\Psi}(t) \\ 0 \end{pmatrix} \tag{B.8}$$

and subsequently consider each subproblem individually, i.e.:

$$\partial_t \begin{pmatrix} i\mathbf{\Psi}(t) \\ \tau \end{pmatrix} = \begin{pmatrix} \hat{H}_K \mathbf{\Psi}(t) \\ 1 \end{pmatrix} \tag{B.9}$$

$$\partial_t \begin{pmatrix} i\mathbf{\Psi}(t) \\ \tau \end{pmatrix} = \begin{pmatrix} \hat{H}_V(\tau)\mathbf{\Psi}(t) \\ 0 \end{pmatrix} \tag{B.10}$$

It is clear that τ *does not change* in the potential subproblem. In this formulation τ is to be understood as a parameter set by the evolution of the kinetic problem only. Moreover, its evolution $\tau(t) = t$ is trivial.

Let $\hat{U}_V(\Delta t; \tau)$ denote the evolution operator which depends parametrically on τ and in accordance with eq. (4.29) reads:

$$\hat{U}_V(\Delta t, \tau) = \exp\left(-ia(\tau)\boldsymbol{V}(|\boldsymbol{\Psi}(t_0)|^2)\Delta t\right) \ . \tag{B.11}$$

The $\mathcal{BM}^{[4]}$ splitting of the augmented problem (B.7) then takes the form:

$$\begin{aligned}\mathcal{BM}^{[4]} = \hat{U}_K(b_7\Delta t) \circ \hat{U}_V\left(a_6\Delta t; \Delta t \sum_{i=1}^{6} b_i\right) \circ \hat{U}_K(b_6\Delta t) \\ \circ \cdots \circ \hat{U}_K(b_2\Delta t) \circ \hat{U}_V(a_1\Delta t; b_1\Delta t) \circ \hat{U}_K(b_1\Delta t) + \mathcal{O}(\Delta t^5) \ .\end{aligned} \tag{B.12}$$

Notice how we eliminated the auxiliary variable τ by propagating it through all application of $U_K(\Delta t)$. In practice this means the scale factor at stage k is evaluated at $a\left(t_0 + \Delta t \sum_{i=1}^{k} b_i\right)$.

This concludes the extension to the non-autonomous case and *no additional work is done* for the extension of $\mathcal{BM}^{[4]}$.

B.2 Convergence Analysis

This section provides a detailed analysis of the convergence and stability properties of $\mathcal{SM}^{[2]}$. Preliminary results for $\mathcal{BM}^{[4]}$ introduced in section B.1 are also shown.

The range of imaginable scenarios to investigate is vast. We limit the scope of the discussion in multiple respects:

Firstly, we focus on static, $a = 1$, and dynamic expansion models. For the latter we demand $1 = \Omega_m + \Omega_\Lambda$ with $\Omega_m = 0.3$. Dynamic studies are started at $z = 100$ and integrated until present time.

Secondly, only *artificial, spatially localized* initial conditions are examined. Equivalent tests were conducted for spectrally localized conditions and the results are identical to what is presented in the following. Specifically, we set:

$$\psi_0(x) = \sqrt{\mathcal{N}} e^{-\frac{x^2}{4\sigma^2}} \tag{B.13}$$

and enforce "periodicity" via $L = 30\sigma$ so that the initial wave function decays down to 10^{-30} at the boundaries. The normalization constant $\mathcal{N}$ follows numerically from:

$$L = \mathcal{N}\Delta x \sum_{n=0}^{N-1} |\psi_{0,n}|^2 \ . \tag{B.14}$$

What remains is the standard deviation σ. In the unit convention (2.52) the critical Jeans scale is:

$$\lambda_{\text{Jeans}}(z) = \sqrt{2}\pi(1+z)^{1/4} \tag{B.15}$$

and we set σ so that the initial spectrum is unstable withing the 1σ-interval at $z = 100$:

$$\sigma = \frac{\lambda_{\text{Jeans}}(100)}{2\pi} > \frac{\lambda_{\text{Jeans}}(0)}{2\pi} \,. \tag{B.16}$$

Thus we only consider a gravitationally unstable scenarios.

Since no analytic solution is available, the convergence study is performed self-consistently, i.e. we integrate a reference solution on a fine spatio-temporal grid $\{N_{\text{ref}}, \Delta t_{\text{ref}}\}$ and accept it tacitly as correct. In run i, we increase N_{ref} and Δt_{ref} by constant factors and compare ψ_i with ψ_{ref}. To this end, we measure the numerical error ϵ_i^j at time t_j by the approximating the continuous L_2-norm:

$$\epsilon_i^j = \frac{\left\|\psi^j_{\text{ref}} - \psi^j_i\right\|_2}{\left\|\psi^j_{\text{ref}}\right\|_2} = \frac{N_{\text{ref}}}{N_i} \sum_{n=0}^{N_i-1} \left\|\psi^j_{\text{ref}}(x_k) - \psi^j_{k,i}\right\|_2 \,. \tag{B.17}$$

To get the wave function value of the reference solution at the coarse grained grid sites x_k a downsampling is performed:

$$\psi^j_{\text{ref}}(x_k) \sum_{n=-N/2}^{N/2-1} \widetilde{\psi^j_{\text{ref}n}} e^{ik_n x_k} \,. \tag{B.18}$$

B.2.1 Dominance of the Temporal Error

We chose $N_{\text{ref}} = 2^{18} = 262144$ and $\Delta t_{\text{ref}} = 10^{-5}$ and only present results for (1+1)-SP.

Figure B.1 and B.2 illustrate the numerical error ϵ as a function of the spatio-temporal grid parameters in a static and dynamic expansion scenario. For a cross section at $\Delta t = 10^{-5}$ (the green line in Figure B.1 and B.2) consult Figure B.3.

Apart from $N = 512$, the results show uniformity of ϵ in the number of spatial grid points. The distinctive behavior of $N = 512$ is not due to a non-convergent integration but arises because the Fourier basis is not large enough to capture the entire spectrum. Initial conditions set by eq. (B.16) are extremely unstable at $a = 1$. Collapse and mode-coupling set in immediately and considerable spectral power is already transported past $k_{\max} = \frac{512\pi}{L}$ at $t = 1$. This explains the discrepancy to ψ_{ref} which easily resolves these spectral features due to its larger Fourier basis. The collapse is less violent for dynamic $a(t)$ and no significant power is transported past $k_{\max}$.

Concerning convergence, we conclude there is no numerical constraint on the value of N — at least in the patch of the parameter space probed here.

B.2.2 Behavior of the Temporal Error

In the light of section B.2.1, we specialize to a single spatial with grid $N = 8192$ small enough to allow the integration of a reference solution with $\Delta t_{\text{ref}} = 10^{-6}$ in reasonable time.

Figure B.4 illustrates the error scaling as a function of Δt for both reduction models under static space time conditions. The quadratic scaling $\epsilon \propto \Delta t$ is apparent and is in alignment with our expectation.

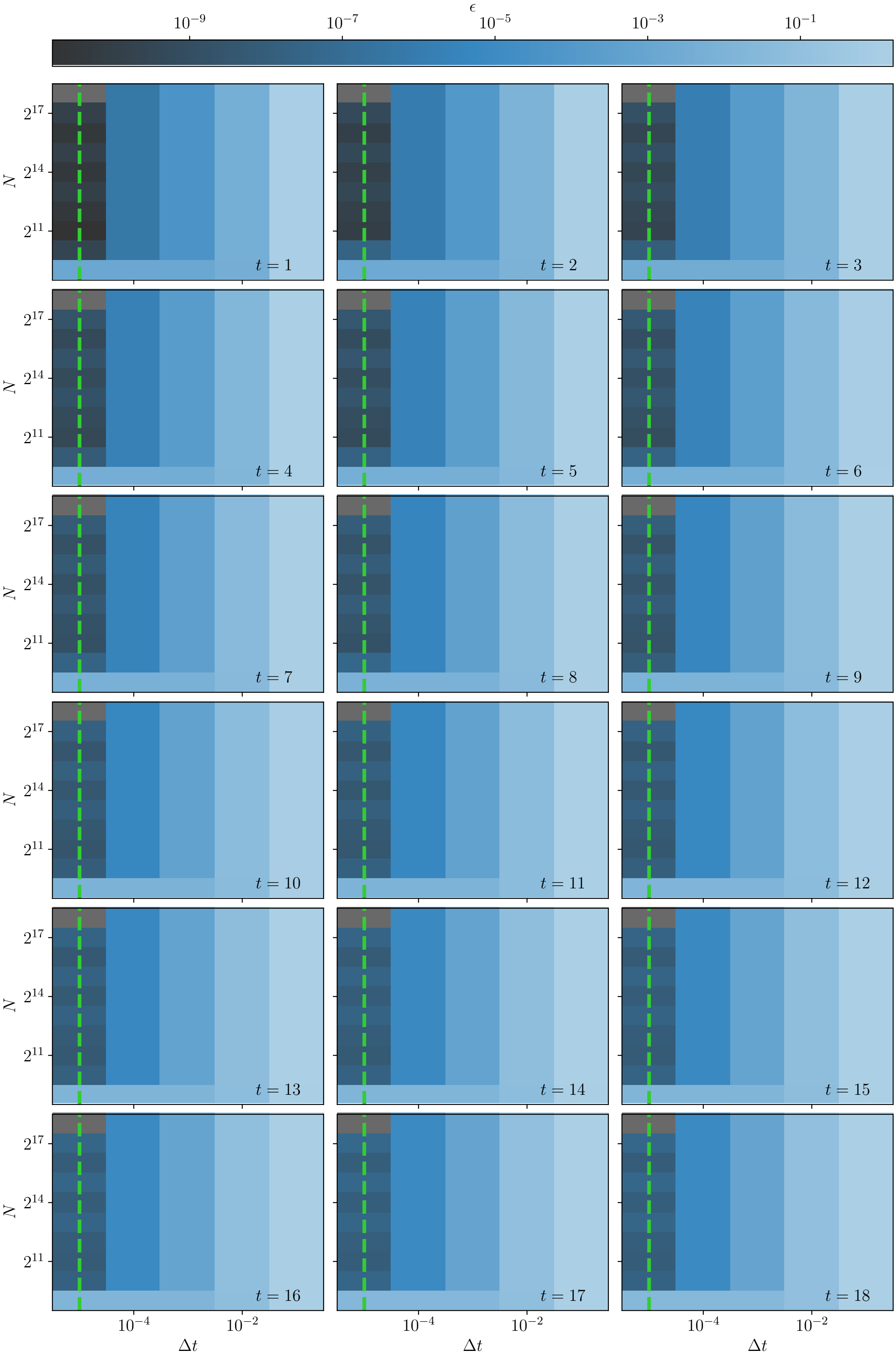

Figure B.1: Numerical error as a function of the spatio-temporal grid for $a = 1$ under SP evolution. Note the uniformity of ϵ in N.

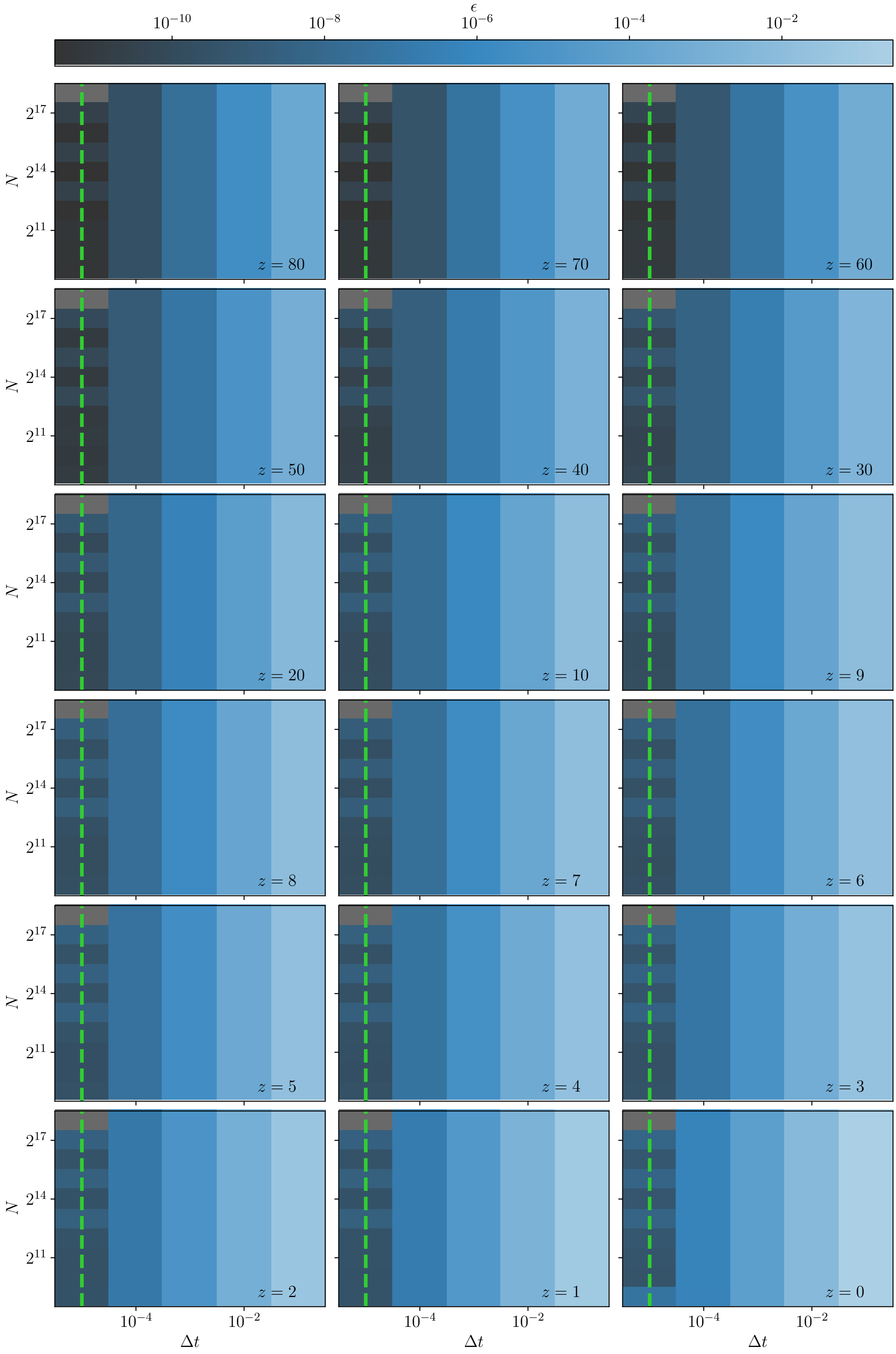

Figure B.2: Numerical error as a function of the spatio-temporal grid for dynamic a. Again, ϵ is independent of N.

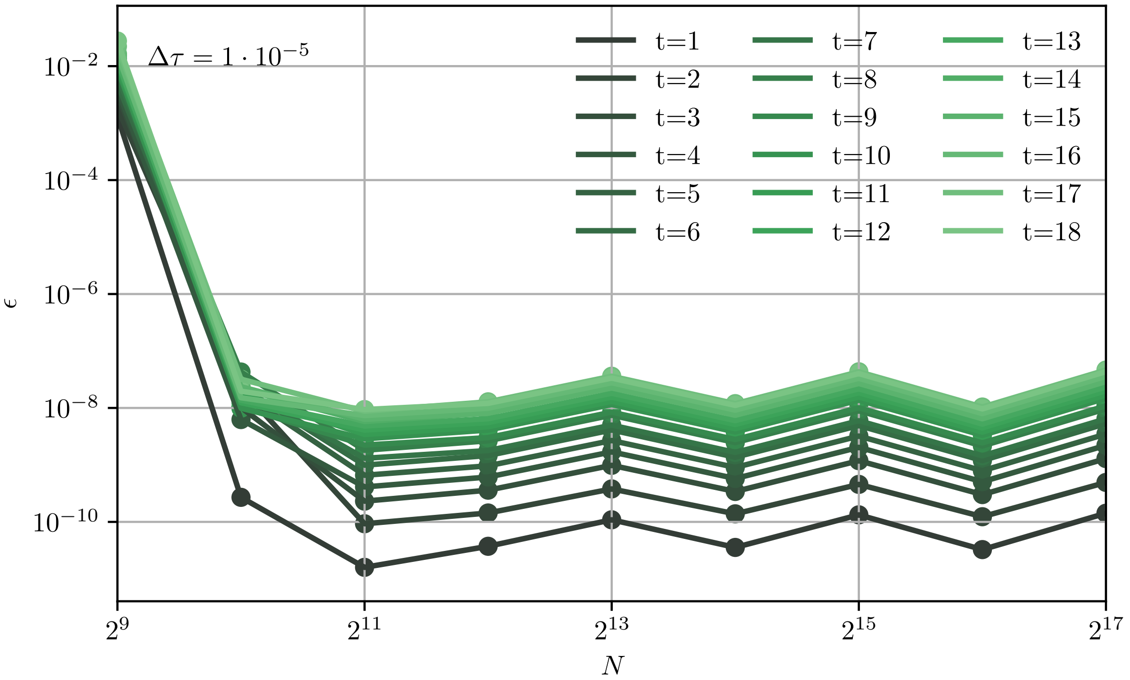

(a) static $a = 1$ space-time

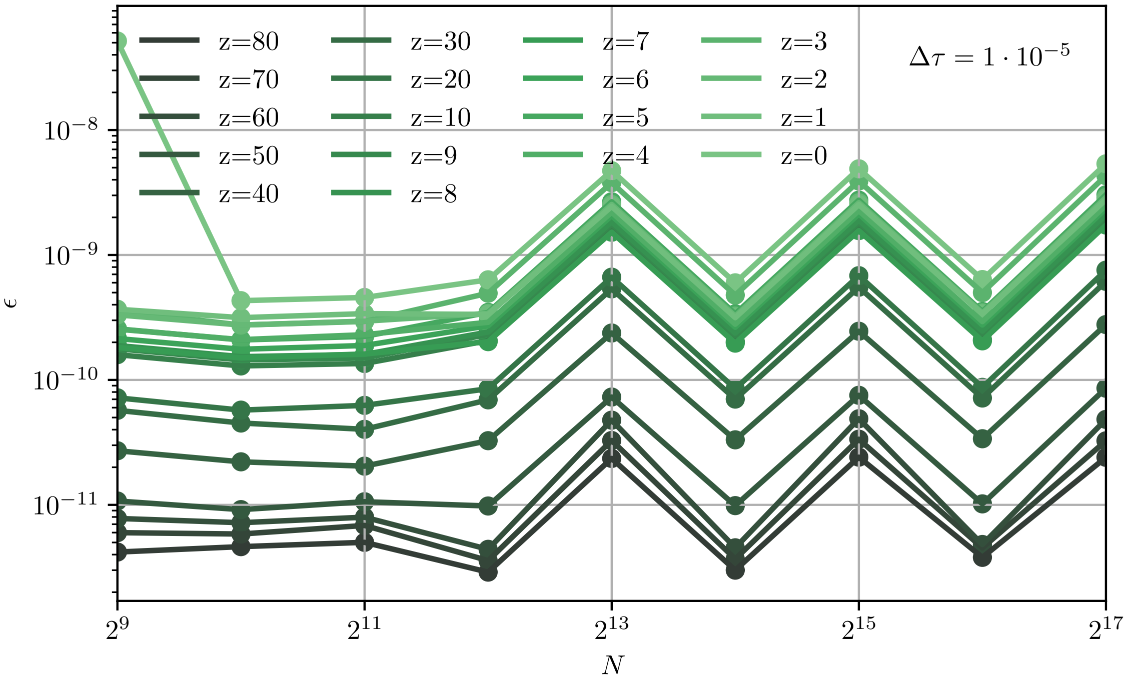

(b) expanding space-time.

Figure B.3: Numerical error at fixed $\Delta t = 10^{-5}$ under static (green line in Figure B.1) and expanding conditions (green line in Figure B.2).

An equal error scaling is found under expanding conditions which is depicted in Figure B.5. We conclude that the simplistic first-term Magnus approximation is effective for the non-autonomous Hamiltonian.

At last, $\mathcal{SM}^{[2]}$'s stability is assessed by following the numerical error as a function of the integration time. As indicated in section 4.4, a distinction has to be made based on the underlying cosmology. In a static-spacetime, Figure B.6 shows the numerical error is well under control for the entire integration time. In fact, ϵ scales roughly linearly in t for $(1+1)$-SP and PLAM. Figure B.6b shows additional oscillatory features under strong confinement. One can check by inspection of $|\psi|^2$ that these are associated with a periodic variation of the height and width of the emerging ground state. Such oscillations were also reported for $(3+1)$-SP in [60] and it was conjectured they arise due to interactions with the fluctuating background density.

For understanding the stability behavior of $\mathcal{SM}^{[2]}$ under *static* (1+1)-SP evolution, we can make contact with the mathematical literature. The author of [56] proofs the following for $(3+1)$-SP under free space conditions

Theorem. *Suppose the exact solution $\psi(\boldsymbol{x}, t')$ of $(3+1)$-SP is in $H^4(\mathbb{R}^3)$ for $0 \leq t' \leq t$. Then the numerical solution under $\mathcal{S}^{[2]}$, ψ^n, at time $t_n = n\Delta t$ has a second-order error bound in L_2:*

$$\|\psi^n - \psi(t_n)\|_2 \leq C(t)\Delta t^2 \ . \tag{B.19}$$

Here H^4 denotes the function space:

$$H^4(\mathbb{R}^3) \equiv \left\{\psi \in L^2(\mathbb{R}^3) : D^{\boldsymbol{\alpha}}\psi \in L^2(\mathbb{R}^3) \quad \forall \boldsymbol{\alpha} \quad \text{with} \quad |\boldsymbol{\alpha}| \leq 4\right\} \tag{B.20}$$

and recall $\mathcal{SM}^{[2]} = \mathcal{S}^{[2]}$ for $a = 1$. The author claims this result is easily extended to $(1+1)$-SP under periodic boundary conditions.

In fact, if we pick simulation runs with Δt_i and Δt_j then by application of the triangle inequality it is easy to see that eq. (B.19) implies:

$$\epsilon(t) \leq C(t)\Delta t_i^2 \left[1 + \left(\frac{\Delta t_j}{\Delta t_i}\right)^2\right] \ . \tag{B.21}$$

To check if this bound is satisfied, we revisit Figure B.6a and find cases with $\left(\frac{\Delta t_j}{\Delta t_i}\right) \approx 10$ lying at most two orders of magnitude apart. This is precisely the statement of the bracket term in eq. (B.19).

Once we allow space-time to expand, Figure B.7, the situation changes and an exponential error growth is observable past $z \lessapprox 10$. That said, if we restrict ourselves the small enough step sizes $\Delta t \leq 10^{-4}$ the error magnitude is still within reasonable limits.

B.2.3 $\mathcal{SM}^{[2]}$ vs. $\mathcal{BM}^{[4]}$

We conclude this section with a preliminary comparison between $\mathcal{SM}^{[2]}$ and $\mathcal{BM}^{[4]}$. To this end, the experimental setup of section B.2.2 was adopted. ψ_{ref} was integrated via $\mathcal{BM}^{[4]}$. We only focus on $(1+1)$-SP in the following. Results for PLAM are qualitatively identical.

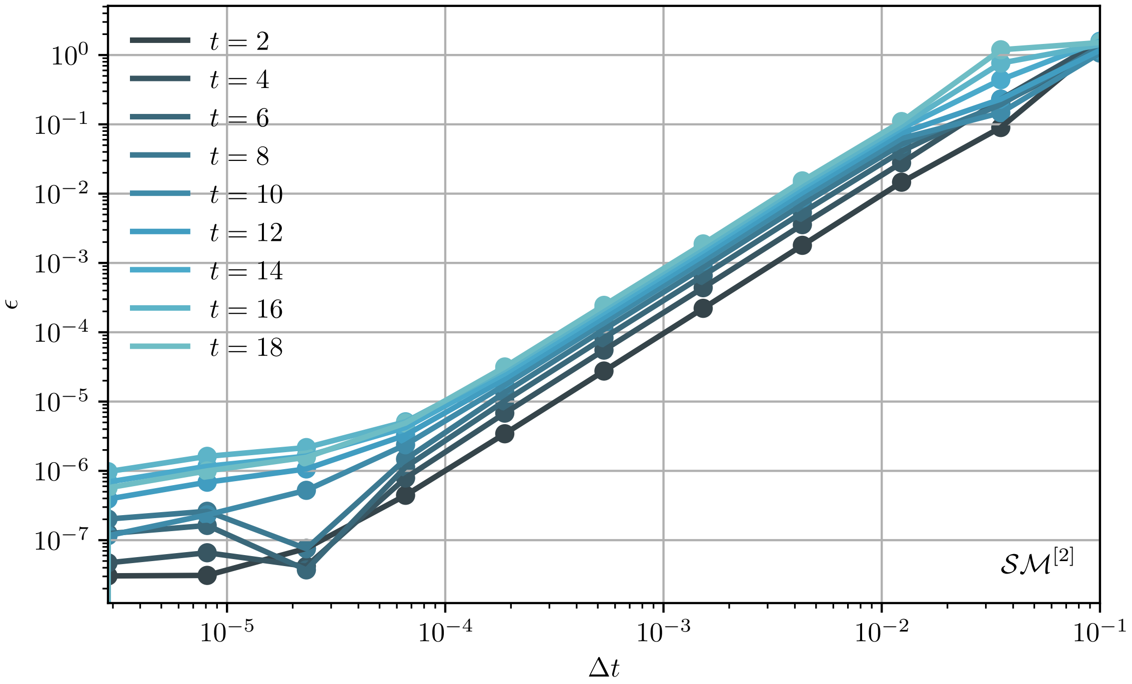

(a) $(1+1)$-SP

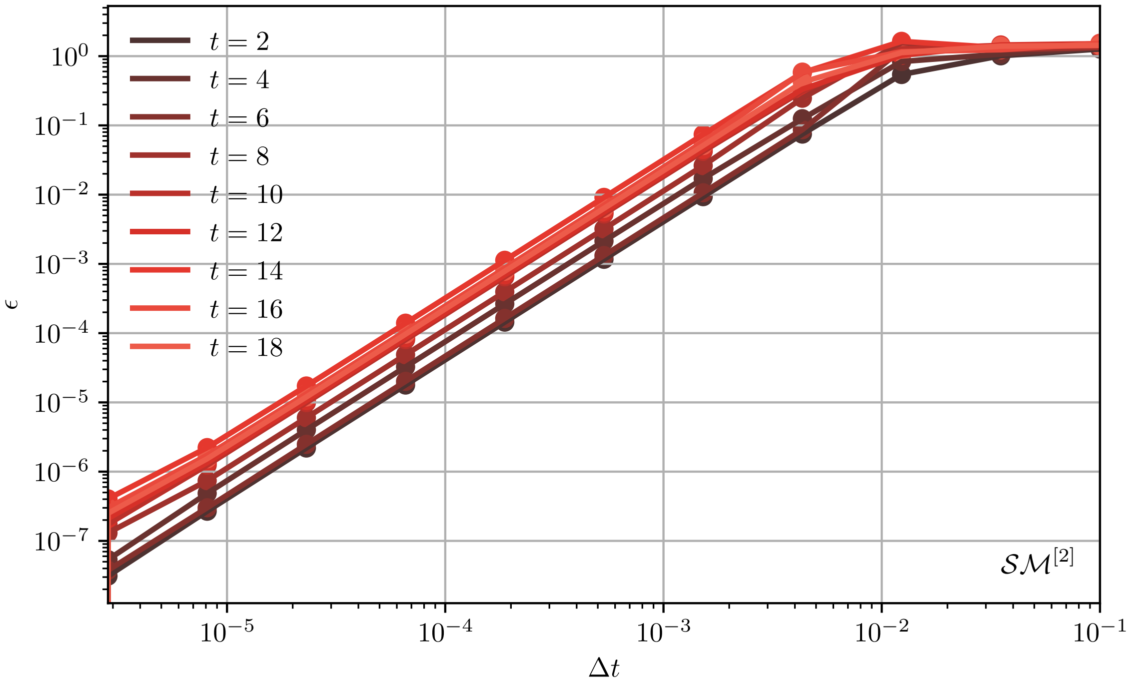

(b) PLAM

Figure B.4: Error scaling as a function of Δt for $a = 1$

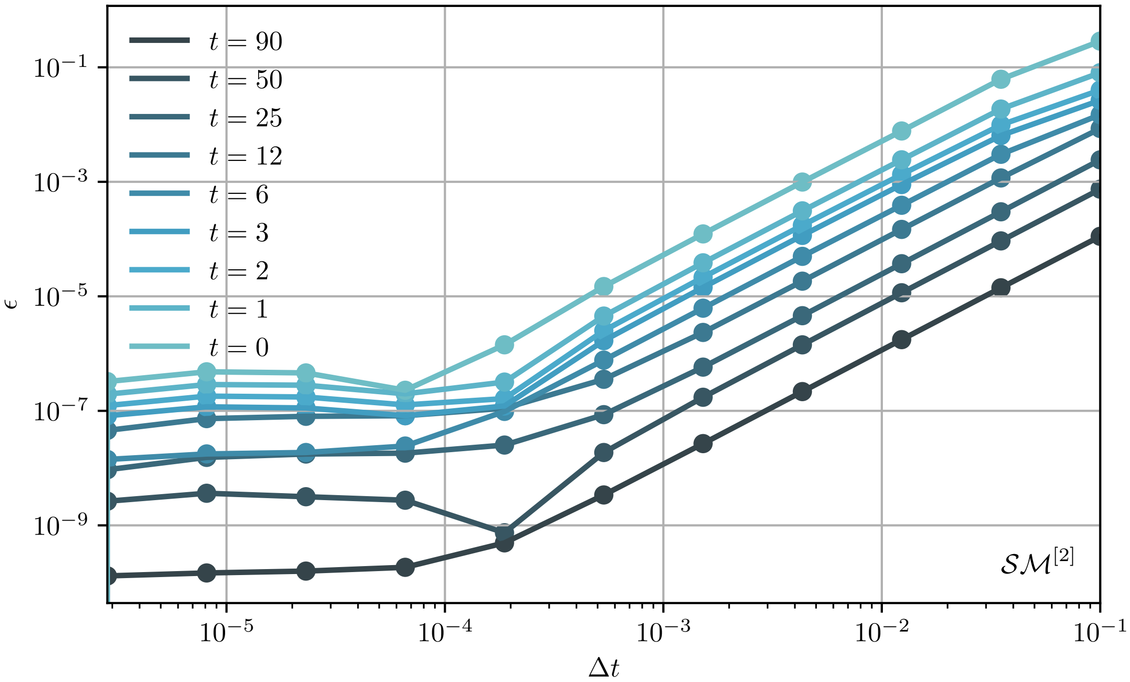

(a) $(1+1)$-SP

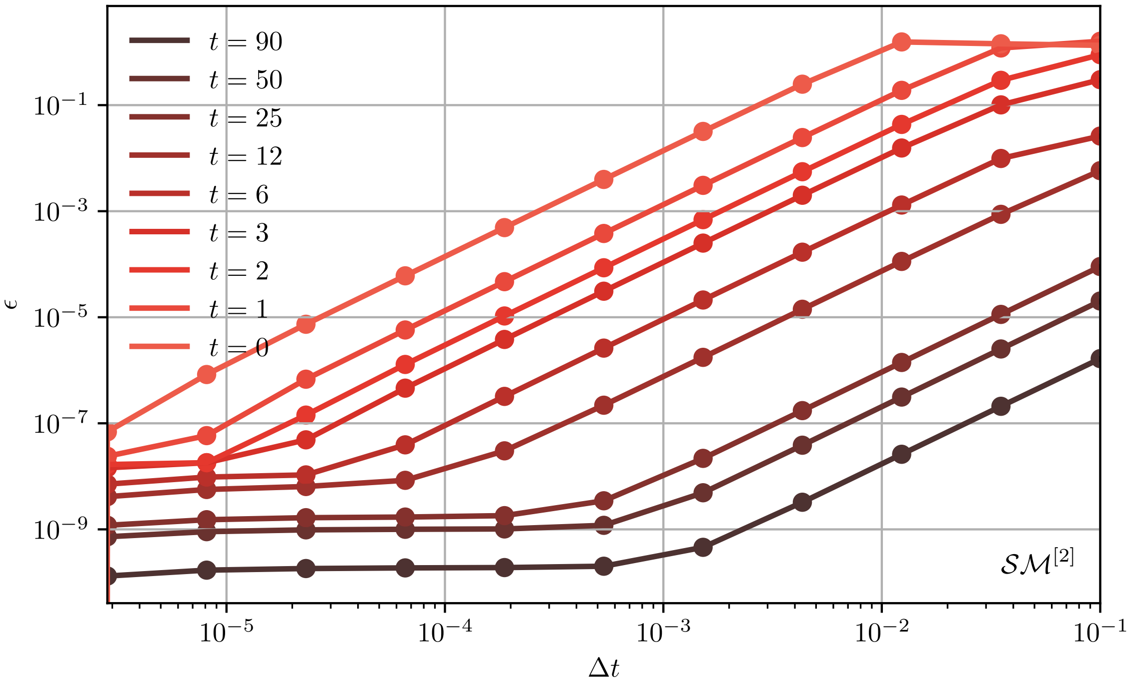

(b) PLAM

Figure B.5: Error scaling as a function of Δt in an expanding space-time

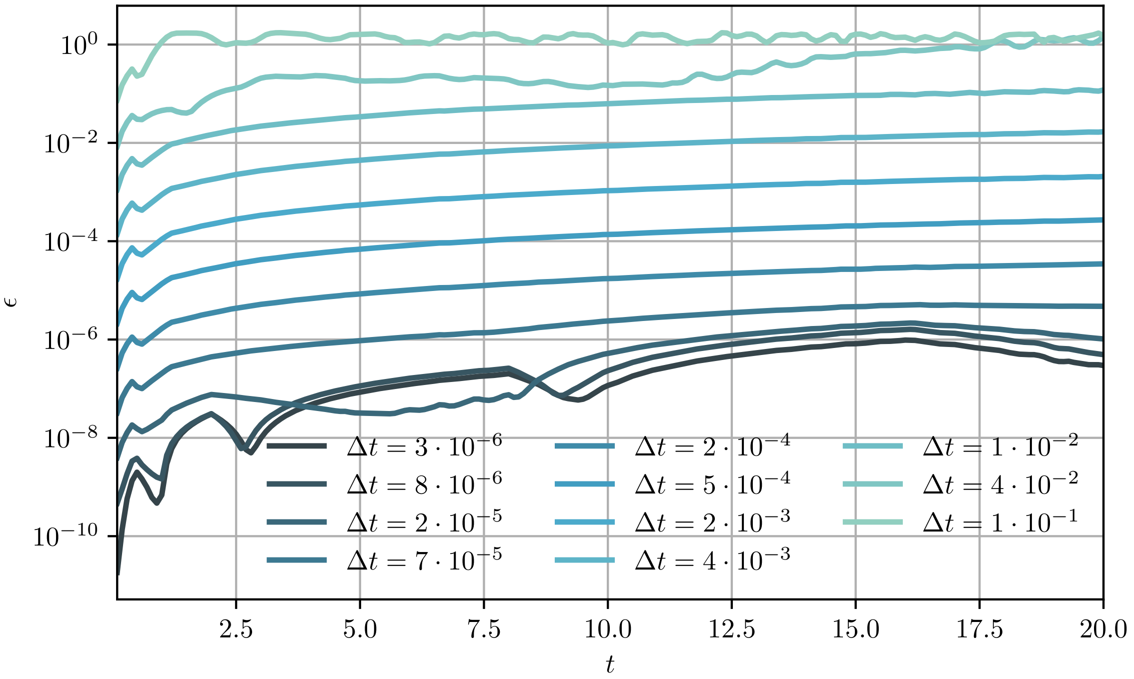

(a) $(1+1)$-SP

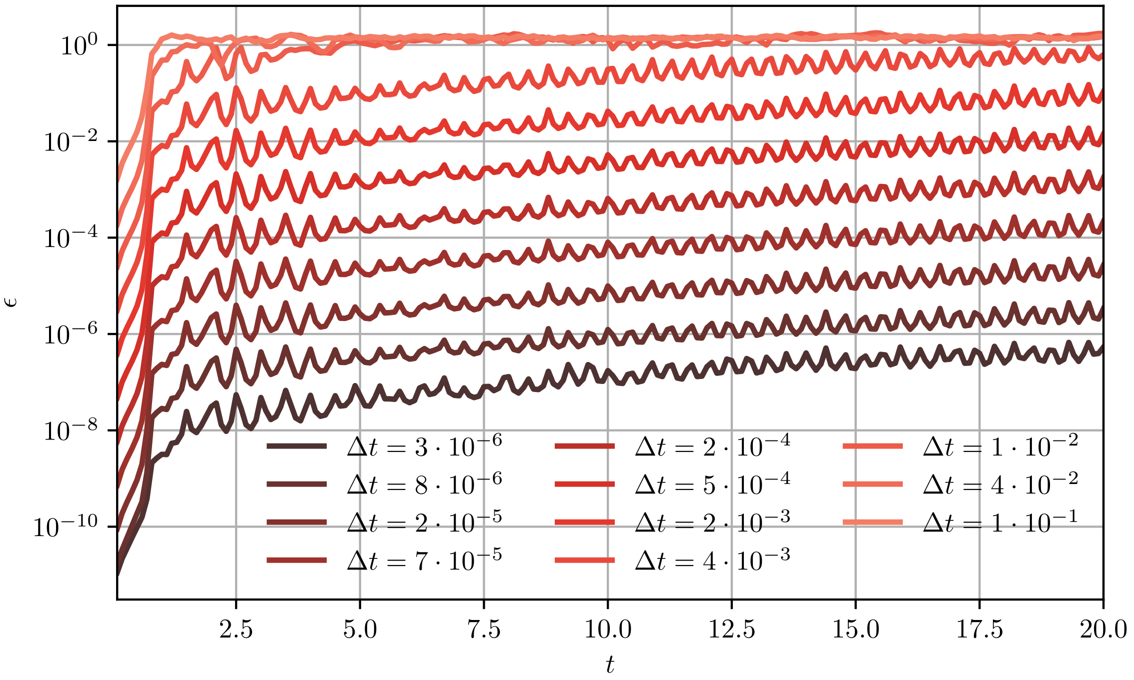

(b) PLAM. Oscillations are associated with the oscillation of the emerging ground state caused by interactions with the background density. See chapter 6.

Figure B.6: Error evolution of $\mathcal{SM}^{[2]}$ as a function of integration time t for $a = 1$.

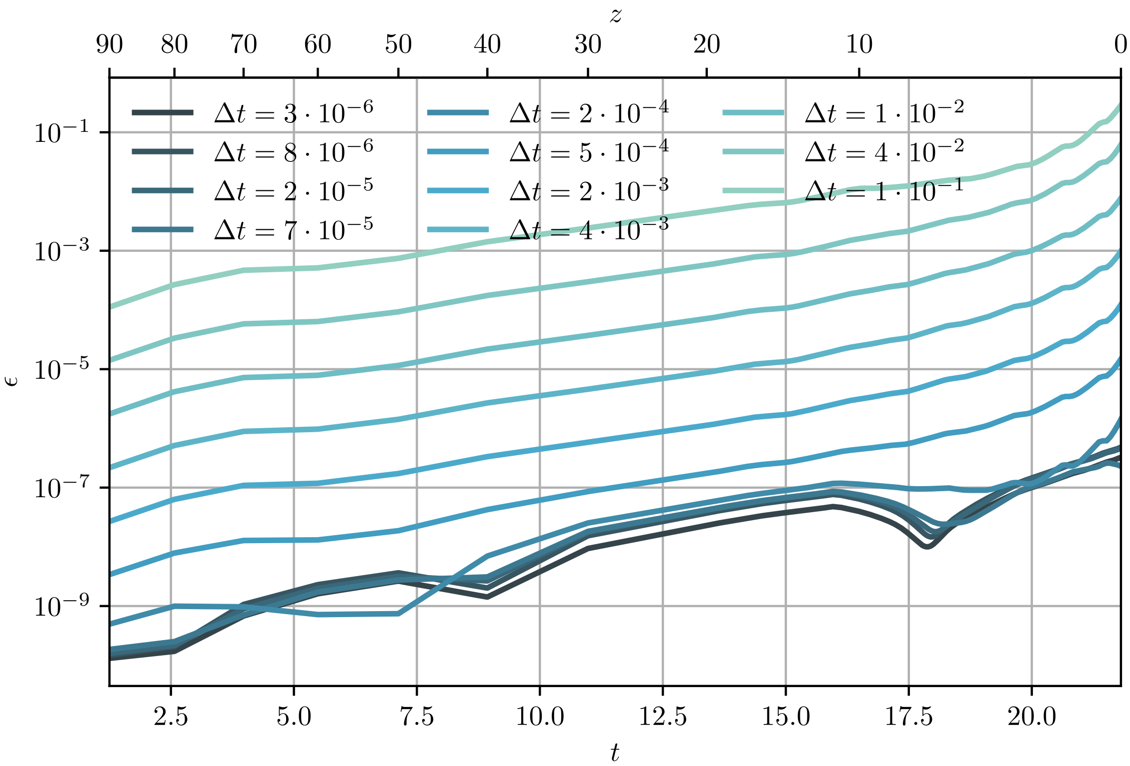

(a) $(1+1)$-SP

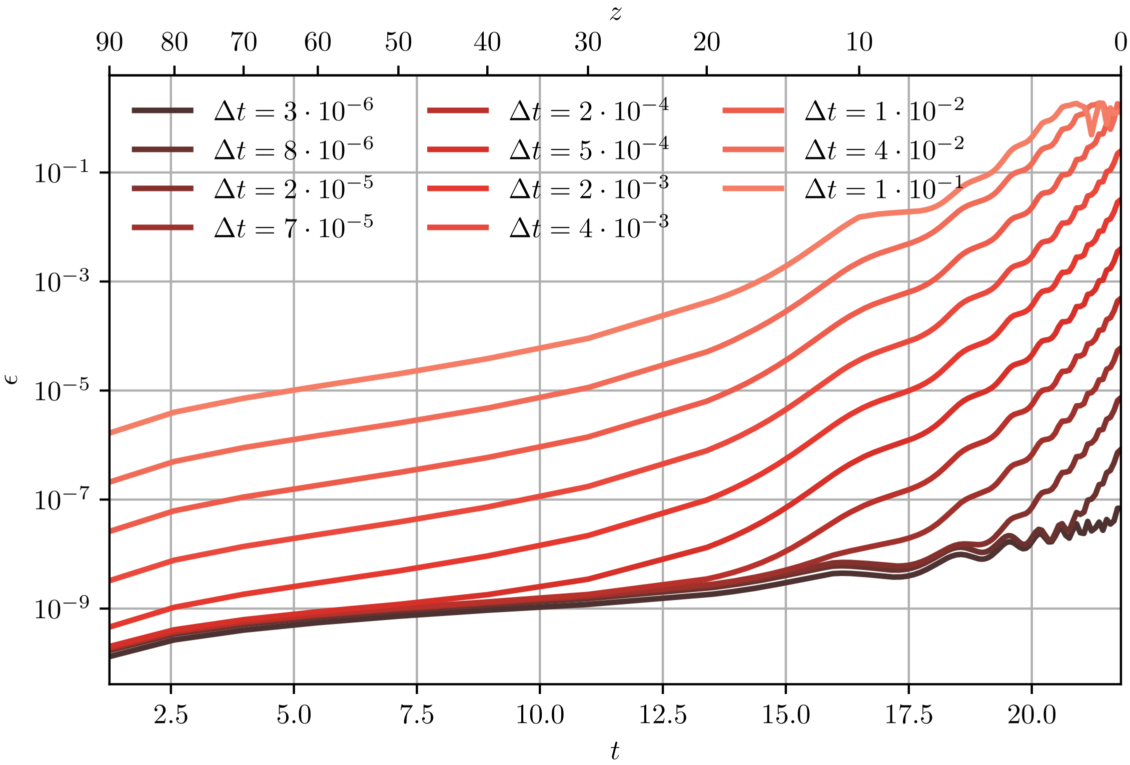

(b) PLAM

Figure B.7: Error evolution of $\mathcal{SM}^{[2]}$ as a function of integration time t under expansion.

Figure B.8 depicts the Δt scaling of the numerical error at final times $t_{\text{final}} = 20$ and $z_{\text{final}} = 0$ respectively. The quartic scaling of $\mathcal{BM}^{[4]}$ is clearly visible under static space-time conditions. Independently of whether the scale factor changes with time or not $\mathcal{BM}^{[4]}$ reaches a convergence plateau already for comparatively large time increments. This does not mean the $\mathcal{BM}^{[4]}$-integration is closer to the true solution than the result of $\mathcal{SM}^{[2]}$ — without an analytical solution to compare to we can only measure relative distances.

For the stability properties of $\mathcal{BM}^{[4]}$ consult Figure B.9. The behavior is generally the same as for $\mathcal{SM}^{[2]}$, i.e. linear stability for $a = 1$ but exponential error growth under expansion.

As discussed in section B.1, $\mathcal{BM}^{[4]}$ is a 6-stage method and therefore six times more expensive per step than $\mathcal{SM}^{[2]}$. Hence, its application is only justifiable if an increased time increment compensates or even outweighs the higher cost per step. Figure B.10 illustrates the efficiency of both integrators by plotting the final error as a function of required number of Fourier transformations. Based on this data, $\mathcal{BM}^{[4]}$ requires roughly a factor of 10^2 less transformations to achieve the same numerical error.

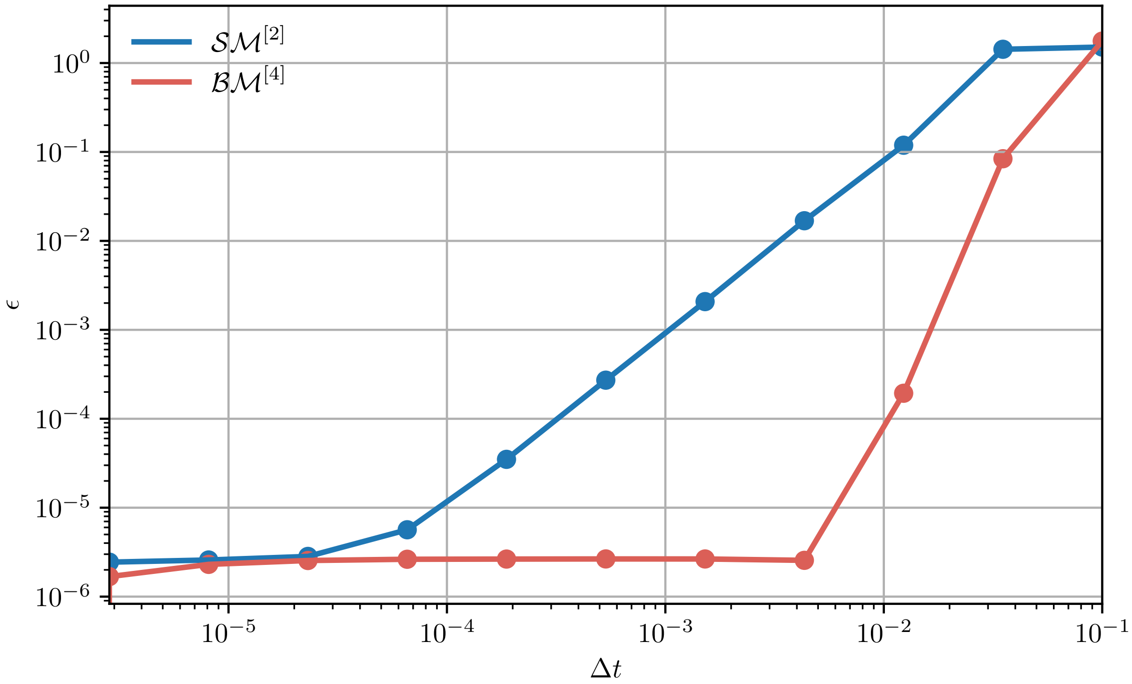

(a) Static Space-Time

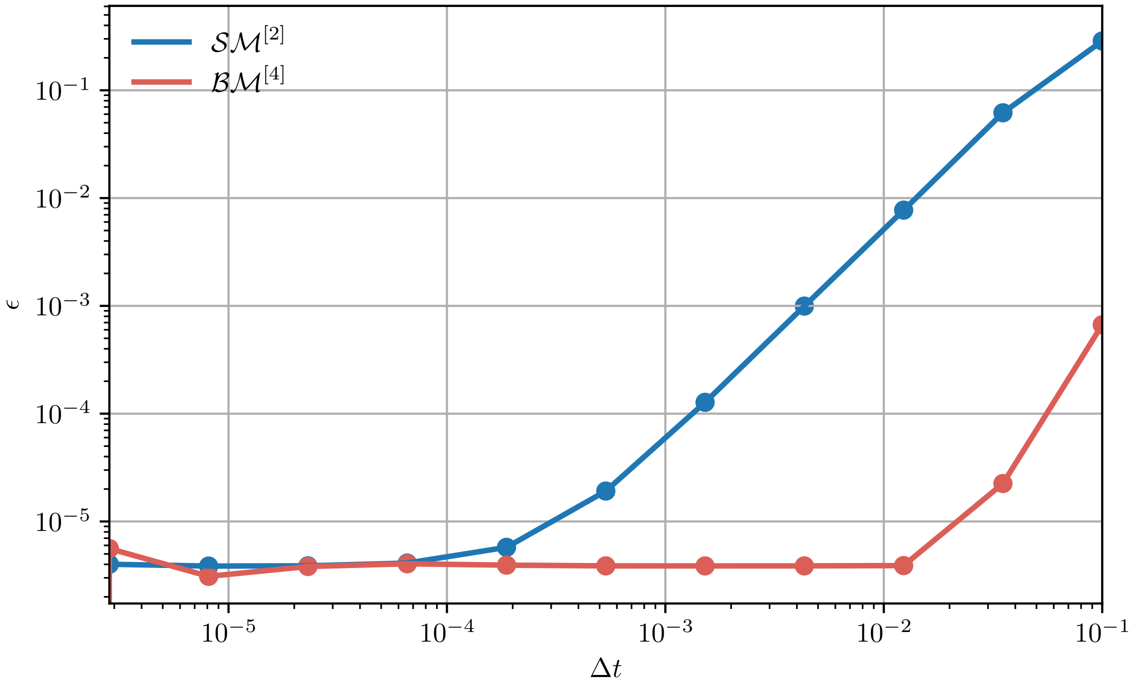

(b) Expanding Space-Time

Figure B.8: Comparison of the error scaling in $\mathcal{SM}^{[2]}$ and $\mathcal{BM}^{[4]}$ as a function of Δt at $t = 20$ (Figure B.8a) and $z = 0$ (Figure B.8b).

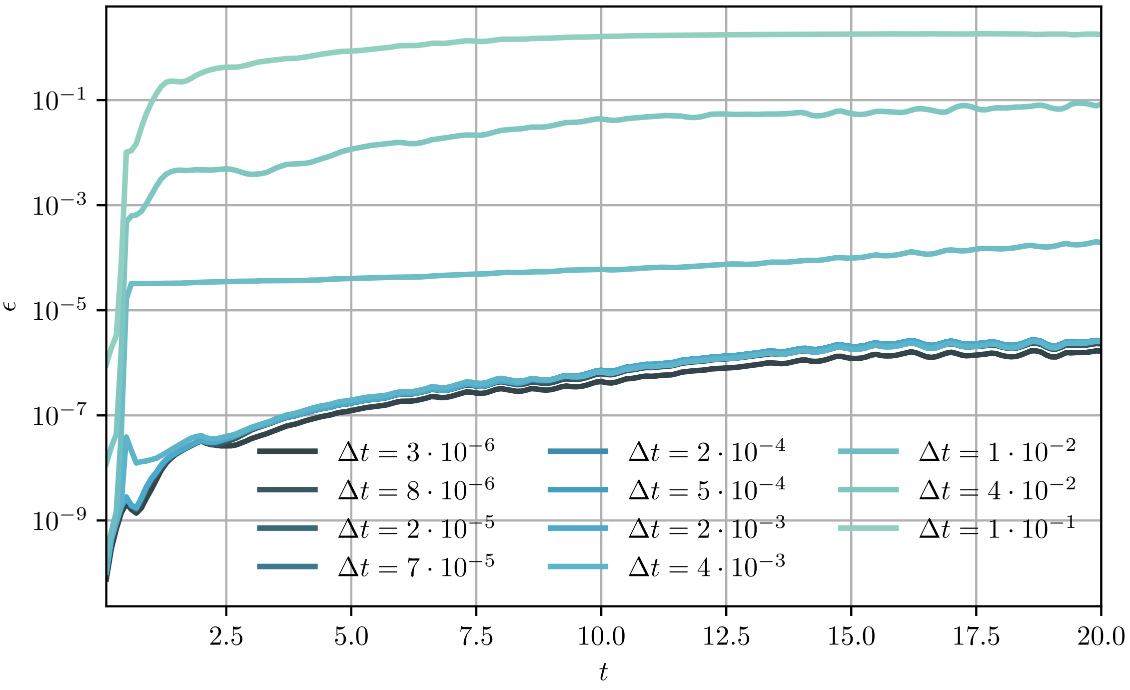

(a) Static Space-Time

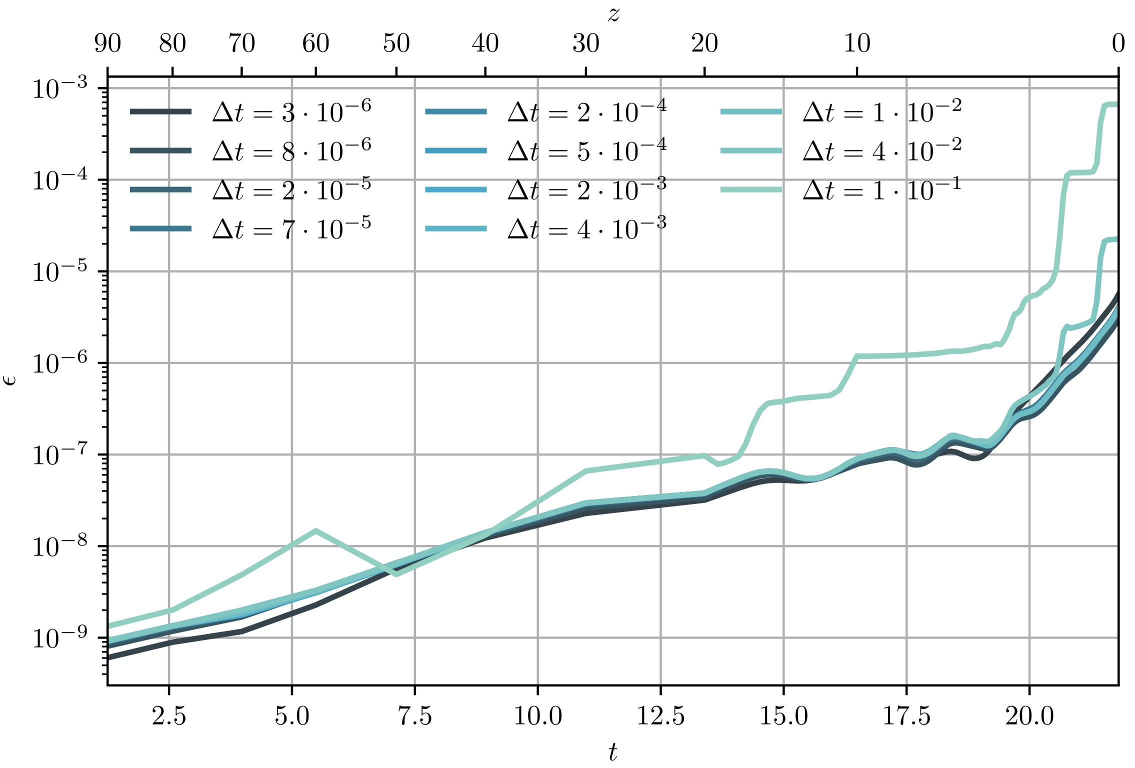

(b) Expanding Space-Time

Figure B.9: Error evolution of $\mathcal{BM}^{[4]}$ as a function of integration time t.

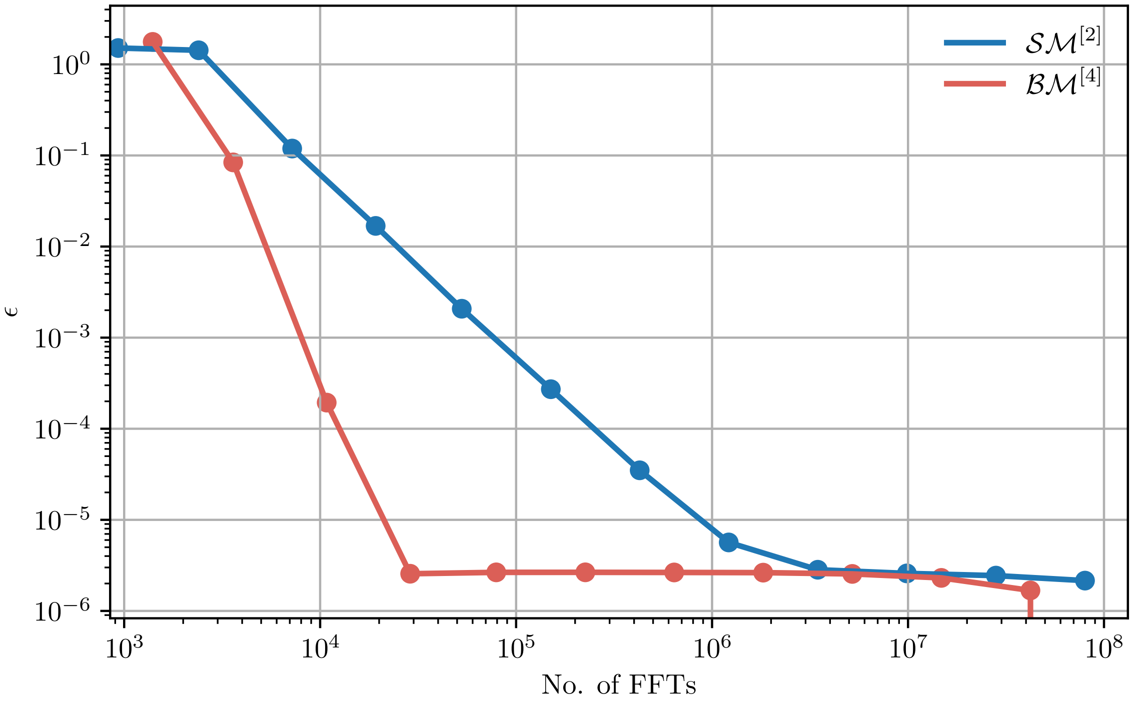

(a) Static Space-Time

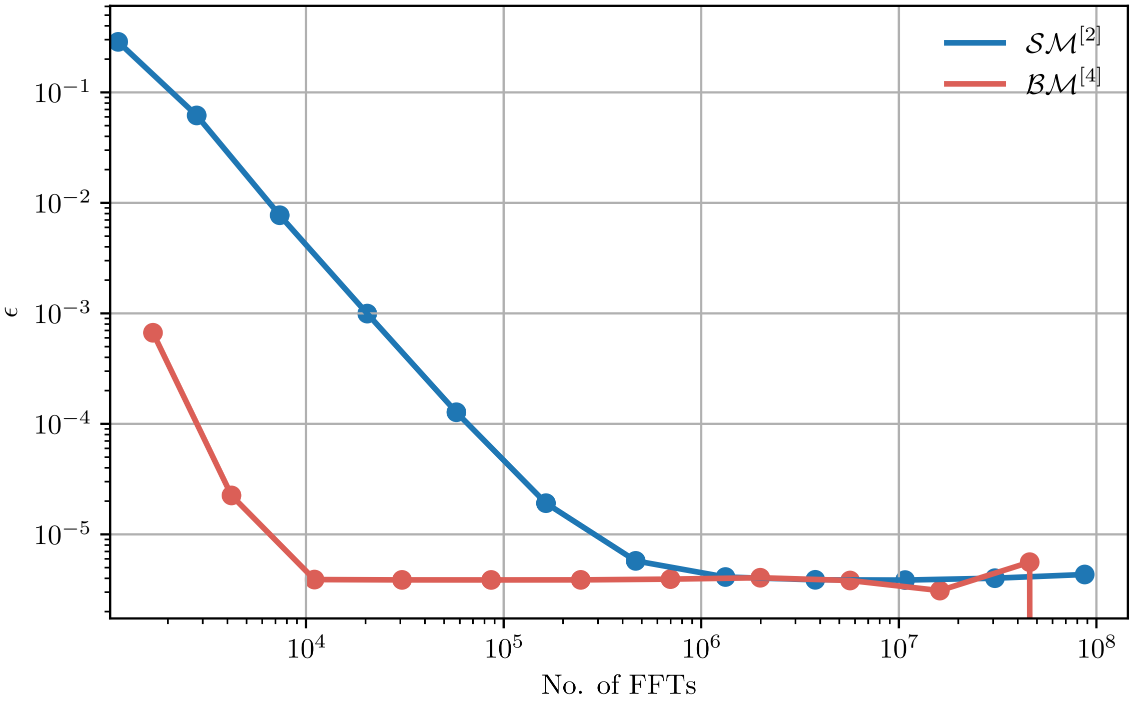

(b) Expanding Space-Time

Figure B.10: Comparison of the efficiency of $\mathcal{SM}^{[2]}$ and $\mathcal{BM}^{[4]}$ measured by the number of required FFTs to achieve a prescribed numerical error at $t = 20$ (Figure B.10a) and $z = 0$ (Figure B.10b).

Appendix C

Asymptotic Dynamics

C.1 Quantum Virial Theorem

Our task is to show:

$$-i\left\langle\psi\right|\left[\hat{G},\hat{H}\right]\left|\psi\right\rangle = 2\left\langle T\right\rangle - a(t)\left\langle x\partial_x V\right\rangle \tag{C.1}$$

with Hamiltonian:

$$\hat{H} = \frac{\hat{p}^2}{2} + a(t)\hat{V}(\hat{x}) \tag{C.2}$$

and $\hat{G} = \hat{p}\hat{x}$. Insertion yields:

$$-i\left\langle\psi\right|\left[\hat{G},\hat{H}\right]\left|\psi\right\rangle = -i\left\langle\psi\right|\frac{1}{2}\left[\hat{p}\hat{x},\hat{p}^2\right] + a(t)\left[\hat{p}\hat{x},\hat{V}\right]\left|\psi\right\rangle\ . \tag{C.3}$$

Consider the remaining two commutators individually:

$$\begin{aligned}\left[\hat{p}\hat{x},\hat{p}^2\right] = \hat{p}\hat{x}\hat{p}^2 - \hat{p}^3\hat{x} &= \hat{p}\left(\hat{x}\hat{p}^2 - \hat{p}^2\hat{x}\right)\\ &= \hat{p}\left(([\hat{x},\hat{p}] + \hat{p}\hat{x})\hat{p} - \hat{p}([\hat{p},\hat{x}] + \hat{x}\hat{p})\right)\\ &= \hat{p}\left((i + \hat{p}\hat{x})\hat{p} - \hat{p}(\hat{x}\hat{p} - i)\right)\\ &= 2i\hat{p}^2\ .\end{aligned} \tag{C.4}$$

To compute $\left[\hat{p}\hat{x},\hat{V}\right]$ we let it act on ψ:

$$\begin{aligned}\left[\hat{p}\hat{x},\hat{V}\right]\psi &= -i\left(\partial_x\left(xV\psi\right) - V\partial_x\left(x\psi\right)\right)\\ &= -i\left(V + x\partial_x V + xV\partial_x - V - Vx\partial_x\right)\psi\\ &= -ix\partial_x V\psi\ .\end{aligned} \tag{C.5}$$

So in total we have $\left[\hat{G},\hat{H}\right] = i\left(\hat{p}^2 - a(t)\hat{x}\widehat{\partial_x V}\right)$ and therefore:

$$-i\left\langle\psi\right|\left[\hat{G},\hat{H}\right]\left|\psi\right\rangle = \left\langle\hat{p}^2\right\rangle - a(t)\left\langle x\partial_x V\right\rangle = 2\left\langle T\right\rangle - a(t)\left\langle x\partial_x V\right\rangle\ . \tag{C.6}$$

C.2 Discrete Normalized Gradient Flow

Recall the equations of the continuous normalized gradient flow:

$$\partial_\tau \varphi = \frac{1}{2}\partial_x^2 \varphi - a(U^\pi * \varphi^2)\varphi + \mu[\varphi]\varphi \tag{C.7}$$

$$\mu[\varphi] = \frac{1}{\|\varphi\|_2^2}\int_\Omega \mathrm{d}x \left\{ \frac{1}{2}(\partial_x \varphi)^2 + a(U^\pi * \varphi^2)\varphi^2 \right\} \tag{C.8}$$

for which we need to devise a numerical method. Following [8, 7] we apply a *Lie-Trotter splitting* to eq. (C.7). Advancing the descent from $\tau_n \to \tau_{n+1} = \tau + \Delta\tau$ is then a two step process:

$$\begin{aligned} \varphi_1(\tau_n) &= \varphi_2(\tau_n)\ , \\ \partial_\tau \varphi_1 &= \frac{1}{2}\partial_x^2 \varphi_1 - a(U^\pi * \varphi_1^2)\varphi\ , \qquad \tau_n \le \tau \le \tau_{n+1}\ , \end{aligned} \tag{C.9}$$

followed by:

$$\begin{aligned} \varphi_2(\tau_n) &= \varphi_1(\tau_{n+1})\ , \\ \partial_\tau \varphi_2 &= \mu[\varphi_2]\varphi_2\ , \qquad \tau_n \le \tau \le \tau_{n+1}\ . \end{aligned} \tag{C.10}$$

Eq. (C.10) is a hard problem given the nonlinear, integral form of μ in eq. (C.8). So let's simplify even further and replace μ with a piecewise constant approximation:

To this end, we realize if one computes μ with φ_1 instead of φ_2 we find the convenient result:

$$\begin{aligned} \mu[\varphi_1] &= \frac{1}{\|\varphi_1\|_2^2}\int_\Omega \mathrm{d}x \left\{ \frac{1}{2}(\partial_x \varphi_1)^2 + a(U^\pi * \varphi_1^2)\varphi_1^2 \right\} \\ &\overset{(C.9)}{=} -\frac{1}{\|\varphi_1\|_2^2} \cdot \frac{1}{2}\frac{\mathrm{d}}{\mathrm{d}t}\left(\|\varphi_1\|_2^2\right) \\ &= -\frac{1}{2}\frac{\mathrm{d}}{\mathrm{d}t}\log\left(\|\varphi_1\|_2^2\right)\ . \end{aligned} \tag{C.11}$$

Hence, a simple approximation is:

$$\mu[\varphi_1] = -\frac{1}{2\Delta\tau}\log\left(\|\varphi_1(\tau_{n+1})\|_2^2\right)\ . \tag{C.12}$$

By replacing $\mu[\varphi_2]$ with the approximation for $\mu[\varphi_1]$ in eq. (C.10), we can solve the latter exactly:

$$\partial_\tau \varphi_2 = -\frac{1}{2\Delta\tau}\log\left(\|\varphi_1(\tau_{n+1})\|_2^2\right)\varphi_2 \quad \Rightarrow \quad \varphi_2(\tau_{n+1}) = \frac{\varphi_1(\tau_{n+1})}{\|\varphi_1(\tau_{n+1})\|_2}\ . \tag{C.13}$$

Thus, the approximated second splitting step is equivalent to a re-normalization of φ. We are left with the *discrete normalzied gradient flow*:

$$\begin{aligned} \varphi_1(\tau_n) &= \varphi_2(\tau_n)\ , \\ \partial_\tau \varphi_1 &= \frac{1}{2}\partial_x^2 \varphi_1 - a(U^\pi * \varphi_1^2)\varphi\ , \qquad \tau_n \le \tau \le \tau_{n+1}\ , \\ \varphi_2(\tau_{n+1}) &= \frac{\varphi_1(\tau_{n+1})}{\|\varphi_1(\tau_{n+1})\|_2}\ . \end{aligned} \tag{C.14}$$

The physics literature often terms eq. (C.14) *imaginary time propagation* as it follows directly by setting $\tau = it$ in the NLSE of eq. (4.1).

To make eq. (C.14) practical, [7] suggests a *forward, backward Euler* method:

$$\frac{\varphi_1^{n+1} - \varphi_1^n}{\Delta\tau} = \frac{1}{2}\partial_x^2 \varphi_1^{n+1} + \alpha(\varphi_1^n - \varphi_1^{n+1}) - a\left(U^\pi * (\varphi_1^n)^2\right)\varphi_1^n \, . \tag{C.15}$$

Here all nonlinear terms are evaluated at known time τ_n whereas the linear kinetic term is evaluated implicitly. Consequently, one linear system needs to be solved per step. To enlarge the stability region a stabilization parameter α is introduced. For the optimal choice of α and $\Delta\tau$ we refer to [7].

At last, we remark that the spatial discretization proceeds as in section 4.2.

C.3 Mass-Size Relation from Dimensional Analysis

This section derives eq. (6.36) by means of a dimensional analysis, [62], for eq. (6.29). To this end, we return to eq. (6.29), take its derivative and use Poisson's equation to eliminate the potential:

$$4\pi G m \rho_{\mathrm{GS}} = \frac{\hbar^2}{2ma^2}\partial_x^2\left(\frac{\partial_x^2\sqrt{\rho_{\mathrm{GS}}}}{\sqrt{\rho_{\mathrm{GS}}}}\right) \, . \tag{C.16}$$

Careful attention must be paid to ρ_{GS}. Recall from section 2.3.1 that in order to derive $(1+1)$-SP we assumed matter to be uniformly distributed in the orthogonal plane. Therefore, the surface density in orthogonal direction σ is constant and ρ_{GS} factorizes into:

$$\rho_{\mathrm{GS}}(x) = \varphi_{\mathrm{GS}}^2(x)\sigma \tag{C.17}$$

with φ_{GS}^2 having dimension $[\varphi_{\mathrm{GS}}^2] = ML^{-1}$. Accordingly, deriving the ground state φ_{GS} with mass M'_{GS} using the equation of hydrostatic equilibrium means simultaneously solving:

$$4\pi \cdot G m\sigma \cdot \varphi_{\mathrm{GS}}^2(x) = \frac{1}{2a^2}\cdot\frac{\hbar^2}{m}\cdot\partial_x^2\left(\frac{\partial_x^2\sqrt{\varphi_{\mathrm{GS}}^2}}{\sqrt{\varphi_{\mathrm{GS}}^2}}\right), \quad M'_{\mathrm{GS}} = \int \mathrm{d}x\varphi_{\mathrm{GS}}^2(x) \, . \tag{C.18}$$

To apply dimensional analysis we identify the dimensional and adimensional input parameters to eq. (C.18).

$$[Gm\sigma] = \frac{E}{ML}, \qquad \left[\frac{\hbar^2}{m}\right] = EL^2, \qquad [M'_{\mathrm{GS}}] = M, \qquad [a] = 1 \, . \tag{C.19}$$

All parameters can be dimensionally fully specified by the three fundamental, linearly independent, dimensions $\{E, L, M\}$. The *Buckingham-*Π*-Theorem* now assures that the total number of independent dimensionless parameters involved in eq. (C.18) is the number of adimensional input parameters (1) plus the number of dimensional input parameters (3) minus the number of fundamental dimensions involved (3). In other words, apart from the fixed scale factor a no product of rational powers of the input parameters exists which is free of dimensions. We conclude, any length scale of interest, R, must be of the form:

$$R = f(a)L' \tag{C.20}$$

with L' the length scale set by the dimensional input parameters of eq. (C.18) and f a function. One can easily check:

$$[L'] = \left[\left(\frac{\hbar^2}{m \cdot Gm\sigma \cdot M'_{\mathrm{GS}}}\right)^{\frac{1}{3}}\right] = L \tag{C.21}$$

so that

$$R = f(a)\left(\frac{\hbar^2}{Gm^2 M'_{\mathrm{GS}}}\right)^{\frac{1}{3}} . \tag{C.22}$$

To test this claim, we return to our dimensionless convention (2.52) and find:

$$RL^{\frac{1}{3}} = \text{const.} \cdot f(a) . \tag{C.23}$$

It should be noted that R is now the length scale of interest in dimensionless form as opposed to eq. (C.22) and L is the adimensional box size. If we specialize to $a = 1$, we expect:

$$R_{\mathrm{GS}} \propto L^{-\frac{1}{3}} = M_{\mathrm{GS}}^{-\frac{1}{3}} \tag{C.24}$$

for the extend of the ground state.

Bibliography

[1] Robert J. Adler. *The Geometry of Random Fields*. CAMBRIDGE, 2010. 184 pp. ISBN: 0898716934.

[2] Ann S. Almgren et al. “Nyx: A Massively Parallel AMR Code for Computational Cosmology”. In: *The Astrophysical Journal* 765.1 (Feb. 2013), p. 39. DOI: 10.1088/0004-637x/765/1/39.

[3] V. Alonso, Salvatore De Vincenzo, and Luis Gonzalez-Diaz. “On the Ehrenfest theorem in a one-dimensional box”. In: *Il Nuovo Cimento B* 115 (Feb. 2000).

[4] Luca Amendola and Riccardo Barbieri. “Dark matter from an ultra-light pseudo-Goldsone-boson”. In: *Physics Letters B* 642.3 (Nov. 2006), pp. 192–196. DOI: 10.1016/j.physletb.2006.08.069.

[5] Enrique Ruíz Arriola and Juan Soler. In: *Journal of Statistical Physics* 103.5/6 (2001), pp. 1069–1105. DOI: 10.1023/a:1010369224196.

[6] Winfried Auzinger et al. “Practical splitting methods for the adaptive integration of nonlinear evolution equations. Part I: Construction of optimized schemes and pairs of schemes”. In: *BIT Numerical Mathematics* 57.1 (July 2016), pp. 55–74. DOI: 10.1007/s10543-016-0626-9.

[7] Weizhu Bao, I-Liang Chern, and Fong Yin Lim. “Efficient and spectrally accurate numerical methods for computing ground and first excited states in Bose–Einstein condensates”. In: *Journal of Computational Physics* 219.2 (Dec. 2006), pp. 836–854. DOI: 10.1016/j.jcp.2006.04.019.

[8] Weizhu Bao and Qiang Du. “Computing the Ground State Solution of Bose–Einstein Condensates by a Normalized Gradient Flow”. In: *SIAM Journal on Scientific Computing* 25.5 (Jan. 2004), pp. 1674–1697. DOI: 10.1137/s1064827503422956.

[9] Weizhu Bao et al. “Dimension Reduction of the Schrödinger Equation with Coulomb and Anisotropic Confining Potentials”. In: *SIAM Journal on Applied Mathematics* 73.6 (Jan. 2013), pp. 2100–2123. DOI: 10.1137/13091436x.

[10] J. M. Bardeen et al. “The statistics of peaks of Gaussian random fields”. In: *The Astrophysical Journal* 304 (May 1986), p. 15. DOI: 10.1086/164143.

[11] Matthias Bartelmann. “General Relativity”. In: *Lecture Notes* (2019). DOI: 10.17885/HEIUP.534.

[12] Stefan Bildhauer, Thomas Buchert, and Masumi Kasai. “Solutions in Newtonian cosmology - The pancake theory with cosmological constant”. In: *Astronomy & Astrophysics* 263.1-2 (Sept. 1992), pp. 23–29. URL: https://ui.adsabs.harvard.edu/abs/1992A&A...263...23B.

[13] James Binney. “Discreteness effects in cosmological N-body simulations”. In: *Monthly Notices of the Royal Astronomical Society* 350.3 (May 2004), pp. 939–948. DOI: `10.1111/j.1365-2966.2004.07699.x`.

[14] S Blanes and F Casas. “Splitting methods for non-autonomous separable dynamical systems”. In: *Journal of Physics A: Mathematical and General* 39.19 (Apr. 2006), pp. 5405–5423. DOI: `10.1088/0305-4470/39/19/s05`.

[15] S. Blanes and P.C. Moan. “Practical symplectic partitioned Runge–Kutta and Runge–Kutta–Nyström methods”. In: *Journal of Computational and Applied Mathematics* 142.2 (May 2002), pp. 313–330. DOI: `10.1016/s0377-0427(01)00492-7`.

[16] S. Blanes et al. “The Magnus expansion and some of its applications”. In: *Physics Reports* 470.5-6 (Jan. 2009), pp. 151–238. DOI: `10.1016/j.physrep.2008.11.001`.

[17] James S. Bullock and Michael Boylan-Kolchin. “Small-Scale Challenges to the ΛCDM Paradigm”. In: *Annual Review of Astronomy and Astrophysics, vol. 55, pp. 343-387 (2017)* (2017). DOI: `10.1146/annurev-astro-091916-055313`. arXiv: `http://arxiv.org/abs/1707.04256v2 [astro-ph.CO]`.

[18] Carl DeBoor Carl de Boor. *A Practical Guide to Splines*. Springer-Verlag GmbH, 2001. ISBN: 0387953663.

[19] N.D. Cartwright. “A non-negative Wigner-type distribution”. In: *Physica A: Statistical Mechanics and its Applications* 83.1 (1976), pp. 210–212. DOI: `10.1016/0378-4371(76)90145-x`.

[20] P. H. Chavanis. “Growth of perturbations in an expanding universe with Bose-Einstein condensate dark matter”. In: *Astronomy & Astrophysics* 537 (Jan. 2012), A127. DOI: `10.1051/0004-6361/201116905`.

[21] Philippe Choquard, Joachim Stubbe, Marc Vuffray, et al. “Stationary solutions of the Schrödinger-Newton model—an ODE approach”. In: *Differential and integral equations* 21.7-8 (2008), pp. 665–679.

[22] Planck Collaboration. “Planck 2018 results. VI. Cosmological parameters”. In: (July 17, 2018). arXiv: `http://arxiv.org/abs/1807.06209v1 [astro-ph.CO]`.

[23] Scott Dodelson. *Modern Cosmology*. Elsevier LTD, Oxford, 2003. 440 pp. ISBN: 0122191412.

[24] Xuanchun Dong. “A short note on simplified pseudospectral methods for computing ground state and dynamics of spherically symmetric Schrödinger-Poisson-Slater system”. In: *Journal of Computational Physics* 230.22 (Sept. 2011), pp. 7917–7922. DOI: `10.1016/j.jcp.2011.07.026`.

[25] P. Ehrenfest. “Bemerkung über die angenäherte Gültigkeit der klassischen Mechanik innerhalb der Quantenmechanik”. In: *Zeitschrift für Physik* 45.7-8 (July 1927), pp. 455–457. DOI: `10.1007/bf01329203`.

[26] Jaan Einasto. “On the Construction of a Composite Model for the Galaxy and on the Determination of the System of Galactic Parameters”. In: *Trudy Astrofizicheskogo Instituta Alma-Ata* 5 (1965), pp. 87–100.

[27] Gerhard Wanner Ernst Hairer Christian Lubich. *Geometric Numerical Integration*. Springer-Verlag, 2006. DOI: 10.1007/3-540-30666-8.

[28] J. G. Esteve, F. Falceto, and Pulak Ranjan Giri. “Boundary contributions to the hypervirial theorem”. In: *Physical Review A* 85.2 (Feb. 2012). DOI: 10.1103/physreva.85.022104.

[29] V. Fock. “Bemerkung zum Virialsatz”. In: *Zeitschrift fuer Physik* 63.11-12 (Nov. 1930), pp. 855–858. DOI: 10.1007/bf01339281.

[30] Mark Galassi. *GNU scientific library : reference manual*. Bristol: Network Theory, 2009. ISBN: 0954612078.

[31] M. Garny and T. Konstandin. “Gravitational collapse in the Schrödinger-Poisson system”. In: *Journal of Cosmology and Astroparticle Physics* 2018.01 (Jan. 2018), pp. 009–009. DOI: 10.1088/1475-7516/2018/01/009.

[32] Mathias Garny, Thomas Konstandin, and Henrique Rubira. “The Schrödinger-Poisson method for Large-Scale Structure”. In: *Journal of Cosmology and Astroparticle Physics* 2020.04 (Apr. 2020), pp. 003–003. DOI: 10.1088/1475-7516/2020/04/003.

[33] Domenico Giulini and André Großardt. “The Schrödinger–Newton equation as a non-relativistic limit of self-gravitating Klein–Gordon and Dirac fields”. In: *Classical and Quantum Gravity* 29.21 (Oct. 2012), p. 215010. DOI: 10.1088/0264-9381/29/21/215010.

[34] Herbert Goldstein. *Classical mechanics*. San Francisco: Addison Wesley, 2002. ISBN: 9780201657029.

[35] Alma X. González-Morales, David J. E. Marsh, and Jorge Peñarrubiaand Luis A. Ureña-López. “Unbiased constraints on ultralight axion mass from dwarf spheroidal galaxies”. In: *Monthly Notices of the Royal Astronomical Society* 472.2 (Aug. 2017), pp. 1346–1360. DOI: 10.1093/mnras/stx1941.

[36] Gradshteyn, I. S. and Ryzhik, I. M. *Table of Integrals, Series, and Products*. Elsevier LTD, Oxford, 2014. ISBN: 0123849330.

[37] F. Siddhartha Guzman and L. Arturo Urena-Lopez. “Gravitational Cooling of Self-gravitating Bose Condensates”. In: *The Astrophysical Journal* 645.2 (July 2006), pp. 814–819. DOI: 10.1086/504508.

[38] F. Siddhartha Guzmán and L. Arturo Ureña-López. “Evolution of the Schrödinger-Newton system for a self-gravitating scalar field”. In: *Physical Review D* 69.12 (June 2004). DOI: 10.1103/physrevd.69.124033.

[39] Howard E. Haber and H. Arthur Weldon. “Thermodynamics of an Ultra-relativistic Ideal Bose Gas”. In: *Physical Review Letters* 46.23 (June 1981), pp. 1497–1500. DOI: 10.1103/physrevlett.46.1497.

[40] Renée Hlozek et al. “A search for ultralight axions using precision cosmological data”. In: *Physical Review D* 91.10 (May 2015). DOI: 10.1103/physrevd.91.103512.

[41] Wayne Hu, Rennan Barkana, and Andrei Gruzinov. “Fuzzy Cold Dark Matter: The Wave Properties of Ultralight Particles”. In: *Physical Review Letters* 85.6 (Aug. 2000), pp. 1158–1161. DOI: 10.1103/physrevlett.85.1158.

[42] Lam Hui et al. “Ultralight scalars as cosmological dark matter”. In: *Physical Review D* 95.4 (Feb. 2017). DOI: `10.1103/physrevd.95.043541`.

[43] Reinhard Illner, Paul F. Zweifel, and Horst Lange. “Global existence, uniqueness and asymptotic behaviour of solutions of the Wigner-Poisson and Schrödinger-Poisson systems”. In: *Mathematical Methods in the Applied Sciences* 17.5 (Apr. 1994), pp. 349–376. DOI: `10.1002/mma.1670170504`.

[44] Vid Iršič et al. “First Constraints on Fuzzy Dark Matter from Lyman- α Forest Data and Hydrodynamical Simulations”. In: *Physical Review Letters* 119.3 (July 2017). DOI: `10.1103/physrevlett.119.031302`.

[45] Tremaine Scott James Binney. *Galactic Dynamics*. Princeton University Press, 2008.

[46] Richard Jordan and Christophe Josserand. “Self-organization in nonlinear wave turbulence”. In: *Phys. Rev. E* 61 (2 Feb. 2000), pp. 1527–1539. DOI: `10.1103/PhysRevE.61.1527`.

[47] Oliver Dimon Kellogg. *Foundations of Potential Theory*. Springer Berlin Heidelberg, 1967. DOI: `10.1007/978-3-642-86748-4`.

[48] Claus Kiefer and Tejinder P. Singh. “Quantum gravitational corrections to the functional Schrödinger equation”. In: *Physical Review D* 44.4 (Aug. 1991), pp. 1067–1076. DOI: `10.1103/physrevd.44.1067`.

[49] Jonathan Klos. “Examining Numerical Accuracy of Cosmological Simulations based on the Schrödinger-Poisson System”. Bachelor Thesis. Heidelberg University, 2018.

[50] Georgios Konstantinou, Kyriakos Kyriakou, and Konstantinos Moulopoulos. “Emergent non-Hermitian contributions to the Ehrenfest and Hellmann-Feynman theorems”. In: (May 17, 2016). arXiv: `1605.06534v3 [quant-ph]`.

[51] Michael Kopp, Kyriakos Vattis, and Constantinos Skordis. “Solving the Vlasov equation in two spatial dimensions with the Schrödinger method”. In: *Physical Review D* 96.12 (Dec. 2017). DOI: `10.1103/physrevd.96.123532`.

[52] Sandro Stringari Lev. P. Pitaevskii. *Bose-Einstein Condensation and Superfluidity*. Oxford University Press, 2016. 576 pp. ISBN: 019875888X.

[53] Antony Lewis, Anthony Challinor, and Anthony Lasenby. “Efficient computation of CMB anisotropies in closed FRW models”. In: *ApJ* 538 (2000), pp. 473–476. DOI: `10.1086/309179`. arXiv: `astro-ph/9911177 [astro-ph]`.

[54] Xinyu Li, Lam Hui, and Greg L. Bryan. “Numerical and perturbative computations of the fuzzy dark matter model”. In: *Physical Review D* 99.6 (Mar. 2019). DOI: `10.1103/physrevd.99.063509`.

[55] Rainald Löhner. “An adaptive finite element scheme for transient problems in CFD”. In: *Computer Methods in Applied Mechanics and Engineering* 61.3 (Apr. 1987), pp. 323–338. DOI: `10.1016/0045-7825(87)90098-3`.

[56] Christian Lubich. “On splitting methods for Schrödinger-Poisson and cubic nonlinear Schrödinger equations”. In: *Mathematics of Computation* 77.264 (Feb. 2008), pp. 2141–2153. DOI: `10.1090/s0025-5718-08-02101-7`.

[57] D. Lynden-Bell. “Statistical Mechanics of Violent Relaxation in Stellar Systems”. In: *Monthly Notices of the Royal Astronomical Society* 136.1 (May 1967), pp. 101–121. DOI: `10.1093/mnras/136.1.101`.

[58] E. Madelung. “Quantentheorie in hydrodynamischer Form”. In: *Zeitschrift für Physik* 40.3-4 (Mar. 1927), pp. 322–326. DOI: `10.1007/bf01400372`.

[59] Simon L Marshall. “A periodic Green function for calculation of coloumbic lattice potentials”. In: *Journal of Physics: Condensed Matter* 12.21 (May 2000), pp. 4575–4601. DOI: `10.1088/0953-8984/12/21/304`.

[60] Philip Mocz et al. “Galaxy formation with BECDM – I. Turbulence and relaxation of idealized haloes”. In: *Monthly Notices of the Royal Astronomical Society* 471.4 (July 2017), pp. 4559–4570. DOI: `10.1093/mnras/stx1887`.

[61] Julio F. Navarro, Carlos S. Frenk, and Simon D. M. White. “The Structure of Cold Dark Matter Halos”. In: *The Astrophysical Journal* 462 (May 1996), p. 563. DOI: `10.1086/177173`.

[62] Maxim Olshanii. *Back-of-the-Envelope Quantum Mechanics*. WORLD SCIENTIFIC, Apr. 2013. DOI: `10.1142/8811`.

[63] D. B. Owen, Milton Abramowitz, and Irene A. Stegun. “Handbook of Mathematical Functions with Formulas, Graphs, and Mathematical Tables”. In: *Technometrics* 7.1 (Feb. 1965), p. 78. DOI: `10.2307/1266136`.

[64] P. J. E. Peebles. *Large-Scale Structure of the Universe*. Princeton University Press, 1980. 440 pp. ISBN: 0691082405.

[65] Antonio Picozzi and Josselin Garnier. “Incoherent Soliton Turbulence in Nonlocal Nonlinear Media”. In: *Physical Review Letters* 107.23 (Nov. 2011). DOI: `10.1103/physrevlett.107.233901`.

[66] J. M. Sanz-Serna and A. Portillo. “Classical numerical integrators for wave-packet dynamics”. In: *The Journal of Chemical Physics* 104.6 (Feb. 1996), pp. 2349–2355. DOI: `10.1063/1.470930`.

[67] Hsi-Yu Schive, Tzihong Chiueh, and Tom Broadhurst. “Cosmic structure as the quantum interference of a coherent dark wave”. In: *Nature Physics* 10.7 (June 2014), pp. 496–499. DOI: `10.1038/nphys2996`.

[68] Hsi-Yu Schive, Yu-Chih Tsai, and Tzihong Chiueh. “GAMER : A Graphic Processing Unit Accelerated Adaptive-Mesh-Refinement Code For Astrophysics”. In: *The Astrophysical Journal Supplement Series* 186.2 (Feb. 2010), pp. 457–484. DOI: `10.1088/0067-0049/186/2/457`.

[69] Hsi-Yu Schive et al. “Understanding the Core-Halo Relation of Quantum Wave Dark Matter from 3D Simulations”. In: *Physical Review Letters* 113.26 (Dec. 2014). DOI: `10.1103/physrevlett.113.261302`.

[70] A. E. Schulz et al. “Gravitational collapse in one dimension”. In: *Monthly Notices of the Royal Astronomical Society* 431.1 (Mar. 2013), pp. 49–62. DOI: `10.1093/mnras/stt073`.

[71] Bodo Schwabe, Jens C. Niemeyer, and Jan F. Engels. “Simulations of solitonic core mergers in ultralight axion dark matter cosmologies”. In: *Physical Review D* 94.4 (Aug. 2016). DOI: `10.1103/physrevd.94.043513`.

[72] Fernando Casas Sergio Blanes. *A Concise Introduction to Geometric Numerical Integration.* Apple Academic Press Inc., 2016. 218 pp. ISBN: 1482263424.

[73] Volker Springel et al. “Simulations of the formation, evolution and clustering of galaxies and quasars”. In: *Nature* 435.7042 (June 2005), pp. 629–636. DOI: `10.1038/nature03597`.

[74] A. Suárez and T. Matos. “Structure formation with scalar-field dark matter: the fluid approach”. In: *Monthly Notices of the Royal Astronomical Society* (July 2011), no–no. DOI: `10.1111/j.1365-2966.2011.19012.x`.

[75] Abril Suárez and Pierre-Henri Chavanis. “Hydrodynamic representation of the Klein-Gordon-Einstein equations in the weak field limit: General formalism and perturbations analysis”. In: *Physical Review D* 92.2 (July 2015). DOI: `10.1103/physrevd.92.023510`.

[76] Cora Uhlemann, Michael Kopp, and Thomas Haugg. “Schrödinger method as N-body double and UV completion of dust”. In: *Physical Review D* 90.2 (July 2014). DOI: `10.1103/physrevd.90.023517`.

[77] Timothy C. Wallstrom. “Inequivalence between the Schrödinger equation and the Madelung hydrodynamic equations”. In: *Physical Review A* 49.3 (Mar. 1994), pp. 1613–1617. DOI: `10.1103/physreva.49.1613`.

[78] Alfred Wehrl. “On the relation between classical and quantum-mechanical entropy”. In: *Reports on Mathematical Physics* 16.3 (Dec. 1979), pp. 353–358. DOI: `10.1016/0034-4877(79)90070-3`.

[79] Weinberg. *Gravitation and Cosmology.* John Wiley & Sons, 1972. 688 pp. ISBN: 0471925675.

[80] Edmond Weislinger and Gabriel Olivier. “The classical and quantum mechanical virial theorem”. In: *International Journal of Quantum Chemistry* 8.S8 (June 2009), pp. 389–401. DOI: `10.1002/qua.560080842`.

[81] Lawrence M. Widrow and Nick Kaiser. “Using the Schroedinger Equation to Simulate Collisionless Matter”. In: *The Astrophysical Journal* 416 (Oct. 1993), p. L71. DOI: `10.1086/187073`.

[82] Tak-Pong Woo and Tzihong Chiueh. “High-Resolution Simulation on Structure Formation with Extremely Light Bosonic Matter”. In: *The Astrophysical Journal* 697.1 (May 2009), pp. 850–861. DOI: `10.1088/0004-637x/697/1/850`.

[83] VE Zakharov et al. “Soliton turbulence”. In: *JETP Lett* 48.2 (1988), pp. 79–82.

[84] Jiajun Zhang, Hantao Liu, and Ming-Chung Chu. “Cosmological Simulation for Fuzzy Dark Matter Model”. In: *Frontiers in Astronomy and Space Sciences* 5 (Jan. 2019). DOI: `10.3389/fspas.2018.00048`.

[85] Tim Zimmermann. “A Simple Model for the Temporal Evolution of Cold Dark Matter”. Master Thesis. Heidelberg University, 2018.

[86] Tim Zimmermann et al. “A Quantum Model for the Dynamics of Cold Dark Matter”. In: *Condensed Matter* 4.4 (Nov. 2019), p. 89. DOI: `10.3390/condmat4040089`.

Acknowledgement

The author acknowledges support by the state of Baden-Württemberg through bwHPC, the DAAD through granting of a PROMOS scholarship and the kind hospitality of the Physics Department of the Univeristy of Parma during a 2 month research stay in Nov-Dev 2019.

On a more personal note, I would like to offer my special thanks to Luca Amendola, Massimo Pietroni and Javier Madroñero for all the insightful discussions on cosmology, fuzzy dark matter and numerics in general. These discussions formed the backbone of my research and made this thesis possible in the first place.

My special appreciation goes to Sandro Wimberger for his continuous support throughout the entire time of this research project and his endless patience and confidence in my work, especially when I went through personal, somewhat rough waters. *Grazie mille!*

Erklärung

Ich versichere, dass ich diese Arbeit selbstständig verfasst und keine anderen als die angegebenen Quellen und Hilfsmittel benutzt habe.

Heidelberg, den 30.07.2020.